AN INTEGRATED SECURITY-CONSTRAINED MODEL-BASED DYNAMIC POWER MANAGEMENT APPROACH FOR ISOLATED MICROGRID POWER SYSTEMS

A Dissertation

by

SALMAN MASHAYEKH

Submitted to the Office of Graduate and Professional Studies of
Texas A&M University
in partial fulfillment of the requirements for the degree of

DOCTOR OF PHILOSOPHY

Chair of Committee,	Karen L. Butler-Purry
Committee Members,	Sergiy Butenko
	Mehrdad Ehsani
	Jose Silva-Martinez
Head of Department,	Chanan Singh

December 2013

Major Subject: Electrical Engineering

ABSTRACT

Microgrid power systems draw lots of interests in marine, aerospace, and electric vehicle applications and are drawing increased attention for terrestrial applications. These power systems, however, are prone to large frequency and voltage deviations, when disturbances happen. Therefore, an effective power management method is needed to operate microgrids optimally, while satisfying operating and security constraints.

In this dissertation, a new Integrated Security-Constrained Power Management (ISCPM) method is presented for isolated microgrid power systems during normal/alert operating states. The new ISCPM method was formulated as a multi-objective optimal control problem, in which set-points of several system control methods are minimally adjusted, subject to operating and security constraints, over a period in the future. To solve the ISCPM multi-objective optimal control problem, an evolutionary algorithm based on the Nondominated Sorting GA II (NSGA-II) was developed, in which the optimization solver is linked to a fast simulation core. A fuzzy membership based method was developed to identify the best compromise solution.

The new power management method was implemented on a notional computer model for an all-electric ship. The NSGA-II was developed in MATLAB, by adapting a general purpose GA toolbox, IlliGAL. To conduct transient simulations during the GA iterations, the simulation core of the TSAT Tool of *Tools*$^{\text{TM}}$ software package was used. The best compromise solution identification method was developed in MATLAB.

To illustrate how the new ISCPM method works in the notional all-electric ship model, several case studies were presented. Also, to evaluate the performance of the new ISCPM method, extensive studies were conducted. For these studies, a detailed electromagnetic transient model of the system in PSCAD was used. The performance analysis addressed quality of the new method from power system operation and multi-objective optimization perspectives. The results indicated that the new ISCPM method could effectively operate the system in an overall near-optimal condition, in which security and operating constraints

are also satisfied.

The application of the new power management method is not limited to all-electric shipboard power systems and it has great potential to be extended to other types of isolated microgrid power systems.

DEDICATION

To my lovely wife, Fatemeh,

who supported me each step of the way.

ACKNOWLEDGEMENTS

First and foremost, I thank God for giving me strength and confidence in every step of my life and for helping me succeed.

Thanks to my advisor, Dr. Karen L. Butler-Purry, for her patience, guidance and support. I thank her for encouraging me at difficult times and always believing in me. Thanks for all her efforts to support me, financially, throughout my PhD study. I learned from her not only about academics, but also about discipline and hard work.

I thank Dr. Shankar Bhattacharyya, Dr. Sergiy Butenko, Dr. Mehrdad Ehsani, and Dr. Jose Silva-Martinez for their time in serving on my committee. I would also like to thank the faculty and staff in the electrical and computer engineering department, for making my PhD years at Texas A&M University a great experience. My special thanks go to Tammy Carda and Jeanie Marshall in the department graduate office for patiently answering our questions day by day and helping us in any way they could.

Thanks to all of my friends and colleagues at the Power System Automation Laboratory. I thank them for all of the discussions we had, for all of the problems we solved together, and all of the fun we had together. During my years at PSAL, I came to know people from all around the world. I made very good friends from America, China, Ghana, India, Iran, Peru, Taiwan, and Trinidad and Tobago. I wish all of them the bests.

Last but not least, countless thanks to my wife, mother, father, and two brothers for their love, support, encouragement, and patience. My wife stood by me and encouraged me any time I struggled during these years. My parents always encouraged me towards higher education and provided me with anything I needed to succeed. Although they are far away, I always feel their warm presence and support. I owe my family everything that I have ever achieved in my life.

TABLE OF CONTENTS

LIST OF FIGURES

LIST OF TABLES

1 INTRODUCTION

1.1 Preface

Microgrid power systems draw lots of interests in marine, aerospace, and electric vehicle applications and are drawing increased attention for terrestrial applications. Microgrid power systems have limited generation and finite inertia compared with large power systems. Moreover, these systems usually include large portions of dynamic loads and nonlinear loads relative to the total system capacity, which may reduce the stability margin. Also, some microgrid power systems include high energy pulse loads, which draw large amounts of power in short periods of time [1], and may cause significant frequency and voltage oscillations. Thus, an effective power management method is needed for isolated microgrid power systems, which operates the system optimally, while satisfying the operating and security constraints.

The power management objectives depend on the operating conditions of the system [2], which are classified into several operating states, including normal state, alert state, emergency state, and restorative state [2]. The concept that distinguishes the normal and alert states from the other two states, is power system security. The concept of system security is defined as the ability of the power system to withstand credible events or contingencies without supply interruption of system loads [3]. In the normal/alert operating states, a Power Management System (PMS) aims to operate the system optimally, while satisfying the security constraints [2].

In a power system, several control methods are responsible for achieving the power management objectives. Some of these control methods operate directly on individual system elements (local controllers) and others operate in higher levels in the system [4]. Examples of local controllers are generator prime mover and excitation controls, and generation dispatch and reactive power control methods are examples of higher level controllers. To develop a security-constrained power management method, set-points from a single control method [5, 6] or several control methods [7] can be manipulated.

The advantage of the latter option, or integrated security-constrained power management methods, is that they can effectively maintain the system security regarding various security aspects, such as frequency, voltage, and transient stability.

The main shortcoming of many of the existing security-constrained power management methods for use in isolated microgrid power systems is that they only take into consideration the security constraints against N-1 contingencies [5, 6, 8–11]. However, in isolated microgrid power systems, normal load changes may also cause significant frequency and voltage oscillations [12]. Thus, the security constraints against planned events must also be included in the power management methods for many isolated microgrid power systems.

In this dissertation, a new Integrated Security-Constrained Power Management (ISCPM) method is presented for use during the normal/alert states in isolated microgrid power systems. The new power management method is formulated as a Multi-Objective Optimal Control (MOOC) problem, in which the set-points provided by various system control methods are minimally adjusted, to satisfy the security constraints against planned and unplanned events. To solve the formulated MOOC problem in the new ISCPM method, an approach based on an evolutionary multi-objective optimization solver called Nondominated Sorting GA II (NSGA-II), is developed. To illustrate how the new ISCPM method works and evaluate its performance, a notional isolated microgrid power system computer model for an all-electric ship is studied in this work.

The major contributions in this dissertation are in five areas. First, a new integrated security-constrained power management method for isolated microgrid power systems during normal/alert operating states was developed. The new power management method was formulated as a multi-objective optimal control problem, in which adjustments to set-points of the dynamic generation dispatch and dynamic voltage/VAr control methods are minimized, while satisfying the security constraints. Unlike many of the existing power management approaches (mostly for transmission networks), the new power management method uses a dynamic optimization approach, which optimizes the system behavior

over a time horizon including several operating points. This feature enables the new power management method to effectively control the magnitude and duration of frequency, voltage, and current oscillations, during disturbances including load changes in an isolated power system.

Second, a heuristic multi-objective optimization solving method was developed, based on the Nondominated Sorting GA II (NSGA-II). A model-based approach was developed which links the multi-objective optimization solver to a fast simulation core that conducts transient simulations of the power system model during the GA iterations. The results of the transient simulations are used to evaluate the power management constraints, which include generation-load balance constraints, dynamic security constraints for planned events, and dynamic security constraints for unplanned events. To mimic real-life decision making, a fuzzy membership-based approach was developed to identify the best compromise solution from among the NSGA-II Pareto solutions.

Third, a comprehensive security study was conducted on the AC network in a notional all-electric shipboard power system computer model. In this study, all of the N$-$1 contingencies along with several extreme load disturbances were included in the contingency list. The dynamic security of an operating point was assessed for four time-dependent security aspects defined on system frequency, generator angles (transient stability), load bus voltages, and cable currents. The results of the comprehensive security study showed the security problems and the severe contingencies in the notional all-electric ship computer model. Moreover, the results indicated that deterministic security assessment approaches may not be suitable for small isolated power systems, like the notional all-electric shipboard power system. It was shown that probabilistic (risk-based) security assessment approaches may be advantageous over deterministic methods, in such power systems.

Fourth, an approach for assessing an approximation of the system Dynamic Secure Region (DSR) was developed, for isolated microgrid power systems. The DSR is a sub-space of the system operating space, in which system operation is secure against unplanned events. In the region-based security assessment methods used in conventional large scale

power systems, the system DSR is obtained in the neighborhood of the current operating point. This DSR, however, must be updated when the system operating point significantly changes. On the other hand, the operating point changes in small isolated power systems may be large and frequent. Hence, determining the DSR in the neighborhood of the current operating point may not practical. The DSR assessment approach developed in this work alleviated this problem, by providing an approximation of the DSR in the entire operating space. The developed approach can be used to assess the deterministic DSR (DDSR) or the Risk-based DSR (RDSR).

Fifth, as part of the DSR assessment method, a systematic approach was developed to determine a good set of Critical Parameters (CPs), in isolated microgrid power systems. The common practice in choosing the critical parameters in a conventional large scale power system is to rely on the experience of the engineers familiar with that particular system. An isolated microgrid power system, however, includes only a few generators and loads. As a result, the CPs can be chosen using a brute-force-like method. In the new method, several Critical Parameter Candidate (CPC) sets are developed, first, where each candidate set includes several critical parameter candidates. Next, the DSR is determined for each CPC set. Then, the quality of the DSRs are compared to determine the best CPC set. As part of the risk-based DSR assessment method, a new severity function was also developed, which can accommodate time-dependent security criteria. In the new severity function, the severity of an operating point with respect to a contingency is defined as the total duration of time that the system constrained quantities spend in the constrained bands.

1.2 Organization

This dissertation consists of six sections. Section 1 provides introduction and organization of the dissertation. Section 2 is devoted to the literature review on security-constrained power management approaches. The problem statement for the new power management method is presented in section 3. In section 4, the new integrated

security-constrained power management method is presented. Section 5 includes case studies and performance analysis for the new integrated security constrained power management method applied to a notional all-electric ship power system model. Finally, the conclusions and future work are presented in section 6.

2 POWER MANAGEMENT METHODS IN LITERATURE

The power management objectives in a power system depend on the system operating conditions. Therefore, to determine the objective of a Power Management System (PMS), system operating conditions are conceptually classified into several operating states [4]. Several schemes for power system operating states are used in [2, 4, 13–16]. In a popular scheme, system operating conditions are classified into four states [2, 16–18]: 1) normal state, 2) alert state, 3) emergency state, and 4) restorative state. To define the operating states, the concept of power system security is used [3]. Power system security is the ability of a power system to withstand credible contingencies without supply interruption of system loads [3]. Consequently, a system operating point is secure, if it is able to withstand the contingencies in the contingency list without service interruption to loads, violation of operating constraints, or instability problems [15, 19–21].

Table 2.1 shows operating state definitions [2,16]. This table also shows possible events that may cause operating constraint violations, load sheds, and degradation of the system security. This table also explains the PMS objectives in each operating state. In the normal state, all quality and stability constraints are satisfied, all of the loads are served, and the system is secure. Therefore, the PMS aims to minimize system operating cost while maintaining secure state of the system. In this state, a load change or a generation change may degrade system security and lead the system into the alert state. In the alert state, although all the constraints are still satisfied and the loads are served, the system is not secure against at least one contingency.Therefore, the objective of the PMS is to enhance system security by performing preventive actions. Severe faults or component outages that cause constraint violations or load shedding bring the system into the emergency state. In this state, the main goal of the PMS is to keep the system intact by performing control actions, immediately. The control actions, if performed in time, can bring the system back to normal or alert state. However, direct recovery of the system from emergency state may not be possible. In this case, before recovering to the normal or alert states, the system

goes through a temporary state, called the restorative state, in which the system is stable and the constraints are satisfied, but some loads are disconnected.

Table 2.1: Definitions and objectives of power system operating states [2]

operating state	constraint violation	disconnected loads	security condition	objective of the power management system
normal	no	no	secure	optimal operation while maintaining the current state
alert	no	no	insecure, possible security degradation causes are load change, gen change, and equipment outage	bringing the system back to normal by redispatching gens, bringing de-committed gens into service, and changing the voltage set-points
emergency	yes, possible causes are severe faults and component outages	maybe	–	preventing system instability by actions such as load shedding and gen shedding, and then bringing the system to one of the other three states
restorative	no	yes, some loads may be shed to prevent instability	–	re-connecting disconnected loads to bring the system back to normal or alert

The operating state transition diagram is shown in Figure 2.1 [2]. This figure shows how PMS control actions and uncontrolled events cause transitions between different operating states. Performing control actions in the normal state keeps the system operating in this state. In other states, performing control actions improves system security and leads the system to a more secure state. In the emergency state, power system instability is likely to happen. Therefore, corrective actions must be taken immediately to bring the system back to the normal or alert states.

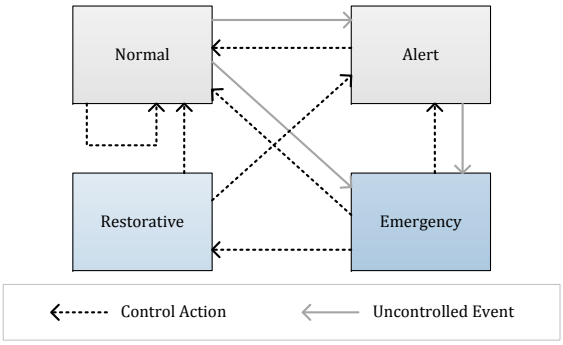

Figure 2.1: Operating state transition diagram [2]

Since developing a single control function which seeks all of the PMS goals is not practical due its complexity, PMS objectives are usually distributed among several control functions. As a result, the power management system manipulates several control functions to achieve its objective [4]. Control of a power system using several control blocks is shown in Figure 2.2 [4]. This figure shows that some controllers operate directly on individual system elements (local controllers) and some controllers operate in a higher level. The local controllers in a generating unit are prime mover and excitation controls, which regulate generator's speed and voltage/reactive power, respectively. The set-points for these controllers are determined by higher level controllers. System generation control balances the total generation against system loads and losses, in order to maintain the desired system frequency. In determining the generator set-points, other factors such as costs or environmental effects may also be taken into consideration. Load frequency control, shown in this figure as part of the system generation control, may reduce the connected loads to a safe level, based on the available generation. Reactive power and voltage control block determines the voltage set-points such that bus voltages are maintained in an acceptable range.

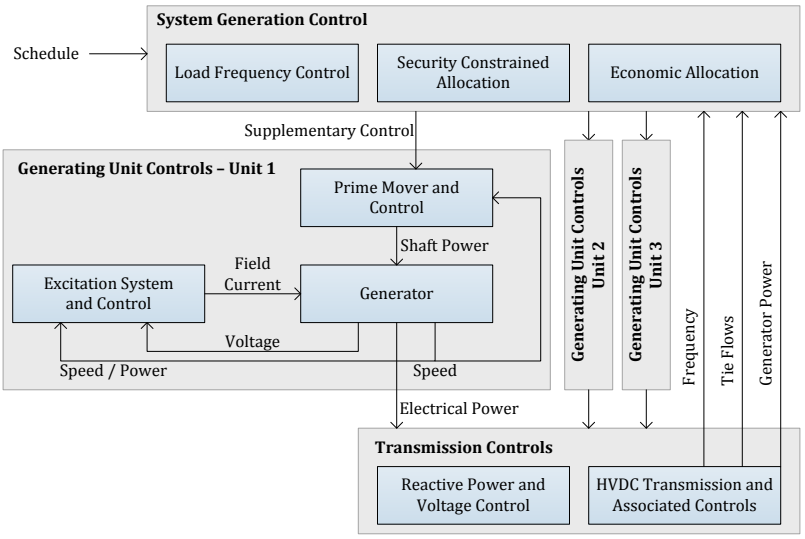

Figure 2.2: Subsystems of a power system and associated controls [4]

Based on the objective and the controlled variables (set-points), at least four distinct control functions can be distinguished in a power system [4]. The first function, *generation dispatch function*, maintains the system desired frequency by balancing total system generation against system load and losses. It is desirable to supply the required total power with minimum cost and environmental impact. The controlled variables, or set-points, in this function are generator power set-points [4, 22–24].

The second function, *load management function*, balances generation and load in the system, while achieving certain objectives. The set-points manipulated by the load management function are load connection statuses and power levels [12]. The purpose of the third function, *voltage and reactive power control function*, is to keep the voltage at some buses in the system within acceptable limits. In some cases, this function also aims to minimize active power loss in the system. To achieve its goal, this function controls reactive power flow in the system by manipulating generator voltage/reactive power set-points, transformer tap positions, shunt capacitor and reactor levels, etc [4, 25–28].

Unlike the previous three functions, the fourth control function is not used in the normal or alert operating states. The fourth function, *reconfiguration for restoration function*, is

used to restore de-energized loads or to keep the important loads in the system supplied. This function manipulates network configuration switches to change flow of power in the system and achieve its goal [29, 30]. The control functions used in each operating state are shown in Table 2.2. As shown in this table and explained above, generation dispatch, load management, and voltage/VAr control functions are active in the normal and alert states. In the emergency and restorative states, reconfiguration function may also be used to help restore de-energized loads.

Table 2.2: Control methods in each operating state

operating state	generation dispatch	load management	voltage/VAr control	reconfiguration for restoration
normal	✓	✓	✓	
alert	✓	✓	✓	
emergency	✓	✓	✓	✓
restorative	✓	✓	✓	✓

One of the main objectives of a PMS is to ensure secure operation of the system [2, 4, 16, 20]. There are several schemes to integrate security constraints into a PMS. In some schemes, security constraints are integrated with the individual control functions. For instance, security-constrained generation dispatch methods manipulate generation dispatch set-points to satisfy security constraints [5, 6, 9, 31–33]. The main shortcoming of such power management schemes is that all of the security constraints cannot be satisfied by manipulating a single control function's set-points. For example, security-constrained generation dispatch methods cannot effectively improve voltage security, since reactive power flow in power system is influenced mainly by voltage control function's set-points [7]. To overcome this problem, some power management schemes manipulate the set-points from several control functions to meet security requirements [7]. Examples of such approaches are security-constrained generation and load dispatch [34, 35], security-constrained generation and voltage dispatch [36], and security-constrained generation, load, and voltage dispatch [7, 8, 37–39]. The new power management approach

proposed in this dissertation manipulates the set-points of several control functions to improve system security in the all-electric shipboard power systems in normal/alert operating state.

In this section, several power management methods available in the literature are reviewed. This section is organized as follows. In subsection 2.1, several individual control functions that do not take security constraints into consideration are described. These functions determine the optimum values for the generator, load, and voltage set-points, independently. Several security-constrained generation dispatch methods are reviewed in subsection 2.2. Subsections 2.3 and 2.4 include security-constrained generation and load dispatch and security-constrained generation and voltage dispatch approaches, respectively. Security-constrained reactive power dispatch methods are discussed in subsection 2.5. The methods that manipulate the set-points of all of the three control functions to improve system security are discussed in subsection 2.6. Finally, this section is summarized in subsection 2.7, where the motivations for this dissertation are also discussed. This subsection also includes a table that summarizes the power management methods reviewed in this section.

2.1 Individual Control Methods

Several individual control methods that do not integrate security constraints are described. Figure 2.3 depicts a schematic representation for a power management method in which individual control functions send their set-points to the system without including security constraints. In this figure, G, L, and V blocks denote the generation dispatch, load management, and voltage/VAr control functions, respectively. Several examples from each of these control functions are reviewed in subsections 2.1.1, 2.1.2, and 2.1.3. These examples use either a static or a dynamic formulation. Here, the terms static and dynamic are from an optimization perspective. In a static optimization, the decision variables are obtained for a single snapshot in time. On the contrary, a dynamic optimization determines what the optimum value of a variables is, in each period of time within the planning period [40].

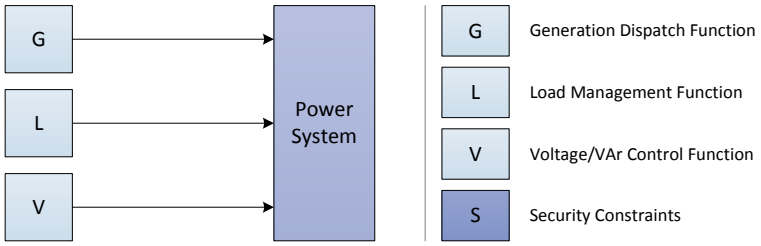

Figure 2.3: Power management scheme with individual control methods without security constraints

2.1.1 Generation Dispatch Method

The generation capacity in the system, under normal operating conditions, is more than the demand load. Thus, there are many options for scheduling the generators. In a power system, it is usually desired to find the power scheduling of each power plant in such a way as to minimize the operating cost. This well-known problem is usually referred to as Optimal Power Flow (OPF) [41] and was initially introduced in the early 1960s [42]. An example of a relatively old OPF formulation is given in [22]. In this paper, Burchett et. al. developed an OPF method to minimize operating cost in large scale power systems. They solved the problem by transforming the original nonlinear optimization problem into a sequence of linearly constrained sub-problems. The performance of the algorithm was tested on IEEE 118-bus test system and a larger test system with 600 buses.

While the optimization objective can be cost minimization, it can also entail other goals. For instance, the power management approaches developed in [23, 24, 43, 44] intended to minimize operating cost and environmental impacts (emission), simultaneously, by manipulating generator power set-points. Among these four methods, the method proposed in [24] was developed for distribution microgrids and the rest were developed for transmission networks. The IEEE 30-bus test system was used in [23], [43], and [44] to demonstrate how the proposed methods work. In all of these articles, static generation dispatch methods were developed.

An example for a dynamic method is given in [45], in which Xie et. al. developed a dynamic optimization method that minimized operating cost over a time horizon,

by finding the optimum generator power set-points during that horizon. To solve this Dynamic OPF (DOPF) problem for transmission power systems, an algorithm based on nonlinear interior point method was used. In addition to the static (time-separated) constraints included in static OPF methods, authors in this article took into consideration some dynamic (time-related) constraints such as generator ramp rate constraints or energy-related constraints. In this reference, IEEE 30-bus and 118-bus transmission test systems were used for illustrative purposes. In another DOPF example, discrete-time Markov decision process was utilized in [46], to formulate dynamic optimal generation scheduling for shipboard power systems. In this paper, generator active power set-points over a study horizon were manipulated to minimize total system operating cost over that time horizon.

2.1.2 Load Management Method

The objective of load management function is to optimally determine connection status or power level of each load, while satisfying some system constraints, considering the load priorities [12]. A load management method was developed in [47] to maximize the weighted sum of the served loads without violating cable current or bus voltage constraints, in a special isolated DC power system composed of underwater cables on the floor of Pacific Ocean. The load weights in this method were determined based on the load priorities. In another load management approach, Feng proposed a real-time load management technique based on multi-agent systems for all-electric shipboard power systems [48]. The proposed approach determined the optimum switch status and power level for the loads, in real-time. The objective of this load management method was to continuously match the demand and generation powers, considering the load priorities.

In contrast with the previous two articles in which static methods were developed, a dynamic load management approach for industrial power systems was formulated in [49]. The method proposed in this article utilized integer linear programming to manipulate the load power set-points in order to minimize the operating cost over a time horizon, while

satisfying process, storage, and production constraints. To illustrate how the method works, electrical network of an actual flour mill plant was used in this reference.

2.1.3 Voltage/VAr Control Method

Voltage/VAr control function manipulates voltage/reactive power set-points in the system to achieve its goal. Typically, the goal of this function is to minimize voltage deviations or to minimize active power loss in the system. An example of a reactive power control function, formulated as a static optimization problem, is given in [25]. In this method, reactive power set-points (such as generator voltages, transformer tap positions, and injection of reactive power sources) were manipulated, in order to minimize active power loss in transmission level power systems. To solve the obtained nonlinear optimization problem, particle swarm optimization approach was used. To illustrate how the method works, IEEE 30-bus and 118-bus transmission test systems were used.

In contrast with static voltage control methods, dynamic voltage control methods seek an objective over a time horizon. For instance, a dynamic optimization approach was utilized in [26] to minimize load bus voltage deviations during a time horizon. This approach was developed for distribution systems including Distributed Generators (DG). In this approach, generator voltage set-points were manipulated. To solve the formulated dynamic optimization problem, an approach based on nested evolutionary programming was used in this paper. In another dynamic method, authors in [27] formulated a dynamic reactive power optimization to minimize total active power loss during the study horizon. This method was developed for transmission level power systems and was tested on IEEE 30-bus test system.

In another example, also developed for transmission power systems, a reactive power control function was developed in [50]. In this paper, a dynamic optimization method was used to minimize total active power loss during the study horizon, via manipulating continuous and discrete reactive power set-points. To solve the problem, it was proposed to use the interior-point algorithm to determine the continuous control variables such

as generator voltage set-points. To determine the discrete control variables such as the transformer tap positions or switchable shunt compensators, Also, it was proposed to use the immune genetic algorithm. In this paper, performance of the proposed method was illustrated on IEEE 14-bus test system. The same approach was used by Pan et. al. in [51], where they proposed to solve the dynamic loss minimization problem by separating the decision loops for continuous and discrete reactive power set-points. This method was developed for transmission power systems and was tested on a 6-bus test system.

2.2 Security-Constrained Generation Dispatch and Redispatch Methods

Power system security has several aspects. In other words, power system security is defined based on various criteria, such as transient angle stability, frequency deviation, voltage deviation, and cable current ampacity criteria. Each security aspect is more affected by one of the control functions, compared to the other ones. For instance, transient angle criterion or frequency criterion depend more on generation and load set-points, compared to reactive power set-points. Also, voltage security criterion depends on reactive power set-points more than generation dispatch or load management set-points. Thus, depending on the type of security being studied, researchers may decide to integrate security constraints into generation dispatch, load management, or voltage control functions.

Figure 2.4 shows two power management schemes in which security constraints are integrated into generation dispatch function. The schemes shown in Figure 2.4(a) and (b) are called security-constrained generation dispatch (scheduling) and security-constrained generation redispatch (rescheduling), respectively [52–55]. The difference between dispatch and redispatch methods is that in a redispatch scheme, a system dispatch (generator active power set-points) is already available. However, since this dispatch is not secure, the goal of the redispatch method is to adjust the initial dispatch and make it secure. On the contrary, in security-constrained dispatch method, generator active power set-points are obtained such that security constraints are satisfied. Hence, set-point adjustment is not required.

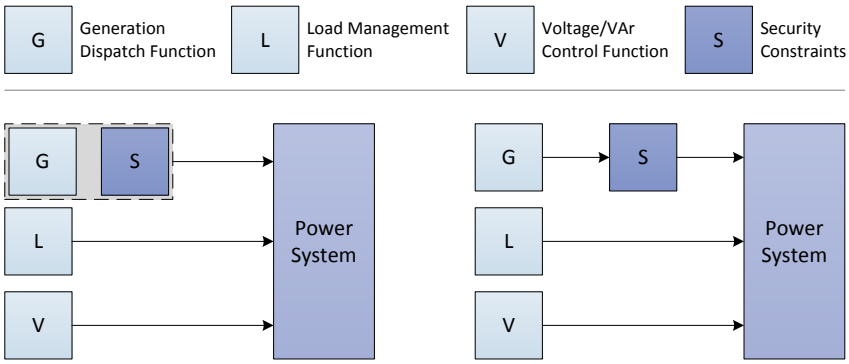

(a) Dispatch method (b) Redispatch method

Figure 2.4: Security-constrained generation dispatch and redispatch methods. a) dispatch method, and b) redispatch method

2.2.1 Generation Dispatch Methods

A security-constrained generation dispatch method was formulated in [56]. This approach determined the optimum generator active power set-points that maximized secure (transient angel security) power transfer over a tie-line. This method was developed for transmission networks. To assess the security of the operating points, the authors relied on the SIME (Single Machine Infinite bus Equivalent) approximation. The SIME transforms the trajectory of a multi-machine system obtained from time-domain simulation into the trajectory of an equivalent single-machine infinite bus system. The south-southeast Brazilian network model was used as the test system in this paper. In contrast with [56], the objective in the majority of the security-constrained generation dispatch methods is to minimize operating cost. The problem of minimizing the operating cost subject to some security constraints is usually referred to as Transient Security-Constrained Optimal Power Flow (TSCOPF or SCOPF). Some examples of these methods, all developed for transmission power systems, are given in [5, 6, 9, 31–33].

In the methods proposed in [6] and [9] for transmission networks, the optimum generator active power set-points where determined such that system operating cost was minimized. Security constraints in these two methods were defined on the generator angles. To include

these security constraints in the optimization problems, contingency DAEs were converted into algebraic equations, using an integration method. Then, the converted constraints were included in the optimization problems as equality constraints. In [6], IEEE 9-bus system, New England 39-bus system, and a 162-bus test system were used as the test systems. In [9], a simplified model of Japan power system, called IEEJ WEST10, was used as the test system.

The DAE conversion approach adds many equality constraints into the optimization problem, which makes optimization solving inefficient [5, 31, 32]. Therefore, several researchers proposed to convert transient security constraints using a technique called constraint transcription. This technique converts the optimization problem from the functional space into the Euclidean space. Hence, it reduces the number of constraints required for the transient security. Some examples of security-constrained generation dispatch method for transmission networks, which used this constraint transcription technique, are given in [5, 31, 32].

To solve the converted TSCOPF problem in the Euclidean space, a combination of the interior-point penalty function and improved Broyden-Fletcher-Goldfarb-Shanno (BFGS) method was used in [31]. The New England 39-bus system was used in this paper as the test system. In [5], a penalty-based approach was proposed, in which the adjoint equation method was applied to evaluate the gradient of the penalty terms associated with the stability constraints. In this paper, the working principles of the method was illustrated using a 36-bus model of a reduced size regional power system in China. In [32], a concept referred to as the "most effective section of transient stability constraints" was introduced, in order to reduce the massive calculation of Jacobian and Hessian matrices of the stability constraints. In this paper, WSCC 9-bus test system and a realistic 686-bus system were used as the test systems.

Direct contingency DAE integration or constraint transcription methods are not the only options to include security constraints into security-constrained optimization problem. For instance, Fu formulated a problem which minimized system operating cost by

manipulating generator active power set-points. He proposed to use the risk-based static security region to ensure the security of the obtained operating point [33]. The test system in this reference was IEEE 24-bus RTS96 system.

It is also possible to define security as an objective to be maximized along with operating cost minimization. Some examples of such methods for transmission networks are given in [11, 57, 58]. Authors in [57] and [58] used the loading margin as an index for voltage security. They proposed multi-objective methods to determine the optimum generator active power set-points, that minimized operating cost and maximized loading margin. To solve the resulting multi-objective optimization problems, normal boundary intersection method was used in [57]. In this paper, IEEE 30-bus test system was used to demonstrate how the method works. In [58], the resulting problem was solved using weighted sum approach, ϵ-constrained technique, and goal programming method, and their performances on IEEE 57-bus and 118-bus test systems were compared. In another example in [11], Xiao proposed a multi-objective method for security-constrained optimal power flow problem, which minimized operating cost and operating risk, simultaneously. In this paper, application of classical and evolutionary methods to solve the formulated optimization problem were compared, using IEEE 24-bus RTS96 system.

Some of the security-constrained optimal power flow methods include more than two objectives. For instance, two multi-objective optimization methods were formulated in [59] and [60], in order to simultaneously minimize operating cost, environmental impacts, and transmission line over-loading (as a security index). The manipulated set-points in these two formulations, developed for the transmission power systems, were generator active power set-points. To solve the three-objective optimization problems, a technique was used in [59], in which the third objective was eliminated, first, and the Pareto front for the bi-criteria problem was found using ϵ-constraint approach. Then, the third objective, security objective, was used as an index to pick the best solution among the Pareto solutions. IEEE 30-bus test system was used in this paper to illustrate how the method works. Chang in [60] used the same technique to solve the three-objective problem, except

that he used weighted sum approach to solve the obtained bi-criteria problem. A 7-bus example power system model was used in this paper as the test system.

2.2.2 Generation Redispatch Methods

In a redispatch method, it is assumed that an insecure operating point is already available. Thus, the objective is to adjust the available set-points, in order to make the system secure. Some examples of security-constrained generation redispatch schemes for transmission power systems are given in [52–55]. An optimization method which minimized excess cost due to generation rescheduling, subject to some line loading constraints (static security constraints), was proposed in [52]. To formulate this problem, a linear model was used, based on the sensitivity of system quantities (such as line flows) with respect to generator powers. Thus, the resulting optimization problem was linear and the linear programming was used to solve it. To illustrate how the method works, a 5-bus test system was used.

In another security-constrained redispatch method for transmission networks, an approach was developed in [53], which adjusted an insecure operating point (in terms of transient angle security) and made it secure, by manipulating generator active power set-points. In this paper, an expression for sensitivity of the transient energy function with respect to the changes in generator active powers was derived, first. Then, a two-level solution approach using the obtained sensitivity equations was proposed. In the proposed approach, the sensitivity expression was used to find a rough predication of the solution, in the first level. In the second level, the sensitivity values calculated at the rough prediction were used to refine the rough solution and find a more accurate solution. This method was illustrated using New England 39-bus test system and a 68-bus test system.

In another sensitivity-based redispatch method, an approach to determine the required generator active power set-point adjustments in order to make the system operating point transiently secure was proposed in [54]. In this "trial and error" approach developed for transmission networks, the sensitivity of the generator relative angles with respect to the

generator power set-points were calculated, first. Then, the initial solution was adjusted to obtain a new operating point, using the calculated sensitivity factors. If the obtained solution was transiently secure, the algorithm stopped, otherwise, this procedure continued until a secure operating point was obtained. WSCC 9-bus and New England 39-bus test systems were used in this paper to demonstrate how the method works.

Sun et. al. proposed another trial and error approach for generation redispatch problem in transmission power systems [55]. In this approach, an optimization problem was formulated which minimized the generator active power set-point adjustments, subject to security constraints. This problem was solved, successively, to obtain the optimum generator set-point adjustments. To define the security constraints, the transient energy function method, which is an approximation method, was used in this paper. The test system in this paper was New England 39-bus system.

2.3 Security-Constrained Generation and Load Redispatch Methods

Power system transient security is more affected by active power flow in the system, rather than reactive power flow. Since active power set-points in the system are mainly generator and load power set-points, some researchers chose to manipulate both of these set-points to satisfy security constraints. This scheme, called security-constrained generation and load redispatch, is shown in Figure 2.5. Two examples for the power management methods using this scheme are given in [34] and [35].

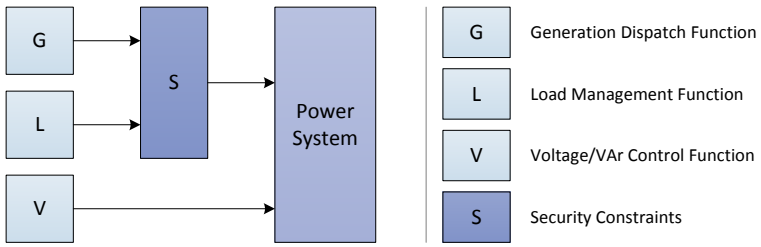

Figure 2.5: Security-constrained generation and load redispatch method

In these two papers, developed for transmission level power systems, the objective functions were defined as the weighted sum of the generator and load set-point adjustments. Load weighting factors were chosen much higher than generator weighting factors, in order to discourage load adjustments (load sheds). Authors in [34] modeled the system with decoupled power flow equations and defined transient security constraints on the angle difference between the sending and receiving ends of transmission lines. They used a heuristic search algorithm to solve the optimization problem. An 8-bus example system was used in this paper to demonstrate how the method works. In [35], Kaltenbach et. al. used the same security constraints, however, they modeled the system using linear active power flow equations. It resulted in a linear optimization problem, which was solved using linear programming. To demonstrate how the method works, an 8-bus example system was used in this paper.

2.4 Security-Constrained Generation and Voltage Redispatch Methods

Some power management schemes manipulate generation and voltage set-points to improve system security, as depicted in Figure 2.6. An example of such a power management scheme is given in [36]. In this paper, it was analytically shown that there is a linear relationship between fault Critical Clearing Time (CCT) and generator steady state pre-fault angle, in one machine infinite bus transmission systems. Based on this analytical derivation, the results of several simulations were used to conclude that there is a similar relationship between CCT and pre-fault generator angles, in multi-machine systems. Based on these results, an approach was proposed for generator active power and voltage set-point rescheduling, using the linear relationship between CCT and pre-fault generator angles. The test system in this paper was IEEJ EAST10 system.

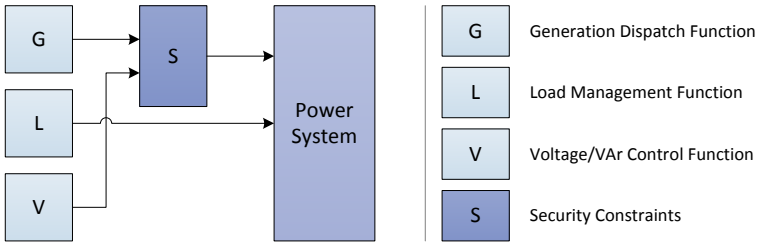

Figure 2.6: Security-constrained generation and voltage redispatch methods

2.5 Security-Constrained Reactive Power Dispatch and Redispatch Methods

Some power management schemes, especially the ones including voltage security, manipulate reactive power set-points to improve system security. This method, referred to as security-constrained reactive power dispatch or redispatch, is schematically depicted in Figure 2.7.

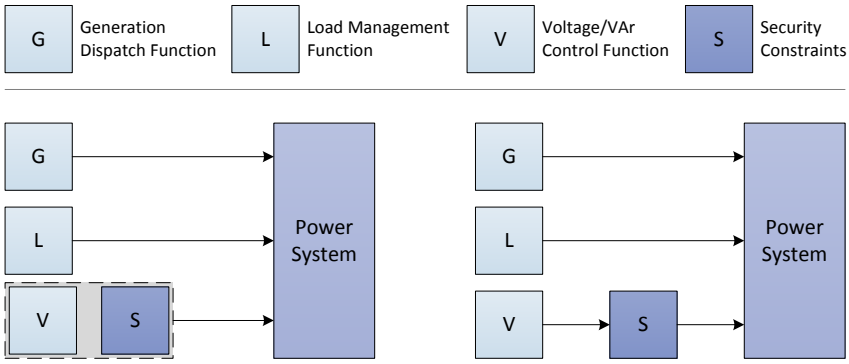

(a) Dispatch method (b) Redispatch method

Figure 2.7: Security-constrained reactive power dispatch and redispatch methods. a) dispatch method, and b) redispatch method

2.5.1 Reactive Power Dispatch Methods

Authors in [61] proposed a security-constrained reactive power dispatch method to minimize system active power loss and maximize system reactive power reserve, while satisfying steady state security constraints on bus voltages and generator reactive power

outputs. To achieve this goal in transmission networks, generator reactive power set-points were manipulated. To solve the problem, weighted sum approach was used to convert the multi-objective optimization problem into a single-objective one. Then, pseudo-gradient evolutionary programming was used to solve the resulting single-objective optimization problem. The working principles of the method was demonstrated using New England 39-bus test system.

2.5.2 Reactive Power Redispatch Methods

Some examples of security-constrained reactive power redispatch methods for transmission power systems are given in [62–64]. Shoults in [62] used sensitivity factors obtained from a linearized reactive power model to obtain the relationship between reactive power set-points (generator voltages and transformer tap positions) and system quantities such as line reactive power flows and bus voltages. This approach led to a set of linear equations between required control variable adjustments and required controlled variable changes. Required controlled variable changes were determined based on the extent of security constraint violations. This method was tested on New England 39-bus and IEEE 118-bus test systems.

To alleviate reactive power constraint violations, such as over/under bus voltages, authors in [63] and [64] formulated optimization problems, which minimized the weighted sum of reactive power set-point adjustments (such as generator voltages, transformer tap positions, and reactive power compensators). The sensitivity factors and the linear programming were used in these two papers to solve the formulated problems, respectively. IEEE 39-bus test system was used in [63] and [64] to demonstrate how the methods work.

2.6 Security-Constrained Generation, Load, and Voltage Dispatch and Redispatch Methods

Out of the three active control functions in the normal or alert operating states, the power management schemes reviewed so far manipulated set-points from one or two control

functions. However, there are some methods that manipulate the set-points from all of the control functions. These power management approaches are divided into dispatch and redispatch methods and discussed in subsections 2.6.1 and 2.6.2, respectively. Also, they are depicted in Figure 2.8(a) and (b), correspondingly.

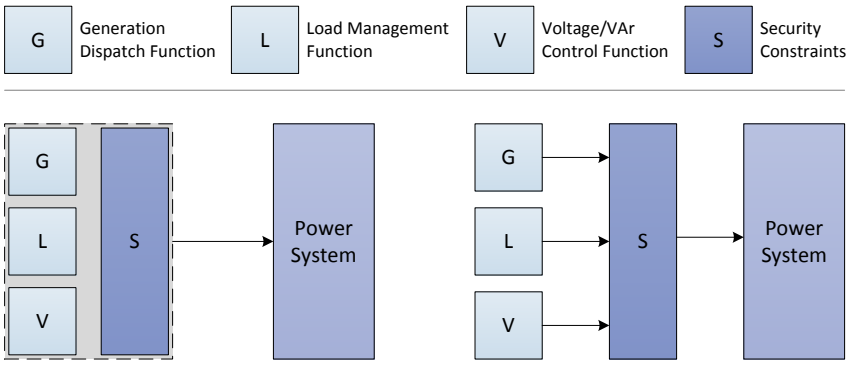

(a) Dispatch method (b) Redispatch method

Figure 2.8: Security-constrained generation, load, and voltage dispatch and redispatch methods. a) dispatch method, and b) redispatch method

2.6.1 Generation, Load, and Voltage Dispatch Methods

Two examples for security-constrained generation, load, and voltage dispatch method are given in [8,37]. In [8], La Scala formulated an optimization method which manipulated generator, load, and voltage set-points to minimize system operating cost, while satisfying transient security constraints. Security constraints in this method, developed for transmission networks, were defined on the trajectory of some system quantities in post-contingency. La Scala proposed to convert the contingency DAEs into algebraic equations using an integration method and then add them to the optimization problem as equality constraints. In this paper, a 600-bus test system was used to demonstrate how the method works.

In a similar method developed for transmission level power systems, generator, load, and reactive power set-points in the system were manipulated, in order to determine

maximum allowable power transfer over a tie-line subject to transient security constraints [37]. Similar to the previous method, it was proposed to convert contingency DAEs into algebraic equations and include them in the problem as equality constraints. To solve the optimization problem, the generalized gradient method was adapted in this paper. The test system used in this paper was ENEL 614-bus transmission system.

2.6.2 Generation, Load, and Voltage Redispatch Methods

Several examples for generation, load, and voltage redispatch method in transmission networks are given in [7, 38, 39]. An approach which manipulated the set-points from the generation dispatch, load management, and voltage/VAr control functions was formulated in [38], for transmission level power systems. The objective function in this optimization problem was to minimize the weighted sum set-point adjustments, in order to make the system secure. To ensure the security of an operating point, some constraints were defined on the angle difference between transmission line sending and receiving ends. To reduce the execution time, it was proposed to linearize the nonlinear optimization problem around the initial operating point. Also, a relaxation method was used, in which the security constraints were included only for the transmission lines that violated the security criterion. The test system used in this paper was a an example 17-bus power system.

Beides and Heydt formulated another security-constrained redispatch method for transmission networks in [7]. In this paper, two different methods were proposed for the normal/alert and the emergency operating states. In the normal/alert state, the objective of the power management system was to minimize total system loss by making minimal adjustments to reactive power set-points (such as generator voltages, transformer tap positions, and shunt compensators). In the emergency state, the power management system had two goals. First, it aimed to alleviate line flow overloads by adjusting generator and load set-points, minimally. Second, It aimed to fix over/under bus voltages by adjusting reactive power set-points, minimally. In this paper, complete decoupling between active and reactive power in the system was assumed. The problem was linearized, using the

sensitivity relationship between constrained quantities and decision variables. To solve the problem, dual simplex linear programming with a relaxation technique was used. To demonstrate how the method works, IEEE 39-bus and 118-bus test systems were used.

In another security-constrained redispatch scheme, an optimization problem to minimize the extra cost due to generator, load, and reactive power set-point rescheduling, while alleviating transmission line overload violations, was proposed in [39]. This method was developed for transmission level power systems. To solve the problem, a trial and error approach was used. The test systems used in this paper were IEEE 30-bus and 57-bus systems.

2.7 Motivation of Research

The literature review conducted in this section, which reviewed several power management methods in the literature, is summarized in Table 2.3 . For each reference, this table indicates manipulated set-points, method type (dispatch or redispatch), optimization type (static or dynamic), security constraint type (static or dynamic), system type (transmission, distribution, shipboard, etc.), and optimization objective(s). Most of these methods were developed for transmission power systems and cannot be applied to isolated microgrids. Due to the features of isolated microgrids, an effective power management approach for these systems should optimize the control methods together, must ensure the system is dynamically secure, and must be based on a dynamic optimization approach. An effective PMS needs to have these characteristics, since these systems are tightly coupled and constantly experience small and large disturbances.

The power management approaches summarized in Table 2.3 do not meet the requirements of a PMS for isolated microgrids. Most of these approaches did not integrate the control functions. From the 43 power management methods in Table 2.3, only seven methods integrated two or three control functions. The methods proposed in [34, 35] integrated generation dispatch and load management functions, and the methods proposed in [7, 8, 37–39] integrated generation dispatch, load management, and voltage/VAr control

functions. The methods which do not manipulate set-points from several control functions cannot effectively control the magnitude and duration of operational constraint violations.

From among the integrated methods, the methods presented in [7, 34, 35, 38, 39] only included steady state operational constraints. In other words, they included static security constraints in the formulation. Since isolated microgrid power systems are fast dynamic systems which are prone to large voltage and frequency variations during disturbances, these power management methods cannot be used in isolated microgrids. Instead, power management methods which include dynamic security constraints are required.

Table 2.3 shows that the methods proposed in [8,37] were the only integrated methods which included dynamic security constraints against contingencies. However, these methods, developed for transmission power systems, did not include transient operating constraints during load changes, since load and generator changes in transmission networks occur smoothly. On the contrary, due to low inertia of isolated microgrids and relatively large generator and load sizes, sharp load changes occur in these systems, frequently. Consequently, the operating constraints during load changes should also be included in power management methods. Including these constraints in the power management method requires a dynamic optimization formulation, since a static optimization formulation optimizes the system behavior for a single operating point and cannot include security constraints during load changes.

Table 2.3: Summary of the reviewed power management schemes

Reference	Redispatch	Dyn Sec	Dyn Opt	Manipulated Set-Points			System Type	Objective(s)
				Gen Disp	Load Mngt	VAr Ctrl		
[22]				✓			transmission	min operating cost
[23]				✓			transmission	min operating cost, min environmental impact
[24]				✓			dist μ-grid	min operating cost, min environmental impact
[43]				✓			transmission	min operating cost min environmental impact
[44]				✓			transmission	min operating cost, min environmental impact
[45]			✓	✓			transmission	min operating cost over a time horizon

Table 2.3: continued

Reference	Redispatch	Dyn Sec	Dyn Opt	Manipulated Set-Points: Gen Disp	Manipulated Set-Points: Load Mngt	Manipulated Set-Points: VAr Ctrl	System Type	Objective(s)
[46]			✓	✓			shipboard	min operating cost over a time horizon
[47]					✓		DC μ-grid	max the weighted sum of the served loads
[48]		✓			✓		shipboard	max the weighted sum of the served loads
[49]			✓		✓		industrial	min operating cost over a time horizon
[25]						✓	transmission	min active power loss
[26]			✓			✓	dist μ-grid	min bus voltage deviations over a time horizon
[27]			✓			✓	transmission	min active power loss over a time horizon
[50]			✓			✓	transmission	min active power loss over a time horizon
[51]			✓			✓	transmission	min active power loss over a time horizon
[56]		✓		✓			transmission	max tie-line flow s.t. transient security
[6]		✓		✓			transmission	min operating cost s.t. transient security
[9]		✓		✓			transmission	min operating cost s.t. transient security
[31]		✓		✓			transmission	min operating cost s.t. transient security
[5]		✓		✓			transmission	min operating cost s.t. transient security
[32]		✓		✓			transmission	min operating cost s.t. transient security
[33]		✓		✓			transmission	min operating cost s.t. a risk threshold
[57]				✓			transmission	min operating cost, max loading margin
[58]				✓			transmission	min operating cost, max loading margin
[11]		✓		✓			transmission	min operating cost, min operating risk
[59]				✓			transmission	min operating cost, min env. impacts, min line over-loadings
[60]				✓			transmission	min operating cost, min env. impacts, min line over-loadings
[52]	✓			✓			transmission	min rescheduling excess cost s.t. line constraints
[53]	✓	✓		✓			transmission	min set-point adjustments s.t. transient security
[54]	✓	✓		✓			transmission	min set-point adjustments s.t. transient security
[55]	✓	✓		✓			transmission	min set-point adjustments s.t. transient security
[34]	✓			✓	✓		transmission	min set-point adjustments s.t. transient security
[35]	✓			✓	✓		transmission	min set-point adjustments s.t. transient security
[36]	✓	✓		✓		✓	transmission	min set-point adjustments s.t. transient security
[61]						✓	transmission	min active power loss, max VAr reserve
[62]	✓					✓	transmission	min set-point adjustments s.t. voltage security
[63]	✓					✓	transmission	min set-point adjustments s.t. voltage security
[64]	✓					✓	transmission	min set-point adjustments s.t. voltage security
[8]		✓		✓	✓	✓	transmission	min operating cost s.t. transient security
[37]		✓		✓	✓	✓	transmission	max tie-line flow s.t. transient security
[38]	✓			✓	✓	✓	transmission	min set-point adjustments s.t. transient security
[7]	✓			✓	✓	✓	transmission	min set-point adjustments s.t. static security
[39]	✓			✓	✓	✓	transmission	min rescheduling excess cost s.t. line constraints

To fill the gap in the literature, a new integrated security-constrained power management approach is developed for isolated microgrid power systems during normal/alert state. This new power management approach has the following features:

- It is an integrated approach. It means that in order to meet the power management objectives and satisfy the requirements, it manipulates the set-points from several control methods.

- To enhance the system security and meet the minimum security level requirements, it uses a dynamic security assessment approach.

- It is formulated as a dynamic optimization problem. The dynamic formulation provides two important features for the new power management approach. First, the new power management approach ensures that the current system operating point along with all of the system operating points in a time window in future are secure against unplanned events, such as faults and component outages. Second, the new power management approach ensures that the planned events, such as generator and load changes, in the study period do not result in operating constraint violations.

2.8 Section Summary

This section reviewed some of the existing security-constrained power management methods. Based on the manipulated set-points, these methods were classified into security-constrained generation dispatch and redispatch methods, security-constrained generation and load dispatch and redispatch methods, security-constrained generation and voltage dispatch and redispatch methods, security-constrained reactive power dispatch and redispatch methods, and security-constrained generation, load, and voltage dispatch and redispatch methods. Several examples were reviewed from each category. The shortcomings of the methods were discussed and the motivations for this research were explained. In the next section, the problem formulation for the new integrated security-constrained power management method is presented.

3 ISCPM PROBLEM STATEMENT

It is common practice to classify power system operating conditions into several operating states. In a popular scheme, system operating conditions are classified into normal state, alert state, emergency state, and restorative state [2, 16]. These operating states are shown in Figure 3.1. This figure shows the operating states and the transitions between the operating states, caused by controlled and uncontrolled actions. In the normal state, all of the quality and stability constraints are satisfied, all of the loads are served, and the system is secure. Therefore in the normal state, the PMS aims to minimize system operating cost while maintaining the secure state of the system. Power system stability is defined as "the ability of an electric power system, for a given initial operating condition, to regain a state of operating equilibrium after being subjected to a physical disturbance, with most system variables bounded so that practically the entire system remains intact " [65]. Power system security refers to "the degree of risk in its ability to survive imminent disturbances (contingencies) without interruption of customer service" [65].

In the alert state, although all of the constraints are satisfied and the loads are served, the system is not secure. Therefore in the alert state, the objective of the PMS is to enhance system security by performing preventive actions. The union of the normal and alert states is referred to as the normal/alert operating state. In the emergency state, the main goal of the PMS is to keep the system stable by performing control actions, immediately, to bring the system back to the normal or alert states. However, direct recovery of the system from the emergency state to the normal or alert states may not be possible. In this case, before recovering to the normal or alert states, the system goes through a temporary state, called the restorative state, in which the system is stable and the constraints are satisfied, but some loads are disconnected.

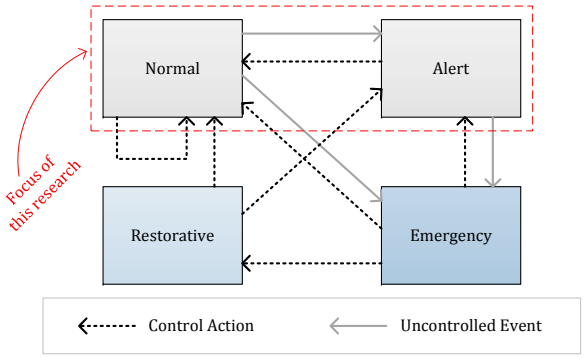

Figure 3.1: Diagram of the operating states in power systems. In this work, the focus is on the power management in isolated microgird power systems during normal/alert operating state.

To achieve the PMS goals, several control method operate in each operating state. In this work, a new power management method is presented which could be used during the normal/alert operating state in isolated microgird power systems. In the new power management approach, the high level (tertiary level) control functions operating in the normal/alert state are integrated together, in order to operate the system in an overall near-optimal state, while satisfying the security constraints.

This section is organized as follows. The control hierarchy in isolated power systems is discussed in subsection 3.1. Then, the multi-objective optimal control formulation for the new power management method is presented and discussed in subsection 3.2.

3.1 Control Hierarchy in Isolated Power Systems

To achieve PMS objectives in a power system, several control functions operate in the normal/alert operating state. Various subsystems and controls in a transmission power system are depicted in Figure 3.2 [4]. As shown in this figure, some controls operate directly on individual system elements (local controllers) and some control methods operate in higher levels. Prime mover and excitation system are two examples of local controllers. Prime mover is concerned with speed regulation in generators and excitation system regulates generator voltage and reactive power output. The desired generator power

outputs are determined by system generation control. The system generation control aims to balance total system generation with load. To set generator power set-points, some security constraints and economical operation of the system may be taken into consideration. Transmission controls in this figure include voltage control devices, such as STATCOMs, switched capacitors and reactors, etc [4].

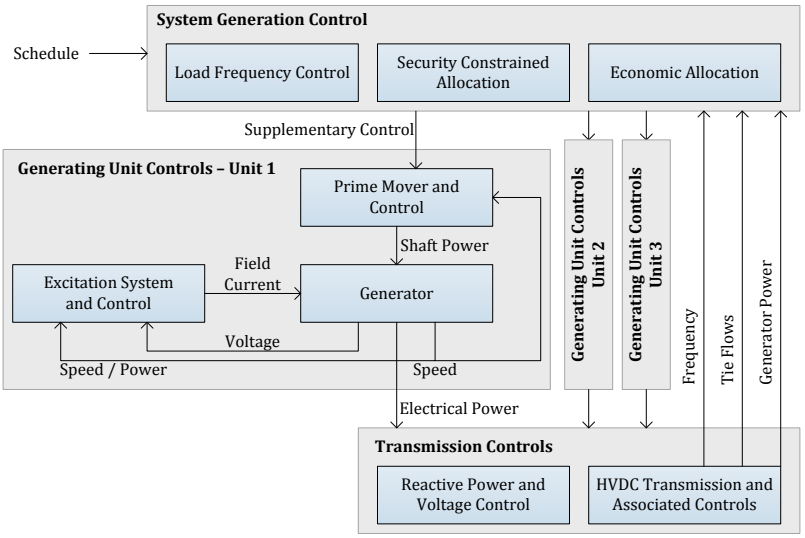

Figure 3.2: Subsystems and control methods in a power system [4]

Various controllers in a power system, like the ones in Figure 3.2, operate in different control levels. In an isolated power system, controls can be classified into three control levels: primary control, secondary control, and tertiary control [12, 66, 67]. A diagram of the control hierarchy in isolated power systems is shown in Figure 3.3. Figure 3.3 shows that the information flows from the bottom to the top and the decision flows from the top to the bottom. The primary controls are the fastest controls and have the smallest decision intervals (microseconds to milliseconds). These controls ensure that frequency and voltage in the system track their reference signals (set-points). The secondary control is responsible for balancing active and reactive power in the system, by providing appropriate set-points for primary level controllers. The time frame of the controllers in this level is in

the order of milliseconds to seconds. The tertiary control level determines the set-points for the secondary level controllers, based on some system requirements.

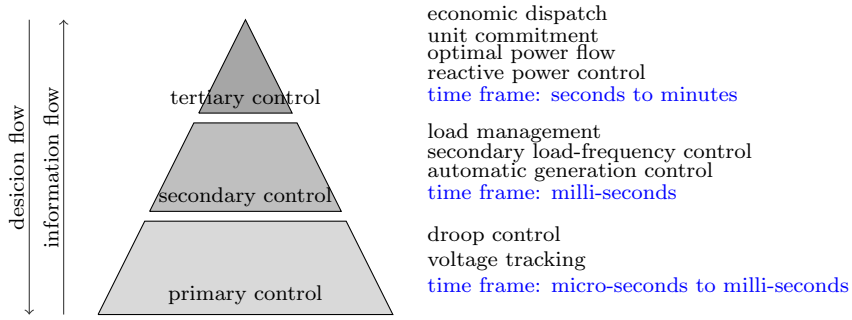

Figure 3.3: Control operations in isolated power systems (adapted from [12])

Power systems must serve the load demand, which is continually changing, at minimum cost or ecological impact, and maintain their frequency and voltage [4]. In this work, it is assumed that three control methods operate during the normal/alert state in isolated power systems, to meet these requirements. These control methods are generation dispatch, voltage/VAr control, and load management methods and are shown in Figure 3.4. The generation dispatch and voltage/VAr control methods operate in the tertiary level and the load management method operates in the secondary level.

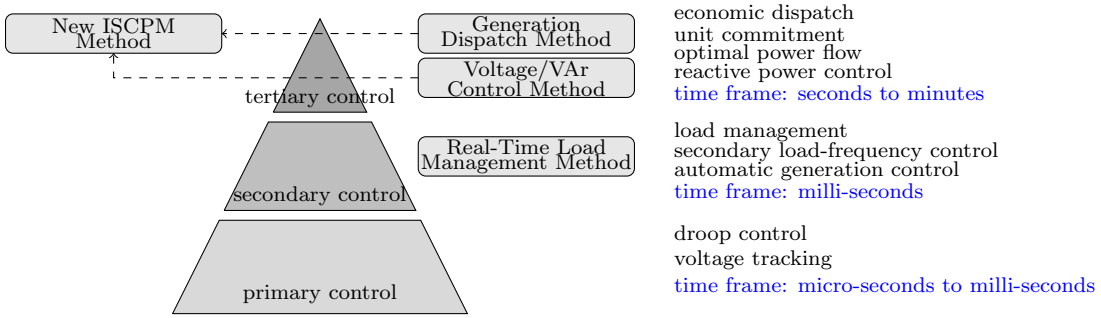

Figure 3.4: Control methods assumed to be operating in isolated microgrid power systems during normal/alert operating state (adapted from [12])

In an isolated microgrid power system, active and reactive power set-points, provided by the generation dispatch and voltage/VAr control methods, may result in the violation of system operating constraints, due to the strong interaction of controllers. The set-points may also result in the violation of dynamic security constraints against contingencies, since the individual control methods may not be security-constrained. Thus, the new ISCPM method intends to minimally adjust the set-points of generation dispatch and voltage/VAr control methods to operate the system in an overall near-optimal state, where operating and security constraints are also satisfied.

The ISCPM method optimizes power system operation for a time period in the future, called the study period, $[0, T]$. It is assumed that the generation dispatch and voltage/VAr control methods use dynamic optimization formulations and provide their set-points ahead of time. A dynamic optimization method determines the optimum values of decision variables for each period of time within the study period [40]. Dynamic Generation Dispatch (DGD) methods determine the optimum generator power set-points during the study period, to minimize operating cost or fuel consumption [68–70]. Dynamic Voltage/VAr Control (DVC) methods determine the optimum set-points for reactive power control devices in power systems during the study period, to minimize system active power loss or maintain a particular voltage profile [71–73]. Also in this work, a load management method is assumed to operate in real-time. A Real-time Load Management (RLM) method, such as the method in [12], determines the loads that should be connected or disconnected and the power levels for various system loads, based on the available generation capacity, load priorities, and some system constraints. Since the load management method operates in real-time, its set-points are not adjusted by the ISCPM method.

A block diagram for the integration of the control methods is shown in Figure 3.5. The dynamic generation dispatch and the dynamic voltage/VAr control methods determine the power set-points for the generators and the voltage (or reactive power) set-points for the reactive power control devices in the power system. The set-points provided by the former function are referred to as generation dispatch method set-points and are denoted

with $P_G^*(t)$. The set-points provided by the latter function are referred to as voltage/VAr control method set-points and are denoted with $V_Q^*(t)$ and $Q_Q^*(t)$. This figure shows that these set-points are not sent to the power system, directly. Instead, they are sent to the ISCPM method. The ISCPM method may modify the set-points, to operate the system in an overall near-optimal state in which the system operating and security constraints are also satisfied. The adjusted set-points are denoted with $\hat{P}_G(t)$, $\hat{V}_Q(t)$, and $\hat{Q}_Q(t)$.

The real-time load management method is assumed to operate in the secondary control level. Unlike the dynamic generation dispatch and dynamic voltage control set-points, the set-points determined by the real-time load management method are not modified by the ISCPM method. However, the actions of the real-time load management method are influenced by the ISCPM method, indirectly. For instance, if the ISCPM method reduces the generator power set-points, the RLM method will reduce the total connected load in the system, since the total power output of the generators is reduced.

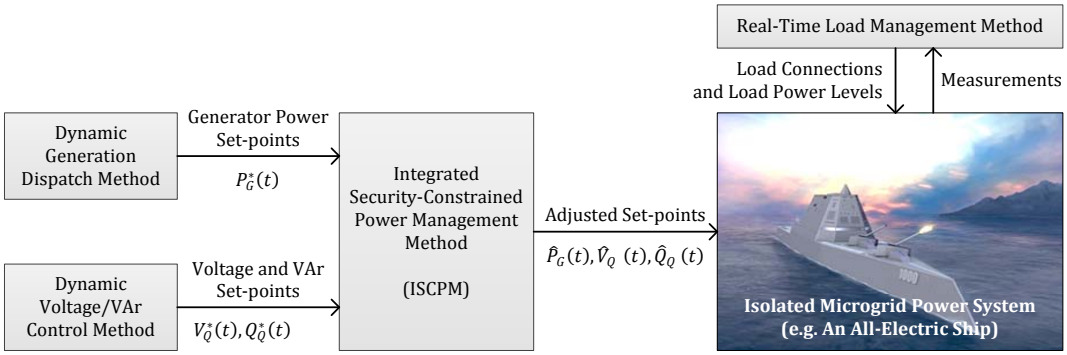

Figure 3.5: Integration of the control methods in the new ISCPM method

3.2 ISCPM Mathematical Problem Formulation

The new integrated security-constrained power management problem is formulated as a Multi-Objective Optimal Control (MOOC) problem [74], in which adjustments to the set-points provided by DGD and DVC methods are minimized, subject to operating and security constraints, over the study period $[0, T]$ in the future. The set-points provided by

the DGD method are denoted with $P^*_{G_i}(l)$, where $i = 1, 2, ..., n_g$ is the generator number, $l = 1, 2, ..., n_{\tau_g}$ is the DGD decision interval number, and n_{τ_g} is the number of DGD decision intervals in the study period. The voltage and VAr set-points provided by the DVC method are denoted with $V^*_{Q_j}(m)$ and $Q^*_{Q_k}(m)$, respectively, where $j = 1, 2, ..., n_v$ and $k = 1, 2, ..., n_q$ are voltage-controlled and VAr-controlled device numbers, correspondingly, $m = 1, 2, ..., n_{\tau_q}$ is the DVC decision interval number, and n_{τ_q} is the number of DVC decision intervals in the study period. Hence, the DGD active power set-points, and the DVC voltage and reactive power set-points, for the $[0, T]$ study period are as shown in (3.1)-(3.3), respectively. Equations (3.1)-(3.3) show that the decision intervals for the DGD and DVC methods are τ_g and τ_q seconds, respectively.

$$\text{the DGD power set} - \text{point for the } i-\text{th generator} = \begin{cases} P^*_{G_i}(1) & 0 \le t < \tau_g \\ P^*_{G_i}(2) & \tau_g \le t < 2\tau_g \\ \vdots & \\ P^*_{G_i}(n_{\tau_g}) & (n_{\tau_g} - 1)\tau_g \le t < n_{\tau_g}\tau_g \end{cases} \tag{3.1}$$

$$\text{the DVC voltage set} - \text{point for the } j-\text{th voltage} - \text{controlled device} = \begin{cases} V^*_{Q_j}(1) & 0 \le t < \tau_q \\ V^*_{Q_j}(2) & \tau_q \le t < 2\tau_q \\ \vdots & \\ V^*_{Q_j}(n_{\tau_q}) & (n_{\tau_q} - 1)\tau_q \le t < n_{\tau_q}\tau_q \end{cases} \tag{3.2}$$

$$\text{the DVC VAr set} - \text{point for the } k-\text{th VAr} - \text{controlled device} = \begin{cases} Q^*_{Q_k}(1) & 0 \le t < \tau_q \\ Q^*_{Q_k}(2) & \tau_q \le t < 2\tau_q \\ \vdots & \\ Q^*_{Q_k}(n_{\tau_q}) & (n_{\tau_q} - 1)\tau_q \le t < n_{\tau_q}\tau_q \end{cases} \tag{3.3}$$

In an MOOC problem, optimal values of control variables during the study period are determined, such that the optimization objectives are minimized [74]. Equations (3.4)-(3.8) show a general MOOC problem [74], in which $[0, T]$ is the study period, $\mathbf{x}$ and $\mathbf{u}$ are the vectors of state and control variables, respectively, and functions $\mathbf{f}$ are dynamic system equations representing the system dynamic model. The notation [.], in (3.4), (3.6), and (3.7), is the notation for *functional* [40], which is a mapping from paths to numbers, and is more general than *function*, denoted with (.), which is a mapping from numbers to numbers. A mapping from paths to numbers assigns a scalar value to a time path. In (3.4), $F_1, ..., F_N$ are the MOOC objectives. Also, (3.6) and (3.7) are equality and inequality constraints, respectively, (3.8) are control variables' boundaries, and M is the number of

control variables.

$$\min_{\mathbf{u}(t)} \quad \left\{ F_1 \left[\mathbf{x}\left(t\right), \mathbf{u}\left(t\right) \right], ..., F_N \left[\mathbf{x}\left(t\right), \mathbf{u}\left(t\right) \right] \right\} \tag{3.4}$$

$$s.t. \quad \dot{\mathbf{x}}\left(t\right) = \mathbf{f}\left(\mathbf{x}\left(t\right), \mathbf{u}\left(t\right)\right) \quad t \in [0, T] \tag{3.5}$$

$$\mathbf{g}\left[\mathbf{x}\left(t\right), \mathbf{u}\left(t\right)\right] = \mathbf{0} \tag{3.6}$$

$$\mathbf{h}\left[\mathbf{x}\left(t\right), \mathbf{u}\left(t\right)\right] \leq \mathbf{0} \tag{3.7}$$

$$u_d^{\min} \leq u_d\left(t\right) \leq u_d^{\max} \quad d = 1, 2, ..., M, \ t \in [0, T] \tag{3.8}$$

In the ISCPM formulation, the control variables, $u_1(t), u_2(t), ...$ in (3.4)-(3.8), are adjusted generator power set-points, adjusted voltage set-points of voltage-controlled devices, and adjusted VAr set-points of VAr-controlled devices. It is assumed that the ISCPM adjusted set-points have the same decision intervals as the set-points provided by the DGD and DVC methods. Therefore, the control variables $\mathbf{u}(t)$ for $t \in [0, T]$ will be determined, if the adjusted power set-points, $\hat{P}_{G_i}(l)$'s, adjusted voltage set-points, $\hat{V}_{Q_j}(m)$'s, and adjusted VAr set-points, $\hat{Q}_{Q_j}(m)$'s, are determined, for decision intervals $l = 1, \cdots, n_{\tau_g}$ and $m = 1, \cdots, n_{\tau_q}$.

The ISCPM optimization problem is formulated as (3.9)-(3.17) and contains three objectives. The first objective, f_{o_1} in (3.10), minimizes the generator power set-point adjustments. The second objective, f_{o_2} in (3.11), minimizes the difference between the total generator power set-points determined by the DGD method and the ISCPM method. The third objective, f_{o_3} in (3.12), minimizes the voltage and VAr set-point adjustments. In (3.12), α and β are weighting factors.

$$\underset{\hat{\mathbf{P}}_G, \hat{\mathbf{V}}_Q, \hat{\mathbf{Q}}_Q \text{ in next } [0,T]}{\text{minimize}} \quad \left\{ f_{o_1}(\hat{\mathbf{P}}_G), f_{o_2}(\hat{\mathbf{P}}_G), f_{o_3}(\hat{\mathbf{V}}_Q, \hat{\mathbf{Q}}_Q) \right\} \tag{3.9}$$

$$f_{o_1}(\hat{\mathbf{P}}_G) = \sum_{l=1}^{n_{\tau_g}} \sum_{i=1}^{ng} \left(\hat{P}_{G_i}(l) - P_{G_i}^*(l) \right)^2 \tag{3.10}$$

$$f_{o_2}(\hat{\mathbf{P}}_G) = \sum_{l=1}^{n_{\tau_g}} \left(\sum_{i=1}^{ng} \hat{P}_{G_i}(l) - \sum_{i=1}^{ng} P_{G_i}^*(l) \right)^2 \tag{3.11}$$

$$f_{o3}(\hat{\mathbf{V}}_Q, \hat{\mathbf{Q}}_Q) = \alpha \sum_{m=1}^{n_{\tau_q}} \sum_{j=1}^{n_v} \Big(\hat{V}_{Q_j}(m) - V^*_{Q_j}(m) \Big)^2 + \beta \sum_{m=1}^{n_{\tau_q}} \sum_{k=1}^{n_q} \Big(\hat{Q}_{Q_k}(m) - Q^*_{Q_k}(m) \Big)^2 \quad (3.12)$$

$$\sum_{i=1}^{n_g} P^e_{G_i}(t) = \text{total load plus loss at time } t, \quad 0 \le t \le T \quad (3.13)$$

$$\sum_{i=1}^{n_g} \hat{P}_{G_i}(l) \ge \sum_{i=1}^{ng} P^e_{G_i}(t), \quad (l-1)\tau_g \le t < l\tau_g \quad (3.14)$$

$$\text{time} - \text{restricted constraints on system quantities in } [0, T] \quad (3.15)$$

$$\text{dynamic security constraints against contingencies in } [0, T] \quad (3.16)$$

$$\begin{cases} \dot{\mathbf{x}}(t) = \mathbf{f}_{sys}\big(\mathbf{x}(t), \hat{\mathbf{P}}_G, \hat{\mathbf{V}}_Q, \hat{\mathbf{Q}}_Q\big) \\ \mathbf{0} = \mathbf{g}_{sys}\big(\mathbf{x}(t), \hat{\mathbf{P}}_G, \hat{\mathbf{V}}_Q, \hat{\mathbf{Q}}_Q\big) \end{cases} \quad t \in [0, T] \quad (3.17)$$

The optimization decision variables are generator power set-points in decision intervals $l = 1, ..., n_{\tau_g}$, $\hat{\mathbf{P}}_G$ in (3.18), voltage set-points of voltage-controlled devices in decision intervals $m = 1, ..., n_{\tau_q}$, $\hat{\mathbf{V}}_Q$ in (3.19), and VAr set-points of VAr-controlled devices in decision intervals $m = 1, ..., n_{\tau_q}$, $\hat{\mathbf{Q}}_Q$ in (3.20). Hence, the number of decision variables in the ISCPM optimization problem is as shown in (3.22). In (3.18)-(3.20), n_g, n_v, and n_q are the number of generators, number of voltage controlled devices, and number of reactive power controlled devices, respectively. Equation (3.21) shows that T is assumed to be a multiple of τ_g and τ_q.

$$\hat{\mathbf{P}}_G = \Big[\hat{P}_{G_1}(1) \ ... \ \hat{P}_{G_1}(n_{\tau_g}) \ ... \ \hat{P}_{G_{n_g}}(1) \ ... \ \hat{P}_{G_{n_g}}(n_{\tau_g}) \Big]^T \quad (3.18)$$

$$\hat{\mathbf{V}}_Q = \Big[\hat{V}_{Q_1}(1) \ ... \ \hat{V}_{Q_1}(n_{\tau_q}) \ ... \ \hat{V}_{Q_{n_v}}(1) \ ... \ \hat{V}_{Q_{n_v}}(n_{\tau_q}) \Big]^T \quad (3.19)$$

$$\hat{\mathbf{Q}}_Q = \Big[\hat{Q}_{Q_1}(1) \ ... \ \hat{Q}_{Q_1}(n_{\tau_q}) \ ... \ \hat{Q}_{Q_{n_q}}(1) \ ... \ \hat{Q}_{Q_{n_q}}(n_{\tau_q}) \Big]^T \quad (3.20)$$

$$T = n_{\tau_g} \times \tau_g \quad , \quad T = n_{\tau_q} \times \tau_q \quad (3.21)$$

$$\text{num of decision variables} = n_g \times n_{\tau_g} + n_v \times n_{\tau_q} + n_q \times n_{\tau_q} \quad (3.22)$$

The generation-load balance requirement is included in the optimization problem, since the generator power set-points are adjusted by the ISCPM method. Available dynamic economic dispatch methods in literature, such as [68–70], only consider system steady

state operating points. Therefore, with the assumption of 100% efficiency, a generator's mechanical power set-point, $\hat{P}_G$, equals its electrical power, P_G^e [41]. The new ISCPM formulation, however, takes system transients into consideration. During transients $\hat{P}_G \neq P_G^e$ [41]. To maintain system frequency, a generator's governor adjusts its set-point, $\hat{P}_G$, to match its electrical and mechanical powers [4], or $P_G^m(t) \simeq P_G^e(t)$. Since the total system load plus loss equals the total generator output powers at any time t, as shown in (3.13), the generation-load balance constraint for the ISCPM is formulated as (3.14). In (3.13)-(3.14), $P_{G_i}^e$ is the generator terminal power and $\hat{P}_{G_i}$ is the generator power set-point. Equations (3.13)-(3.14) limit the total load plus loss in the system, at any time t, to not exceed the total planned generation power for that time. A similar constraint has been used in the dynamic optimal power generation scheduling method in [46].

Power system operation must meet certain quality of power requirements, during normal transients or transients caused by extreme contingencies, which are mainly defined for system frequency, generator angles, bus voltages, and cable/line currents [8]. To meet these requirements, the ISCPM optimization problem includes two sets of constraints. The first set, shown in (3.15), ensures that the operating constraints defined on various system quantities are satisfied during transients caused by the planned load changes in $[0, T]$ study period. The second set, shown in (3.16), ensures that the operating constraints will not be violated, if contingencies happen. In this work, the former and latter are referred to as security constraints against planned events (load changes), and security constraints against unplanned events (contingencies), respectively.

In order to operate an isolated microgrid power system subject to the constraints in (3.13)-(3.16), a model-based approach is used in the ISCPM method. Hence, the optimization formulation contains the system model, as shown in (3.17). In (3.17), $\mathbf{f}_{sys}(.)$ and $\mathbf{g}_{sys}(.)$ are the system dynamic and algebraic equations, respectively, and $\mathbf{x}(t)$ is the system state vector.

3.3 Section Summary

In this section, the mathematical formulation for the new integrated model-based security-constrained power management approach was presented. The problem was formulated as a multi-objective optimal control problem, whose objectives were the minimization of the adjustments to the set-points determined by dynamic generation dispatch and dynamic voltage/VAr control methods. Moreover, the optimization constraints were presented, which included generation-load balance constraints, dynamic security constraints against unplanned events, and dynamic security constraints against planned events. In the next section, the proposed solution methodology for the new ISCPM method is discussed.

4 ISCPM SOLUTION METHOD

The solution method for the new integrated security-constrained power management is presented in this section. An overview of the solution methodology is shown in Figure 4.1. The ISCPM overall procedure to solve the optimization problem for each study period, shown in this figure, is as follows. First, the DGD and DVC methods compute their set-points for the next T seconds. Then, the ISCPM multi-objective optimization problem of (3.9)-(3.17) is solved, using a method developed based on an evolutionary algorithm called Nondominated Sorting Genetic Algorithm II (NSGA-II) [75]. To apply the new ISCPM method on a notional microgrid power system in an all-electric ship, the multi-objective optimization solver was developed in MATLAB, which is discussed in subsection 4.2. This all-electric shipboard power system is introduced in subsection 4.1. To evaluate the optimization constraints in the developed method, the optimization solver is linked to a fast transient simulation core. The developed methods to evaluate the ISCPM security constraints are also discussed in subsection 4.2. In this work, the TSAT tool of DSA*Tools*$^{\text{TM}}$ was used as the fast simulation core. The outcome of NSGA-II is a set of Pareto optimal solutions. To identify the best compromise solution from among the Pareto solutions, a method based on fuzzy membership was developed, which is discussed in section 4.3. In this work, this method was developed in MATLAB.

Later in this section, it will be explained that to evaluate the security constraints against unplanned events, dynamic secure region of the system must be known. For that purpose, a new method to assess the dynamic secure region in isolated microgrid power systems is developed in this research, which is discussed in subsection 4.4.

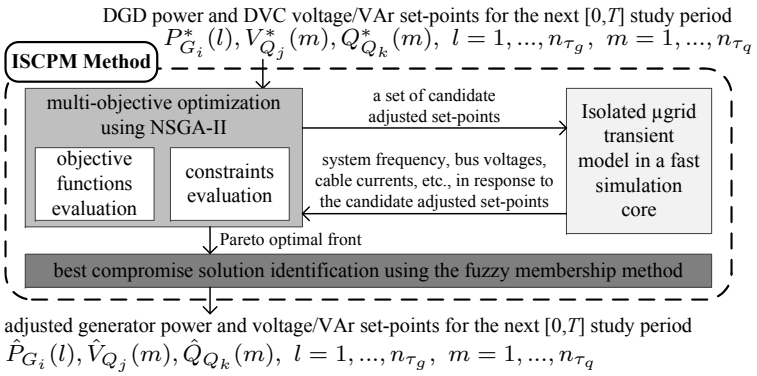

Figure 4.1: Overview of the ISCPM solution methodology

The ISCPM optimization problem is solved every T seconds. Variations of the control variables during T-seconds-length periods are depicted in Figure 4.2. When the ISCPM optimization problem is solved at the start of the first study period, $t = 0$, the values for $\hat{P}_{G_i}(l)$'s, $\hat{V}_{Q_j}(m)$'s, and $\hat{Q}_{Q_k}(m)$'s during the first study period will be determined, which will be applied to the system from $t = 0$ to $t = T$. At the start of the second study period, at $t = T$, the ISCPM optimization problem is solved again, which provides the values for $\hat{P}_{G_i}(l)$'s, $\hat{V}_{Q_j}(m)$'s, and $\hat{Q}_{Q_k}(m)$'s to be applied to the system from $t = T$ to $t = 2T$.

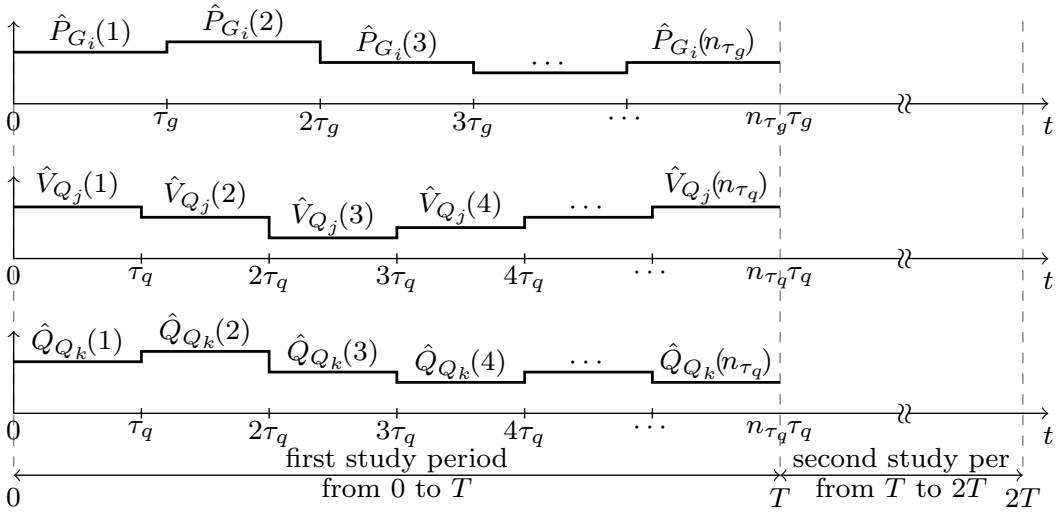

Figure 4.2: Variations of the control variables during the study period in the ISCPM method

4.1 Notional Isolated Microgrid Power System Overview

An all-electric shipboard power system is a type of isolated microgrid power system. In this work, the new ISCPM method proposed for isolated power systems is applied to a notional all-electric shipboard power system. Researchers in the Power System Automation Lab (PSAL) at Texas A&M University have developed a notional computer model for an all-electric ship.

This notional system includes several fast gas turbine generators and huge propulsion induction motors, and uses a DC zonal architecture to supply service loads. The single line diagram of the notional all-electric ship model is depicted in Figure 4.3 [76–80]. This system is composed of two Main Turbine Generators (MTG1 and MTG2), and two Auxiliary Turbine Generators (ATG1 and ATG2). The main and auxiliary turbine generators have 36MW and 4MW capacities, respectively, and both are at the 13.8kV AC voltage level. Using four transformers, this voltage is stepped down to 4.16kV AC, in order to supply two Propulsion Motors (PM1 and PM2), four DC Zones (Z1 to Z4), and Pulse Power Loads (PL). In this system, the two propulsion motors are 36MW induction motors and the capacity of each DC zone is 2MW.

Each DC zone is served through a specially designed rectifier module called PCM4, where PCM stands for Power Conversion Module. Once the voltage is rectified, a PCM1 module (DC/DC converter) is used to provide various DC voltage levels (0.375kV, 0.650kV and 0.800kV in the notional model) for the zonal loads. To supply AC loads within the zones, inverters (PCM2 modules) are used to convert the DC voltage to AC voltage. This system also has a Distribution STATCOM (DSTATCOM) connected to the pulse power load bus, to minimize voltage deviations caused by the pulse load [81].

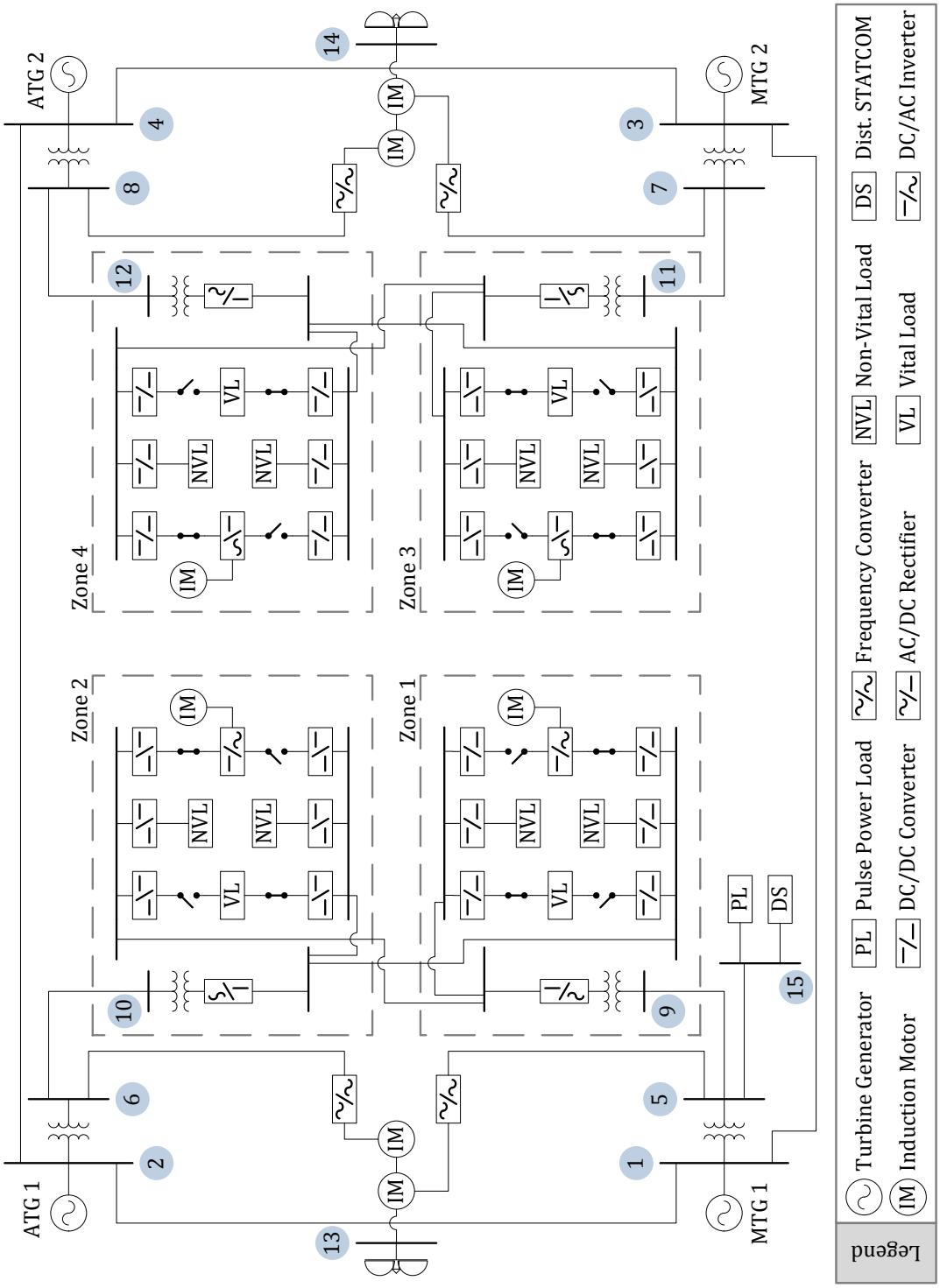

Figure 4.3: Single line diagram of the notional all-electric ship model

4.2 Multi-Objective Optimization Using NSGA-II

The optimization formulation for the new ISCPM method, discussed in section 3, has three conflicting objectives. It means that improving one objective results in degradation of other objectives. An optimization problem with several conflicting objective functions is referred to as multi-objective or multi-criterion optimization [82]. In multi-objective optimization, a solution $\mathbf{s}_1$ is said to dominate another solution $\mathbf{s}_2$, denoted with $\mathbf{s}_1 \prec \mathbf{s}_2$, if "solution $\mathbf{s}_1$ is not worse than solution $\mathbf{s}_2$ for any objective, and solution $\mathbf{s}_1$ is strictly better than solution $\mathbf{s}_2$ in at least one objective" [82]. Therefore, the concept of dominance in the new ISCPM formulation with three minimization objectives, is mathematically shown as in (4.1). In the ISCPM formulation, each solution $\mathbf{s}$ is a vector that contains each of the adjusted set-points in each of the decision intervals, as shown in (4.2). In solving a multi-objective optimization problem, the goal is to find the nondominated solutions in the entire feasible search space. This set of nondominated solutions is called the Pareto optimal front or Pareto optimal set [82].

$$\forall i \in \{1,2,3\} : f_{o_i}(\mathbf{s}_1) \leq f_{o_i}(\mathbf{s}_2) \ , \ \exists i \in \{1,2,3\} : f_{o_i}(\mathbf{s}_1) < f_{o_i}(\mathbf{s}_2) \tag{4.1}$$

$$\mathbf{s} = \begin{bmatrix} \hat{\mathbf{P}}_G^T & \hat{\mathbf{V}}_Q^T & \hat{\mathbf{Q}}_Q^T \end{bmatrix}^T \tag{4.2}$$

Multi-objective optimization methods can be classified into a) scalar or deterministic methods, and 2) stochastic or metaheuristic methods. A classification of deterministic and stochastic multi-objective optimization methods is depicted in Figure 4.4. Detailed explanation of the deterministic and stochastic methods shown in this figure can be found in [82–85] and [82, 86, 87], respectively.

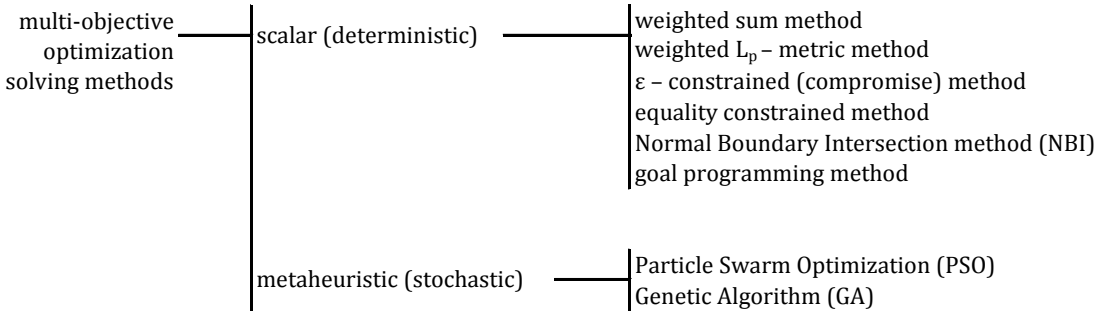

Figure 4.4: Classification of multi-objective optimization methods

Deterministic methods, also known as scalar or classical methods, transform a multi-objective optimization problem into a single-objective optimization problem with a parameter, such that each value of the parameter gives one of the Pareto solutions. Therefore, the Pareto optimal set can be found by varying the parameter and solving the resulting single-objective optimization problems [84]. Some of the popular scalar multi-objective optimization solving methods are weighted sum method, weighted L_p-method, ϵ-constrained method, equality constrained method, normal boundary intersection method, and goal programming method [82–85].

General optimization methods dedicated to "hard optimization" problems are called metaheuristic [88]. Two of the main optimization methods that fall into metaheuristic class are Particle Swarm optimization (PSO) and Genetic Algorithm (GA). Particle Swarm Optimization is a population-based search algorithm that mimics behavior of the birds in a flock [87]. Similarly, Genetic Algorithm is a population-based search algorithm that borrows its working principles from natural genetics [82]. Due to the population-based nature of stochastic multi-objective optimization methods, these methods are able to find several Pareto optimal solutions in each run, which is in contrast with deterministic methods [82].

In general, there are several difficulties associated with classical multi-objective optimization solving methods [44, 89]. Firstly, since each run of a classical method results

in a single Pareto solution, the algorithm must be applied many times, in order to find the Pareto front. Secondly, some of the classical approaches are sensitive to the shape of the Pareto front. For instance, some of them cannot find all of the Pareto solutions in nonconvex multi-objective problems. Thirdly, all of the classical algorithms require some knowledge about the problem, prior to finding the Pareto front. This knowledge could be the aggregation weights in the weighted sum approach [83] or the ϵ values in the ϵ-constrained approach [83]. Lastly, they are sensitive to the starting point.

Recent studies on the application of stochastic approaches for solving multi-objective optimization problems have shown that these methods can eliminate most of the problems associated with the classical approaches [44, 90]. The main advantage of the metaheuristic multi-objective solving approaches, over the classical ones, is that they use a population of solutions in each iteration, instead of a single solution. Hence, the outcome of a metaheuristic approach is also a population of solutions. This ability of the metaheuristic methods to find several optimal solutions in a single run makes them unique in solving multi-objective optimization problems [82].

Due to effectiveness of the stochastic approaches in solving multi-objective optimization problems, especially complex problems, a stochastic multi-objective optimization solver was chosen in this research. Between the particle swarm optimization and the genetic algorithm, the genetic algorithm was chosen, since it is much more popular [91]. In multi-objective genetic algorithm, an approximation of the Pareto optimal front exists in the GA population, at each generation. This approximation improves in generations. Having an approximation of the Pareto optimal front in each generation is an important feature for applications with limited run times, like online applications.

The general working principles of a single-objective GA are as follows [82]. After initializing the population, the solutions are evaluated and fitness values are assigned to the solutions. Then, in each generation, selection, crossover, and mutation operations are performed. The goal of the selection operator is to duplicate good solutions and eliminate bad solutions, such that the population size remains constant. The goal of the crossover

operator is to create some new solutions. For this purpose, two solutions (parent solutions) from the solutions pool are picked randomly, and two new solutions are generated by combining the two parent solutions. The goal of the mutation operator is to keep diversity in the solutions pool, by disturbing the solutions. After conducting these operations, the GA proceeds to the next generation by assigning fitness values to the solutions in the pool.

Several variations of the multi-objective GA exist in the literature. Some of the main variations are Vector Evaluated GA (VEGA), Multi-Objective GA (MOGA), Non-Dominated Sorting GA (NSGA and NSGA-II), and Niched-Pareto GA (NPGA) [82]. The difference between these variations is mainly in the way a fitness is assigned to an individual (solution). VEGA is simple and easy to implement. However, it tends to find solutions near individual best solutions, since the fitness assignment in this method is based on the individual objectives. Hence, the resulting Pareto front is not diverse [82, 91]. MOGA may be sensitive to the shape of the Pareto front and the density of solutions in the search space, since some of the solutions are, undesirably, biased over the other solutions in this method. Another disadvantage of MOGA is its slow convergence [82, 91].

In NSGA method, the progress towards the Pareto front is front-wise, since the nondominated solutions are emphasized front-wise. Another advantage of this method is that it usually converges quickly [82, 91]. The main advantage of NPGA method is that the complexity of the problem will not depend on the number of objectives, if the algorithm parameters are appropriately selected. Therefore, it could be computationally efficient in solving problems with many objectives. The disadvantage of this method is that it is more sensitive to parameter selection, compared to NSGA method [82, 91].

Based on the above discussion, from among the four GA multi-objective solving methods, NSGA method was chosen to solve the new ISCPM formulation. VEGA and MOGA methods were not chosen, due to their tendency to find solutions near individual optimum solutions and slow convergence, respectively. Moreover, since the formulated ISCPM problem does not have many objectives (only three objectives), using NPGA method was not required. Therefore, NSGA method was preferred over NPGA due to

its fast convergence and lower sensitivity to parameter setting.

NSGA approach to solve multi-objective optimization problems is sometimes criticized for being $O(mN^3)$ computationally complex (m is the number of objectives and N is the population size) [75]. In order to alleviate this problems, Deb et. al. proposed a modified nondominated sorting based multi-objective evolutionary algorithm, called NSGA-II [75]. The computational complexity in this approach was reduced to $O(mN^2)$. Due to the improvements in NSGA-II compared to NSGA, this approach was used to solve the multi-objective optimization in the new ISCPM method.

4.2.1 NSGA-II in the ISCPM Method

For the ISCPM method, which has several constraints, the constrained tournament approach [82], which does not require any penalty parameters, was chosen for constraint handling. Compared to the well known penalty function approach [82], the constrained tournament approach is less sensitive to parameter selection. The flowchart of the NSGA-II, developed for the new ISCPM method in MATLAB, is depicted in Figure 4.5, in which each step of the algorithm is numbered for further explanation.

Assume the current population at generation t, $\boldsymbol{\mathcal{P}}_t$, is known. For $t = 1$, this population is obtained by initialization, as shown in steps 1-5. For $t > 1$, this population is the population obtained at the end of the previous generation, as shown in steps 4-5. In step 6, the offspring population, $\boldsymbol{\mathcal{Q}}_t$, is obtained by performing selection, crossover, and mutation operations on $\boldsymbol{\mathcal{P}}_t$. The ISCPM method was developed using the constrained tournament selection [82], in which tournaments are played between two solutions and the solution that constrain-dominates [82] the other solution is chosen and placed in the mating pool. Constrain-domination is an adjusted definition for domination, which can be used in constrained optimization problems. A solution $\mathbf{s}_1$ is said to constrain-dominate another solution $\mathbf{s}_2$, denoted with $\mathbf{s}_1 \prec_c \mathbf{s}_2$, if any of the conditions in (4.3) are true [82]. In the ISCPM method, the structure of a chromosome is as shown in Figure 4.6, in which each solution (or individual or chromosome) includes all of the generator power set-points,

voltage set-points, and VAr set-points, in the next $[0, T]$ study period.

$$\begin{aligned} \mathbf{s}_1 \prec_c \mathbf{s}_2 \quad & \text{if } \mathbf{s}_1 \text{ is feasible and } \mathbf{s}_2 \text{ is not,} \\ & \text{or if } \mathbf{s}_1 \text{ and } \mathbf{s}_2 \text{ are infeasible and } \mathbf{s}_1 \text{ has a smaller constraint violation,} \\ & \text{or if } \mathbf{s}_1 \text{ and } \mathbf{s}_2 \text{ are feasible and } \mathbf{s}_1 \text{ dominates } \mathbf{s}_2. \end{aligned} \tag{4.3}$$

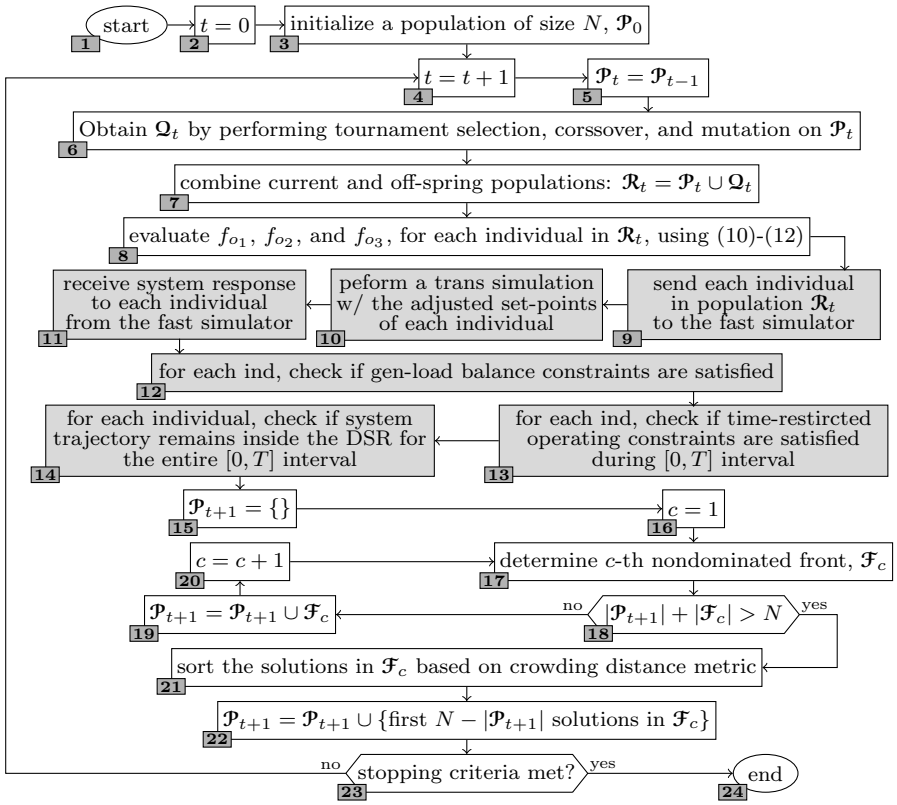

Figure 4.5: NSGA-II flowchart in the ISCPM method

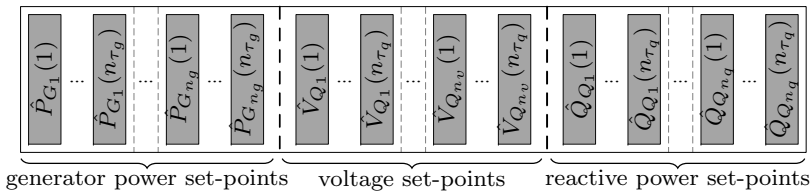

Figure 4.6: Structure of the GA chromosomes in the ISCPM method

For the crossover and mutation operators in step 6 in Figure 4.5, Simulated Binary Crossover (SBX) and polynomial mutation [82] were chosen, respectively, since several studies in the literature reported successful employment of the two operators together. Also, [92] showed that these two operators can effectively work together, in highly nonlinear optimization problems.

The Simulated Binary Crossover (SBX) [82] in real parameter GA is to a large extent similar to the single point crossover operator in binary coded GA. Simulation results from several real parameter GA problems, with various difficulty and dimensionality, have shown that real coded GA with the SBX operator works as good as or better than binary coded GA with the single point crossover operator [93]. Since binary coded GA with the single point crossover has proven to be successful, the SBX operator, which provides the same search power as the single point crossover operator in binary-coded GA, is likely to be a successful crossover operator in real parameter GA [92]. The SBX operator is particularly useful in problems in which the lower and the upper bounds of the global optimum are not known [92]. Since these bounds are not known in the new ISCPM multi-objective optimization problem, the SBX operator appears to be a good fit.

The simulated binary crossover works as follows [82]. From the k-th gene of the two parent solutions $\mathbf{s}_1$ and $\mathbf{s}_2$, $s_1^{(k)}$ and $s_2^{(k)}$, the two offspring solutions shown in (4.4) are created. Parameter β^* in (4.4) is calculated such that the area under the probability curve $P(\beta)$, defined in (4.5), from 0 to β^* is equal to a random number r, as shown in (4.6). In (4.5), η_c is a constant parameter and β is the ratio of the absolute difference in the offspring values to that of the parents, as shown in (4.7).

$$\begin{cases} s_1^{(k)} \\ s_2^{(k)} \end{cases} \longrightarrow \begin{cases} \mathbf{s'}_1^{(k)} = 1/2 \times [(1+\beta^*)\mathbf{s}_1^{(k)} + (1-\beta^*)\mathbf{s}_2^{(k)}] \\ \mathbf{s'}_2^{(k)} = 1/2 \times [(1-\beta^*)\mathbf{s}_1^{(k)} + (1+\beta^*)\mathbf{s}_2^{(k)}] \end{cases} \tag{4.4}$$

$$P(\beta) = \begin{cases} 0.5(\eta_c+1)\beta^{\eta_c}, & \text{if } \beta_i \leq 1, \\ 0.5(\eta_c+1)\frac{1}{\beta^{\eta_c+2}}, & \text{oterwise.} \end{cases} \tag{4.5}$$

$$\int_0^{\beta^*} P(\beta)d\beta = r \quad \rightarrow \quad \beta^* = \begin{cases} (2r)^{\frac{1}{\eta_c+1}} & r \leq 0.5 \\ \left(\frac{1}{2(1-r)}\right)^{\frac{1}{\eta_c+1}} & r > 0.5 \end{cases} \tag{4.6}$$

$$\beta = \left| \frac{\mathbf{s'}_2^{(k)} - \mathbf{s'}_1^{(k)}}{\mathbf{s}_2^{(k)} - \mathbf{s}_1^{(k)}} \right| \tag{4.7}$$

As an example, the probability density functions for creating offspring solutions under the SBX operator with $\eta_c = 2$ and $\eta_c = 5$ are shown in Figure 4.7. In this figure, the two parents are 3 and 6 and shown with the circles. The two offspring in SBX operator are symmetric about the parents, which avoids bias toward any particular parent.

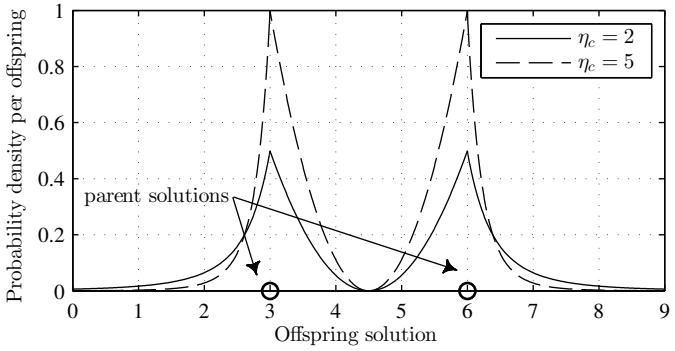

Figure 4.7: Probability density function for creating offspring solutions under SBX-η_c operator [82]

For the mutation operator for the new ISCPM method, the polynomial mutation was chosen. In polynomial mutation, a perturbed solution $\mathbf{s'}^{(k)}$ is obtained from the k-th gene of the parent solution $\mathbf{s}$, $\mathbf{s}^{(k)}$, using (4.8). In (4.8), $s^{k,\max}$ and $s^{k,\min}$ are the maximum and minimum values for the k-th gene of a chromosome, respectively. Also, the parameter δ^* is calculated such that the area under the polynomial probability distribution $P(\delta)$, defined in (4.9), from 0 to δ^* is equal to a random number r, as shown in (4.10). In (4.9), η_m is a constant parameter [82].

$$\mathbf{s'}^{(k)} = \mathbf{s}^{(k)} + (s^{k,\max} - s^{k,\min})\delta^* \tag{4.8}$$

$$P(\delta) = 1/2 \times (\eta_m + 1)(1 - |\delta|)^{\eta_m} \tag{4.9}$$

$$\int_0^{\delta^*} P(\delta)d\delta = r \quad \rightarrow \quad \delta^* = \begin{cases} (2r_i)^{\frac{1}{\eta_m+1}} - 1, & \text{if } r_i < 0.5, \\ 1 - [2(1-r_i)]^{\frac{1}{\eta_m+1}}, & \text{it } r_i \geq 0.5 \end{cases} \tag{4.10}$$

After obtaining the offspring population, $\mathbf{\mathcal{Q}}_t$, a combined population, $\mathbf{\mathcal{R}}_t$, is formed in step 7, where $\mathbf{\mathcal{R}}_t = \mathbf{\mathcal{P}}_t \cup \mathbf{\mathcal{Q}}_t$. Next, the individuals in $\mathbf{\mathcal{R}}_t$ are sorted based on constrain-domination to form several nondominated fronts, denoted with $\mathbf{\mathcal{F}}_1, \mathbf{\mathcal{F}}_2, \cdots$. To determine non-constrain-dominated fronts, the optimization objectives and constraints must be evaluated. In the ISCPM method, the three objectives are evaluated for each solution in $\mathbf{\mathcal{R}}_t$, in step 8. The gray blocks in steps 9-14 show that to evaluate the ISCPM constraints, each individual in $\mathbf{\mathcal{R}}_t$ is sent to a fast transient simulation core. A transient simulation is conducted with the adjusted set-points of each individual and the system response is sent back to the NSGA-II, where the generation-load balance constraints and security constraints for planned and unplanned events are evaluated. In this work, the TSAT tool of DSA *Tools*$^{\text{TM}}$ was linked to the NSGA-II algorithm developed in MATLAB. Details for the evaluation of the ISCPM constraints will be discussed later.

Next, to fill out the next population, $\mathbf{\mathcal{P}}_{t+1}$, with the best N individuals in $\mathbf{\mathcal{R}}_t$, individuals are taken from nondominated fronts $\mathbf{\mathcal{F}}_1, \mathbf{\mathcal{F}}_2, \cdots$, in ascending order, as shown in steps 15-20 in Figure 4.5. Assume $\mathbf{\mathcal{F}}_l$ is the last accommodated front, beyond which no other front can be accommodated, since

$$\textstyle\sum_{i=1}^{l-1} |\mathbf{\mathcal{F}}_i| < N \text{ and } \sum_{i=1}^{l} |\mathbf{\mathcal{F}}_i| > N. \tag{4.11}$$

Since all of the solutions in $\mathbf{\mathcal{F}}_l$ cannot be picked, the solutions in $\mathbf{\mathcal{F}}_l$ are sorted in step 21, using an index called the crowding distance index [75]. Thus, as shown in step 22, the best solutions in $\mathbf{\mathcal{F}}_l$ are added to $\mathbf{\mathcal{P}}_{t+1}$ to complete the next population. Next, if the stopping criteria is not met, the procedure continues to the next generation. Otherwise, the NSGA-II stops and the Pareto optimal set will be the set of Pareto solutions contained in the last population.

The crowding distance index, used in step 21, guides the selection process in NSGA-II toward a uniformly distributed Pareto front. This index assigns a distance value to each

solution, which is equal to the normalized absolute difference of the objectives of its two adjacent solutions. The crowding distance value is defined as the sum of individual distance values associated with each objective [75]. Equation (4.12) shows how this index is calculated for a solution $\mathbf{s}'$. Note that exclusions apply to extreme solutions in each objective [75]. In (4.12), $\mathbf{s}'_{i,\geq}$ and $\mathbf{s}'_{i,\leq}$ are the two adjacent solutions of $\mathbf{s}'$ on its right and left, respectively, in the i-th objective. This equation shows that the difference in the function values of adjacent solutions is normalized over the difference between the maximum and the minimum values of the objective function.

$$d(\mathbf{s}') = \sum_{i=1}^{3} \left| \frac{f_{o_i}(\mathbf{s}'_{i,\geq}) - f_{o_r}(\mathbf{s}'_{i,\leq})}{\max\limits_{\mathbf{s}\in\mathcal{F}_l}\{f_{o_i}(\mathbf{s})\} - \min\limits_{\mathbf{s}\in\mathcal{F}_l}\{f_{o_i}(\mathbf{s})\}} \right| \tag{4.12}$$

4.2.2 Evaluation of the Security Constraints in the ISCPM Method

4.2.2.1 Time-Restricted Operating Criteria

The operation of power systems is limited by some constraints. Power systems must satisfy these constraints in normal conditions or in case a contingency, such as a fault or a component outage, happens. These constraints help to define secure operation of power systems. If the system does not operate within the acceptable limits, system protection is used to isolate part of the system or the entire system, in order to prevent component damage. An operating point of the system is dynamically secure against credible contingencies, if the system transients following a contingency satisfy the aforementioned constraints, for all the contingencies in the contingency list. Similarly, a system is secure against a set of planned events, such as load changes, if the transients caused by the planned events satisfy the constraints. These constraints are mainly defined for system frequency, generator angles, bus voltages, and cable/line currents [26, 94–98].

For the ISCPM method, to be applied to the notional all-electric shipboard power system, several operating constraints were defined on system frequency, generator angles, load bus voltages, and cable currents. These constraints are depicted in Figure 4.8 and explained in the following paragraphs.

Frequency is a sensitive variable in power systems. It is a good indicator of generation-load balance and should remain nearly constant [4]. System operation in off-nominal frequency can harm the system components. For instance, significant frequency drop may cause high magnetizing currents in induction motors and transformers [4]. Therefore, tight bands are usually defined for the frequency in steady state operation. Moreover, frequency deviations during transients have to be bounded in terms of magnitude and duration, in order to ensure effective operation of system components.

For shipboard power systems, section 4.5 of IEEE Std 45-2002 [99] suggests the following values for frequency deviations from the nominal frequency: $\pm 3\%$ for steady state operation and $\pm 4\%$ for transients less than 2 seconds. These constraints can be graphically represented as shown in Figure 4.8(a). In this figure, the x and y axis show time and frequency, respectively. The frequency-time plane is divided into prohibited, restricted time, and continuous regions. System frequency can never enter the prohibited regions. It can stay in restricted-time regions for limited time lengths. It can be in the continuous region for an unlimited time.

The time-restricted constraints of this figure are also listed in Table 4.1 [99]. In this table, the first and the fifth constraints define minimum and maximum acceptable system frequency limits, 57.6Hz and 62.4Hz, respectively. Moreover, rows two and four define limits, in which system operation within [57.6Hz,58.2Hz] and [61.8Hz,62.4Hz] frequency bands is limited to less than 2 seconds, respectively. The third row in this table shows the steady state operation range. For the steady state operation, the system is allowed to operate in [58.2Hz,61.8Hz] frequency band, continuously.

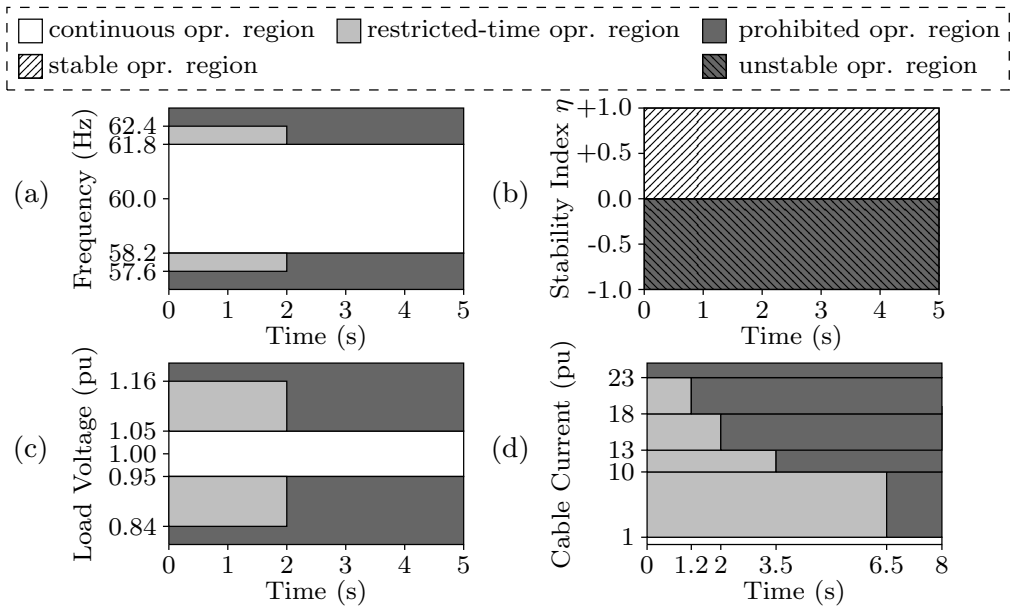

Figure 4.8: Time-dependent operating constraints for the notional AES. a) system frequency, b) transient angle stability index η, c) load bus voltage, and d) cable current

Table 4.1: Time-dependent frequency constraints for the notional AES

Constraint Band No.	Min. Frequency (Hz)	Max. Frequency (Hz)	Max. Allowable Time (s)
1	0	57.6	0
2	57.6	58.2	2
3	58.2	61.8	∞
4	61.8	62.4	2
5	62.4	∞	0

Transient angle stability is "the ability of the power system to maintain synchronism when subjected to a severe transient disturbance" such as a line/cable fault, loss of generation, or loss of load [4]. Power system usually responds to such disturbances with large excursions of generator rotor angles. After a large disturbance happens, if the resulting angular separation between the machines in the system remains within certain bounds, the system maintains synchronism. Otherwise, the system loses synchronism.

The loss of synchronism will usually be evident withing 2 to 3 seconds [4]. In order to maintain transient stability of the system generators, a constraint is usually defined on generator angles. In this research, the power angle-based stability index defined by (4.13) [100] was used for transient stability. Since this index is directly proportional to system angle separation, it provides a good indication of system stability status following a contingency [100].

$$\eta = \frac{360 - \delta_{max}}{360 + \delta_{max}} \tag{4.13}$$

In (4.13), δ_{max} is the maximum angle difference between any two generators in the same island (in degrees), and $\eta > 0$ and $\eta \leq 0$ correspond to stable and unstable transients, respectively. Thus, the index η must not be negative. Also, any positive value for this index is acceptable. These constraints are depicted in Figure 4.8(b) and also listed in Table 4.2. Figure 4.8(b) shows that the system will be operating in prohibited regions, if index η is below zero. It also shows that the system operation is acceptable, if index η is above zero. Table 4.2 shows that this index should not fall inside the [-1,0] band. On the contrary, it could have any positive value for an unlimited time and the system will be stable in terms of transient angle stability.

Table 4.2: Transient angle stability constraints for the notional AES

Constraint Band No.	Min. η Index	Max. η Index	Max. Allowable Time (s)
1	-1.0	0.0	0
2	0.0	+1.0	∞

Power system equipment are designed to operate at certain voltage ratings and hence, their prolonged operation at off-nominal voltages maybe harmful. Thus, for efficient operation of power systems, voltages at equipment terminals (load buses) in the system must be kept within acceptable limits [4].

Section 4.5 of IEEE Std 45-2002 [99] suggests the following ranges for bus voltage

deviations at user nodes in shipboard power systems: ±5% for continuous (steady state) operation and ±16% for transients lasting less than 2s. These constraints are shown in Figure 4.8(c). Figure 4.8(c) shows that the system operation is not acceptable, when load bus voltages are below 0.84pu or above 1.16pu. It also shows that bus voltages can operate in [0.84pu,0.95pu] or [1.05pu,1.16pu] bands for less than 2 seconds. It also depicts that [0.95pu,1.05pu] is the continuous operating range for load bus voltages. In other words, load bus voltages can be in this range for an unlimited time. These constraints are listed in Table 4.3, too. In this table, the first and the fifth rows indicate the two prohibited regions, the second and the fourth rows indicate the two restricted-time regions, and the third row indicates the continuous region.

Table 4.3: Time-dependent load bus voltage constraints for the notional AES

Constraint Band No.	Min. Voltage (pu)	Max. Voltage (pu)	Max. Allowable Time (s)
1	0	0.84	0
2	0.84	0.95	2
3	0.95	1.05	∞
4	1.05	1.16	2
5	1.16	∞	0

Cables in power systems transmit active and reactive power from one bus to another. The current that flows in a cable produces heat which may increases the cable's conductor and insulator temperatures. More specifically, the cable conductor temperature is determined based on the difference between the heating powers and the cooling powers. The heating power is mainly the joule power, P_j, which is the heat caused by the cable current passing through the cable resistance. The cooling powers are radiation, P_r, and convection, P_c heat loss [101]. Cable operation at elevated temperatures damages the cable by causing loss of tensile and permanent elongation of cable conductors. As a result, the current that flows in a cable mus be within an acceptable range [101].

The amount of current that can flow through a cable, without damaging its insulation and conductor, is time dependent. As a result, current carrying capacity of cables are

usually defined for steady state operation, long term (dynamic) operation, and short term (transient) operation. In steady state operation, the cable current is considered to be constant. Dynamic operation is defined as a step change in the cable current. For instance, when the load from the faulted circuit in a double circuit line is transferred to the healthy circuit. Transient operation is defined as a short-circuit. The thermal equations of a cable result in different current carrying capacities, for these different time-frames [101].

For each cable in the all-electric ship model, the discretized current carrying capacity curve shown in Figure 4.8(d) was used, arbitrarily. This figure defines the continuous operation range for the cable current to be less than 1pu. Also, it defines a time-restricted constraint in which the cable current can be up to 10pu for less than 6.5s. Similarly, for transients lasting less than 3.5s, 2.0s, and 1.2s, the cable currents up to 13pu, 18pu, and 23pu are acceptable, respectively. Moreover, the cable current should not exceed 23pu. These constraints are also listed in Table 4.4. In this table, the first row indicates the constraint associated with the steady state operation. Also, rows 2, 3, 4, and 5 show the restricted-time constraints. Moreover, the sixth row indicates the constraint associated with the prohibited region.

Table 4.4: Time-restricted cable ampacity constraints for the notional AES

Constraint Band No.	Min. Current (pu)	Max. Current (pu)	Max. Allowable Time (s)
1	0	1	∞
2	1	10	6.5
3	10	13	3.5
4	13	18	2.0
5	18	23	1.2
6	23	∞	0.0

4.2.2.2 Discussion of Dynamic Security Assessment Methods

Security analysis in power systems is handled for two time frames: static and dynamic [20, 102]. In static security analysis, for each contingency, only the steady state post contingency snapshot of the network is monitored for operating constraint

violations. In other words, it is assumed that the system operates in the transient period without any constraint violation. Hence, static security analysis is based on steady state operating constraints. The steady state operating constraints are usually defined on: transmission line/cable loadings, bus voltage deviations, and static stability limits for generator angles [8]. On the contrary, dynamic security analysis not only considers the steady state post-contingency snapshot of the system, but also monitors the transient period for operational constraint violations. Hence, in addition to the steady state constraints included in the static analysis, dynamic analysis includes the following constraints: transmission line/cable loadings in the transient period, voltage and frequency variations in the transient period, and power system stability constraints [8].

Security assessment methods can be classified into *deterministic* or *probabilistic*, *integration* or *Lyapunov (direct)*, and *point-wise* or *region-based* categories. These categories overlap each other, since they are defined based on different criteria. First, depending on whether a method takes power system uncertainties into account, security assessment methods can be divided into deterministic and probabilistic methods [103]. Second, depending on how contingency simulations are performed, security assessment methods can be classified into integration or direct (Lyapunov) methods [102]. Third, depending on whether contingency simulations are performed online or offline, security assessment methods can be classified into point-wise or region-based methods [104].

Power systems are subject to some uncertainties at all times. Deterministic security assessment methods do not take into consideration the probabilistic nature of the power system. Instead, they analyze the worst case scenarios. On the other hand, probabilistic methods take into account the uncertainties in system operating point, fault parameters, etc. These methods calculate the risk of operation at any operating point, where the risk is defined as the product of probability of occurrence and the severity of the event [17].

Deterministic methods have several shortcomings [103–107]: First, as they are based on worst case scenarios, they usually result in over conservative dispatches, which may increase system operating cost. Secondly, they do not usually provide a quantitative index

for system security. Thirdly, they do not take into account the occurrence frequency of the events. Fourthly, performance requirements in deterministic methods are not uniform. Probabilistic methods have some drawbacks, too [103–107]. Compared to deterministic methods, these methods require more computation time. Also, providing a good severity function is difficult. Moreover, these methods need more information such as the probability of faults, probability of load changes, etc., which may not be available.

Integration methods are distinguished from direct methods based on how the contingency simulations are performed [102, 108, 109]. To assess security of an operating point against a particular contingency in numerical integration method, that contingency event is simulated, using an integration method, e.g. Euler method. The simulation time must be long enough to reflect the impact of the contingency on the security aspect under study. In direct security assessment method, security of a contingency is determined using Lyapunov method. Hence, the contingency is simulated until the last switching event, which reduces the computation burden.

The main advantage of direct methods over numerical integration methods is their shorter computation time, which makes them advantageous for online security assessment applications. Direct methods, however, have several disadvantages [102, 108]. First, they are approximate methods. Second, finding a good Lyapunov function is difficult. Third, direct methods are mostly limited to transient angle stability or voltage stability aspects of security and do not provide any information regarding other security aspects, such as component overload or bus over/under voltage or system over/under frequency.

Point-wise methods for security assessment usually use time domain simulations to assess security of the current operating point. Then when the system operating point changes, they assess security of the new operating point, by conducting contingency simulations. Therefore, they need to perform many contingency simulation in online mode. In contrast, region-based methods determine the Dynamic Secure Region (DSR) of the system, in advance (offline). Hence, assessing security of the current system operating point in online mode is easy as checking if the current system operating point falls inside

the secure region [104].

The DSR is usually shown on a diagram called a *Nomogram*. A Nomogram is a diagram that shows the post-contingency performance measure of the system as a function of the pre-contingency values of the critical parameters [20, 110]. Critical parameters are some pre-contingency quantities that affect the post-contingency behavior of the system [111]. The dynamic secure region is a sub-space of the system operating space, and is defined by the boundaries forced by various security criteria [112]. An example of a dynamic secure region is shown in Figure 4.9 [112]. This figure shows a two dimensional DSR for a system that has two critical parameters, i.e. the generation of groups one and two. It can be seen that the boundaries are determined by various security aspects such as transmission line thermal loading, transient security, voltage security, and small-signal stability [112].

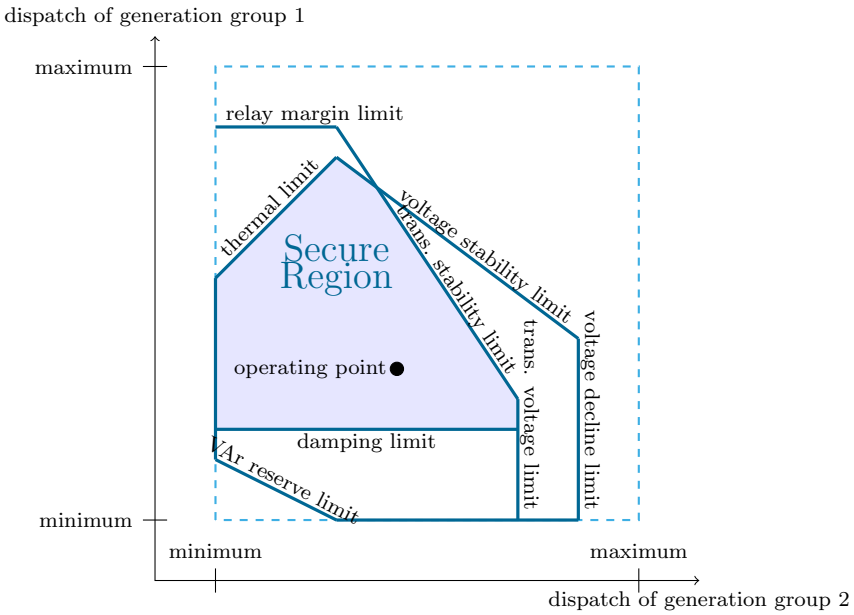

Figure 4.9: Illustration of the DSR in a conventional power system [112]

Point-wise methods are more accurate compared to region-based methods. However, region-based methods are more effective in online security monitoring, assessment, and

enhancement, due to their short execution time (in online mode). Also, they provide global information about the secure operating region of the system for the operator. Moreover, the distance between the current operating point and the system security border in these methods can be used as a security index [113].

Security-constrained power management methods, like the new ISCPM method, use the aforementioned security assessment methods in order to form their security constraints. Some of the security-constrained power management approaches [114] use the direct (Lyapunov or transient energy function) method to assess security of an operating point. In these methods, the dynamic equations of the system up to the last switching event are included in the optimization problem. The value of the Lyapunov function is calculated at the last switching event time and is limited to be less than the previously found critical value of the Lyapunov function.

Some of the security-constrained power management approaches [5,6,8,9,31,32,37,115] use the integration method to assess security of an operating point. In these methods, the Differential Algebraic Equations (DAE) describing each contingency are added to the problem. There are two alternatives for adding the DAEs in the optimization problems. In the first and more straight forward method [6,8,9,37], called direct integration method, the DAE set is converted into a set of equivalent algebraic constraints, using an integration method. The resulting set of algebraic equations are included in the optimization problem as a set of equality constraints.

The direct integration of DAEs imposes many equality and inequality constraints to the optimization problem. This problem is resolved in the second method, called constraint transcription [116]. The constraint transcription method [5,31,32,115] converts the problem from the functional space into the Euclidean space, in order to reduce the number of equality and inequality constraints. Therefore, security-constrained power management methods which are based on DAE integration using the constraint transcription technique do not impose many equality and inequality constraints to the optimization problem.

Some of the security-constrained power management approaches [11, 33, 89, 105] use

region-based method to assess security of an operating point. The region-based method for security assessment can be used in security-constrained optimization problems, efficiently [113, 117]. In these security-constrained power management approaches, some constraints are included in the optimization problem that force the system operating point to be inside the dynamic secure region.

The transient energy function method for security assessment is efficient for online applications, however, it can only determine the security of an operating point regarding transient angle stability or voltage stability. This method cannot assess the security of an operating point regarding other aspects of security such as over/under frequency, over/under voltage, or line ampacity. Thus, the Lyapunov method cannot be used in the formulation of the new ISCPM method.

Developing a security-constrained power management method by direct integration of the contingency DAEs is straight forward. However, this approach imposes many equality and inequality constraints to the optimization problem. Thus, the direct integration of the contingency DAEs into the optimization problem is not efficient. Compared to the direct integration approach, the constraint transcription approach is more efficient. This approach resolves the need to add many equality and inequality constraints by converting the optimization problem from the functional space into the Euclidean space. Hence, this method is an efficient method for security assessment in the new ISCPM formulation.

In the region-based method, the secure operating region of the system is determined in advance. Therefore, it is computationally expensive in offline mode. In contrast, it is efficient in online mode, since the security of an operating point is assessed by checking whether or not that operating point falls inside the secure region. Hence, the region-based security assessment method is a promising candidate for online applications or optimization formulations such as the new ISCPM, due to its simplicity and execution speed.

In the new ISCPM method presented in this dissertation, to ensure system dynamic security against planned events, some concepts from the constraint transcription method are adapted and security constraints against planned events are defined on the time that

constrained quantities spend in constraint bands. This method to evaluate the security constraints against planned events is discussed in subsection 4.2.2.3. On the other hand, security of an operating point against unplanned events is assessed using the dynamic security region of the system. In this method, a few simple constraints are included in the optimization problem, which force the power system operating point to be inside the DSR. This method to evaluate the security constraints against unplanned events is discussed in subsection 4.2.2.4.

4.2.2.3 Evaluation of the Dynamic Security Constraints against Planned Events in the ISCPM Method

The mathematical problem formulation for the ISCPM method in (3.9)-(3.17) showed that the ISCPM optimization problem includes two sets of security constraints against planned and unplanned events. To ensure system dynamic security against planned events in the new ISCPM method for (3.15), a point-wise approach is developed, since point-wise approaches are more accurate compared to the region-based approaches [112].

Consider a set of general time-restricted operating constraints for an arbitrary quantity, $z(t)$. These constraints are shown in Figure 4.10. Figure 4.10 shows that the operating space for this quantity is divided into continuous, restricted-time, and prohibited regions. The quantity $z(t)$ can be in the continuous region for an unlimited time. In this example, the continuous operating region for this quantity is from z_3^* to z_4^*, or $[z_3^*, z_4^*]$. The operation of a quantity in a time-restricted region is limited to a maximum time duration. In this example, $z(t)$ cannot be in $[z_2^*, z_3^*]$ region for more than τ_1^* seconds. Another time-restricted region is from z_4^* to z_5^*. The quantity $z(t)$ cannot be in this region for more than τ_2^* seconds. This figure also shows that $z(t)$ can never be below z_2^* or above z_5^*. These regions are called the prohibited regions.

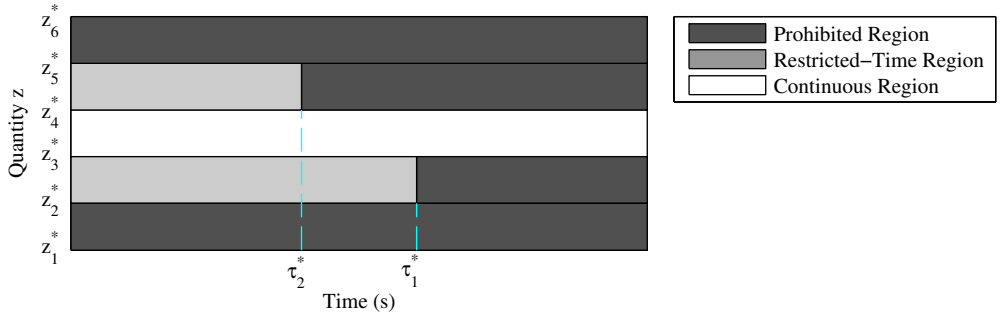

Figure 4.10: Time-restricted operating constraints for a constrained quantity $z(t)$

The constraints derived from Figure 4.10 can also be listed in a table, as shown in Table 4.5. For each constraint band w, this table shows the minimum ($z_w^{\min}$) and the maximum ($z_w^{\max}$) boundaries of the constraint band. It also shows the maximum time that variable $z(t)$ can stay in that band, $\tau_w^{\max}$.

Table 4.5: Time-restricted operating constraints for a constrained quantity $z(t)$

Const. Band No.	Min. Value ($z_w^{\min}$)	Max. Value ($z_w^{\max}$)	Max. Allowable Time ($\tau_w^{\max}$)
1	z_1^*	z_2^*	0
2	z_2^*	z_3^*	τ_1^*
3	z_3^*	z_4^*	∞
4	z_4^*	z_5^*	τ_2^*
5	z_5^*	z_6^*	0

To ensure the system security against planned events, it is desired to develop an approach in which the number of equality and inequality constraints imposed to the optimization problem is kept at a minimum. In the new ISCPM method, security constraints against planned events were developed by limiting the time that each constrained quantity, such as $z(t)$, spends in each constraint band. Following this approach, only the five inequality constraints shown of (4.14) are needed to define the requirements of Figure 4.10.

$$\tau_w \leq \tau_w^{\max}, \;\; w = 1, 2, 3, 4, 5 \tag{4.14}$$

In (4.14), $\tau_w^{\max}$ is the maximum time that $z(t)$ can spend in the w-th constraint band and τ_w is the duration of time that $z(t)$ stays in this band. This time, τ_w, can be calculated using (4.15). In (4.15), $sgn(.)$ is the *sign function*, which is 0 when its argument is negative and is 1, otherwise. The term $\frac{1}{2}\left[1 + sgn\left(+z(t) - z_w^{\min}\right)\right]$ is 1 when $z(t) > z_w^{\min}$, and is 0 otherwise. Also, the term $\frac{1}{2}\left[1 + sgn\left(-z(t) + z_w^{\max}\right)\right]$ is 1 when $z(t) < z_w^{\max}$, and is 0 otherwise. Therefore, the multiplication of these two terms is 1 when $z_w^{\min} < z(t) < z_w^{\max}$, and is 0 otherwise. That is why the integration of the multiplication of these two terms from 0 to T, shown in (4.15), gives the duration of time that $z(t)$ spends in $[z_w^{\min}, z_w^{\max}]$ constraint band.

$$\tau_w = \int_0^T \left[\frac{1}{2}\left[1 + sgn\left(+z(t) - z_w^{\min}\right)\right] \times \frac{1}{2}\left[1 + sgn\left(-z(t) + z_w^{\max}\right)\right]\right] dt \tag{4.15}$$

Thus, secure operation of quantity $z(t)$, when the planned events occur, can be ensured by including inequality constraints of (4.16)-(4.20) in the ISCPM optimization problem.

$$\tau_1 = \int_0^T \left[\frac{1}{2}\left[1 + sgn\left(+z(t) - z_1^*\right)\right] \times \frac{1}{2}\left[1 + sgn\left(-z(t) + z_2^*\right)\right]\right] dt \leq 0 \tag{4.16}$$

$$\tau_2 = \int_0^T \left[\frac{1}{2}\left[1 + sgn\left(+z(t) - z_2^*\right)\right] \times \frac{1}{2}\left[1 + sgn\left(-z(t) + z_3^*\right)\right]\right] dt \leq \tau_1^* \tag{4.17}$$

$$\tau_3 = \int_0^T \left[\frac{1}{2}\left[1 + sgn\left(+z(t) - z_3^*\right)\right] \times \frac{1}{2}\left[1 + sgn\left(-z(t) + z_4^*\right)\right]\right] dt \leq \infty \tag{4.18}$$

$$\tau_4 = \int_0^T \left[\frac{1}{2}\left[1 + sgn\left(+z(t) - z_4^*\right)\right] \times \frac{1}{2}\left[1 + sgn\left(-z(t) + z_5^*\right)\right]\right] dt \leq \tau_2^* \tag{4.19}$$

$$\tau_5 = \int_0^T \left[\frac{1}{2}\left[1 + sgn\left(+z(t) - z_5^*\right)\right] \times \frac{1}{2}\left[1 + sgn\left(-z(t) + z_6^*\right)\right]\right] dt \leq 0 \tag{4.20}$$

As an example, to limit the operation of the system frequency between 61.8Hz and 62.4Hz to less than 2s, which is one of the operating constraints in Figure 4.8(a), the constraint of (4.21) was included in the ISCPM method for the notional all-electric ship. In (4.21), $f(t)$ is the system frequency during the study period $[0, T]$.

$$\int_0^T \frac{1}{4}\Big[1 + \mathrm{sgn}\big(f(t) - 61.8\big)\Big]\Big[1 + \mathrm{sgn}\big(62.4 - f(t)\big)\Big] dt \leq 2 \tag{4.21}$$

The inequality constraint in (4.15) is non-differentiable, since the sign function is not a continuous function. Therefore, this constraint is not appropriate if optimization solving

computations require derivatives of the constraints. In this case, the non-continuous sign function can be approximated by (4.22) [118], in which arctan(.) is the *arc tan function*. Consequently, the non-differentiable constraint of (4.15) can be replaced with the differentiable constraint of (4.23).

$$sgn(u) \approx \frac{2}{\pi} \times \arctan(K \times u) \ , \ \ K >> 0 \tag{4.22}$$

$$\tau_w = \int_0^T \left[\frac{1}{2}+\frac{1}{\pi}\arctan\left(K\big(z(t)-z_w^{\min}\big)\right)\right]\left[\frac{1}{2}+\frac{1}{\pi}\arctan\left(K(z_w^{\max}-z(t))\right)\right]dt \leq \tau_w^{\max} \tag{4.23}$$

To summarize the evaluation of dynamic security constraints against planned events in the ISCPM method, consider the flowchart of Figure 4.5, again. In each generation, the ISCPM constraints are evaluated for each individual in $\mathcal{R}_t$. The gray blocks in the figure show that the multi-objective optimization solver (developed in MATLAB) is linked to a fast transient simulation core (TSAT). The NSGA-II is developed such that each individual in $\mathcal{R}_t$ is sent to the simulation core, for which a transient simulation is conducted and the system response is obtained. The system response to each individual is then passed to the NSGA-II. Then, (4.15) is used for each constrained quantity and constraint band, to evaluate dynamic security constraints against planned events, during the study period.

4.2.2.4 Evaluation of the Dynamic Security Constraints against Unplanned Events in the ISCPM Method

The mathematical problem formulation for the ISCPM method in (3.9)-(3.17) showed that the ISCPM optimization problem includes two sets of security constraints against planned and unplanned events. To ensure system dynamic security against unplanned events in the new ISCPM method for (3.16), a region-based approach is developed, since region-based approaches are fast and effective for online security assessment. In region-based security assessment methods, the Dynamic Secure Region (DSR) of the system is determined, in advance (offline) [113]. Hence, assessing security of an operating point in online mode is as easy as checking if that operating point falls inside the secure region. System DSR is characterized in the space of several Critical Parameters (CPs), where

each CP is a pre-contingency quantity that affects the post-contingency behavior of the system [111], and is usually a combination of the generator and load powers. In the new ISCPM method, the constraint of (4.24) was used to keep the system trajectory inside the DSR for the entire study period from 0 to T. In (4.24), $\mathbf{f}_{\text{DSR}}(\cdot) \leq 0$ is the DSR description, which is a function of generator output and load demand powers, $P^e_{G_1}(t), ..., P^e_{G_{n_g}}(t)$, and $P_{L_1}(t), ..., P_{L_{n_l}}(t)$, respectively.

$$\mathbf{f}_{\text{DSR}}\Big(P^e_{G_1}(t), ..., P^e_{G_{n_g}}(t), P_{L_1}(t), ..., P_{L_{n_l}}(t)\Big) \leq 0, \;\; t \in [0, T] \tag{4.24}$$

To develop the $\mathbf{f}_{\text{DSR}}(\cdot)$ function in (4.24), or to determine the system DSR, a deterministic or a probabilistic (risk-based) security assessment approach can be used [119]. In the new ISCPM method for isolated microgrid power systems, new methods are developed to determine deterministic or probabilistic DSRs in isolated microgrid power systems, which will be discussed in detail in subsection 4.4.

To summarize the NSGA-II procedure in the new ISCPM method, consider Figure 4.11. At each generation t, the offspring population, $\boldsymbol{\mathfrak{Q}}_t$, is obtained by performing the constrained tournament selection, crossover, and mutation operators on the current population, $\boldsymbol{\mathcal{P}}_t$. Next, the combined population, $\boldsymbol{\mathcal{R}}_t$, is divided into nondominated fronts, $\boldsymbol{\mathcal{F}}_1, \boldsymbol{\mathcal{F}}_2, \cdots$, for which evaluation of the objectives and constraints is required. To evaluate the ISCPM objectives, (3.10)-(3.12) are used. To evaluate the ISCPM constraints on generation-load balance and security for planned and unplanned events, (3.14), (4.15), and (4.24), are used, respectively. The next population, $\boldsymbol{\mathcal{P}}_{t+1}$, is filled by adding individuals from the nondominated fronts, in ascending order. If a front cannot be fully accommodated, the solutions in that front will be sorted, based on crowding distance index.

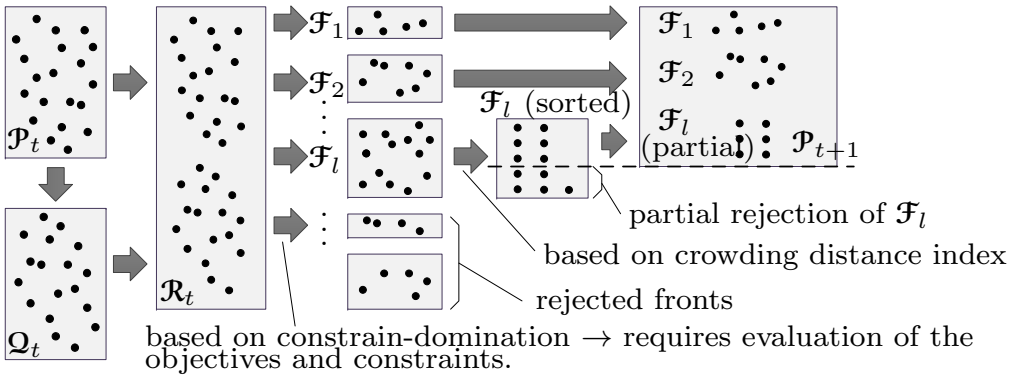

Figure 4.11: NSGA-II procedure in the ISCPM method (adapted from [75])

4.3 Best Compromise Solution Identification in the ISCPM Method

After obtaining the Pareto optimal front, a final solution is picked, which satisfies various goals of the optimization problem to some extent. Such a solution is called the Best Compromise Solution (BCS) [120]. In the ISCPM method, a fuzzy membership approach is developed to identify the BCS, since it mimics the real-life decision making process [43]. In this work, this approach was developed in MATLAB. The problem of identifying the best compromise solution is viewed as the optimization problem of (4.25) [121], in which the solution that maximizes an aggregation function $\mu_D(.)$, $\mathbf{s}_{\text{BCS}}$, is sought. In (4.25), $\mu_i(\mathbf{s})$ is the membership function for the i-th objective and reflects a degree of achievement for the objective function.

$$\mathbf{s}_{\text{BCS}} = \underset{\mathbf{s}}{\text{argmax}}\Big\{\mu_D\Big(\mu_1(\mathbf{s}),\mu_2(\mathbf{s}),\mu_3(\mathbf{s})\Big)\Big\} \tag{4.25}$$

For the ISCPM method, the membership function in (4.26) [44] is developed, using fuzzy sets theory, in which any objective f_{o_i} better than a threshold f_i^m is totally acceptable (quality equal to one), and any f_{o_i} worse than a threshold f_i^M is completely unacceptable (quality equal to zero). Moreover, it shows that the quality grade linearly decreases from f_i^m to f_i^M. In the developed method, f_i^m and f_i^M for each objective were the best and the worst values of the i-th objective among the solutions in the Pareto optimal set, $\mathbf{O}$, as

shown in (4.27).

$$\mu_i(\mathbf{s}) = \begin{cases} 0 & f_{o_i}(\mathbf{s}) \geq f_i^M \\ \frac{f_i^M - f_{o_i}(\mathbf{s})}{f_i^M - f_i^m} & f_i^m < f_{o_i}(\mathbf{s}) < f_i^M \\ 1 & f_{o_i}(\mathbf{s}) \leq f_i^m \end{cases} \tag{4.26}$$

$$f_i^m = \min_{i \in \mathfrak{O}} \{f_{o_i}\} \ , \ \ f_i^M = \max_{i \in \mathfrak{O}} \{f_{o_i}\} \ , \ \ i = 1, 2, 3 \tag{4.27}$$

The linear membership function of (4.26) is depicted in Figure 4.12. It shows that the membership function is one when $f_i(\mathbf{s}) \leq f_i^m$, and zero when $f_i(\mathbf{s}) \geq f_i^M$. This figure also shows that $\mu_i\big(f_i(\mathbf{s})\big)$ is linearly decreasing between f_i^m and f_i^M. An advantage of such a membership function is that it provides a measure of zero to one for each objective, regardless of its unit [120].

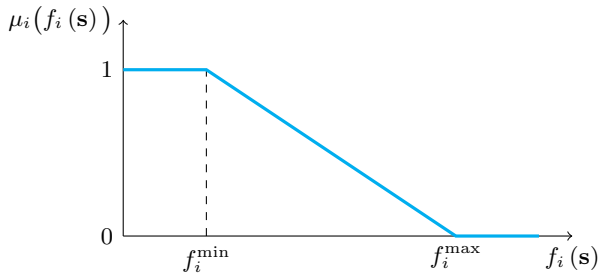

Figure 4.12: Linear membership function to identify the BCS in the ISCPM method

For the aggregation function, a popular aggregation function, which is the normalization of the individual membership functions [44], is developed, as shown in (4.28). In (4.28), ω_i is the i-th objective weight and $|\mathfrak{O}|$ is the number of Pareto solutions. In this work, the highest weight was given to the total generation objective, f_{o_2}, the second highest to the generation set-point deviation objective, f_{o_1}, and the lowest to the voltage/VAr set-point deviation objective, f_{o_3}.

$$\mu_D(\mathbf{s}_k) = \frac{\omega_1\mu_1(\mathbf{s}_k) + \omega_2\mu_2(\mathbf{s}_k) + \omega_3\mu_3(\mathbf{s}_k)}{\sum_{j=1}^{|\mathfrak{O}|}\Big(\omega_1\mu_1(\mathbf{s}_j) + \omega_2\mu_2(\mathbf{s}_j) + \omega_3\mu_3(\mathbf{s}_j)\Big)} \tag{4.28}$$

4.4 Developed DSR Assessment Method for Isolated Power Systems

In the new ISCPM method, a region-based approach is developed to assess power system dynamic security against contingencies. In this approach, an operating point is secure, if it falls inside the system Dynamic Secure Region (DSR). Dynamic secure region of a power system is defined in the space of some critical parameters of the system. Critical parameters are some pre-contingency quantities that affect the post-contingency behavior of the system [111]. Each critical parameter is a combination of the generator and load powers in the system. Some examples of critical parameters could be total system load, total power of a group of generators, total power of a group of loads, etc.

A new method is developed to assess the system DSR in an isolated microgird power system. This method differs from the methods available in literature for transmission power systems. In transmission power systems, the system DSR is determined in the neighborhood of an operating point [110, 111]. Hence, the system DSR changes when the system operating point significantly moves. Since the operating point variations in transmission power systems are normally small, and hence, the operating point neighborhood does not frequently change, it is not required to update the system DSR frequently. On the contrary, the operating point changes in isolated microgrid power systems may be large and frequent, due to large load sizes with respect to the system size. Hence, determining the DSR in the neighborhood of the current operating point is not practical, since this neighborhood constantly changes. To overcome this problem, a DSR assessment method for isolated microgrid power systems is developed in this work, in which an approximate DSR is obtained for the entire system operating space.

Next, subsection 4.4.2 discusses the developed DSR assessment approach using deterministic security. Then, limitations of the deterministic DSR in an isolated microgrid power system are discussed in subsection 4.4.3. Next, the developed method to assess the risk-based DSR in an isolated microgrid power system in discussed in subsection 4.4.4. Since the DSR assessment for the notional AES power system was carried out in DSA*Tools*$^{\text{TM}}$, the next subsection (subsection 4.4.1) explains the notional all-electric

ship model in TSAT.

4.4.1 Notional AES Power System Model in TSAT

Earlier in this section, it was explained that a model-based approach is developed for the new integrated security-constrained power management method. It was also explained that to apply the developed ISCPM method on the notional all-electric power system, the system model was developed in TSAT (Transient Security Assessment Tool of DSA *Tools* software package) and TSAT's fast simulation core was used to conduct transient simulations during iterations of the NSGA-II algorithm. TSAT was also used to assess the notional all-electric ship's deterministic and probabilistic DSRs, using the methods developed that will be discussed in subsections 4.4.2-4.4.4. Hence, the notional all-electric ship model developed in TSAT is discussed here.

TSAT includes a detailed time-domain simulation engine that can process complex power system models [100]. TSAT operates based on *case*, *scenario*, and *contingency* concepts [100, 122]. *Case* is the unit of analysis task and includes several *scenarios* (*power flows*). The following two features of TSAT [100, 122] motivated its use in this research: First, TSAT interfaces with user using *case* files, *power flow* files, and *contingency* files, all of which can be prepared in any text editor. Also, TSAT simulating results can be opened and read in other software. Second, TSAT has a feature called *batch mode*. Using the *batch mode*, TSAT can be called from any other software to perform the simulations described in a *case* file.

4.4.1.1 Generator Model

Each generator was modeled with its governor, turbine, and exciter. For the generators, a sixth order synchronous generator model (DG0S1) from TSAT's model library was used [123]. The parameters for this model, provided by ABB support group, are listed in Table 4.6 [12].

Table 4.6: Generator parameters for the notional AES

Gen	MVA	H	K_D	R_a	X_d	X_q	X'_d	T'_{d0}	X''_d	T''_{d0}	X''_q	T''_{q0}
$MTG1$	45	1.49	0.2	0.01	1.55	0.76	0.22	8.95	0.14	0.036	0.14	0.12
$ATG1$	5	1.06	0.2	0.20	1.25	0.62	0.24	4.11	0.17	0.023	0.17	0.06
$MTG2$	45	1.49	0.2	0.01	1.55	0.76	0.22	8.95	0.14	0.036	0.14	0.12
$ATG2$	5	1.06	0.2	0.20	1.25	0.62	0.24	4.11	0.17	0.023	0.17	0.06

In the simulations, one of the generators (MTG1) was chosen as the slack generator. Therefore, its governor was different from the other generators and was modeled in isochronous mode [12]. Governor models for the slack generator and non-slack generators are depicted in Figure 4.13(a) and (b), respectively. The only difference between these two governor models is the integrator block, $\frac{K}{s}$, in Figure 4.13(a). This block adjusts the slack generator's set-point until the frequency deviation in the system is zero. These models were implemented using TSAT's User Defined Model Editor (UDM Editor).

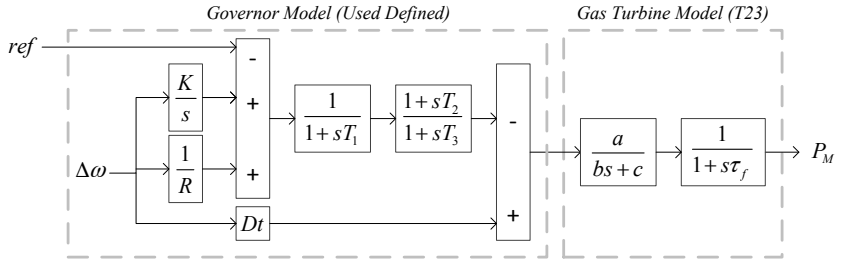

(a) Slack generator

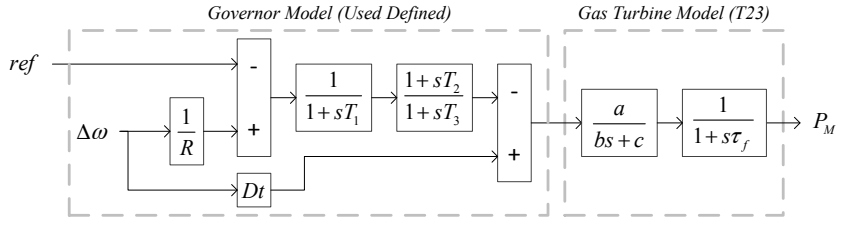

(b) Non-slack generators

Figure 4.13: Governor model implemented as a TSAT's user defined model for the notional AES. a) slack generator model, and b) non-slack generator model

For the turbines, the gas turbine model T23 from TSAT's built-in library was used [124].

Typical values were used for the governors and turbines parameters [124]. These values are listed in Table 4.7. For the exciters, TSAT's built-in AC exciter model E5 was used with its default parameters [123]. Moreover, the excitation control systems were modeled using the block diagram shown in Figure 4.14 and the typical parameters shown in Table 4.8.

Table 4.7: Governor and turbine parameters for the notional AES

Apparatus	Governor						Turbine			
Param	K	R	Dt	T_1	T_2	T_3	a	b	c	τ_f
Value	5	0.05	0.5	0.4	0.3	0.5	1.0	0.05	1.0	0.05

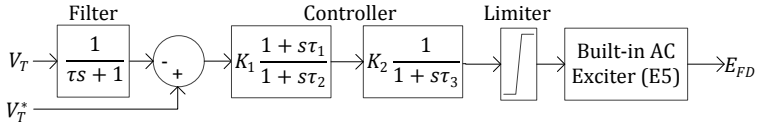

Figure 4.14: Generator excitation control system for the notional AES

Table 4.8: Excitation control system parameters for the notional AES

Param	τ	K_1	τ_1	τ_2	K_2	τ_3
Value	0.02	1	0.7	0.02	200	0.02

4.4.1.2 Propulsion Motor Model

The notional all-electric ship model used in the dissertation work includes two propulsion motors that act as the ship propellers. These propulsion motors can operate in two modes: power control mode or speed control mode. As the names suggest, in power control mode, propulsion motor's power is maintained at its set-point. On the contrary, when the propulsion motor is operating in speed control mode, ship's speed (usually expressed in knots) is maintained at its set-point [12]. During battle or extreme

maneuvers (sharp load changes), these motors operate in power control mode [12]. Since the case studies conducted in this research focus on such circumstances, the propulsion motors were used in the power control mode.

Feng in [12] reported some studies on propulsion motor model behavior in this control mode and concluded that the propulsion motor's output power reaches the new power set-point in about 5 seconds, when a step change is applied to the set-point. Thus, the simple model shown in Figure 4.15 was used for the propulsion motors. In this figure, $P(t)$ and $Q(t)$ are propulsion motor's active and reactive powers, respectively, and $P^*(t)$ is the active power set-point. Also, $\cos\phi$ is the motor's power factor. It was assumed that the power factor remained constant at all times. This assumption was made, since it was observed from the detailed propulsion motor model in PSCAD that the power factor remains almost constant when the propulsion power changes.

In order to implement this model, a TSAT built-in renewable generator block (called End Block PQW) was used. This block injects or absorbs active and reactive power, based on the provided set-points and can be used in custom modeling of generators or loads [123, 124]. The time constant T in this figure was set to 1s, in order to have a 5s delay between the time the set-point changes and the time the output reaches the set value.

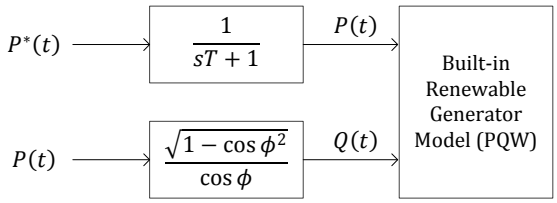

Figure 4.15: Propulsion motor model in power control mode in TSAT for the notional AES

To verify this model, a case study similar to the one reported in [12] was performed. In this study, the propulsion motor's power set-point (P^*) was changed from 35MW to 15MW, then to 25MW, and finally to 5MW, at times 10s, 20s, and 30s, respectively. The

output power of the propulsion motor, shown in Figure 4.16, matches the results reported in [12]. As can be seen, the output power reached the set-point in 5s.

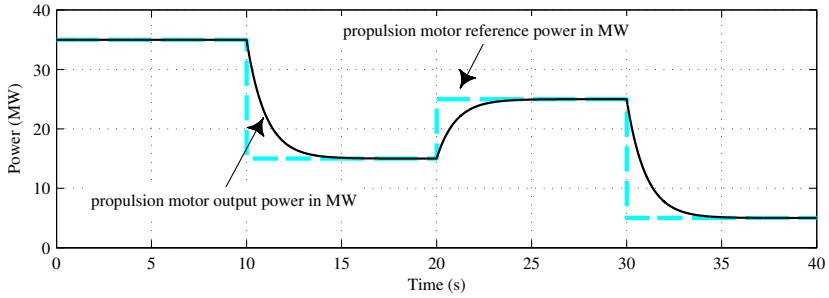

Figure 4.16: Behavior of propulsion motor output power in power control mode

4.4.1.3 DC Zone Model

Since the focus of the power management approach developed in this research is on the AC network, power electronic devices in the DC zones were not modeled. As a result, all of the DC loads inside each zone were connected to the zone's supplying AC bus, i.e. buses 9-12 in Figure 4.3. Consequently, each load inside a DC zone was modeled as a purely resistive AC load.

The process of eliminating power electronic conversion stages in modeling the DC zones in depicted in Figure 4.17. On the left side in this figure, the detailed structure of a DC zone is shown. It can be seen that the input voltage to the zone is 4.16kV AC. A rectifier converts this AC voltage to 1.1kV DC. This DC voltage is fed to three DC/DC converters to provide 0.375kV DC, 0.650kV DC, and 0.800kV DC voltage levels. These converters supply zonal loads. As an example, this figure shows two loads under each DC/DC converter. These loads maybe AC or DC motors or constant loads. On the right side in this figure, the simplified model for the DC zone is shown. In this simplified model, all of the DC loads under the three DC/DC converters were converted into their equivalent purely resistive AC loads and were connected to the incoming AC bus.

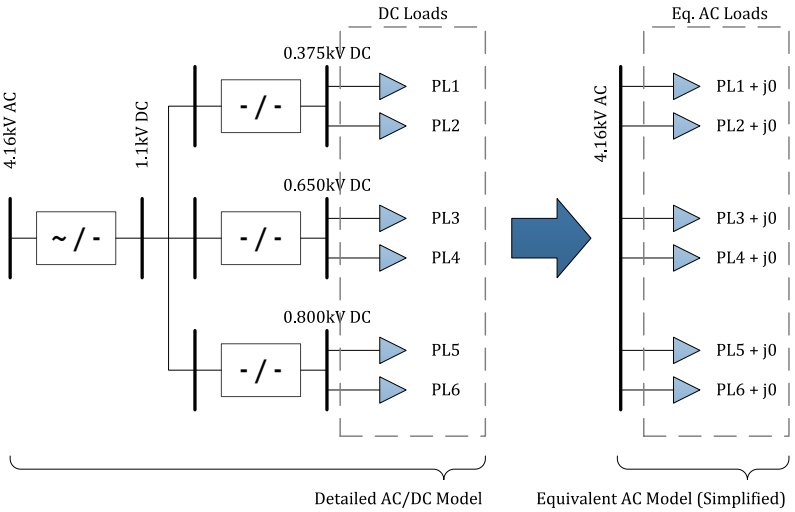

Figure 4.17: Elimination of power electronic devices in DC zone models for the notional AES

Table 4.9 lists the loads that were included in each DC zone in this system [12]. For each load, this table shows the priority (vital, semi-vital, or non-vital), type (fixed or variable), power rating, and time constant. The load priority is an indicator of how important a load is, compared to the other loads. The load priorities are used to determine which loads to supply and which loads to shed, in case the available generation power is less than the demand power. The load priorities can be vital, semi-vital, and non-vital. The fixed loads are the loads that operate in rated power, when they are connected. In other words, the demand power for a fixed load is either zero (when disconnected) or its rated power (when connected). On the contrary, variables loads can demand any power from zero to their rated power.

The load time constant determines how fast the output power reaches the new power set-power, when a step change is applied to the power set-point. The time constant for the constant loads (non-motor loads) is zero. To determine the time constant for the AC and DC motors inside the DC zones, Feng conducted a study in which a step change was applied to the power set-point of each motor and the time for the output power to reach the new power set-point was calculated [12]. The results of this study indicated that there is

an average 1s delay between the time the power set-point changes and the time the output power reaches the new power set-point. It means that the time constant for AC and DC motors inside the DC zones was 0.2s in average. As a result, the time constants in Table 4.9 were arbitrarily chosen from 0.15s to 0.25s to provide delays of 0.75s to 1.25s.

Table 4.9: Load characteristics in each DC zone in the notional AES [12]

No	Priority	Rated Power (kW)	Type	Time Constant (s)
1	non-vital	36	fixed, DC motor	0.23
2	non-vital	36	fixed, DC motor	0.24
3	non-vital	192.6	fixed, AC motor	0.23
4	non-vital	115.4	fixed, AC motor	0.17
5	non-vital	72	variable, constant load	0
6	non-vital	199	variable, constant load	0
7	non-vital	85	variable, constant load	0
8	non-vital	177	variable, constant load	0
9	semi-vital	115.4	fixed, DC motor	0.22
10	semi-vital	115.4	fixed, DC motor	0.20
11	semi-vital	115.4	fixed, DC motor	0.16
12	semi-vital	47.6	fixed, DC motor	0.16
13	semi-vital	79.4	fixed, AC motor	0.17
14	semi-vital	115.4	variable, constant load	0
15	semi-vital	70	variable, constant load	0
16	semi-vital	115.4	variable, constant load	0
17	semi-vital	22	variable, constant load	0
18	semi-vital	40	variable, constant load	0
19	semi-vital	119.6	variable, constant load	0
20	vital	181	fixed, AC motor	0.23
21	vital	151.4	variable, constant load	0
22	vital	42.6	variable, constant load	0

To implement loads with time constant in TSAT, the model shown in Figure 4.18 was used. This figure shows that the output power follows the set-point with a time constant T. It also shows that the built-in block PQW was used to implement this model in TSAT. This block injects/absorbs the desired amount of active and reactive power to/from the network. This model was used to replace each load listed in Table 4.9 with its equivalent AC model as shown in Figure 4.18.

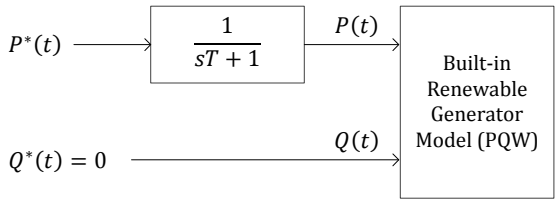

Figure 4.18: zonal load models in TSAT for the notional AES

4.4.1.4 Cable and Transformer Model

Cables in this system were modeled with π models. The values used for R and X parameters were obtained from an estimate of the physical ship layout prepared previously in PSAL. These parameters are shown in Table 4.10. Note that the bus numbers in this table are consistent with the bus numbers used in the single line diagram in Figure 4.3. The transformers were modeled with π models with 45MVA capacity, 13.8kV to 4.16kV ratio, and 13.75% reactance.

Table 4.10: Cable parameters for the notional AES

Application	AC Ring Cables				PM Feeders				DC Zone Feeders				DSTAT
$From-To$	1-2	1-3	2-4	3-4	5-13	6-13	7-14	8-14	5-9	6-10	7-11	8-12	5-15
$R\,(pu)\times 10^{-3}$	22	53	53	22	40	40	40	40	22	22	22	22	40
$X\,(pu)\times 10^{-3}$	27	64	64	27	6	6	6	6	4	4	4	4	6
$Rated\,MVA$	45	45	45	45	45	45	45	45	2	2	2	2	10
$Rated\,kV$	13.8	13.8	13.8	13.8	4.16	4.16	4.16	4.16	4.16	4.16	4.16	4.16	4.16

4.4.1.5 Distribution STATCOM Model

Some papers propose the use of Distribution Static Compensator (DSTATCOM) in all-electric ship power systems to improve bus voltages during transients, especially transients following pulse power load applications [81, 125]. DSTATCOM is a shunt compensation device which is usually used to improve voltage profile in distribution systems [81]. In the notional shipboard model studied in this dissertation, a 5MVAr DSTATCOM was connected to the pulse power load bus, bus 15 in Figure 4.3. For a STATCOM, the voltage – current characteristic is usually as depicted in Figure 4.19 [126]. In this figure,

V and I are the DSTATCOM voltage and current measured at the DSTATCOM bus, respectively. This figure shows that the STATCOM is not operated as a perfect voltage regulator, because zero droop regulation results in a poorly defined operating point and does not allow automatic load sharing among the VAr compensators [126]. Instead, its controller allows voltage, V, to deviate from the set value, V^*, proportional to its current, I. For the DSTATCOM used in the shipboard model, a 2% regulation slope was used.

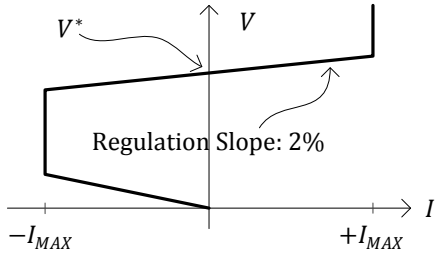

Figure 4.19: Voltage – current characteristic of a STATCOM [126]

Based on the characteristic shown in Figure 4.19, the model shown in Figure 4.20 was developed for the DSTATCOM in TSAT [100]. This figure shows that the voltage set point, V^*, is adjusted proportional to the DSTATCOM current measured at its terminal, I, first. Then, it is compared to the DSTATCOM voltage measured its terminal, V, and the error is determined. Finally, this error is passed through a PID controller which determines the current injection of the DSTATCOM, I. Note that the "minimum voltage limit" block in this figure blocks the controller if the terminal voltage of the DSTATCOM falls below 0.7pu. Parameters a and b in this figure were set to 0.02 and 1, respectively.

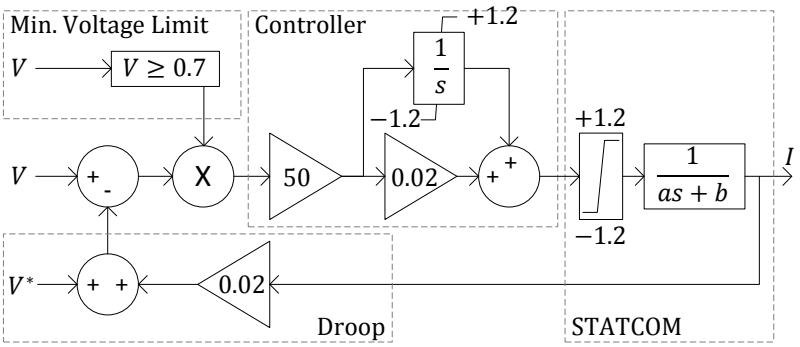

Figure 4.20: DSTATCOM model in TSAT for the notional AES

4.4.1.6 Pulse Power Load Model

All-electric ships may include combat systems such as railguns, lasers, and high power radars that require large amounts of power in short pulses [79]. These special loads with high power and short duration are called pulse power loads [127, 128]. Pulse loads can be classified as kinetic energy weapons, direct energy weapons, and high power sensors. Kinetic energy weapons use electric power to accelerate a projectile, such as electromagnetic guns, coil guns, electrothermal guns, and electrothermal-chemical guns. Direct energy weapons emit a high power electromagnetic wave to the target, such as high energy laser, high power microwave. High power sensors include pulse sonar and pulse radar [12,129,130].

Each pulse load can be characterized by its power (in MW), its width (in seconds), and its ramp rate (in MW per second) [12]. These characteristics for a sample pulse load with 20MW power, 1s width, and 200MW per second rate are shown in Figure 4.21. Note that the rise time for the pulse load equals its height divided by its ramp rate, which is 0.1s in this example. In the shipboard power system computer model for this research, pulse power loads were modeled as constant PQ loads with appropriate rise times. The results of the pulse power load simulations reported in [12] showed that the power factor for the pulse load is about 0.96. Hence, this power factor was also used for the pulse power load model in TSAT.

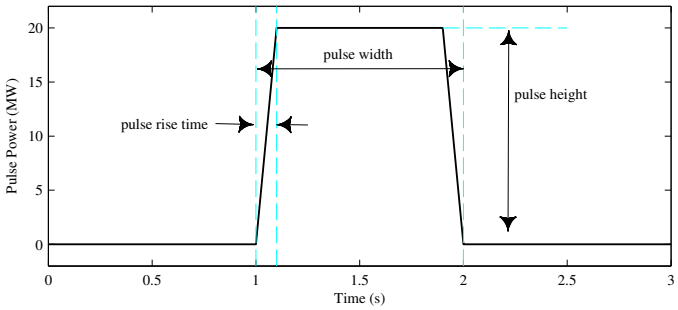

Figure 4.21: Pulse power load characteristics (width, height, and ramp rate)

4.4.2 Deterministic DSR Assessment in Isolated Microgrids

The deterministic DSR assessment method developed in this work for isolated microgrid power systems is discussed in subsection 4.4.2.1. Then, the details and results of implementing the developed method on the notional all-electric ship model are discussed in subsection 4.4.2.2.

4.4.2.1 Developed Deterministic DSR Assessment Method

Dynamic Secure Region (DSR) in power systems is described in the space of some Critical Parameters (CPs) [20, 110, 112]. Selecting critical parameters in a power system is not a trivial job. Traditionally, power system CPs are selected by a system analyst which is familiar with the system and has a physical understating of the security problems in the system [110, 131]. In this research, a systematic CP selection approach is developed, in which a good set of critical parameters is chosen from among several candidate sets.

Assume there are J critical parameter candidate sets. Each candidate set, denoted with $\mathfrak{C}_j$, is composed of several critical parameter candidates, denoted with c_1^j, c_2^j, and so on, as shown in (4.29).

$$\mathfrak{C}_j = \{c_1^j, c_2^j, ..., c_{I_j}^j\} \tag{4.29}$$

Critical parameters in power system are usually combinations of generator power injections and load power absorptions [110, 111, 113, 131]. Assume the set of generator

and load powers in the system is denoted with $\boldsymbol{\mathcal{E}}$. This set, as shown in (4.30), includes N generator and load powers, i.e. e_1, e_2, and so on. Since these generator and load powers are the ingredients to from critical parameters, they are referred to as Critical Parameter Elements (CPE), in this dissertation.

$$\boldsymbol{\mathcal{E}} = \{e_1, e_2, ..., e_N\} \tag{4.30}$$

Each critical parameter candidate, c_i^j, is a combination of the critical parameter elements in $\boldsymbol{\mathcal{E}}$. Assuming the relationship between a CPC, c_i^j, and the CPEs is linear, which is usually the case, this relationship can be mathematically characterized with a coefficient vector, $\mathbf{w}_i^j$. Consequently, (4.29) can be rewritten as (4.31), in which I_j is the number of CPCs in the j-th candidate set.

$$\boldsymbol{\mathcal{C}}_j = \{c_i^j |\ c_i^j = \mathbf{w}_i^{jT} \begin{bmatrix} e_1 \\ e_2 \\ \vdots \\ e_N \end{bmatrix},\ i = 1, 2, ..., I_j\} \tag{4.31}$$

In order to assess the system DSR, generating a large database containing data characterizing pre-contingency operating conditions (in terms of critical parameters) and corresponding system performance (in terms of security status) regarding each contingency is required [110]. In transmission level power systems, since the DSR is obtained around an operating point, the samples of this database are chosen in the neighborhood of a particular operating point, too [110]. However, since an approximation of the DSR in the entire system operating space is required, in the new method the samples are distributed in the entire operating space.

Each sample, $\mathbf{p}_m$, is a system operating point and is characterized by an N-tuple, since there are N critical parameter elements. The set of all samples, including M samples, is denoted with $\boldsymbol{\mathcal{P}}$ and is defined in (4.32). Equation (4.32) shows that each sampled operating point, $\mathbf{p}_m$, is an N-tuple with the lower and upper bounds $\mathbf{p}^{\min}$ and $\mathbf{p}^{\max}$, respectively.

$$\boldsymbol{\mathcal{P}} = \{\mathbf{p}_m |\ \mathbf{p}_m \in \mathbb{R}^N,\ \mathbf{p}^{\min} \leq \mathbf{p}_m \leq \mathbf{p}^{\max},\ m = 1, 2, ..., M\} \tag{4.32}$$

Assume security status of each sample m regarding each security criterion h is denoted

with s_m^h, and is 1 if $\mathbf{p}_m$ is secure and is 0, otherwise. Then, the set of insecure and secure samples regarding security criterion h, $\mathcal{G}_0^h$ and $\mathcal{G}_1^h$, can be formed as shown in (4.33) and (4.34), respectively.

$$\mathcal{G}_0^h = \{\mathbf{p}_m |\ s_m^h = 0,\ m = 1, 2, ..., M\} \tag{4.33}$$

$$\mathcal{G}_1^h = \{\mathbf{p}_m |\ s_m^h = 1,\ m = 1, 2, ..., M\} \tag{4.34}$$

Each candidate set maps the system operating space from CPE space, $\boldsymbol{\mathcal{E}}$, into a CPC space, $\boldsymbol{\mathcal{C}_j}$. The set of all samples mapped into the space of the j-th candidate set, $\boldsymbol{\mathcal{P}'}_j$, is defined by (4.35), in which $\mathbf{p'}_m^j$ is the projection of the m-th sample in the j-th space.

$$\boldsymbol{\mathcal{P}'}_j = \{\mathbf{p'}_m^j |\ \mathbf{p'}_m^j = \begin{bmatrix} \mathbf{w}_1^{jT} \\ \vdots \\ \mathbf{w}_{I_j}^{j\ T} \end{bmatrix} \mathbf{p}_m = \mathbf{W}_j \mathbf{p}_m\} \tag{4.35}$$

Equation (4.35) shows that the i-th attribute of the m-th projected sample is obtained by $\mathbf{w}_i^{jT}\mathbf{p}_m$. It also shows that the matrix containing all of $\mathbf{w}_i^{jT}$ row vectors is denoted with $\mathbf{W}_j$. Consequently, the sets of projections of the secure and insecure operating points, $\mathcal{G'}_{0,j}^h$ and $\mathcal{G'}_{1,j}^h$, can be obtained by (4.36) and (4.37), respectively.

$$\mathcal{G'}_{0,j}^h = \{\mathbf{p'}_m^j |\ s_m^h = 0,\ m = 1, 2, ..., M\} \tag{4.36}$$

$$\mathcal{G'}_{1,j}^h = \{\mathbf{p'}_m^j |\ s_m^h = 1,\ m = 1, 2, ..., M\} \tag{4.37}$$

The problem of determining the security border can be considered as a classification problem [132], in which two groups of previously classified samples, $\mathcal{G'}_{0,j}^h$ and $\mathcal{G'}_{1,j}^h$, are manipulated in order to develop some rules, which can optimally allocate an unclassified operating point into the secure or insecure groups. Assume the probability density functions for $\mathcal{G'}_{0,j}^h$ and $\mathcal{G'}_{1,j}^h$ are available and denoted with $f_0(\mathbf{p'}^j)$ and $f_1(\mathbf{p'}^j)$, respectively. It is reasonable to allocate an operating point $\mathbf{p'}^j$ to the insecure group, $\mathcal{G'}_{0,j}^h$, if (4.38) is satisfied, and to the secure group, if (4.39) is satisfied.

$$f_{0,j}^h(\mathbf{p'}^j) > f_{1,j}^h(\mathbf{p'}^j) \quad \longrightarrow \quad \mathbf{p'}^j \text{ insecure} \tag{4.38}$$

$$f_{0,j}^h(\mathbf{p'}^j) \leq f_{1,j}^h(\mathbf{p'}^j) \quad \longrightarrow \quad \mathbf{p'}^j \text{ secure} \tag{4.39}$$

Assume mean vectors for $\mathcal{G'}^h_{0,j}$ and $\mathcal{G'}^h_{1,j}$ are denoted with $\boldsymbol{\eta}^h_j$ and $\boldsymbol{\mu}^h_j$, respectively. Moreover, assume covariance matrices for $\mathcal{G'}^h_{0,j}$ and $\mathcal{G'}^h_{1,j}$ are denoted with $\boldsymbol{\Phi}^h_j$ and $\boldsymbol{\Sigma}^h_j$, correspondingly. By performing some mathematical derivations, the allocation rule of (4.38) results in (4.40), in which coefficients $\mathbf{Q}^h_j$, $\mathbf{l}^h_j$, and k^h_j are as defined in (4.41)-(4.43) [132]. Since (4.40) includes both of the squared and cross-product terms, it is usually referred to as quadratic discrimination function [132].

$$g(\mathbf{p'}^j) = \mathbf{p'}^{jT}\mathbf{Q}^h_j\mathbf{p'}^j + \mathbf{p'}^{jT}\mathbf{l}^h_j + k^h_j \geq 0 \quad \longrightarrow \quad \mathbf{p'}^j \text{ insecure} \tag{4.40}$$

$$\mathbf{Q}^h_j = \left(\boldsymbol{\Sigma}^{h^{-1}}_j - \boldsymbol{\Phi}^{h^{-1}}_j\right) \tag{4.41}$$

$$\mathbf{l}^h_j = \left(-2\boldsymbol{\Sigma}^{h^{-1}}_j\boldsymbol{\mu}^h_j + 2\boldsymbol{\Phi}^{h^{-1}}_j\boldsymbol{\eta}^h_j\right) \tag{4.42}$$

$$k^h_j = \left(\boldsymbol{\mu}^{h^T}_j\boldsymbol{\Sigma}^{h^{-1}}_j\boldsymbol{\mu}^h_j - \boldsymbol{\eta}^{h^T}_j\boldsymbol{\Phi}^{h^{-1}}_j\boldsymbol{\eta}^h_j\right) - \ln\frac{|\boldsymbol{\Phi}^h_j|}{|\boldsymbol{\Sigma}^h_j|} \tag{4.43}$$

It is worth mentioning that since $\mathcal{G'}^h_{0,j}$ is the projection of $\mathcal{G}^h_{0,j}$ using projection matrix $\mathbf{W}_j$ in (4.35), its mean and covariance can be calculated using the mean and covariance of $\mathcal{G}^h_{0,j}$, as shown in (4.44). Similarly, mean and covariance of $\mathcal{G'}^h_{1,j}$ can be calculated using (4.45). In (4.44) and (4.45), $\boldsymbol{\eta}^h$ and $\boldsymbol{\mu}^h$ are the mean vectors for $\mathcal{G}^h_0$ and $\mathcal{G}^h_1$, respectively. Furthermore, $\boldsymbol{\Phi}^h$ and $\boldsymbol{\Sigma}^h$ are the covariance matrices for $\mathcal{G}^h_0$ and $\mathcal{G}^h_1$, correspondingly.

$$\boldsymbol{\eta}^h_j = \mathbf{W}_j\boldsymbol{\eta}^h \quad , \quad \boldsymbol{\Phi}^h_j = \mathbf{W}_j\boldsymbol{\Phi}^h\mathbf{W}^T_j \tag{4.44}$$

$$\boldsymbol{\mu}^h_j = \mathbf{W}_j\boldsymbol{\mu}^h \quad , \quad \boldsymbol{\Sigma}^h_j = \mathbf{W}_j\boldsymbol{\Sigma}^h\mathbf{W}^T_j \tag{4.45}$$

In order to compare the quality of security borders in various candidate sets, a discriminant function performance index [132] can be used. Two of the most common approaches to calculate a performance index are "leaving-out-one" method and "misclassification rate" method [132, 133]. In leaving-out-one method, the discriminant function in (4.40) is derived from $M-1$ samples and is used to classify the excluded sample. This procedure is carried out M times leaving out each member, in turn. Then, the percentage of the misclassified members is calculated as the quality index [132]. In misclassification rate method, the discrimination function in (4.40) is obtained from all of

the M samples and is applied to the same data. Then, the percentage of the misclassified samples is calculated as the quality index [132]. Compared to leaving-out-one method, misclassification rate method is simpler [132]. However, it may result in an optimistic index in some cases [132].

The discrimination quality may not be the only criterion to pick the best set among all of the critical parameter candidate sets. For instance, in order to provide the system operator with security enhancement actions, it is preferred to have at least one controllable parameter among critical parameters [110, 111, 131]. Another important criterion maybe the number of critical parameters in the set. The number of critical parameters is preferred to be less than four or five, since it is difficult to compactly present DSR information to the operator when there are many critical parameters [110]. Therefore, quality of CPC sets in discriminating secure operating points from insecure ones, type of critical parameters (controllable or uncontrollable), number of critical parameters, and some other criteria may be used to pick the best CPC set.

4.4.2.2 Deterministic DSR in the Notional AES

The procedure to assess Deterministic Dynamic Secure Region (DDSR) in the notional all-electric ship model, using the method proposed in subsection 4.4.2.1, was divided into data preparation (part I) and data processing (part II). In the first part, dynamic security of a wide range of system operating points was assessed. In the second part, mathematical description of the system approximate DSR in the space of system Critical Parameters (CP) was obtained. The required steps to accomplish each part are depicted in Figure 4.22 and explained in the following paragraphs.

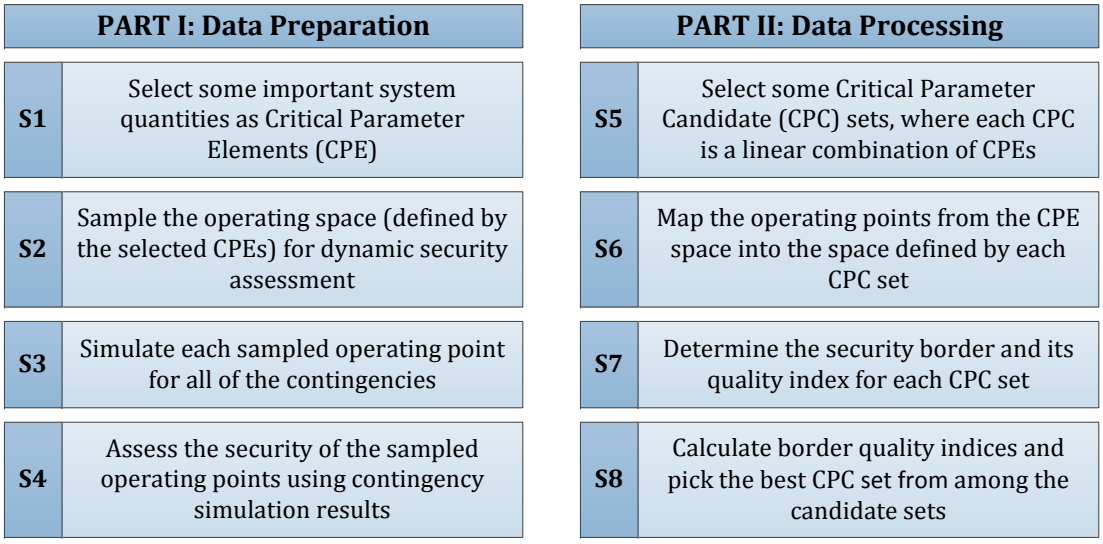

Figure 4.22: Procedure to assess deterministic DSR in the notional AES

In the first step, the CPEs were chosen. All of the bus active power injections and absorptions in the notional all-electric ship model, shown in Figure 4.3, were chosen as Critical Parameter Elements (CPEs). Power injections were the four generator powers, P_{MTG1}, P_{ATG1}, P_{MTG2}, and P_{ATG2}, at buses 1-4. Power absorptions were the six load powers, P_{Z1}, P_{Z2}, P_{Z3}, P_{Z4}, P_{PM1}, and P_{PM2}, at buses 9-13. Therefore, the set of system CPEs was defined by (4.46).

$$\mathcal{E} = \{P_{MTG1}, P_{ATG1}, P_{MTG2}, P_{ATG2}, P_{PM1}, P_{PM2}, P_{Z1}, P_{Z2}, P_{Z3}, P_{Z4}\} \tag{4.46}$$

In the second step, the operating space was sampled. In order to sample the ship's operating space, *Latin hypercube random sampling* [111] method was used. This method is a mixture of random and systematic sampling and ensures that each interval of a system quantity is sampled, exactly, by a pre-determined number of samples [111]. This sampling method is originally motivated by the assumption that neural network accuracy, for a given number of samples, is best when each parameter is maximally resolved [111, 131]. In this research, latin hypercube sampling method was used, since it was observed that higher resolved data sets resulted in higher quality security borders.

Uniform and Latin hypercube random sampling methods are illustrated and compared in Figure 4.23. This figure shows sampling of a 2-D space using both of the sampling methods. In this example, the operating ranges for parameters one and two, from 0 to 3, are divided into 3 intervals. Therefore, the operating space is divided into 9 areas (squares). Figure 4.23(a) shows that in uniform sampling, the samples are the centers of these 9 squares. Alternatively, the samples could be at any particular corner of the squares. On the contrary in Latin hypercube sampling, a sample is randomly chosen inside each area. Since the samples do not share the same x or y attributes, this sampling method results in a higher resolved data set.

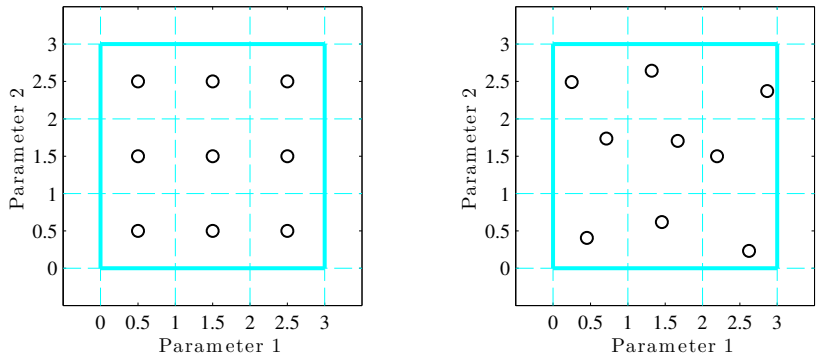

(a) Uniform sampling (b) Latin hypercube random sampling

Figure 4.23: Illustration of operating space sampling methods [111]. a) uniform sampling method, and b) Latin hypercube random sampling method

The intervals defined for the 10 CPEs in the notional all-electric ship model are listed in Table 4.11. For each CPE, this table shows the minimum value, the maximum value, and the number of intervals. For instance, minimum and maximum powers for MTG2 were 4.5MW and 36MW, respectively, and this range was divided into 5 intervals. Hence, the intervals for P_{MTG2} were [4.5,10.8]MW, [10.8,17.1]MW, [17.1,23.4]MW, [23.4,29.7]MW, and [29.7,36.0]MW. Since MTG1 was chosen as the slack generator, its value was not chosen randomly. Instead, its value in each sample was determined based on generation-load

balance in the power system.

Table 4.11: Operating range and number of intervals for each CPE for Latin hypercube sampling in the notional AES

Parameter	P_{MTG1}	P_{ATG1}	P_{MTG2}	P_{ATG2}	P_{PM1}	P_{PM2}	P_{Z1}	P_{Z2}	P_{Z3}	P_{Z4}
Minimum (MW)	–	0.5	4.5	0.5	0	0	0	0	0	0
Maximum (MW)	–	4.0	36.0	4.0	36.0	36.0	2.0	2.0	2.0	2.0
Number of intervals	–	2	5	2	5	5	2	2	2	2

The intervals of Table 4.11 for generation and load powers resulted in 8,000 hypercubes in the ship's operating space. In each hypercube, four operating points were randomly picked and therefore, the operating space of the notional ship model was sampled with 40,000 operating points. Among the 40,000 samples (operating points), 19,160 operating points had load flow solutions. Some combinations of loads and generations led to infeasible slack generator power and were eliminated. Hence, in the second step, the ship's operating space was sampled with $M = 19{,}160$ samples, where each sample was a 10-tuple, whose attributes were four generator and six load powers.

In the third step, each sampled operating point was simulated for all of the contingencies in the contingency list. For the notional all-electric ship model, a contingency list, $\mathfrak{D}$, including 10 contingency categories, denoted with C1-C10, was developed. This contingency list included $D = 39$ contingencies. Here are the 10 contingency categories.

C1. MTG outage: disconnecting any single main turbine generator from the system. This category includes 2 contingencies.

C2. ATG outage: disconnecting any single auxiliary turbine generator from the system. This category includes 2 contingencies.

C3. PM outage: disconnecting any single propulsion motor from the system. This category includes 2 contingencies.

C4. DC zone outage: disconnecting any single DC zone from the system. This

category includes 4 contingencies.

C5. PM step: a 15MW sharp increase in the power demand of any single propulsion motor. This category includes 2 contingencies.

C6. Pulse load: serving a pulse load with 50MW power, 0.707 power factor, and 500ms duration. This category includes 1 contingency.

C7. Faults on the AC cables feeding the DC zones: three-phase faults at 0% and 100% lengths of the lines 5-9, 6-10, 7-11, and 8-12 cleared after 50ms by opening the faulty line. This category includes 8 contingencies.

C8. Faults on the AC ring cables: three-phase faults at 0% and 100% lengths of the lines 1-2, 1-3, 2-4, and 3-4 cleared after 50ms by opening the faulty line. This category includes 8 contingencies.

C9. Faults on the AC cables feeding the PMs: three-phase faults at 0% and 100% lengths of the lines 5-13, 6-13, 7-14, and 8-14 cleared after 50ms by opening the faulty line. This category includes 8 contingencies.

C10. Fault on the AC cable feeding the pulse load: three-phase faults at 0% and 100% lengths of the line 5-15 cleared after 50ms by opening this line. This category includes 2 contingencies.

To conduct contingency simulations, MATLAB and TSAT were used together. TSAT is the Transient Security Assessment Tool of DSA *Tools*$^{\text{TM}}$ software package [100].

In the fourth step, Dynamic security of each sample was assessed based on the four time-restricted operating criteria introduced earlier in Figure 4.8. The four constraints were defined on system frequency, generator angles, load bus voltages, and cable currents. These constraint were mainly obtained from section 4.5 of IEEE Std 45-2002 [99]. In this step, security of each operating point m regarding any of the four security criteria, denoted with s_m^1, s_m^2, s_m^3, and s_m^4, was determined.

Security status of the 19,160 sampled operating points are summarized in Table 4.12. This table shows the percentage of the secure samples, out of 19,160, for each contingency or contingency group, regarding individual security criterion or all of the security criteria together. In this table, the first three columns show contingency category, contingency number, and contingency description, respectively. The following four columns show percentages of the secure samples, considering any of the four security criteria, where criteria 1 to 4 denote system frequency, generator angle, load bus voltage, and cable current criterion, correspondingly. Finally, the last column indicates percentage of the secure samples when all of the security criteria are considered together.

For example, consider the first three rows in this table. The first row indicates that 45%, 100%, 98%, and 100% of the samples were secure regarding security criteria 1-4, respectively, when MTG1 outage happened. Also, the last cell in this row shows the percentage of the secure samples regarding all of the security criteria together, for the same contingency. The next row provides the same information for the second contingency in category C1, i.e. outage of MTG2. The third row indicates that considering both of the contingencies in C1, 18%, 100%, 98%, and 100% of the samples were secure regarding security criteria 1-4, respectively. The last cell in the third row shows that 18% of the studied samples were secure against all of the contingencies in C1, regarding all of the security criteria. This table is a good indicator of security problems and severe contingencies in the notional all-electric ship model.

Table 4.12: Summary of deterministic security analysis in the notional AES

Contingency Category Number	Contingency Number and Contingency Description		Security Criteria				
			Crt. 1	Crt. 2	Crt. 3	Crt. 4	Crt. 1-4
C1	1	MTG1 outage	45	100	98	100	45
	2	MTG2 outage	47	100	100	100	100
	–	All of the contingencies in C1	18	100	98	100	18
C2	3	ATG1 outage	100	100	100	100	100
	4	ATG2 outage	100	100	100	100	100
	–	All of the contingencies in C2	100	100	100	100	100
C3	5	PM1 outage	81	100	100	100	81
	6	PM2 outage	80	100	100	100	80
	–	All of the contingencies in C3	62	100	100	100	62
C4	7	Z1 outage	100	100	100	100	100
	8	Z2 outage	100	100	100	100	100
	9	Z3 outage	100	100	100	100	100
	10	Z4 outage	100	100	100	100	100
	–	All of the contingencies in C4	100	100	100	100	100
C5	11	PM1 Step	100	100	100	100	100
	12	PM2 step	100	100	100	100	100
	–	All contingencies in C5	100	100	100	100	100
C6	13	Pulse load	100	100	100	100	100
	–	All of the contingencies in C6	100	100	100	100	100
C7	14	Fault on 0% of line 5-9	100	100	100	100	100
	15	Fault on 100% of line 5-9	100	100	100	100	100
	16	Fault on 0% of line 6-10	100	100	100	100	100
	17	Fault on 100% of line 6-10	100	100	100	100	100
	18	Fault on 0% of line 11-7	100	100	100	100	100
	19	Fault on 100% of line 11-7	100	100	100	100	100
	20	Fault on 0% of line 12-8	100	100	100	100	100
	21	Fault on 100% of line 12-8	100	100	100	100	100
	–	All of the contingencies in C7	100	100	100	100	100
C8	22	Fault on 0% of line 2-1	75	40	100	100	40
	23	Fault on 100% of line 2-1	54	27	99	100	27
	24	Fault on 0% of line 4-3	78	42	100	100	41
	25	Fault on 100% of line 4-3	58	29	99	100	29
	26	Fault on 0% of line 1-3	69	68	100	100	65
	27	Fault on 100% of line 1-3	71	65	100	100	63
	28	Fault on 0% of line 2-4	91	91	100	100	90
	29	Fault on 100% of line 2-4	91	89	100	100	88
	–	All of the contingencies in C8	43	21	98	100	21
C9	30	Fault on 0% of line 5-13	100	100	100	100	100
	31	Fault on 100% of line 5-13	100	100	100	100	100
	32	Fault on 0% of line 6-13	100	100	100	100	100
	33	Fault on 100% of line 6-13	100	100	100	100	100
	34	Fault on 0% of line 7-14	100	100	98	100	98
	35	Fault on 100% of line 7-14	100	100	98	100	98
	36	Fault on 0% of line 14-8	100	100	100	100	100
	37	Fault on 100% of line 14-8	100	100	100	100	100
	–	All of the contingencies in C9	100	100	98	100	98
C10	38	Fault on 0% of line 5-19	100	100	100	100	100
	39	Fault on 100% of line 5-19	100	100	100	100	100
	–	All contingencies in C10	100	100	100	100	100
C1-C10	–	All of the contingencies in C1-C10	17	21	95	100	16

Here are some of the important observations from this table.

1. Outage of an MTG resulted in under frequency problems in the system in many samples, because a significant part of the system generation was lost. It can be seen that 82% of the studied operating points had frequency security problems, when one of the MTGs got disconnected. In contrast, ATG outages did not cause any security violations.

2. Propulsion motors are the main power consumers in this system. As a result, loss of these loads caused over frequency problems in the system in 38% of the studied operating points.

3. The rows associated with the contingency group C8 show that the faults on AC ring cables caused frequency constraint violations in 57% of the samples. It is because the system generators, especially ATGs, are small and have small inertia, and cause significant frequency oscillations after faults.

4. The only contingencies that caused transient angle instability in this system were the faults on AC ring cables, i.e. contingencies 22-29. This table shows that the power system was transiently unstable after a fault on one of these cables in 79% of the operating points.

5. The column associated with the third security criterion shows that load bus voltage constraint violation was a rare problem in the notional ship model. Only 5% of the operating points were insecure regarding this security criterion.

6. No over current problem was detected in the 19,160 operating points. It may be due to a conservative cable sizing and a more economically concerned cable selection may lead to cable overloading for some operating points and contingencies. As this security criterion was never violated in the performed studies, it was eliminated from discussions in the rest of this dissertation.

7. This table can be used to rank the severity of the contingencies and problematic security criteria in the notional all-electric shipboard power system. It shows that C1, C8, and C3 are the most severe contingency groups, since they included 82%, 79%, and 38% insecure operating points, respectively. Also, the last row of the table indicates that only 17% of the operating points were secure against frequency criterion. Moreover, 79% of the operating points were unstable, regarding transient angle stability, when a contingency from the contingency list happened. It also indicates that 95% of the operating points were secure regarding load bus voltage criterion, and finally, cable current criterion was never violated.

8. In deterministic security analysis, an operating point is insecure if it is insecure against at least one contingency and regarding one security criterion. The highlighted cell in this table shows the percentage of the secure samples regarding the entire contingency list regarding all of the security criteria. It shows that only 16% of the studied operating points were secure, which is a low percentage.

To provide a visual perspective of the secure/insecure operating points in the notional all-electric ship's operating space, Figures 4.24 and 4.25 show two subsets of the operating space in $P_{MTG1} - P_{MTG2}$ plane, with 45 and 59 operating points, respectively. In these figures, crosses and circles denote insecure and secure operating points, correspondingly. Figure 4.24 represents a subset of the 10-D operating space in which P_{ATG1} and P_{ATG2} were sampled from 2.25MW to 4MW interval (interval 2 in Table 4.11), and P_{Z1}, P_{Z2}, P_{Z3}, and P_{Z4} from 1MW to 2MW interval (interval 2 in Table 4.11). Furthermore, P_{PM1} and P_{PM2} were sampled from 0 to 7.2MW (interval 1 in Table 4.11). The samples in Figure 4.25 are from the same CPE intervals, except for P_{PM2} which was sampled from 7.2MW to 14.4MW interval (interval 2 in Table 4.11). It can be observed that many of the operating points in these two figures were insecure regarding frequency and transient angle security criteria. Also, most of them were secure regarding load bus voltage criterion, and no cable current constraint violation was among these operating points.

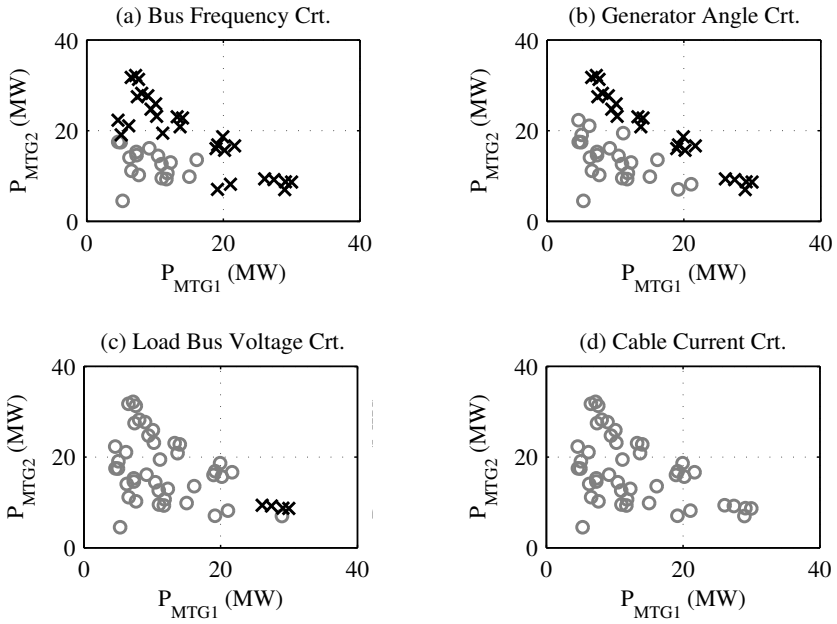

Figure 4.24: First subset of the system operating space. In this subset, $P_{ATG1} \in [2.25, 4]$MW, $P_{ATG2} \in [2.25, 4]$MW, $P_{Z1} \in [1, 2]$MW, $P_{Z2} \in [1, 2]$MW, $P_{Z3} \in [1, 2]$MW, $P_{Z4} \in [1, 2]$MW, $P_{PM1} \in [0, 7.2]$MW, and $P_{PM2} \in [0, 36]$MW.

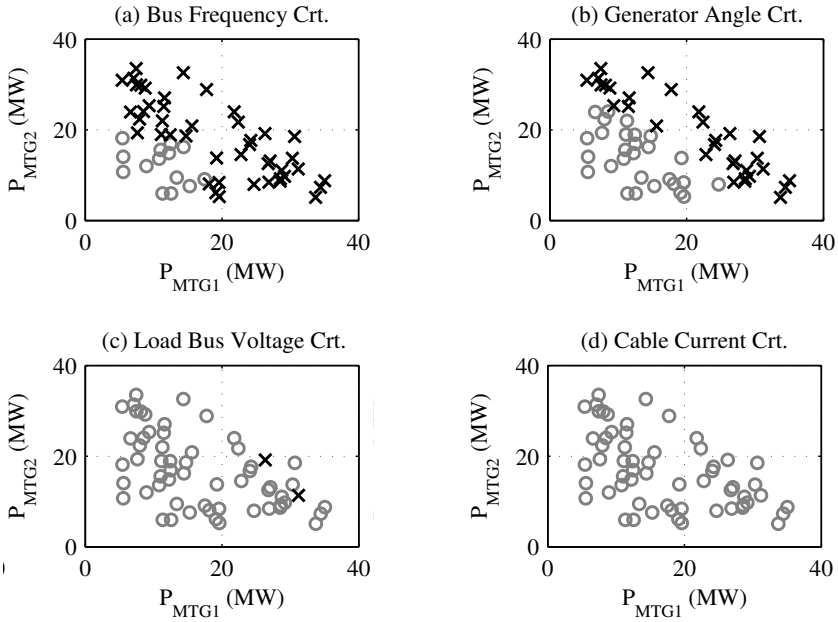

Figure 4.25: Second subset of the system operating space. In this subset, $P_{ATG1} \in [2.25, 4]$MW, $P_{ATG2} \in [2.25, 4]$MW, $P_{Z1} \in [1, 2]$MW, $P_{Z2} \in [1, 2]$MW, $P_{Z3} \in [1, 2]$MW, $P_{Z4} \in [1, 2]$MW, $P_{PM1} \in [7.2, 14]$MW, and $P_{PM2} \in [0, 36]$MW.

In the fifth step, nine critical parameter candidate sets were developed for the notional all-electric ship model. The mapping coefficients for the nine CPC sets, $\mathbf{w}_i^j$'s in (4.31), are shown in Table 4.13. For example, Table 4.13 shows that the first CPC set ($j = 1$) is composed of two critical parameters with the mapping coefficients as shown in (4.47). This set maps the CPE space, $\mathfrak{E}$, into the space of $\mathfrak{C}_1 = \{c_1^1,\ c_2^1\}$, in which c_1^1 and c_2^1 are defined by (4.48). Critical parameter candidates c_1^1 and c_2^1 denote the total generation power and the total load power in the system, respectively.

$$\begin{cases} \mathbf{w}_1^1 = [\ 1 \quad 1 \quad 1 \quad 1 \quad 0 \quad 0 \quad 0 \quad 0 \quad 0 \quad 0\ ]^T \\ \mathbf{w}_2^1 = [\ 0 \quad 0 \quad 0 \quad 0 \quad 1 \quad 1 \quad 1 \quad 1 \quad 1 \quad 1\ ]^T \end{cases} \tag{4.47}$$

$$\begin{cases} c_1^1 = P_{MTG1} + P_{ATG1} + P_{MTG2} + P_{ATG2} \\ c_2^1 = P_{PM1} + P_{PM2} + P_{Z1} + P_{Z2} + P_{Z3} + P_{Z4} \end{cases} \tag{4.48}$$

As another example, the second CPC set ($j = 2$) is composed of three critical parameters with the mapping coefficients as shown in (4.49). This set maps the CPE space, $\mathfrak{E}$, into the space of $\mathfrak{C}_2 = \{c_1^2,\ c_2^2,\ c_3^2\}$, in which c_1^2, c_2^2, and c_3^2 are defined by (4.50) and denote total generation power of MTG1 and ATG1, total generation power of MTG2 and ATG2, and total load power in the system, respectively.

$$\begin{cases} \mathbf{w}_1^2 = [\ 1 \quad 1 \quad 0 \quad 0 \quad 0 \quad 0 \quad 0 \quad 0 \quad 0 \quad 0\ ]^T \\ \mathbf{w}_1^2 = [\ 0 \quad 0 \quad 1 \quad 1 \quad 0 \quad 0 \quad 0 \quad 0 \quad 0 \quad 0\ ]^T \\ \mathbf{w}_3^2 = [\ 0 \quad 0 \quad 0 \quad 0 \quad 1 \quad 1 \quad 1 \quad 1 \quad 1 \quad 1\ ]^T \end{cases} \tag{4.49}$$

$$\begin{cases} c_1^2 = P_{MTG1} + P_{ATG1} \\ c_2^2 = P_{MTG2} + P_{ATG2} \\ c_3^2 = P_{PM1} + P_{PM2} + P_{Z1} + P_{Z2} + P_{Z3} + P_{Z4} \end{cases} \tag{4.50}$$

In the sixth step, the 19,160 sampled operating points were mapped from the CPE space, $\mathfrak{E}$, into the space of each CPC set defined in Table 4.13, in order to obtain $\boldsymbol{\mathcal{P}'}_j$'s, $\boldsymbol{\mathcal{G}'}^h_{0,j}$'s, and $\boldsymbol{\mathcal{G}'}^h_{1,j}$'s in (4.35)-(4.37). For instance, Figure 4.26 shows projection of the sampled operating points in the space of $\mathfrak{C}_2$. In Figure 4.26(a), dark and light colored points represent projection of the insecure and secure samples regarding the first security criterion, i.e. members of sets $\boldsymbol{\mathcal{G}'}^1_{0,2}$ and $\boldsymbol{\mathcal{G}'}^1_{1,2}$, respectively. In this figure, vertical and

horizontal axes are the second and the third critical parameters in this set, c_2^2 and c_3^2 in (4.50), respectively. Since the three critical parameters in this candidate set are dependent, one of the three dimensions of the plot can be eliminated. In this figure, the dimension associated with c_1^2 was eliminated. Figure 4.26(b) shows members of sets $\mathcal{G}'^2_{0,2}$ and $\mathcal{G}'^2_{1,2}$, and Figure 4.26(c) shows members of sets $\mathcal{G}'^2_{0,3}$ and $\mathcal{G}'^2_{1,3}$. Since all of the sampled operating points were secure regarding the fourth security criterion (cable ampacity), this security criterion is not shown in this figure.

Table 4.13: Critical parameter candidate sets definitions in the notional AES model

Set No	CPC No	P_{MTG1}	P_{ATG1}	P_{MTG2}	P_{ATG2}	P_{PM1}	P_{PM2}	P_{Z1}	P_{Z2}	P_{Z3}	P_{Z4}
1	1	1	1	1	1	0	0	0	0	0	0
	2	0	0	0	0	1	1	1	1	1	1
2	1	1	1	0	0	0	0	0	0	0	0
	2	0	0	1	1	0	0	0	0	0	0
	3	0	0	0	0	1	1	1	1	1	1
3	1	1	1	1	1	0	0	0	0	0	0
	2	0	0	0	0	1	0	1	1	0	0
	3	0	0	0	0	0	1	0	0	1	1
4	1	1	1	1	1	0	0	0	0	0	0
	2	0	0	0	0	1	1	0	0	0	0
	3	0	0	0	0	0	0	1	1	1	1
5	1	1	0	1	0	0	0	0	0	0	0
	2	0	1	0	1	0	0	0	0	0	0
	3	0	0	0	0	1	1	1	1	1	1
6	1	1	1	0	0	0	0	0	0	0	0
	2	0	0	1	1	0	0	0	0	0	0
	3	0	0	0	0	1	0	1	1	0	0
	4	0	0	0	0	0	1	0	0	1	1
7	1	1	0	1	0	0	0	0	0	0	0
	2	0	1	0	1	0	0	0	0	0	0
	3	0	0	0	0	1	0	1	1	0	0
	4	0	0	0	0	0	1	0	0	1	1
8	1	1	1	0	0	0	0	0	0	0	0
	2	0	0	1	1	0	0	0	0	0	0
	3	0	0	0	0	1	1	0	0	0	0
	4	0	0	0	0	0	0	1	1	1	1
9	1	1	0	1	0	0	0	0	0	0	0
	2	0	1	0	1	0	0	0	0	0	0
	3	0	0	0	0	1	1	0	0	0	0
	4	0	0	0	0	0	0	1	1	1	1

(a)

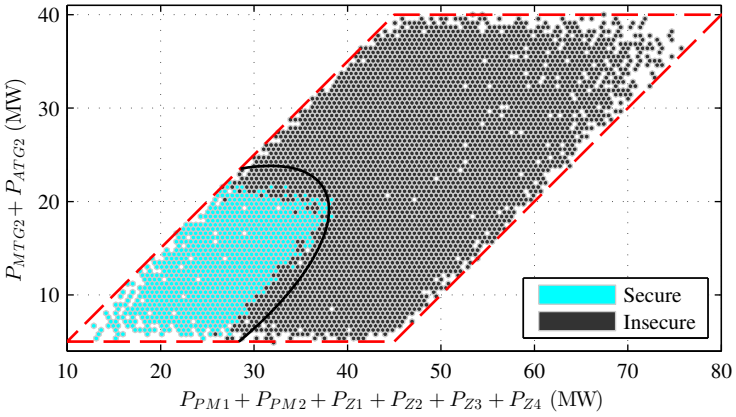

(b)

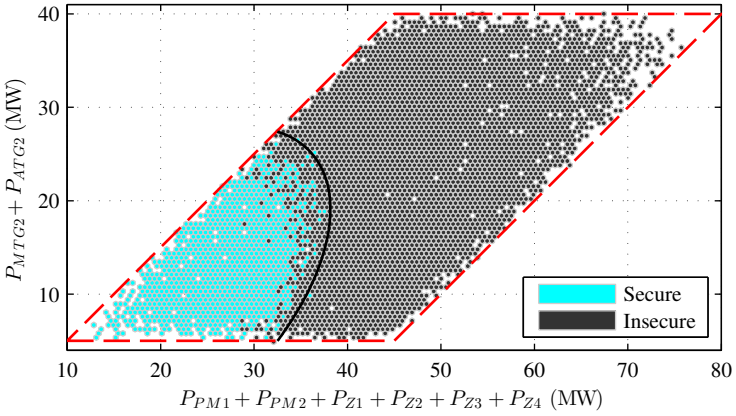

(c)

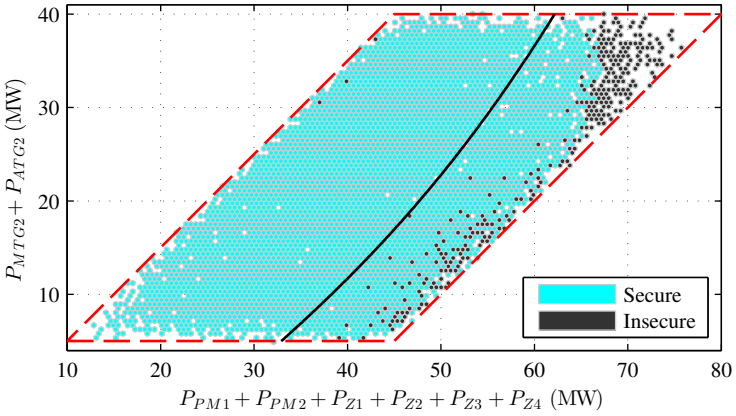

Figure 4.26: Projection of secure and insecure operating points in the space of the second CPC set in the notional AES. a) frequency criterion, b) generator angle criterion, and c) load bus voltage criterion

In the seventh step, security borders were developed. Equations (4.40)-(4.43) were used to determine the security border for each security criterion, $h = 1, 2, 3$, in each CPC set, $j = 1, 2, ..., 9$. As an example, the steps taken to determine the system DSR regarding the first security criterion, $h = 1$, for the second CPC set, $j = 2$, are explained here. First, the mean vectors and the covariance matrices for $\mathcal{G}_0^1$ and $\mathcal{G}_1^1$ in (4.33) and (4.34) were determined, which are shown in (4.51)-(4.54).

$$\boldsymbol{\eta}^1 = \begin{bmatrix} +20.82 & +2.242 & +20.79 & +2.246 & +1.011 & +1.008 & +1.002 & +1.011 & +21.05 & +21.02 \end{bmatrix}^T \tag{4.51}$$

$$\boldsymbol{\mu}^1 = \begin{bmatrix} +11.87 & +2.234 & +11.95 & +2.227 & +1.003 & +1.000 & +0.993 & +1.005 & +12.13 & +12.15 \end{bmatrix}^T \tag{4.52}$$

$$\boldsymbol{\Phi}^1 = \begin{bmatrix} +73.44 & -0.271 & -37.54 & -0.167 & +0.088 & +0.060 & +0.050 & +0.040 & +17.10 & +18.12 \\ -0.271 & +1.024 & -0.156 & +0.008 & -0.007 & +0.004 & +0.001 & -0.002 & +0.289 & +0.320 \\ -37.54 & -0.156 & +73.70 & -0.271 & +0.071 & +0.049 & +0.049 & +0.071 & +17.91 & +17.58 \\ -0.167 & +0.008 & -0.271 & +1.019 & -0.001 & -0.003 & -0.000 & -0.002 & +0.304 & +0.292 \\ +0.088 & -0.007 & +0.071 & -0.001 & +0.336 & +0.000 & -0.001 & -0.000 & -0.104 & -0.081 \\ +0.060 & +0.004 & +0.049 & -0.003 & +0.000 & +0.331 & +0.000 & +0.003 & -0.102 & -0.121 \\ +0.050 & +0.001 & +0.049 & -0.000 & -0.001 & +0.000 & +0.334 & -0.001 & -0.113 & -0.120 \\ +0.040 & -0.002 & +0.071 & -0.002 & -0.000 & +0.003 & -0.001 & +0.332 & -0.139 & -0.086 \\ +17.10 & +0.289 & +17.91 & +0.304 & -0.104 & -0.102 & -0.113 & -0.139 & +87.82 & -51.76 \\ +18.12 & +0.320 & +17.58 & +0.292 & -0.081 & -0.121 & -0.120 & -0.086 & -51.76 & +88.48 \end{bmatrix} \tag{4.53}$$

$$\boldsymbol{\Sigma}^1 = \begin{bmatrix} +15.61 & -0.207 & -2.963 & -0.291 & +0.096 & +0.002 & +0.069 & +0.005 & +5.800 & +6.181 \\ -0.207 & +0.993 & -0.150 & -0.010 & -0.006 & -0.012 & +0.011 & -0.019 & +0.416 & +0.235 \\ -2.963 & -0.150 & +15.95 & -0.208 & -0.001 & +0.030 & +0.019 & +0.029 & +6.994 & +5.555 \\ -0.291 & -0.010 & -0.208 & +0.997 & -0.002 & +0.008 & +0.009 & +0.001 & +0.220 & +0.253 \\ +0.096 & -0.006 & -0.001 & -0.002 & +0.340 & +0.001 & -0.000 & -0.002 & -0.058 & -0.193 \\ +0.002 & -0.012 & +0.030 & +0.008 & +0.001 & +0.329 & +0.004 & +0.002 & -0.129 & -0.179 \\ +0.069 & +0.011 & +0.019 & +0.009 & -0.000 & +0.004 & +0.329 & -0.008 & -0.055 & -0.162 \\ +0.005 & -0.019 & +0.029 & +0.001 & -0.002 & +0.002 & -0.008 & +0.336 & -0.029 & -0.283 \\ +5.800 & +0.416 & +6.994 & +0.220 & -0.058 & -0.129 & -0.055 & -0.029 & +53.56 & -39.86 \\ +6.181 & +0.235 & +5.555 & +0.253 & -0.193 & -0.179 & -0.162 & -0.283 & -39.86 & +52.91 \end{bmatrix} \tag{4.54}$$

Secondly, $\mathbf{W}_2$ from (4.55) was plugged in (4.44) and (4.45), in order to calculate mean and covariance of sets $\mathcal{G}'^1_{0,2}$ and $\mathcal{G}'^1_{1,2}$, as shown in (4.56) and (4.57).

$$\mathbf{W}_2 = \begin{bmatrix} 1 & 1 & 0 & 0 & 0 & 0 & 0 & 0 & 0 & 0 \\ 0 & 0 & 1 & 1 & 0 & 0 & 0 & 0 & 0 & 0 \\ 0 & 0 & 0 & 0 & 1 & 1 & 1 & 1 & 1 & 1 \end{bmatrix} \tag{4.55}$$

$$\boldsymbol{\eta}_2^1 = \begin{bmatrix} +23.06 \\ +23.04 \\ +46.10 \end{bmatrix} \quad , \quad \boldsymbol{\mu}_2^1 = \begin{bmatrix} +14.10 \\ +14.18 \\ +28.28 \end{bmatrix} \tag{4.56}$$

$$\boldsymbol{\Phi}_2^1 = \begin{bmatrix} +73.92 & -37.85 & +36.07 \\ -37.85 & +74.18 & +36.32 \\ +36.07 & +36.32 & +72.39 \end{bmatrix} \quad , \quad \boldsymbol{\Sigma}_2^1 = \begin{bmatrix} +16.19 & -3.414 & +12.78 \\ -3.414 & +16.53 & +13.11 \\ +12.78 & +13.11 & +25.89 \end{bmatrix} \tag{4.57}$$

Thirdly, (4.41)-(4.43) were used to calculate the border coefficients shown in (4.58). Hence, the mathematical description of the border was as shwon in (4.59), in which $\mathbf{p'}^2$ is any operating point in the space of the set $\mathfrak{C}_2$. Moreover, the description of the system DSR regarding the first security criterion for the second CPC set was $g_2^1(\mathbf{p'}^2) \leq 0$.

$$\mathbf{Q}_2^1 = \begin{bmatrix} +0.0000 & +0.0000 & +0.0000 \\ +0.0000 & +0.0416 & -0.0211 \\ +0.0000 & -0.0211 & +0.0231 \end{bmatrix} \quad , \quad \mathbf{l}_2^1 = \begin{bmatrix} +0.0000 \\ +0.0130 \\ -0.4618 \end{bmatrix} \quad , \quad k_2^1 = -0.6193 \tag{4.58}$$

$$g_2^1(\mathbf{p'}^2) = \mathbf{p'}^{2T}\mathbf{Q}_2^1\mathbf{p'}^2 + \mathbf{p'}^{2T}\mathbf{l}_2^1 + k_2^1 = 0 \tag{4.59}$$

The resulting borders for security criteria 1-3 for the second CPC set are depicted in Figure 4.26. Figure 4.26(a) shows how the security border for the first security criterion in the second CPC set separates dark-colored insecure operating points from light-colored secure operating points. It can be seen that the border is not perfect, since some of the secure operating points fall inside the insecure region, and vice versa. The borders for the second and the third security criteria, shown in Figures 4.26(b) and (c), are not perfect, either, since some of the secure operating points fall inside the insecure region, and vice versa.

In the eighth step, to calculate border qualities, between leaving-out-one and missclassification rate methods, the latter was chosen, for the sake of simplicity. The misclassification rate of the j-th CPC set regarding the h-th security criterion, ϵ_j^h, was calculated by (4.60), in which ζ_{mj}^h is the misclassification counter for the m-th sample if it is insecure, and ξ_{mj}^h is the misclassification counter for the m-th sample if it is secure. ζ_{mj}^h and ξ_{mj}^h were calculated using (4.61) and (4.62), respectively.

$$\epsilon_j^h = \frac{1}{M}\sum_{m=1}^{M}\left(\zeta_{mj}^h + \xi_{mj}^h\right) \times 100\% \tag{4.60}$$

$$\zeta_{mj}^{h} = \begin{cases} 1, & g(\mathbf{p'}_{m}^{j}) \leq 0 \text{ and } s_{m}^{h} = 0, \\ 0, & \text{otherwise.} \end{cases} \tag{4.61}$$

$$\xi_{mj}^{h} = \begin{cases} 1, & g(\mathbf{p'}_{m}^{j}) > 0 \text{ and } s_{m}^{h} = 1, \\ 0, & \text{otherwise.} \end{cases} \tag{4.62}$$

In order to pick a CPC set from among the nine candidate sets, border quality in discriminating secure operating points from insecure ones, type of critical parameters (controllable or uncontrollable), and number of critical parameters were taken into consideration, for each CPC set. This information for the nine CPC sets is summarized in Table 4.14. In this table, the first column shows CPC set number, j. The second, third, and fourth columns show misclassification errors for security criteria 1-3, ϵ_j^1, ϵ_j^2, and ϵ_j^3, respectively. The fifth column shows quality of the composite DSR, i.e. the system DSR when all of the security criteria are taken into consideration. The composite DSR is a region of the operating space which is allocated as secure by all of the individual security borders. The composite DSR can also be graphically obtained as the common region between all of the individual secure regions. For instance, the composite DSR for the second CPC set is shown in Figure 4.27. This figure shows the individual security borders for security criteria 1-3. It also shows that the composite DSR (the shaded region in this figure) is the common region between individual secure regions.

Table 4.14: Quality aspects for the critical parameter candidate sets in the notional AES

CPC Set No	Misclassification Error (%)				Rank based on Comp. DSR Err.	Number of Critical Parameters	
	Crt. 1	Crt. 2	Crt. 3	Composite		Controllable	Uncontrollable
No Mapping	4.0	3.1	15.1	5.74	1	–	–
1	8.3	6.7	33.4	10.5	10	1	1
2	4.4	5.7	18.8	7.02	4	2	1
3	8.1	5.7	22.9	9.58	6	1	2
4	8.2	5.8	33.1	10.1	8	1	2
5	8.3	5.9	33.2	10.3	9	2	1
6	4.2	4.9	15.1	6.51	2	2	2
7	8.0	5.0	22.8	9.30	5	2	2
8	4.3	5.0	18.8	6.83	3	2	2
9	8.3	5.3	33.4	9.91	7	2	2

The sixth column is Table 4.14 shows rank of each CPC set, based on the composite DSR misclassification error. The last two columns in this table show number of controllable and number of uncontrollable critical parameter candidates in each set, respectively. Note that generator powers were assumed to be controllable and load powers were assumed to be uncontrollable.

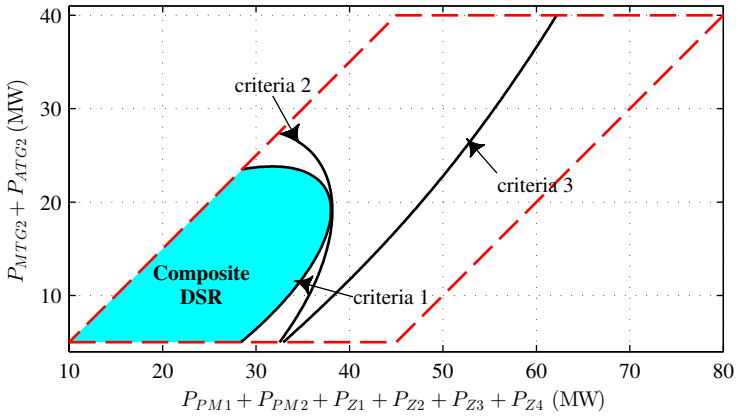

Figure 4.27: Composite DSR for the second CPC set in the notional AES

In order to observe degradation of the border quality (in terms of misclassification error) due to mapping from $\mathfrak{E}$ to $\mathfrak{C}_j$'s, misclassification errors before mapping are shown in the first row in Table 4.14. It can be seen that for each security criterion, the first row has the lowest misclassification errors. It was intuitively expected, since the mappings project the samples from a lower crowded space into a higher crowded space, by reducing the number of parameters. However, increases in the border misclassification errors were not significant, especially for $\mathfrak{C}_2$, $\mathfrak{C}_6$, and $\mathfrak{C}_8$.

Table 4.14 provides all of the required information for choosing a set from among the candidate sets. It can be seen that sets $\mathfrak{C}_6$, $\mathfrak{C}_8$, and $\mathfrak{C}_2$ provided the best composite borders with 6.51%, 6.83%, and 7.02% errors, respectively. Moreover, each of these three sets include 2 controllable parameters. Controllable critical parameters give the system operator or the decision maker the opportunity to come up with some security enhancement

actions [89, 119]. The advantage of set $\mathfrak{C}_2$ over $\mathfrak{C}_6$ and $\mathfrak{C}_8$ is that it can be visualized in a single 2-D graph, as shown in Figure 4.27. On the contrary, since sets $\mathfrak{C}_6$ and $\mathfrak{C}_8$ have an extra dimension compared to set $\mathfrak{C}_2$, they must be visualized either on a 3-D graph or on several 2-D graphs. In this dissertation, $\mathfrak{C}_2$ was chosen as the best CPC set, due to its relatively small misclassification errors and simplicity of visualization.

Figure 4.28 provides a summary of the steps taken, in order to implement the proposed DDSR assessment method in the notional all-electric shipboard power system. As shown in this Figure, to assess the DDSR in the notional AES, MATLAB and TSAT were used together. A contingency list including 39 contingencies was developed. Security status of 19,160 operating points, distributed in the entire ship's operating space, regarding four security criteria, was assessed. Nine critical parameter candidate sets were developed and the 19,160 operating points were mapped into the space of each CPC set. Then, quality of the CPC sets were compared, in terms of missclassification error, number of critical parameters, and type of critical parameters, and the best candidate set was picked.

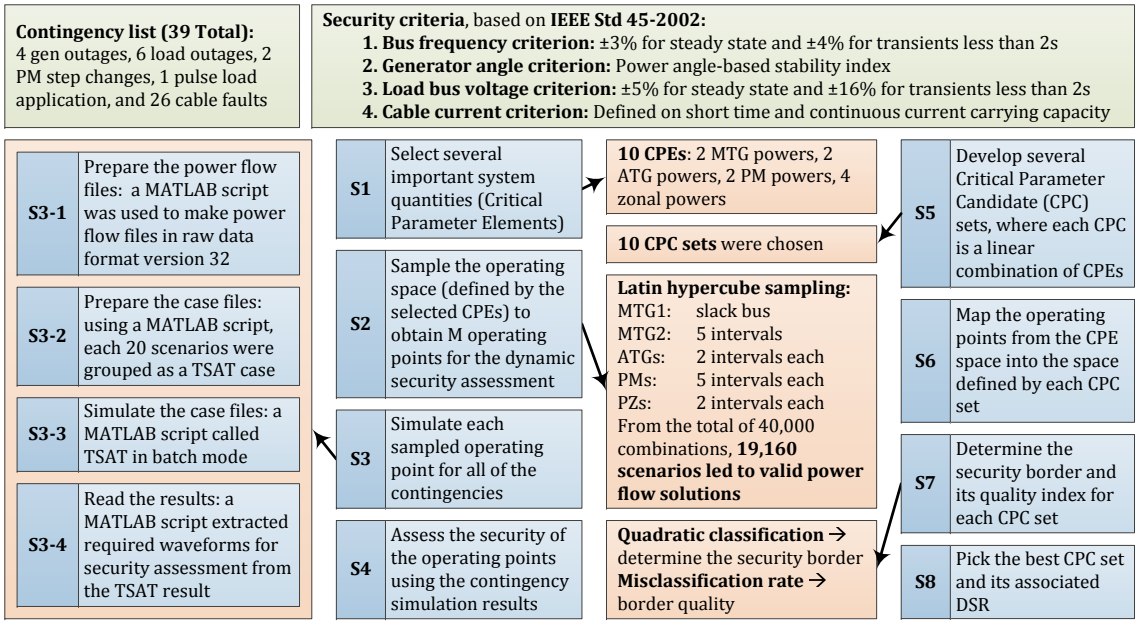

Figure 4.28: Summary of the implementation details for DDSR assessment in the notional AES

4.4.3 Limitations of DDSR in Isolated Microgrid Power Systems

A systematic method to assess an approximation of the deterministic dynamic secure region in isolated microgrid power systems was developed in subsection 4.4.2. The results of the security studies in the notional all-electric ship model showed several limitations for deterministic security assessment in this system. Consider Figure 4.29 which shows the obtained security borders for frequency criterion (criterion 1), generator angle criterion (criterion 2), and load bus voltage criterion (criterion 3). This figure represents the DSR in the space of two critical parameters. The two critical parameters are total power generation of MTG2 and ATG2, and total load power in the system. This figure also shows the composite DSR, i.e. the common area between all of the individual secure regions.

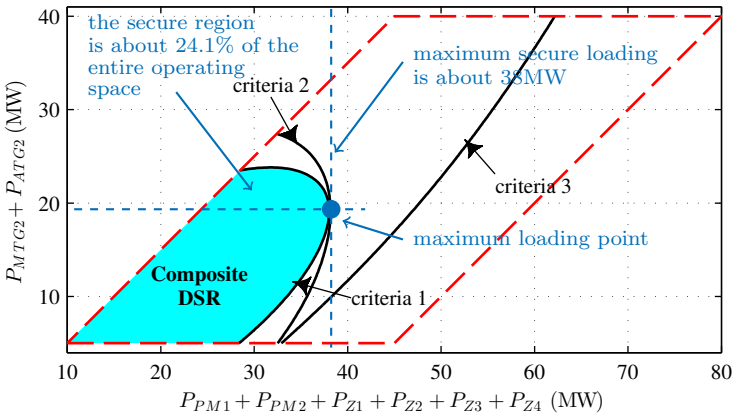

Figure 4.29: Limitations of deterministic DSR in the notional AES

It can be observed that the deterministic DSR in this figure limits the total load in the system to 38MW, which is only 47.5% of the 80MW maximum capacity of the system. The maximum loading point is where $P_{MTG1} + P_{ATG1} = 19.1$MW, $P_{MTG2} + P_{ATG2} = 19.1$MW and $P_{PM1} + P_{PM2} + P_{Z1} + P_{Z2} + P_{Z3} + P_{Z4} = 38$MW. In terms of the area of the secure region, Figure 4.29 shows that the deterministic DSR only covers 24.1% of the operating space.

These two observations, i.e. the maximum secure loading and the DSR coverage area,

clearly indicate that deterministic security assessment method resulted in a very limited secure operating region in the notional all-electric ship model. The reason is threefold. First, the total system generation capacity is supplied by only 4 generators. Second, 90% of the system total demand power is consumed by only 2 loads, i.e. the propulsion motors. consequently, unlike transmission power systems which normally withstand single component outages, single outage of a main generator or a propulsion motor can lead to constraint violations in this system. Third, the generators in this system have low inertia and are more sensitive to disturbances, compared to high inertia generators. As a result, many of the single line fault contingencies in this system can make the system unstable (transient angle) or cause frequency constraint violations.

Overall, over-conservativeness of deterministic security assessment [17, 103] resulted in an unreasonably small DSR, in the notional all-electric ship model, since it has relatively big generators and loads, with respect to the system capacity. The same result is expected to be observed in other small isolated microgrid power systems, due to the same reasons. To overcome the limitations imposed by deterministic security assessment, a method to assess the risk-based dynamic secure region in isolated microgrid power systems is developed in subsection 4.4.4.

4.4.4 Developed Risk-Based DSR Assessment Method

Probabilistic security analysis can be conducted using 1) analytical transformation method, 2) conditional probability method, or 3) Monte-Carlo simulation method [122,134, 135]. In analytical transformation method, probability of system instability is analytically derived as a function of several random variables, such as system load demand, fault clearing time, fault location, etc [136]. Due to the discontinuous and nonlinear nature of power systems, analytical derivation of instability probability is more conceptual than practical [122].

Conditional probability method is the most widely used approach for probabilistic security assessment. In this method, the contingency space is partitioned by enumerating

various aspects of the contingencies. Then, instability probability is calculated for each partition. Finally, individual instability probabilities are combined together to obtain an overall instability probability [122]. In Monte-Carlo simulation method, stochastic behavior of the power system is estimated using repeated probabilistic trials. This method is usually applied to large scale power systems and requires huge computational efforts to obtain reliable estimates [122].

Analytical transformation method cannot be used in all-electric ships, due to their complexity and high nonlinearity. Moreover, analytical transformation method is mainly used to assess risk of transient instability [136] and cannot effectively assess risks associated with other aspects of security. Monte-Carlo simulation method is usually used for very large power systems. Therefore, conditional probability method is the most promising approach for probabilistic security assessment in isolated microgrid power systems. The risk-based DSR assessment method developed in this work for isolated microgrid power systems is discussed in subsection 4.4.4.1. Then, the details and results of implementing the developed method on the notional all-electric ship model are discussed in subsection 4.4.4.2.

4.4.4.1 Developed Risk-Based DSR Assessment Method

The developed risk-based DSR assessment method is, to some extent, similar to the deterministic DSR assessment method discussed in subsection 4.4.2.1. Therefore, to avoid repeating the same material, the focus of this subsection is on material not covered in that subsection 4.4.2.1.

Assume there are N critical parameter elements in set $\mathfrak{E}$, as shown in (4.63). Using the critical parameter elements in $\mathfrak{E}$, J critical parameter candidate sets are developed, where each critical parameter candidate is a linear combination of CPEs, as shown in (4.64).

$$\mathfrak{E} = \{e_1, e_2, ..., e_N\} \tag{4.63}$$

$$\mathfrak{C}_j = \{c_i^j |\ c_i^j = \mathbf{w}_i^{jT} \begin{bmatrix} e_1 \\ e_2 \\ \vdots \\ e_N \end{bmatrix},\ i = 1, 2, ..., I_j\} \tag{4.64}$$

To generate the large database containing data characterizing pre-contingency operating conditions and corresponding operating risk, the entire operating space is sampled with M samples, $\mathbf{p}_m$. The set of all sampled operating points, as shown in (4.65), is denoted with $\boldsymbol{\mathcal{P}}$.

$$\boldsymbol{\mathcal{P}} = \{\mathbf{p}_m |\ \mathbf{p}_m \in \mathbb{R}^N,\ \mathbf{p}^{\min} \leq \mathbf{p}_m \leq \mathbf{p}^{\max},\ m = 1, 2, ..., M\} \tag{4.65}$$

In order to calculate the operation risk using conditional probability approach, the contingency space must be partitioned [134, 135, 137]. Contingency space partitioning can be explained easier with an example. Assume there is a single contingency in the contingency list. This contingency has the two attributes, a and b. Also assume that both of these two attributes are discrete random variables which can take values from $\{a_1, a_2\}$ and $\{b_1, b_2, b_3\}$, respectively. As shown in the tree diagram of Figure 4.30, the contingency space can be divided into six partitions, $\begin{bmatrix} a_1 \\ b_1 \end{bmatrix}$, $\begin{bmatrix} a_1 \\ b_2 \end{bmatrix}$, $\begin{bmatrix} a_1 \\ b_3 \end{bmatrix}$, $\begin{bmatrix} a_2 \\ b_1 \end{bmatrix}$, $\begin{bmatrix} a_2 \\ b_2 \end{bmatrix}$, and $\begin{bmatrix} a_2 \\ b_3 \end{bmatrix}$. The probability of a partition $\begin{bmatrix} a_i \\ b_j \end{bmatrix}$ is $\text{pr}(a = a_i, b = b_j)$, which equals $\text{pr}(a = a_i) \times \text{pr}(b = b_j)$, if the two attributes are independent.

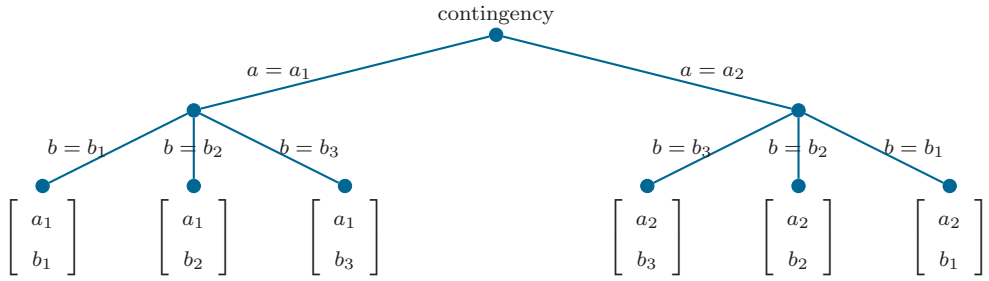

Figure 4.30: An example of partitioning the contingency space using a tree diagram

Since continuous random variables can be approximated with discrete random variables, without loss of generality, all of the contingency attributes can be assumed to be discrete random variables. Hence, the partitioned contingency space, $\boldsymbol{\mathcal{D}}$, is formed as shown in (4.66), in which $\mathbf{a}_d$ is the d-th partition and D is the total number of partitions. $\mathbf{a}_d$ is the

vector that contains the values for all of the contingency attributes in the d-th partition. Moreover, occurrence probability of a partition, p_d, is calculated by (4.67)

$$\mathfrak{D} = \{\mathbf{a}_d | d = 1, 2, ..., D\} \tag{4.66}$$

$$p_d = \text{pr}(\mathbf{a} = \mathbf{a}_d) \tag{4.67}$$

An operating point's risk regarding security aspect h against contingency d, is defined [106] as the multiplication of occurrence probability of the contingency, p_d, and severity of the consequences of the contingency, $s_{h,d,m}$, as shown in (4.68).

$$r_{h,d,m} = s_{h,d,m} \times p_d \tag{4.68}$$

In transmission power systems, the severity function is usually defined based on time-independent security criteria [106, 138]. Hence, the risk-based security assessment literature lacks severity functions which could be used with time-restricted security criteria. To understand the difference between time-independent and time-dependent severity functions, consider cable ampacity security criterion as an example. Assume the steady state constraint $I \leq I^{\max}$, in which I is the cable steady state post-contingency current and $I^{\max}$ is the maximum steady state ampacity for the cable. For this steady state security constraint, the severity function can be defined as shown in Figure 4.31 [106,138]. Figure 4.31(a) shows a discrete severity function which is zero when $I \leq I^{\max}$, and one when $I > I^{\max}$. Figure 4.31(b) shows a smoother severity function in which the severity increases, linearly, as the cable loading exceeds 0.9pu.

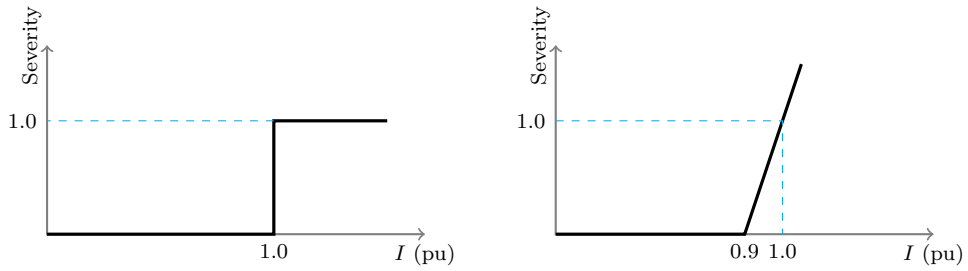

(a) Discrete severity function (b) Continuous severity function

Figure 4.31: Examples of time-independent severity functions for cable ampacity criterion [106, 138]. a) discrete severity function, and b) continuous severity function

On the contrary, defining a severity function for time-dependent security criteria is not trivial. Consider the time-restricted cable ampacity constraints shown in Figure 4.32, which limit the operation of cable current in [18,23]pu constraint band to less than 1.2s, in [13,18]pu constraint band to less than 2.0s, and so on. The constraints in Figure 4.32 are based on the cable current, $I(t)$, in a time period, $[0, T]$, following the contingency.

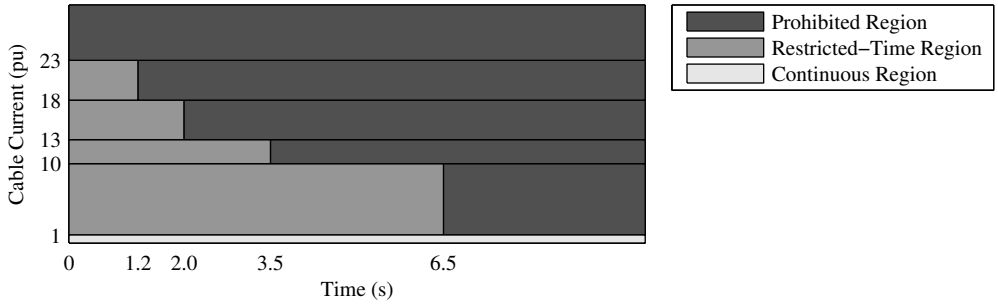

Figure 4.32: Time-dependent cable ampacity constraints

To fill the gap in literature, a new severity function is developed in this work. Assume $x_{v,d,w}(t)$, shown in Figure 4.33, is the v-th constrained quantity (e.g. current of a particular cable) when contingency d happens starting from m-th sampled operating point. Also, assume several constraint bands are defined for the h-th security criterion, and the minimum and the maximum limits for the u-th constraint band are denoted with $x_{u,h}^{\min}$ and

$x_{u,h}^{\max}$, respectively. A constraint band is also shown in Figure 4.33.

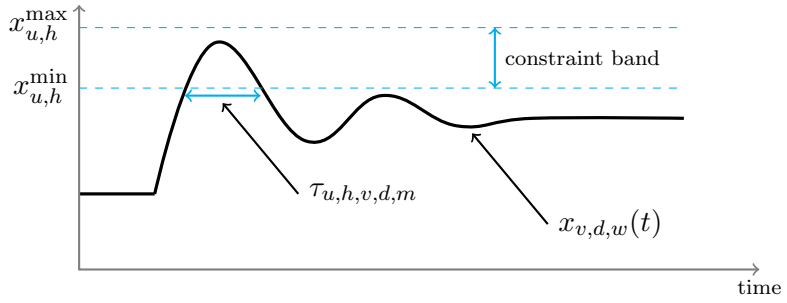

Figure 4.33: Calculation of the proposed severity function for time-restricted security criterion

The severity of a contingency is defined to be the overall extra time that constrained quantities spend in constrained bands, following that contingency. Hence, the severity of the contingency d regarding the h-th security aspect, $s_{h,d,m}$, is mathematically defined by (4.69). In (4.69), $\tau_{u,h,v,d,w}$ is the time that constrained quantity $x_{v,d,m}(t)$ spends in the constraint band $[x_{u,h}^{\min}, x_{u,h}^{\max}]$, following the contingency d. Equation (4.69) shows that to calculate $s_{h,d,m}$, the extra times for all of the constrained quantities in all of the constraint bands are added together. This extra time, $\tau_{u,h,v,d,m}$, can be calculated using (4.70), in which $sgn(.)$ is the sign function.

$$s_{h,d,m} \triangleq \sum_{v} \sum_{u} \left(\tau_{u,h,v,d,w} - \tau_{u,h}^{\max}\right) \times \underbrace{\left(\tau_{u,h,v,d,w} > \tau_{u,h}^{\max}\right)}_{\text{logical term: 0 or 1}} \tag{4.69}$$

$$\tau_{u,h,v,d,m} = \frac{1}{4}\int_{0}^{T}\Big[\Big(1 + sgn\left(x_{v,d,m}(t) - x_{u,h}^{\min}\right)\Big)\Big(1 + sgn\left(x_{u,h}^{\max} - x_{v,d,m}(t)\right)\Big)\Big]dt \tag{4.70}$$

The new severity function, defined in (4.69) and (4.70), has several features. First, it is relatively simple. Second, it has a physical meaning. Third, it is tied to deterministic security criteria, since it is defined based on the same constraints that form deterministic security criteria. Fourth, it measures the extent of constraint violations by calculating the constraint violation durations. Fifth, the unit for the severity function in (4.69) is seconds, and hence, the severity of various security criteria can be added up together in order to

calculate composite indices. These five characteristics make this new severity function a good severity function, based on the severity function requirements discussed in [106, 138].

To calculate the overall risk against all of the contingencies, the risk associated with individual contingencies are added togehtehr, as shown in (4.71).

$$r_{h,m} = \sum_{d=1}^{D} r_{h,d,m} = \sum_{d=1}^{D} s_{h,d,m} \times p_d \tag{4.71}$$

To assess the risk-based dynamic secure region of a power system, system operating points must be divided into secure and insecure, based on their operating risk. Assume r_h^* is the risk threshold for the h-th security criterion. Hence operating points with $r_{m,h} > r_h^*$ are considered to be insecure, and operating points with $r_{m,h} \leq r_h^*$ are considered to be secure. Consequently, insecure and secure sets of operating points can be formed as shown in (4.72) and (4.73), respectively. Moreover, projections of insecure and secure sets of operating points, in the space of each candidate set, can be formed as shown in (4.74) and (4.75), correspondingly. In (4.74) and (4.75), $\mathbf{p'}_m^j$ is the projection of the m-th sampled operating point in $\mathfrak{C}_j$. Equation (4.76) shows that the set including all of the projected operating points is denoted with $\mathcal{P'}_j$.

$$\mathcal{G}_0^h = \{\mathbf{p}_m |\ r_{m,h} > r_h^*,\ m = 1, 2, ..., M\} \tag{4.72}$$

$$\mathcal{G}_1^h = \{\mathbf{p}_m |\ r_{m,h} \leq r_h^*,\ m = 1, 2, ..., M\} \tag{4.73}$$

$$\mathcal{G'}_{0,j}^h = \{\mathbf{p'}_m^j |\ r_{m,h} > r_h^*,\ m = 1, 2, ..., M\} \tag{4.74}$$

$$\mathcal{G'}_{1,j}^h = \{\mathbf{p'}_m^j |\ r_{m,h} \leq r_h^*,\ m = 1, 2, ..., M\} \tag{4.75}$$

$$\mathcal{P'}_j = \{\mathbf{p'}_m^j |\ \mathbf{p'}_m^j = \begin{bmatrix} \mathbf{w}_1^{jT} \\ \vdots \\ \mathbf{w}_{I_j}^{j\ T} \end{bmatrix} \mathbf{p}_m = \mathbf{W}_j \mathbf{p}_m\} \tag{4.76}$$

The problem of determining security borders can be considered as a classification problem [132], in which previously classified secure and insecure samples, $\mathcal{G'}_{0,j}^h$ and $\mathcal{G'}_{1,j}^h$, are manipulated to develop several rules that optimally allocate unclassified operating points. Following the same mathematical derivations discussed in subsection 4.4.2.1, quadratic allocation rules of (4.77) and (4.78) can be obtained, in which quadratic, linear, and scalar

coefficients are as defined in (4.79)-(4.81).

$$g(\mathbf{p'}^j) = \mathbf{p'}^{jT}\mathbf{Q}_j^h\mathbf{p'}^j + \mathbf{p'}^{jT}\mathbf{l}_j^h + k_j^h \geq 0 \quad \longrightarrow \quad \mathbf{p'}^j \text{ insecure} \tag{4.77}$$

$$g(\mathbf{p'}^j) = \mathbf{p'}^{jT}\mathbf{Q}_j^h\mathbf{p'}^j + \mathbf{p'}^{jT}\mathbf{l}_j^h + k_j^h < 0 \quad \longrightarrow \quad \mathbf{p'}^j \text{ secure} \tag{4.78}$$

$$\mathbf{Q}_j^h = \left(\boldsymbol{\Sigma}_j^{h^{-1}} - \boldsymbol{\Phi}_j^{h^{-1}}\right) \tag{4.79}$$

$$\mathbf{l}_j^h = \left(-2\boldsymbol{\Sigma}_j^{h^{-1}}\boldsymbol{\mu}_j^h + 2\boldsymbol{\Phi}_j^{h^{-1}}\boldsymbol{\eta}_j^h\right) \tag{4.80}$$

$$k_j^h = \left(\boldsymbol{\mu}_j^{h^T}\boldsymbol{\Sigma}_j^{h^{-1}}\boldsymbol{\mu}_j^h - \boldsymbol{\eta}_j^{h^T}\boldsymbol{\Phi}_j^{h^{-1}}\boldsymbol{\eta}_j^h\right) - \ln\frac{|\boldsymbol{\Phi}_j^h|}{|\boldsymbol{\Sigma}_j^h|} \tag{4.81}$$

In (4.79)-(4.81), $\boldsymbol{\eta}_j^h$ and $\boldsymbol{\mu}_j^h$ are the mean vectors, and $\boldsymbol{\Phi}_j^h$ and $\boldsymbol{\Sigma}_j^h$ are the covariance matrices, for mapped insecure and secure sets $\mathcal{G}'^h_{0,j}$ and $\mathcal{G}'^h_{1,j}$, respectively, and can be obtained using (4.82) and (4.83). In (4.82) and (4.83), matrix $\mathbf{W}$ is as defined in (4.76). Moreover, $\boldsymbol{\eta}^h$ and $\boldsymbol{\mu}^h$ are the mean vectors for sets $\mathcal{G}_0^h$ and $\mathcal{G}_1^h$, respectively. Furthermore, $\boldsymbol{\Phi}^h$ and $\boldsymbol{\Sigma}^h$ are the covariance matrices for sets $\mathcal{G}_0^h$ and $\mathcal{G}_1^h$, correspondingly.

$$\boldsymbol{\eta}_j^h = \mathbf{W}_j\boldsymbol{\eta}^h \quad , \quad \boldsymbol{\Phi}_j^h = \mathbf{W}_j\boldsymbol{\Phi}^h\mathbf{W}_j^T \tag{4.82}$$

$$\boldsymbol{\mu}_j^h = \mathbf{W}_j\boldsymbol{\mu}^h \quad , \quad \boldsymbol{\Sigma}_j^h = \mathbf{W}_j\boldsymbol{\Sigma}^h\mathbf{W}_j^T \tag{4.83}$$

To pick a set from among the candidate sets, they can be compared based on their quality in discriminating secure operating points from insecure ones, number of critical parameter candidates, and type of critical parameter candidates. As explained earlier in subsection 4.4.2.1, to evaluate quality of the security borders in discriminating secure and insecure operating points, "leaving-out-one" method or "misclassification rate" method can be used [132].

4.4.4.2 Risk-Based DSR in the Notional AES

Since a good set of critical parameters was developed in deterministic DSR assessment in subsection 4.4.2.2, and for comparison purposes, the same critical parameters, defined in (4.50), were used for risk-based DSR assessment in the notional all-electric ship model. Also, the ship's operating space was sampled with the same 19,160 samples used in the

deterministic studies.

For the notional all-electric ship model, a contingency list including 39 contingencies in 10 contingency categories was developed for deterministic security studies in subsection 4.4.2.2. In this contingency list, worst case scenarios were considered for all of the contingencies. For risk-based security assessment, the same contingency groups were used. However, instead of only including the worst case scenarios, various possibilities were taken into consideration for each contingency. Then, the contingency space was partitioned as explained in subsection 4.4.4.1. The contingencies in the contingency list and contingency partitions were as follows.

C1. MTG outage: disconnecting any single main turbine generator from the system. This category includes 2 partitions.

C2. ATG outage: disconnecting any single auxiliary turbine generator from the system. This category includes 2 partitions.

C3. PM outage: disconnecting any single propulsion motor from the system. This category includes 2 partitions.

C4. DC zone outage: disconnecting any single DC zone from the system. This category includes 4 partitions.

C5. PM step: a sharp increase in the power demand of any single propulsion motor. For this contingency, three possible magnitudes of +5MW, +10MW, and +15MW were considered. The tree diagram for the propulsion motor step change is shown in Figure 4.34(a). It can be seen that the contingency space for this category is divided into 3 partitions. Since there are two propulsion motors, this category includes 6 partitions.

C6. Pulse load: Pulse power loads have various heights (power) and widths (duration) [81,125,127,128,139–143]. Three pulse heights of 30MW, 40MW, and 50MW, and two pulse widths of 300ms and 500ms were taken into consideration

in the probabilistic contingency list. As the tree diagram of Figure 4.34(b) shows, this contingency category includes 6 partitions.

C7. Faults on AC cables feeding DC zones: Faults are random events which can happen anywhere on the line. Moreover, they can have various types such as phase to ground, phase to phase to ground, or three phase to ground. Furthermore, the fault clearing time is not fixed and has a random distribution. The three important fault random parameters for transient studies are fault location, fault type, and fault clearing time [137]. Therefore, random distributions were considered for fault location, fault type, and fault clearing time, for the notional all-electric ship.

Fault type is naturally a discrete random variable. Fault type distribution varies based on the power system under study [89, 122, 134, 135, 137, 144]. Fault type distribution, for the notional AES, was defined based on the data given in [89]. It is shown in Table 4.15. It can be seen that single phase fault has the highest probability and three phase fault has the lowest probability.

Fault location on the line is intrinsically a continuous random variable, since fault can happen anywhere on the line. However, it is common practice to assume a discrete probability density function for fault location [135, 137, 144]. For the notional AES, a discrete uniform probability density function [135, 137] was defined for fault location on the line . As shown in Table 4.15, it is assumed that faults happen at 0%, 33%, 66%, or 100% of line length, with the same probability of 25%.

Fault clearing time is also an intrinsically continuous random variable. In most of the probabilistic security-assessment literature, a normal distribution is considered for fault clearing time and instability probability is determined as a function of fault clearing time [135, 137, 144]. However, this method is not applicable for other security aspects, such as time-dependent frequency

criterion. Hence, since as explained in subsection 4.4.4.1 all of the random variables require to be discrete, a discrete density function was considered for fault clearing time, too. It was assumed that clearing time could be 30ms or 50ms with the same probability of 50%. It is shown in Table 4.15.

The probability density functions for fault type, location, and clearing time resulted in the tree diagram of Figure 4.34(c). This diagram shows that there were 2 possibilities for fault clearing time, 3 possibilities for fault type, and 4 possibilities for fault location. Hence, each fault contingency was partitioned into 24 partitions. Since there are four AC cables that feed the DC zones, i.e. cables 5-9, 6-10, 7-11, and 8-12 in Figure 4.3, this category includes a total of 96 partitions.

C8. Faults on AC ring cables: AC ring cables are cables 1-2, 1-3, 2-4, and 3-4 in Figure 4.3. Considering the 24 combinations of fault type, location, and clearing time, shown in the tree diagram of Figure 4.34(c), this category includes a total of 96 partitions.

C9. Faults on AC cables feeding PMs: There are four cables which feed propulsion motors, i.e. cables 5-13, 6-13, 7-14, and 8-14 in Figure 4.3. Considering the 24 combinations of fault type, location, and clearing time, shown in the tree diagram of Figure 4.34(c), this category includes a total of 96 partitions.

C10. Faults on AC cable feeding pulse load: Considering the 24 combinations of fault type, location, and clearing time, shown in the tree diagram of Figure 4.34(c), this category includes 24 partitions.

Table 4.15: Probability density functions for fault type, location, and clearing time in the notional AES

Location	Probability
0%	25%
33%	25%
66%	25%
100%	25%

Type	Probability
1-ph	82%
2-ph	11%
3-ph	7%

Clearing Time	Probability
30ms	50%
50ms	50%

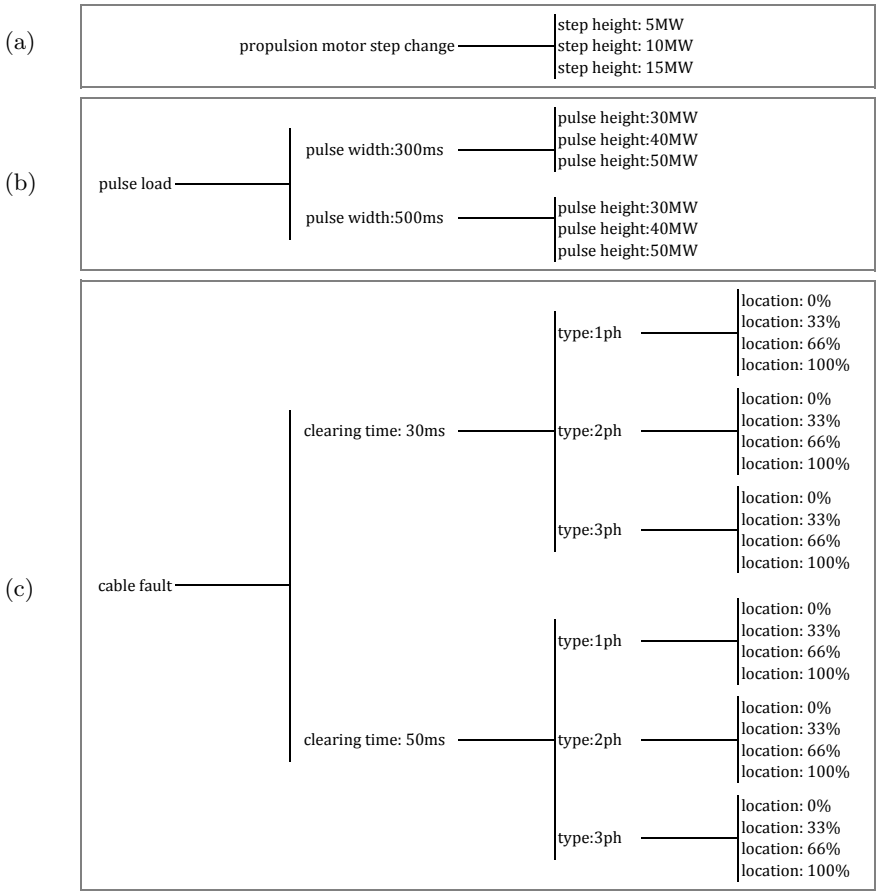

Figure 4.34: Contingency space partitioning for the notional AES

Determining probability of the contingencies in the contingency list is normally an issue in power systems, due to lack of historical data and dependency of probabilities on weather conditions and other factors [89]. In [89, 131], failure rates of 5e-5 to 40e-5 per hour were considered for transmission lines in transmission systems. For the notional all-electric ship, cable failure rate was arbitrarily chosen from this range. Failure rate for the cables was assumed to be 10e-5 per hour. Since undesirable outage of generators and loads is less likely than cables, an outage probability of 5e-5 per hour was considered for generator and load outages, arbitrarily. Propulsion motor sharp changes and pulse power load applications were considered to happen more frequently, compared to cable outages, with a rate of 100e-5 per hour. The contingency occurrence rates are listed in Tables 4.16.

Table 4.16: Contingency occurrence rates for the contingency categories in the notional AES

Description	Generator Trip	Load Trip	PM Step Change	Pulse Load	Fault
Category	C1, C2	C3, C4	C5	C6	C7, C8, C9, C10
Occurrence Rate	5E-5	5E-5	1E-3	1E-3	1E-4

Contingency occurrence rates of Table 4.16 and probability density functions of Table 4.15 were used to calculate contingency probabilities, p_d's, for all of the 334 partitions. The new severity function was used to define severity functions for the four security aspects, i.e. system frequency, generator angle, load bus voltage, and cable current. As an example, for the first security criterion, $h = 1$, there were 4 constraint bands, $u = 1, 2, 3, 4$. There was only one constrained quantity, $v = 1$, which was system frequency. Hence, in the calculation of the severity function for the first security criterion, $x_{v=1,d,m}(t)$ denoted system frequency following contingency d starting from the m-th sampled operating point. Equations (4.84)-(4.87) were used to calculate the time system frequency spent in each constraint band, $\tau_{u,h=1,v=1,d,m}$.

$$\tau_{u=1,h=1,v=1,d,m} = \frac{1}{4}\int_0^5 \Big[1+sgn\left(x_{u,d,m}(t) - 0.00\right)\Big]\Big[1+sgn\left(57.6 - x_{u,d,m}(t)\right)\Big] \qquad (4.84)$$

$$\tau_{u=2,h=1,v=1,d,m} = \frac{1}{4}\int_0^5 \Big[1+sgn\left(x_{u,d,m}(t)-57.6\right)\Big]\Big[1+sgn\left(58.2-x_{u,d,m}(t)\right)\Big] \quad (4.85)$$

$$\tau_{u=3,h=1,v=1,d,m} = \frac{1}{4}\int_0^5 \Big[1+sgn\left(x_{u,d,m}(t)-61.8\right)\Big]\Big[1+sgn\left(62.4-x_{u,d,m}(t)\right)\Big] \quad (4.86)$$

$$\tau_{u=4,h=1,v=1,d,m} = \frac{1}{4}\int_0^5 \Big[1+sgn\left(x_{u,d,m}(t)-62.4\right)\Big]\Big[1+sgn\left(70.0-x_{u,d,m}(t)\right)\Big] \quad (4.87)$$

Then, (4.69) was used to calculate severity of contingency d regarding the first security aspect, $s_{h=1,d,m}$, as shown in (4.88).

$$\begin{aligned} s_{h=1,d,m} = &+ \left(\tau_{u=1,h=1,v=1,d,m}-0\right)\left(\tau_{u=1,h=1,v=1,d,m}>0\right) \\ &+ \left(\tau_{u=2,h=1,v=1,d,m}-2\right)\left(\tau_{u=2,h=1,v=1,d,m}>2\right) \\ &+ \left(\tau_{u=3,h=1,v=1,d,m}-2\right)\left(\tau_{u=3,h=1,v=1,d,m}>2\right) \\ &+ \left(\tau_{u=4,h=1,v=1,d,m}-0\right)\left(\tau_{u=4,h=1,v=1,d,m}>0\right) \end{aligned} \quad (4.88)$$

After calculating the severity for each of the 334 contingencies, starting from each of the 19,160 sampled operating points, (4.71) was used to calculate operation risk at each operating point regarding any of the security aspects, $r_{h,m}$. Then, mapping coefficients shown in (4.49) were used to map system operating space from CPE space, $\mathfrak{E}$, into the space of the second CPC set, $\mathfrak{C}_2$.

The results are depicted in Figure 4.35. Figures 4.35(a), (b), and (c) show over/under frequency risk, transient angle instability risk, and over/under voltage risk, respectively. Figure 4.35(a) shows that as the operating point of the system moved from the lower left corner to the upper right corner, the over/under frequency risk increased. Figure 4.35(b) indicates that the risk associated with the transient angle instability increased as the operating point moved from the left of the operating space to the right. It can be seen in Figure 4.35(c) that the risk of over/under voltage was very small in the entire operating space.

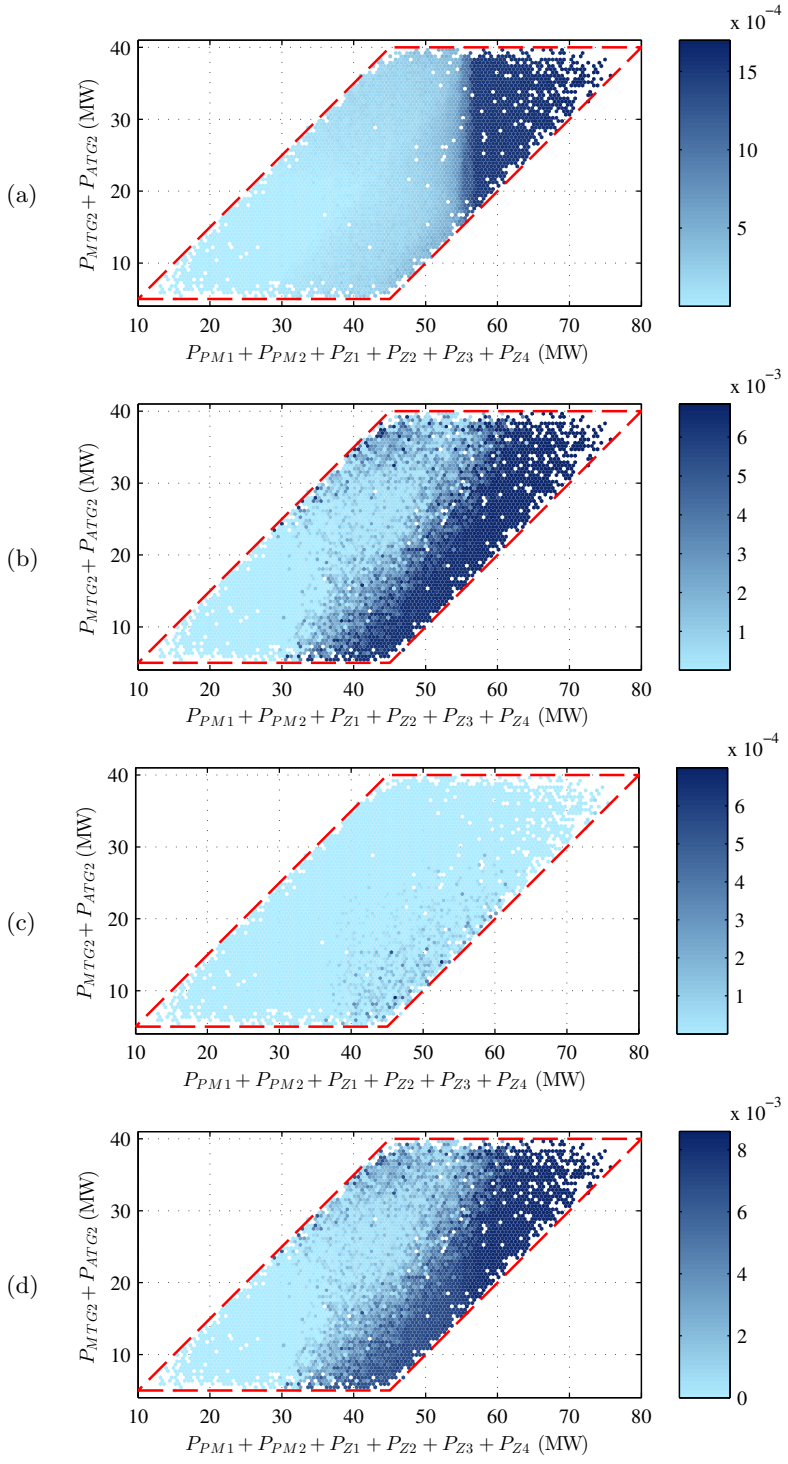

Figure 4.35: Risk of operation associated with various security aspects mapped into the critical parameter space of the notional AES. a) over/under frequency risk, b) transient angle instability risk, c) over/under voltage risk, and d) composite (total) risk

To come up with the total risk of operation at any operating point, the risks associated with various security aspects must be added together. The total operation risk obtained from integrating several security aspects together is referred to as the composite risk [106, 138]. The composite operation risk for any operating point in the ship's operating space is depicted in Figure 4.35(d). This figure shows that the composite risk in the notional all-electric ship model varied from 0 to 0.0086s. It also shows that the ship's operating region which had the highest risk was the region at the top right corner of the operating space, where the system was maximally loaded.

In order to divide the operating space into secure and insecure regions, several risk threshold were arbitrarily chosen, for the composite risk. For instance, assume risk threshold of $r^* = 0.002s$. This risk threshold divided system operating points into insecure and secure operating points, as shown in Figure 4.36(a) with dark and light colors, respectively. Then, (4.77)-(4.81) were used to determine the best quadratic border which discriminates secure operating points from insecure operating points. This border is depicted in Figure 4.36. Also, it is shown in (4.89), mathematically.

$$g(\mathbf{p}') = \mathbf{p}'^T \begin{bmatrix} +0.0000 & +0.0000 & +0.0000 \\ +0.0000 & +0.0095 & -0.0074 \\ +0.0000 & -0.0074 & +0.0055 \end{bmatrix} \mathbf{p}' + \begin{bmatrix} +0.0000 \\ -0.0081 \\ +0.2191 \end{bmatrix}^T \mathbf{p}' - 10.5278 = 0 \tag{4.89}$$

Similarly, Figures 4.36(b) and (c) show the system risk-based DSR, when the composite risk threshold was set to 0.005s and 0.007s, respectively. Table 4.17 shows border coefficients and border misclassification error for each of the three security borders in Figure 4.36. This table also shows the size of each DSR as a percentage of the operating space size. As expected, the size of the secure region increases, when the risk threshold increases. This table shows that the secure region size, with respect to the operating space size, increased from 47.2% to 51.0%, to 71.2%, when the risk threshold increased from 0.002s to 0.005s to 0.007s. It is worth reminding that the size of the deterministic DSR in the notional AES was 24% of the operating space.

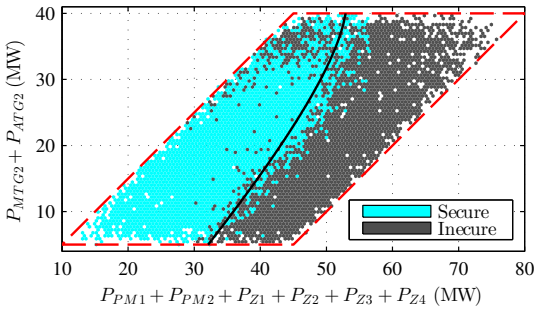

(a) risk threshold = 0.0020

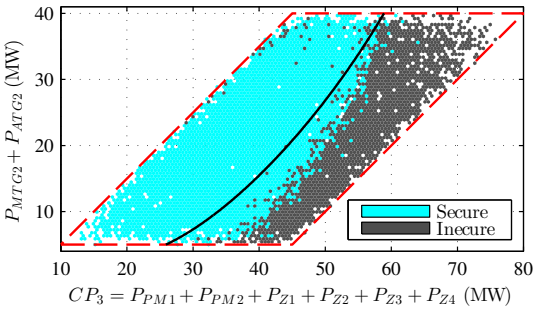

(b) risk threshold = 0.0050

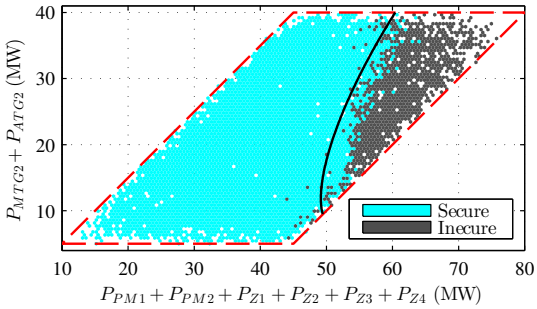

(c) risk threshold = 0.0070

Figure 4.36: Risk-based dynamic secure region for the notional AES

Table 4.17: Properties of the risk-based DSR in the notional AES

Risk Threshold	DSR Size	Missclassification Error (ϵ)	Constant, Linear, and Quadratic Border Coefficients		
			K	L	Q
$0.002s$	47.2%	10.9%	-10.5278	$\begin{bmatrix} +0.0000 \\ -0.0081 \\ +0.2191 \end{bmatrix}$	$\begin{bmatrix} +0.0000 & +0.0000 & +0.0000 \\ +0.0000 & +0.0095 & -0.0074 \\ +0.0000 & -0.0074 & +0.0055 \end{bmatrix}$
$0.005s$	51.0%	8.0%	$+2.0690$	$\begin{bmatrix} +0.0000 \\ -0.0240 \\ -0.1986 \end{bmatrix}$	$\begin{bmatrix} +0.0000 & +0.0000 & +0.0000 \\ +0.0000 & +0.0031 & -0.0031 \\ +0.0000 & -0.0031 & +0.0059 \end{bmatrix}$
$0.007s$	71.2%	5.6%	-77.2743	$\begin{bmatrix} +0.0000 \\ -1.3938 \\ +3.0633 \end{bmatrix}$	$\begin{bmatrix} +0.0000 & +0.0000 & +0.0000 \\ +0.0000 & -0.0152 & +0.0179 \\ +0.0000 & +0.0179 & -0.0312 \end{bmatrix}$

In summary, to implement the proposed RDSR assessment method in the notional all-electric shipboard power system, MATLAB and TSAT were used together. A contingency list including 334 partitions was developed. Operation risk of 19,160 operating points, distributed in the entire ship's operating space, regarding four security criteria, was assessed. Then, the composite risk for each operating point was calculated. Finally, a risk threshold was chosen and the quadratic discrimination function that optimally separated secure operating points from insecure ones was obtained.

4.5 Section Summary

In this section, the solution methodology for the new ISCPM method for all-electric shipboard power systems was discussed. A method was developed to solve the ISCPM multi-objective optimal control problem, which was based on the NSGA-II algorithm. To evaluate optimization constraints, the NSGA-II was linked to a fast simulation core. To apply the new ISCPM method on the notional AES power system, the NSGA-II and the system model were developed in MATLAB and TSAT tool of DSA *Tools*$^{\text{TM}}$, respectively.

Among the ISCPM optimization constraints were the security constraints against planned and unplanned events. In the new ISCPM method, to assess system security against planned events, an approach adapted from constraint transcription technique was developed, in which security constraints were defined on the time that constrained quantities spend in constraint bands. To assess system security against contingencies, a region-based approach was developed. A systematic method to determine deterministic and risk-based dynamic secure region of the system was proposed. Due to the limitations of the deterministic DSR in all-electric ships, using the risk-based DSR was recommended.

To pick the final solution (best compromise solution) from among the Pareto solutions, a method based on fuzzy membership sets was developed. In this method, a membership function was defined for each objective, which showed a degree of achievement for the objective. Then, the membership functions of each solution were used to calculate a normalized membership function for that solution, which showed the degree of achievement

for that solution, compared to other solution. The solution with the highest achievement, or the highest normalized membership value, was then chosen as the winner solution. Next in section 5, case studies and performance analysis are discussed.

5 CASE STUDIES AND PERFORMANCE ANALYSIS

The results of the problem based case studies and performance analysis are presented and discussed in this section. First, in subsection 5.1, the simulation setup for the studies is explained. Next, several problem-based cases are discussed in subsection 5.2. Next, in subsection 5.3, the extensive studies conducted to evaluate the performance of the new ISCPM method are discussed.

5.1 Simulation Setup

An overview of the simulation setup for case studies and performance analysis is depicted in Figure 5.1. This figure shows where each ISCPM module was implemented. It also indicates the inputs and outputs for each module. As shown in this figure, the multi-objective optimization was developed in MATLAB, by adapting the IlliGAL toolbox [145]. Implementation details for the multi-objective optimization solving are discussed in subsection 5.1.1. In this model-based approach, the system model was developed in the TSAT tool of DSA*Tools*$^{\text{TM}}$ [100]. Hence, MATLAB was linked to TSAT for transient simulations during the GA iterations. The details of the notional AES modeling in TSAT were previously discussed in subsection 4.4.1. The best compromise solution identification was also developed in MATLAB, which is discussed in subsection 5.1.2.

In order to evaluate the performance of the ISCPM method, the system response to the adjusted set-points provided by the ISCPM method was obtained, by conducting an electromagnetic transient simulation in PSCAD. The details of the notional AES modeling in PSCAD is discussed in subsection 5.1.3. As shown in Figure 5.1, for each simulation, a propulsion, zonal, and pulse load forecast was prepared, first. Next, arbitrary signals were generated to mimic the DGD and DVC responses to the forecasted load. Then, the ISCPM method was applied to the generated DGD power and DVC voltage set-points, to calculate the adjusted set-points. Next, the PSCAD simulation was conducted, in which the adjusted set-points were applied to the system. For this simulation, the desired propulsion, zonal,

and pulse load powers were assumed to be the same as the forecasted load. Moreover, to compare the system response to the ISCPM adjusted set-points with the system response to the DGD and DVC set-points, another PSCAD simulation was conducted using the set-points provided by the DGD and DVC methods.

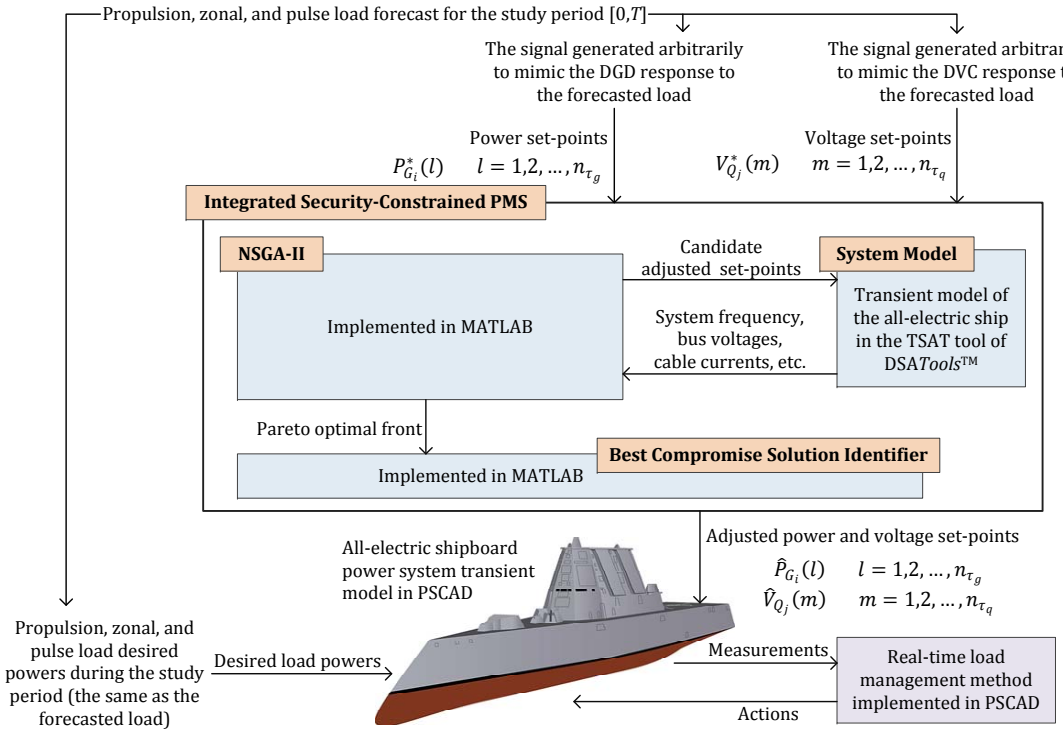

Figure 5.1: Simulation setup for case studies and performance analysis

5.1.1 NSGA-II Algorithm

To solve the ISCPM multi-objective optimization problem using NSGA-II method, a multi-objective genetic algorithm toolbox developed in Illinois GA Laboratory, IlliGAL, was used [145]. This toolbox provides different selection, crossover, mutation, and constraint handling operators, and solves single or multi-objective optimization problems. The multi-objective optimization solving method used in this toolbox is the NSGA-II algorithm. The IlliGAL multi-objective optimization solver solves the multi-objective

optimization problem, whose parameters are defined in a text file. This text file contains parameters such as number of objectives, number of decision variables, decision variable bounds, number of constraints, selection operator properties, crossover operator properties, mutation operator properties, constraint handling technique, etc. For each problem, the appropriate text file was automatically developed in a MATLAB script. Then, the IlliGAL solver was called in MATLAB, to solve the optimization problem whose characteristics were defined in the text file previously developed.

To evaluate the objectives and constraints for each individual, the IlliGAL solver passes the individual to a MATLAB function, which returns the objective and constraint values for the individual. The MATLAB function calls TSAT to perform a transient simulation using the adjusted set-points of that particular individual, first. Then, it calculates the values of the constraints, using TSAT simulation results.

A population size of 150 individuals with a maximum generation of 100 was chosen for the NSGA-II algorithm. For the crossover operator, 90% probability, which is a typical and popular probability [146,147], was used. For the mutation rate, 10% was chosen, arbitrarily. Moreover, η_c parameters for the crossover and mutation operators were arbitrarily set to 10 and 20, respectively, which are in the typical range.

5.1.2 Best Compromise Solution Identification

The IlliGAL multi-objective optimization solver stores the objective and constraint values for all of the evaluated individuals in a text file. A MATLAB script was developed to read the text file and determine the Pareto optimal solutions from among the evaluated solutions. Identification of the best compromise solution was also carried out in MATLAB. In the new ISCPM method, to identify the best compromise solution, the highest weight was given to the total generation objective, f_{o_2} in (3.11), the second highest to the generation set-point deviation objective, f_{o_1} in (3.10), and the lowest to the voltage/VAr set-point deviation objective, f_{o_3} in (3.12). The weighting factors were arbitrarily defined as follows: $\omega_1 = \frac{2}{6}$, $\omega_2 = \frac{3}{6}$, and $\omega_3 = \frac{1}{6}$.

5.1.3 Notional AES Model in PSCAD

The single line diagram of the notional all-electric ship, implemented in PSCAD, is depicted in Figure 5.2. This system includes two main and two auxiliary gas turbine generators. Four transformers are used to step down the voltage from 13.8kV AC to 4.16kV AC and supply two propulsion loads and four DC zones. The details of modeling the notional all-electric ship in PSCAD are discussed in [12, 148]. In summary, each generator model included a synchronous machine, a gas turbine governor, and an exciter. The inertia constants for MTGs and ATGs were 1.49s and 1.06s, respectively. Also, each generator's governor had a 5% droop.

Each propulsion induction motor had a 36MW capacity and was driven by a propulsion converter, which included a rectifier, a DC link, and an inverter. The rectifier converted 4.16kV AC into DC voltage, and a space vector PWM inverter was used to convert the DC voltage into AC voltage to serve the advanced induction motor. The propulsion motors operated in the power control mode. In this mode, propulsion motor's power was maintained at its set-point, provided by the real-time load management method. The pulse load was modeled as a resistor connected to a charging circuit, where the charging circuit was a rectifier. A DSTATCOM was connected to the pulse load bus. The DSTATCOM was modeled with a 6-pulse bridge connected to the output of a transformer that stepped down the voltage from 4.16kV AV to 600V AC. The firing angles of the bridge GTOs were determined by a PI controller to maintain a pre-determined terminal voltage.

Each DC zone had two DC distribution buses, a starboard side bus and a port side bus. The DC distribution buses on the same side were served by the same PCM4 module, which was a rectifier converting 4.16kV AC voltage to 1000V DC voltage with a maximum capacity of 2MW. A PCM4 did not serve the starboard side bus and the port side bus at the same time. The output of each PCM4 module was connected to two PCM1 modules. PCM1 modules were DC/DC converters that provided three voltage levels: 375V DC, 650V DC, and 800V DC. Various AC and DC loads were connected to these three voltage levels. Each DC motor was directly connected to a DC bus. The mechanical torque of a DC motor

was proportional to the square of its rotor speed. To serve each AC load, a PCM2 module, which was an inverter, was used to convert the 800V DC to 450V AC.

The real-time load management method [12] was also implemented in PSCAD. The RLM method received some system measurements and determined the loads that must be connected and their power levels. The loads that could be controlled by the RLM method were the propulsion and zonal loads. This method could not control the pulse power load.

5.2 Case Studies

To illustrate how the new ISCPM method works, several case studies with various load changes are presented and discussed. In case I in subsection 5.2.1, a sharp increase in propulsion load is studied. In case II in subsection 5.2.2, the use of a pulse power load is studied. In case III in subsection 5.2.3, the outage of a main turbine generator is studied. In case IV in subsection 5.2.4, several zonal load changes and pulse load uses are studied.

5.2.1 Case I: Sharp Propulsion Load Increase

In case I, performance of the new ISCPM method during a sharp propulsion power increase in the notional all-electric ship was studied. The main purpose of the study was to illustrate how the ISCPM method keeps the system trajectory inside the secure region when propulsion loads in the system change, significantly. In this case, the study period was $T = 25$ seconds and the simulation duration was also 25s. The decision intervals for the Dynamic Generation Dispatch (DGD) and the Dynamic Voltage/VAr Control (DVC) methods were $\tau_g = 5$ and $\tau_q = 5$ seconds, respectively. Therefore, the study period included $n_{\tau_g} = 5$ decision intervals for the DGD method and $n_{\tau_q} = 5$ decision intervals for the DVC method.

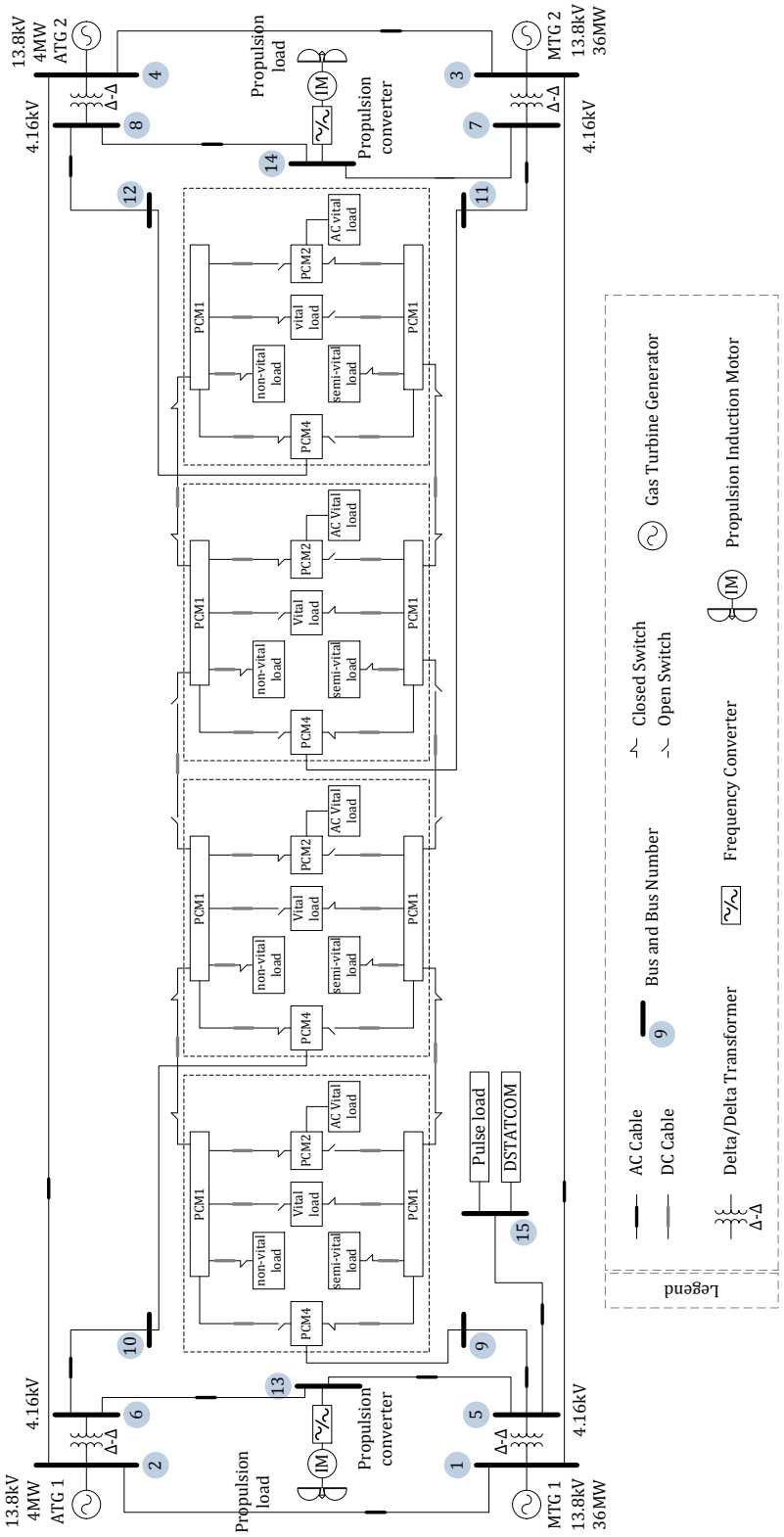

Figure 5.2: Single line diagram of the notional AES computer model in PSCAD

The system was initially ($t = 0$s) operating with 38MW load which was composed of 2×15MW propulsion loads and 4×2MW zonal total loads. The set-points provided by the DGD to serve the loads plus losses for MTG1, ATG1, MTG2, and ATG2 were 20.13MW, 1MW, 16MW, and 1MW, respectively. The MTG1 was the system slack generator and its power set-point was fine tuned by its governor to maintain the system frequency. The DVC voltage set-points for the generators were 0.9690pu, 0.9682pu, 0.9690pu, and 0.9682pu, correspondingly. Moreover, the DVC voltage set-point for the DSTATCOM was 0.9525pu.

The power of each propulsion motor, P_{PM1}, P_{PM2}, was forecasted to increase by 15MW at $t = 7$s. It was assumed the DGD method evenly distributed the 30MW load increase among the two MTGs, which means that the MTG power set-points were as follows: $P^*_{G_1}(1) = 20.13$MW, $P^*_{G_1}(2) = 35.18$MW, $P^*_{G_1}(3) = 35.18$MW, $P^*_{G_1}(4) = 35.18$MW, $P^*_{G_1}(1) = 35.18$MW, $P^*_{G_3}(1) = 16.00$MW, $P^*_{G_3}(2) = 31.05$MW, $P^*_{G_3}(3) = 31.05$MW, $P^*_{G_3}(4) = 31.05$MW, and $P^*_{G_3}(5) = 31.05$MW. Moreover, it was assumed that the DVC method increased each of the voltage set-points by 0.3% starting from the second decision interval, at time 5s, in order to compensate for the voltage drop caused by the load change. As an example, the DVC voltage set-points for the DSTATCOM, the fifth voltage-controlled device in the system, were $V^*_{Q_5}(1) = 0.9525$pu, $V^*_{Q_5}(2) = 0.9554$pu, $V^*_{Q_5}(3) = 0.9554$pu, $V^*_{Q_5}(4) = 0.9554$pu, and $V^*_{Q_5}(5) = 0.9554$pu.

It is worth emphasizing that the DGD and DVC methods were not available for the notional all-electric ship. Hence, some signals were arbitrarily generated to mimic their response to the forecasted load. Throughout this section, "DGD and DVC set-points" or "set-points provided by DGD and DVC methods" refer to the signals arbitrarily generated to mimic the responses of the two methods to the forecasted load.

To determine the operating or security constraint violations that may occur, if the DGD and DVC set-points, $P^*_{G_i}(l)$ and $V^*_{Q_j}(m)$, were used, a PSCAD simulation was conducted using these set-points. The system trajectory obtained from this PSCAD simulation is depicted in Figure 5.3. In this figure, x and y axes are two critical parameters and show the total load in the system and the total power of MTG2 and ATG2. The details for

obtaining the risk-based DSR, shown in this figure, was explained in subsection 4.4.4.2. It was explained that the system was secure against unplanned events, if the system trajectory remained on the left hand side of the security border. To obtain the system trajectory shown in this figure, generator and load terminal powers obtained from the PSCAD simulation were used. This figure shows that the system trajectory during [0,25s]. Several points on the trajectory are time stamped. Using this points, it can be seen that the system trajectory was initially inside the secure region. However, due to the power set-point increases at time 5s and propulsion load increase at time 7s, the system trajectory moved outside of the DSR. Hence, the security constraints against contingencies were violated, if the DGD and DVC set-points were used.

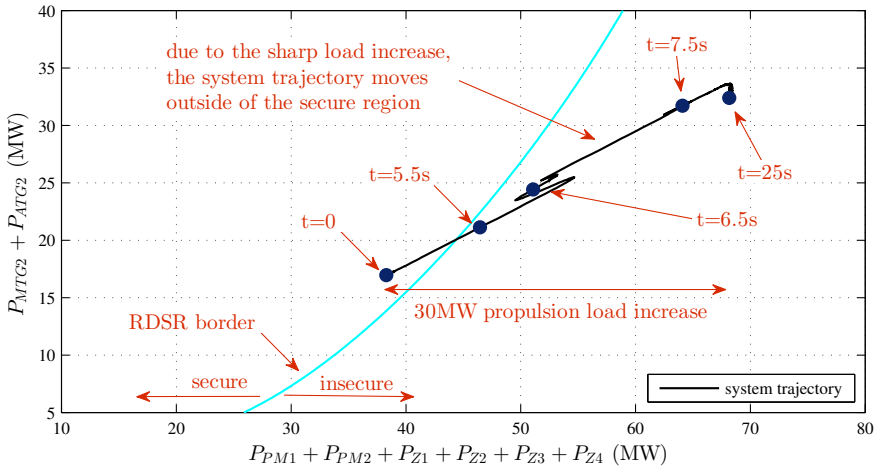

Figure 5.3: System trajectory in the critical parameter space, in the system response to the DGD and DVC set-points (case I)

The set-points provided by the DGD and DVC methods also resulted in violation of the operating constraints on propulsion and pulse load voltages. Figure 5.4 shows the voltage measured at propulsion and pulse load buses, P_{PM1}, P_{PM2}, and P_{PLS}, when the DGD and DVC set-points were applied to the system. It can be observed that the voltage at propulsion motor buses dropped below 0.95pu after the sharp increase and stayed there for

more than 2s. Therefore, the operating constraint on load bus voltages was violated, when the DGD and DVC set-points were applied to the system.

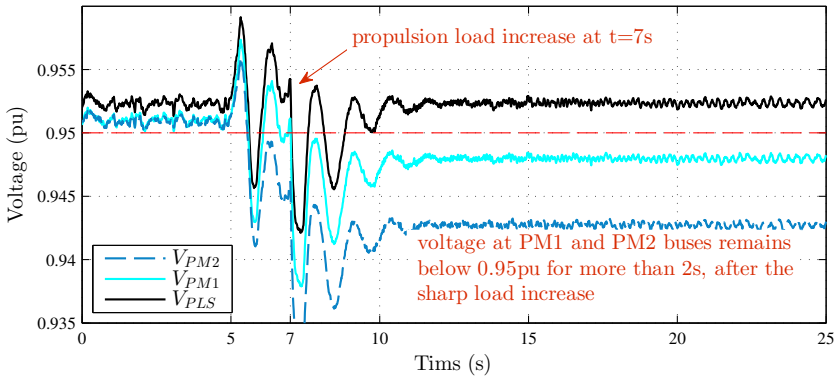

Figure 5.4: Propulsion and pulse load voltages in the system response to the DGD and DVC set-points (case I)

Next, the ISCPM method was applied to the same propulsion load changes. The DGD and DVC set-points for the decision intervals during the [0,25s] study period were the inputs to the ISCPM method. In this study, it was assumed that P_{ATG1} and P_{ATG2} did not participate in power set-point adjustment. The NSGA-II solved the multi-objective optimization problem and obtained a Pareto optimal front. This Pareto front is shown in Figure 5.5. Instead of a 3D plot, the projection of the Pareto optimal front on $f_{o_1} - f_{o_2}$, $f_{o_2} - f_{o_3}$, and $f_{o_3} - f_{o_1}$ planes are depicted in Figure 5.5(a), (b), and (c), respectively. As explained in the problem statement in section 3, f_{o_1}, f_{o_2}, and f_{o_3} are the objectives associated with the generation set-point mismatch, total generation set-point mismatch, and voltage set-point mismatch, correspondingly, and were calculated using (3.10)-(3.12) To obtain the Pareto optimal front shown in this figure, the GA evaluated many solutions during its generations. The evaluated solutions are also depicted in this figure. As explained earlier, for each of these solutions, a TSAT simulation was conducted to evaluate the operating and security constraints. The Pareto optimal front in this case contained 188

Pareto solutions. From among these solutions, the best compromise solution was picked, using the fuzzy membership method. The objective values for the best compromise solution are also shown in this figure.

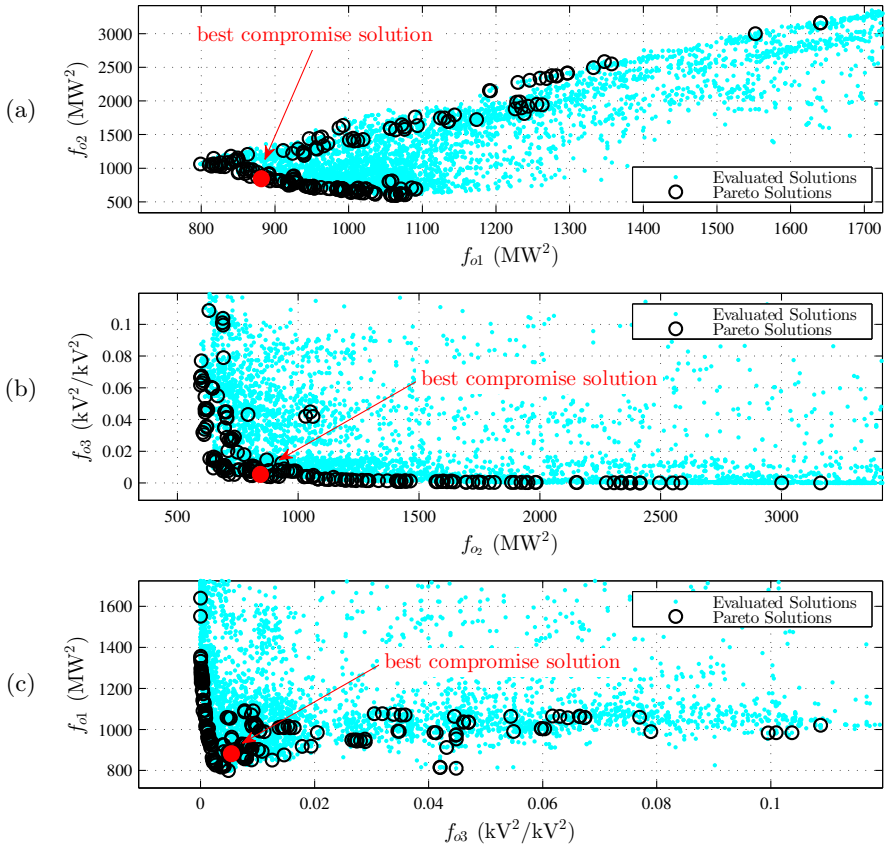

Figure 5.5: Pareto optimal front (case I). a) $f_{o_1} - f_{o_2}$ plane, b) $f_{o_2} - f_{o_3}$ plane, and c) $f_{o_3} - f_{o_1}$ plane

From Figure 5.5, it can be seen that the objectives f_{o_1} and f_{o_2} varied from 799 to 1641 MW^2, and from 596 to 3162 MW^2, in the Pareto solutions, respectively. Also, f_{o_3} varied from 5e-06 to 0.1087 pu^2. The difference in the order of magnitude of f_{o_1} and f_{o_2} with that of f_{o_3} shows the importance of keeping the three objectives separate, as opposed to integrating them together using some weighting factors, which was discussed in section 3. From Figure 5.5, it can also be observed that the three objectives of the best compromise

solution were $f_{o_1} = 881.5\text{MW}^2$, $f_{o_2} = 844.2\text{MW}^2$, and $f_{o_3} = 0.0054\text{pu}^2$.

The adjusted P_{MTG1} and P_{MTG2} set-points of the best compromise solution are listed in Table 5.1. In this table, the second row shows the DGD power set-points for MTG1 for the five decision intervals, $l = 1, ..., 5$, and the third row shows the ISCPM adjusted power set-points for MTG1 for the five decision intervals. Similarly, the next two rows show unadjusted and adjusted set-point values for MTG2. As explained earlier, P_{ATG1} and P_{ATG2} did not participate in power set-point adjustment and were constant at 1MW during the study period. In this table, the set-points with and without adjustment are compared, in each of the five decision intervals. MTG power set-points, with and without ISCPM adjustments, are also shown in Figure 5.6. Figure 5.6(a) shows the forecasted power and the measured power from PSCAD simulation for one of the propulsion motors (the powers for the two propulsion motors were the same). Also, Figures 5.6(b) and (c) show the MTG1 and MTG2 power set-points, respectively, with and without ISCPM adjustments.

Table 5.1: Generator power set-points with and without use of ISCPM method (case I)

interval no, l	$l = 1$	$l = 2$	$l = 3$	$l = 4$	$l = 5$
$P^*_{MTG1}(l)$	20.13 MW	35.18 MW	35.18 MW	35.18 MW	35.18 MW
$\hat{P}_{MTG1}(l)$	18.31 MW	19.87 MW	20.50 MW	20.27 MW	20.14 MW
$P^*_{MTG1}(l)$	16.00 MW	31.00 MW	31.00 MW	31.00 MW	31.00 MW
$\hat{P}_{MTG1}(l)$	15.88 MW	31.54 MW	30.57 MW	31.10 MW	32.03 MW

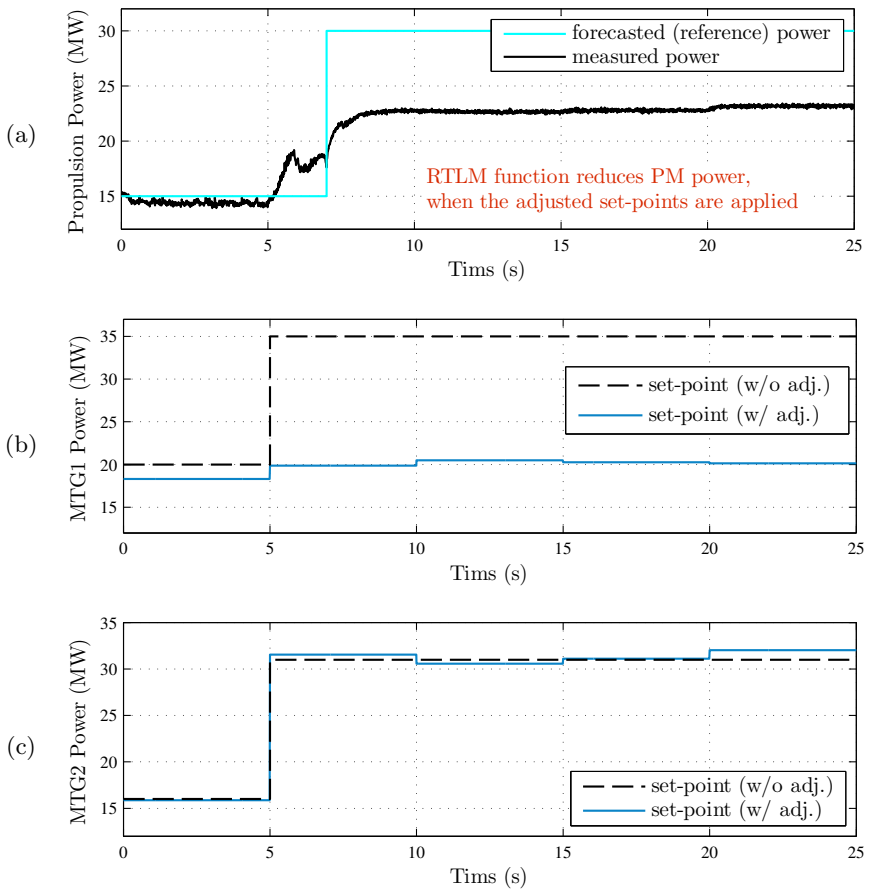

Figure 5.6: Comparison of the generator power set-points with and without use of ISCPM method (case I). a) forecasted and measured propulsion load power, b) MTG1 power set-point, and c) MTG2 power set-point

From Table 5.1 and Figure 5.6(b)-(c), it can be observed that MTG2 power set-point adjustments were very small. However, MTG1 power set-points were reduced, mainly in decision intervals 2-5. The reduction in MTG1 power set-point reduced the total power generation in the system, mainly in intervals 2-5. As a result, the real-time load management method reduced the propulsion power in the system. Figure 5.6(a) shows that the power of each propulsion motor was reduced from 30MW to ∼22MW by the RLM method. The reduction in MTG1 and propulsion power made the system secure against unplanned events, since it caused the system trajectory to remain inside the secure region for the entire [0,25s] study period.

The system trajectory obtained from the PSCAD simulation with the ISCPM set-points is depicted in Figure 5.7. In this figure, x and y axes are two critical parameters and show the total load in the system and the total power of MTG2 and ATG2, respectively. To obtain the system trajectory shown in this figure, generator and load terminal powers obtained from the PSCAD simulation were used. This figure shows that the system trajectory during [0,25s]. Several points on the trajectory are time stamped. It can be observed that the system trajectory remained inside the DSR (left hand side of the border) for the entire study period. Hence, the violation of the dynamic security constraints against contingencies was alleviated, when the ISCPM adjusted set-points were used.

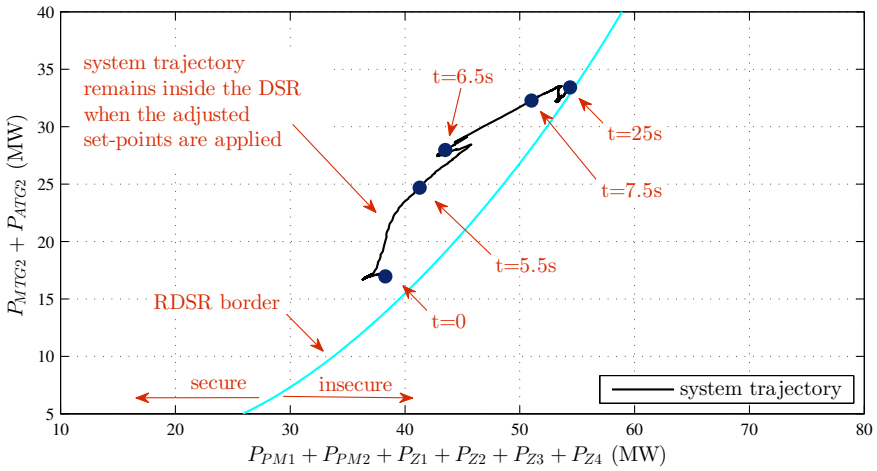

Figure 5.7: System trajectory in the critical parameter space, in the system response to the ISCPM set-points (case I)

Figure 5.8 compares the total planned generator power and the total load plus loss in the system, when the ISCPM adjusted set-points were used. Figure 5.8(a) shows the forecasted and measured power for a propulsion motor. Figure 5.8(b) shows the total planned generator power (summation of the generator power set-points). Figure 5.8(b) also depicts the total load plus loss in the system, obtained from the PSCAD simulation. It can be observed that the total load plus loss was always less than the total planned

generation power, during the [0,25s] study period.

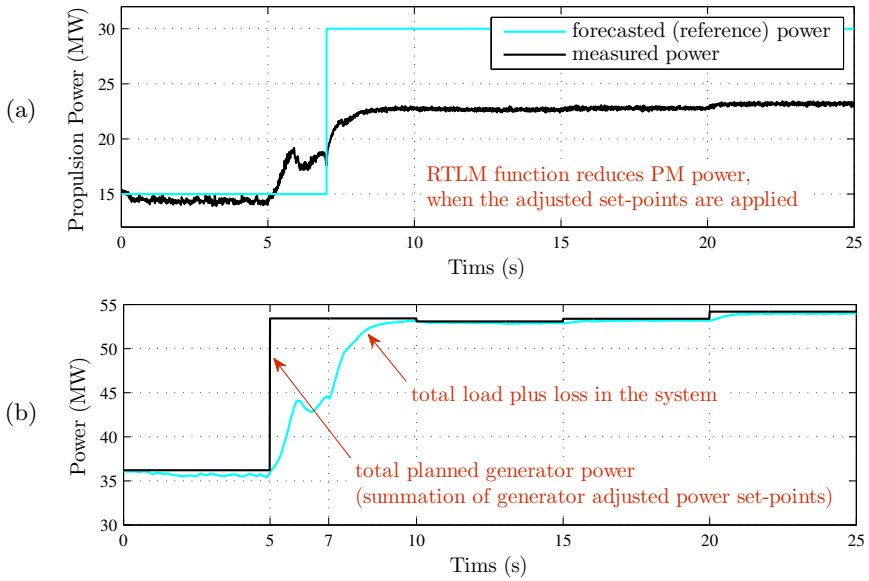

Figure 5.8: Comparison of total generator power and total load plus loss, in the system response to the ISCPM set-points (case I). a) forecasted and measured propulsion load power, and b) total planned generator power and total load plus loss

The adjusted generator and DSTATCOM voltage set-points of the best compromise solution are listed in Table 5.2. In this table, the second row shows MTG1 voltage set-points from the DVC method for any of the five decision intervals, and the third row lists the adjusted ISCPM voltage set-points for MTG1. Similarly, the following rows show the DVC and ISCPM voltage set-points for ATG1, MTG2, ATG2, and DSTATCOM, for the five decision intervals. As an example, DSTATCOM voltage set-points, with and without use of ISCPM method, are also shown in Figure 5.9. In Figure 5.9, DVC and ISCPM voltage set-points for the DSTATCOM are shown with dashed and solid black lines, respectively. Moreover, DSTATCOM terminal voltage, obtained from the PSCAD simulation, is plotted with the lighter solid line.

From Table 5.2 and Figure 5.9, it can be observed that the ISCPM method slightly increased the voltage set-points, in all of the decision intervals. Moreover, the maximum

increase happened in the second decision interval in which the sharp propulsion power increase happened. The ISCPM adjustments to the DGD and DVC set-points alleviated the load voltage operating constraint violations. Figure 5.10 shows PM1, PM2, and DSTATCOM terminal voltages obtained from the PSCAD simulation, when the adjusted ISCPM set-points were used. The dashed line in this figure shows 0.95pu limit, under which voltage cannot operate for more than 2s. It can be observed that the load terminal voltages remained above 0.95pu during the entire study period and hance, the operating constraint violation was alleviated.

Table 5.2: Voltage set-points with and without use of ISCPM method (case I)

interval no, m	$m=1$	$m=2$	$m=3$	$m=4$	$m=5$
$V^*_{MTG1}(m)$	0.9690 pu	0.9719 pu	0.9719 pu	0.9719 pu	0.9719 pu
$\hat{V}_{MTG1}(m)$	0.9800 pu	0.9959 pu	0.9811 pu	0.9763 pu	0.9734 pu
$V^*_{ATG1}(m)$	0.9682 pu	0.9711 pu	0.9711 pu	0.9711 pu	0.9711 pu
$\hat{V}_{ATG1}(m)$	0.9792 pu	0.9951 pu	0.9803 pu	0.9755 pu	0.9726 pu
$V^*_{MTG2}(m)$	0.9690 pu	0.9719 pu	0.9719 pu	0.9719 pu	0.9719 pu
$\hat{V}_{MTG2}(m)$	0.9800 pu	0.9959 pu	0.9811 pu	0.9763 pu	0.9734 pu
$V^*_{ATG2}(m)$	0.9682 pu	0.9711 pu	0.9711 pu	0.9711 pu	0.9711 pu
$\hat{V}_{ATG2}(m)$	0.9792 pu	0.9951 pu	0.9803 pu	0.9755 pu	0.9726 pu
$V^*_{DSTA}(m)$	0.9525 pu	0.9554 pu	0.9554 pu	0.9554 pu	0.9554 pu
$\hat{V}_{DSTA}(m)$	0.9634 pu	0.9790 pu	0.9644 pu	0.9596 pu	0.9568 pu

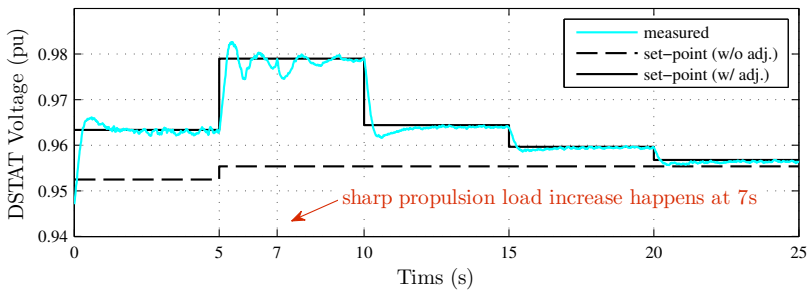

Figure 5.9: Comparison of DSTATCOM voltage set-points with and without use of ISCPM method (case I)

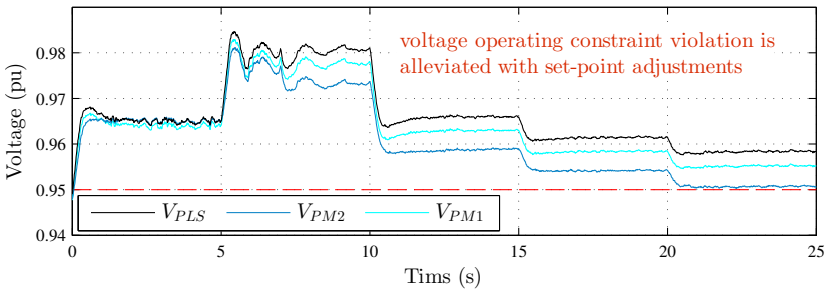

Figure 5.10: Load bus voltages in the system response to the ISCPM set-points (case I)

In summary, a sharp propulsion power increase was studied in this case. It was observed that when the set-points provided by the dynamic generation dispatch and dynamic voltage/VAr control methods were used, the system trajectory moved outside of the system DSR after the load change. Moreover, it was observed that the load change resulted in the violation of load bus voltage operating constraint. Next, the ISCPM method was used for the same propulsion power increase. The simulation results, when the adjusted power and voltage set-points were used, showed that both of the constraint violations were alleviated.

5.2.2 Case II: Pulse Power Load

In case II, performance of the ISCPM method during a pulse power load application is discussed. The main purpose of the study was to illustrate how the ISCPM method keeps the system trajectory inside the secure region and also alleviates frequency and voltage operating constraint violations, when a pulse load is connected to the system. In this case, the study period was $T = 25$ seconds and the simulation duration was also 25s. The decision intervals for the Dynamic Generation Dispatch (DGD) and the Dynamic Voltage/VAr Control (DVC) methods were $\tau_g = 5$ and $\tau_q = 5$ seconds, respectively. Therefore, the study period included $n_{\tau_g} = 5$ decision intervals for the DGD method and $n_{\tau_q} = 5$ decision intervals for the DVC method. For this study, it was assumed that the ATG power set-points were constant at 1MW and did not change.

The system was initially ($t = 0$s) operating with 38MW load which was composed of

2×15MW propulsion loads and 4×2MW zonal total loads. The set-points provided by the DGD to serve the loads plus losses for MTG1, ATG1, MTG2, and ATG2 were 20.13MW, 1MW, 16MW, and 1MW, respectively. The MTG1 was the system slack generator and its power set-point was fine tuned by its governor to maintain the system frequency. The DVC voltage set-points for the generators were 0.9690pu, 0.9682pu, 0.9690pu, and 0.9682pu, correspondingly. Moreover, the DVC voltage set-point for the DSTATCOM was 0.9525pu.

The power of each propulsion motor, P_{PM1} and P_{PM2}, was forecasted to increase by 2.5MW at 7s. To serve the 5MW increase in total system load, it was assumed that the DGD method increased MTG1 power set-point by 5MW, from the second decision interval at $t = 5$s. Two back to back 50MW pulses were forecasted to be connected to the system from 10s to 15s, and from 16s to 21s. Since the pulse load power was more than total system load, the dynamic generation dispatch method increased MTG1 and MTG2 power set-points by 5MW at intervals 3-5. Therefore, MTG power set-points provided by the DGD method were $P^*_{G_1}(1) = 20.13$MW, $P^*_{G_1}(2) = 25.14$MW, $P^*_{G_1}(3) = 30.16$MW, $P^*_{G_1}(4) = 30.16$MW, $P^*_{G_1}(5) = 30.16$MW, $P^*_{G_3}(1) = 16.00$MW, $P^*_{G_3}(2) = 16.00$MW, $P^*_{G_3}(3) = 21.00$MW, $P^*_{G_3}(4) = 21.00$MW, and $P^*_{G_3}(5) = 21.00$MW. Also, it was assumed that the dynamic voltage/VAr control method increased all of the voltage set-points by 0.1% starting from the third decision interval at $t = 10$s, in order to compensate for the voltage drop caused by the pulse load. As an example, the DVC voltage set-points for the DSTATCOM were $V^*_{Q_5}(1) = 0.9525$pu, $V^*_{Q_5}(1) = 0.9525$pu, $V^*_{Q_5}(1) = 0.9535$pu, $V^*_{Q_5}(1) = 0.9535$pu, and $V^*_{Q_5}(1) = 0.9535$pu.

To determine the operating or security constraint violations that may occur, if the DGD and DVC set-points, $P^*_{G_i}(l)$ and $V^*_{Q_j}(m)$, were used, a PSCAD simulation was conducted using these set-points. The propulsion and pulse load powers obtained from the simulation are depicted in Figure 5.11. This figure shows the forecasted and the measured powers for propulsion and pulse loads. It can be seen that the power of each propulsion motor was increased from 15MW to 17.5MW at 7s. It can also be observed that the real-time load management method reduced the propulsion load power, when the pulse was connected.

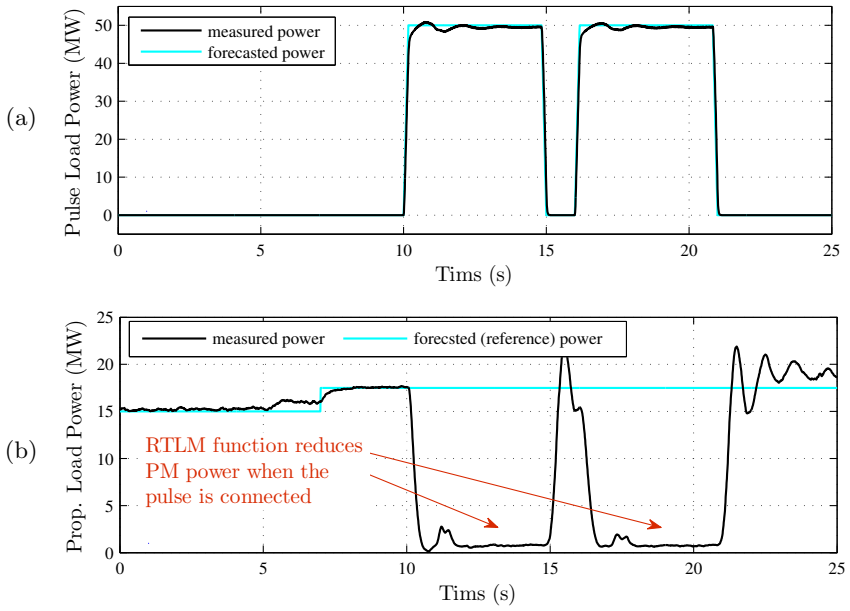

Figure 5.11: Forecasted and measured propulsion and pulse load powers in the system response to the DGD and DVC set-points (case II). a) pulse load, and b) propulsion load

The system trajectory obtained from the PSCAD simulation with DGD and DVC set-points is depicted in Figure 5.12. In this figure, x and y axes are two critical parameters and show the total load in the system and the total power of MTG2 and ATG2. The details for obtaining the risk-based DSR, shown in this figure, was explained in subsection 4.4.4.2. It was explained that the system was secure against unplanned events, if the system trajectory remained on the left hand side of the security border. To obtain the system trajectory shown in this figure, generator and load terminal powers obtained from the PSCAD simulation were used. This figure shows that the system trajectory during [0,25s]. Several points on the trajectory are time stamped. Using this points, it can be seen that the system trajectory was initially inside the secure region. However, due to the power set-point increases at time 5s and propulsion load increase at time 7s, the system trajectory moved outside of the DSR. During pulse connection and disconnection, the load powers changed significantly, which resulted in the big changes in the system trajectory, which are shown in the figure. Finally, the system trajectory was settled outside of the

DSR at $t = 25$s. Hence, the security constraints against contingencies were violated, if the DGD and DVC set-points were used.

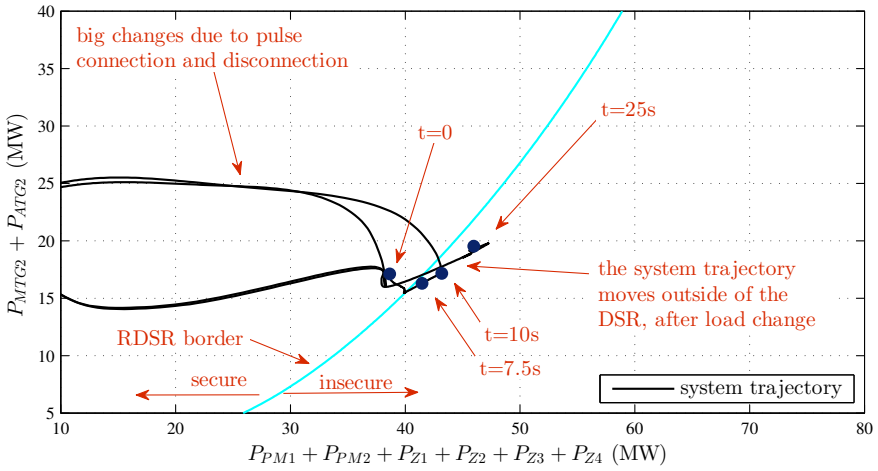

Figure 5.12: System trajectory in the critical parameter space, in the system response to the DGD and DVC set-points (case II)

The set-points provided by the DGD and DVC methods also resulted in violation of the operating constraints, as shown in Figure 5.13. Figure 5.13(a) shows the pulse load power. Figure 5.13(b) shows the system frequency response to the DGD and DVC set-points. It can be seen that the system frequency was more than the maximum allowable value, 62.4Hz, after the second pulse was disconnected at 21s. Therefore, the frequency operating constraint was violated. Figure 5.13(c) shows the voltage measured at propulsion and pulse load buses, P_{PM1}, P_{PM2}, and P_{PLS}. It can be observed that V_{PM1} and V_{PLS} operated below 0.95pu for more than 2s, and hence, the voltage operating constraint was also violated.

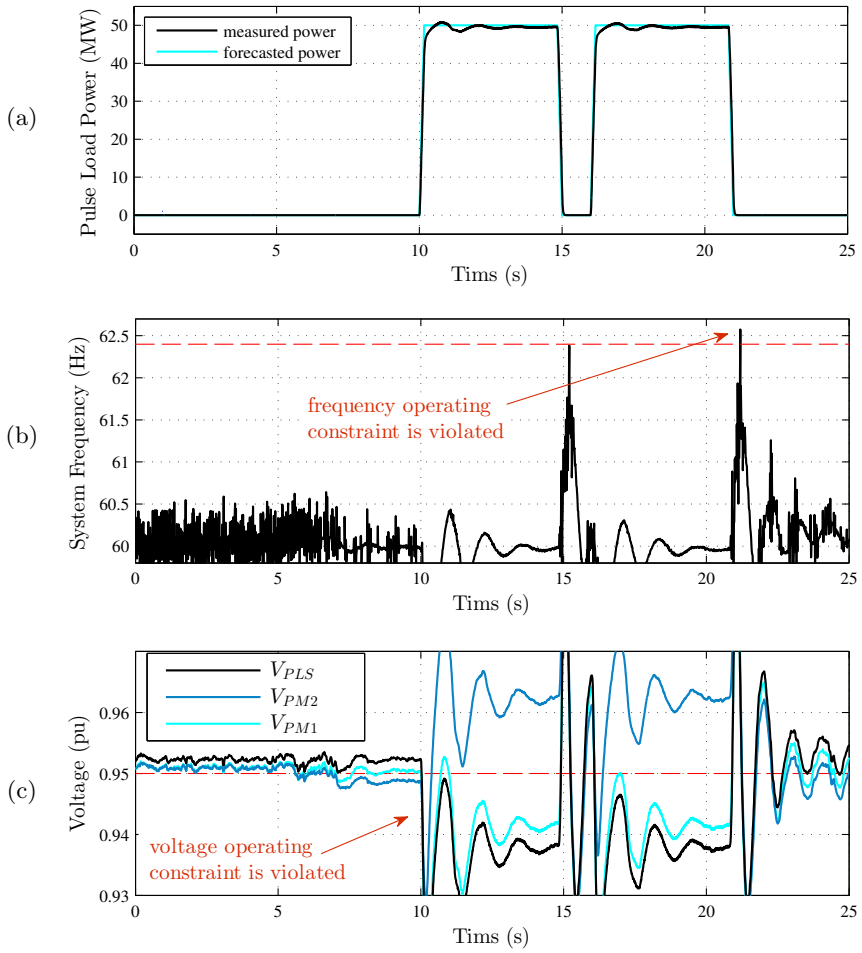

Figure 5.13: Operating constraint violations in the system response to the DGD and DVC set-points (case II). a) pulse load power, b) system frequency, and c) propulsion and pulse load terminal voltages

Next, the ISCPM method was applied to the same propulsion and pulse load changes. The DGD and DVC set-points for the decision intervals during the [0,25s] study period were the inputs to the ISCPM method. In this study, it was assumed that P_{ATG1} and P_{ATG2} did not participate in power set-point adjustment. The NSGA-II solved the multi-objective optimization problem and obtained a Pareto optimal front, which is shown in Figure 5.14. Instead of a 3D plot, the projection of the Pareto optimal front on $f_{o_1} - f_{o_2}$, $f_{o_2} - f_{o_3}$, and $f_{o_3} - f_{o_1}$ planes are depicted in Figure 5.14(a), (b), and (c), respectively. As explained in section 3, f_{o_1}, f_{o_2}, and f_{o_3} are the objectives associated

with the generation set-point mismatch, total generation set-point mismatch, and voltage set-point mismatch, correspondingly, and were calculated using (3.10)-(3.12). To obtain the Pareto optimal front shown in this figure, the GA evaluated many solutions during its generations. The evaluated solutions are also depicted in this figure. As explained earlier, for each of these solutions, a TSAT simulation was conducted to evaluate the operating and security constraints. The Pareto optimal front in this case contained 149 Pareto solutions. From among these solutions, the best compromise solution was picked, using the fuzzy membership method. The objective values for the best compromise solution are also shown in this figure.

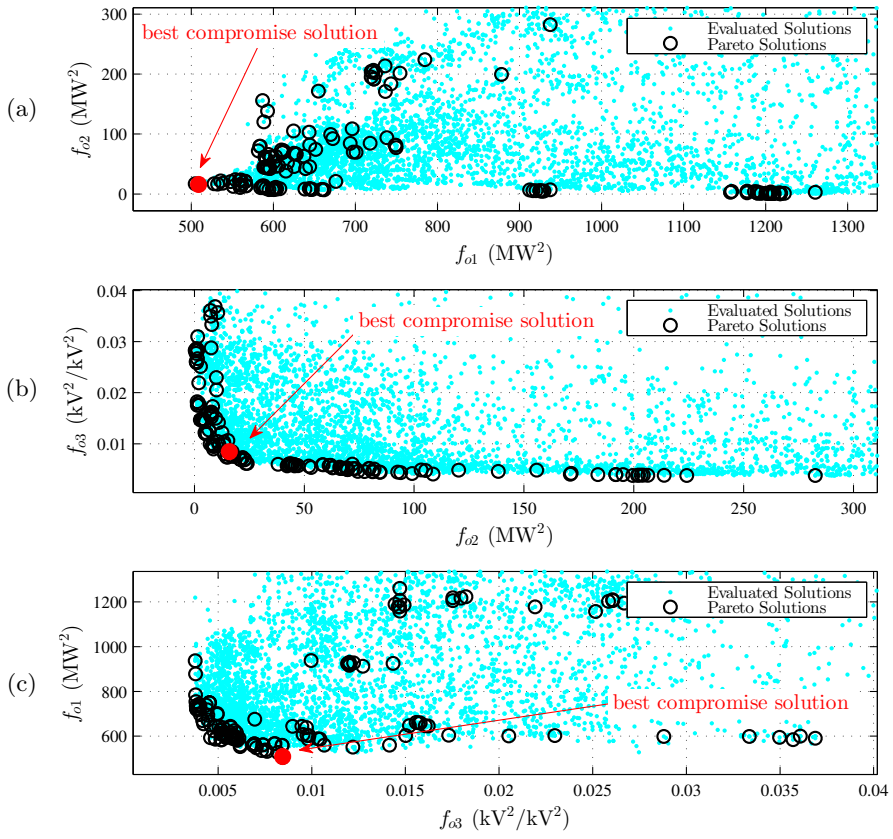

Figure 5.14: Pareto optimal front (case II). a) $f_{o_1} - f_{o_2}$ plane, b) $f_{o_2} - f_{o_3}$ plane, and c) $f_{o_3} - f_{o_1}$ plane

From Figure 5.14, it can be seen that f_{o_1} varied from 505 to 1262 MW^2. Also, f_{o_2} varied from 0.366 to 283 MW^2, and f_{o_3} changed in 5e-06 to 0.1087 pu^2 range. The difference in the order of magnitude between f_{o_1}, f_{o_2}, and f_{o_3} shows the importance of keeping the three objectives separate, as opposed to integrating them together using some weighting factors, which was discussed in section 3. From Figure 5.5, it can also be observed that the three objectives of the best compromise solution were $f_{o_1} = 508.8\text{MW}^2$, $f_{o_2} = 15.9\text{MW}^2$, and $f_{o_3} = 0.0084\text{pu}^2$.

The adjusted P_{MTG1} and P_{MTG2} set-points of the best compromise solution are listed in Table 5.3. In this table, the second row shows the DGD power set-points for MTG1 for the five decision intervals, $l = 1, ..., 5$, and the third row shows the ISCPM adjusted power set-points for MTG1 for the five decision intervals. Similarly, the next two rows show unadjusted and adjusted set-point values for MTG2. As explained earlier, P_{ATG1} and P_{ATG2} did not participate in power set-point adjustment and were constant at 1MW during the study period. In this table, the set-points with and without adjustment are compared, in each of the five decision intervals. MTG power set-points, with and without use of ISCPM method, are also shown and compared in Figure 5.15. Figure 5.15(a) shows the forecasted and measured power from PSCAD simulation for the pulse load, and Figure 5.15(b) shows the forecasted power and the measured power for one of the propulsion motors (the powers for the two propulsion motors were the same). Also, Figures 5.15(c) and (d) show the MTG1 and MTG2 power set-points, respectively, with and without use of ISCPM method.

Table 5.3: Generator power set-points with and without use of ISCPM method (case II)

interval no, l	$l = 1$	$l = 2$	$l = 3$	$l = 4$	$l = 5$
$P^*_{MTG1}(l)$	20.13 MW	25.14 MW	30.16 MW	30.16 MW	30.16 MW
$\hat{P}_{MTG1}(l)$	19.37 MW	21.49 MW	19.83 MW	19.96 MW	20.01 MW
$P^*_{MTG1}(l)$	16.00 MW	16.00 MW	21.00 MW	21.00 MW	21.00 MW
$\hat{P}_{MTG1}(l)$	16.40 MW	18.46 MW	26.68 MW	27.19 MW	26.73 MW

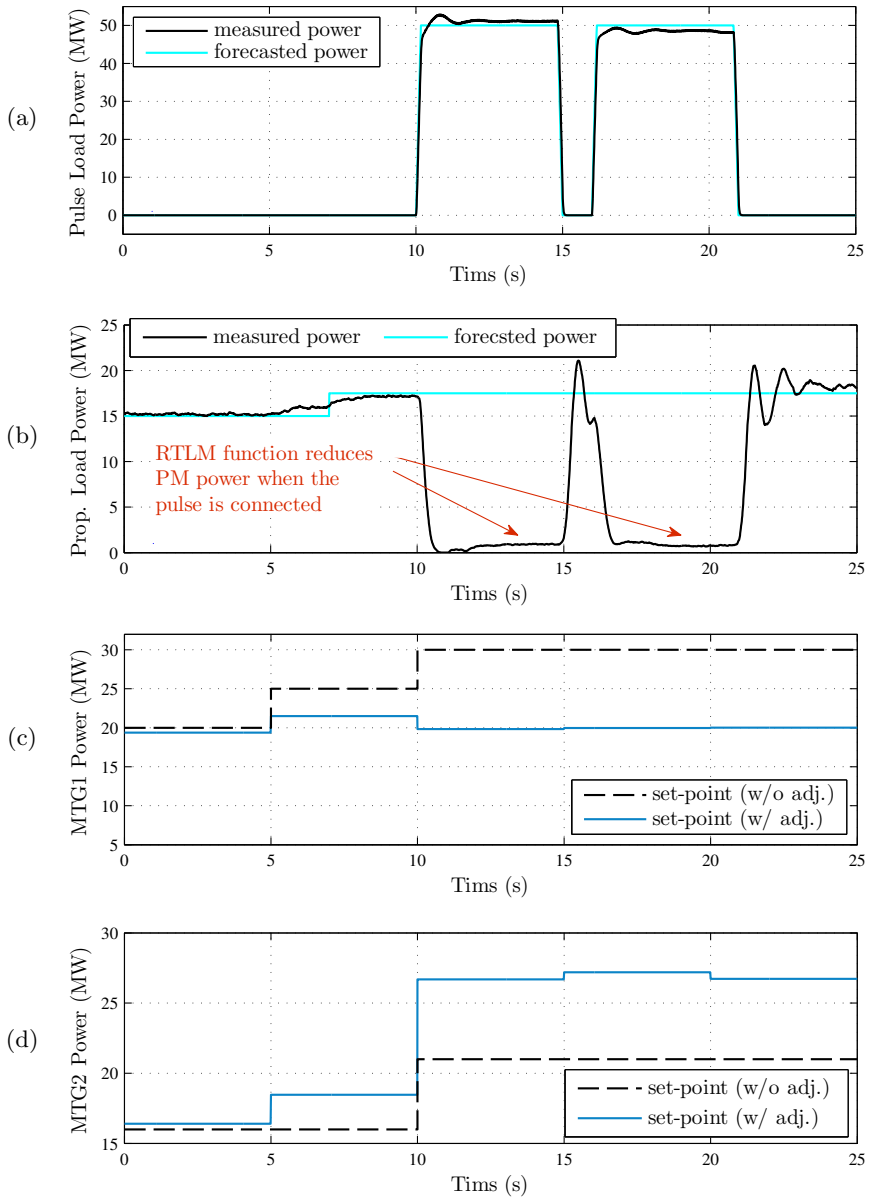

Figure 5.15: Comparison of the generator power set-points with and without use of ISCPM method (case II). a) forecasted and measured pulse load power, b) forecasted and measured propulsion load power, c) MTG1 power set-points with and without ISCPM method, and d) MTG2 power set-points with and without ISCPM method

From Table 5.3 and Figure 5.15, it can be observed that the ISCPM method decreased MTG1 power set-point and increased MTG2 power set-point, in decision intervals 2-5. The adjustments in generator power set-points resulted in alleviating the security constraint violations, as shown in Figure 5.16. The system trajectory obtained from the PSCAD simulation with the ISCPM set-points is depicted in Figure 5.16. In this figure, x and y axes are two critical parameters and show the total load in the system and the total power of MTG2 and ATG2, respectively. To obtain the system trajectory shown in this figure, generator and load terminal powers obtained from the PSCAD simulation were used. This figure shows that the system trajectory during [0,25s]. Several points on the trajectory are time stamped. It can be observed that the system trajectory remained inside the DSR (left hand side of the border) for the entire study period. Hence, the violation of the dynamic security constraints against contingencies was alleviated, when the ISCPM adjusted set-points were used.

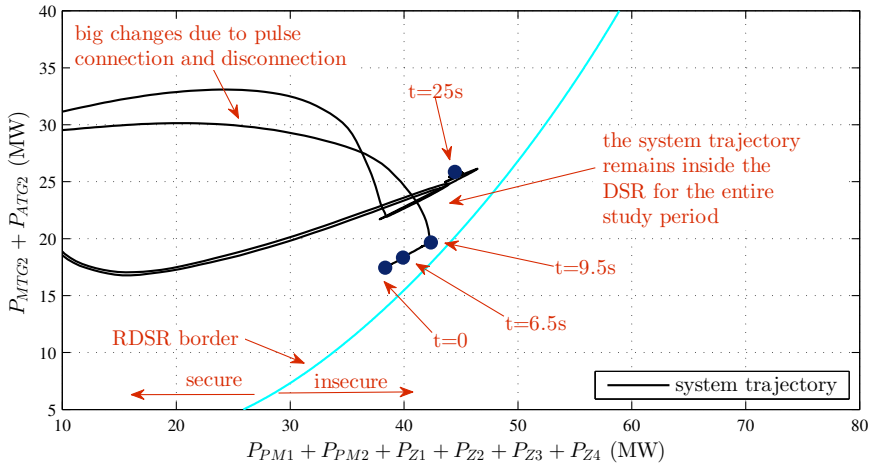

Figure 5.16: System trajectory in the critical parameter space, in the system response to the ISCPM set-points (case II)

Table 5.5 shows that the generator power adjustment was conducted such that the total generation in decision intervals 3-5 was reduced by 4.6MW, 4.0MW, and 4.4MW,

respectively. The reduction in the total generation power in the system during these decision intervals reduced the frequency overshoot caused by the disconnection of the pulse load at 15s and 21s. Frequency response of the system to the adjusted set-points is depicted in Figure 5.17. As shown in this figure, system frequency remained under 62.4Hz during the [0,25s] study period. Therefore, the frequency operating constraint violation was alleviated.

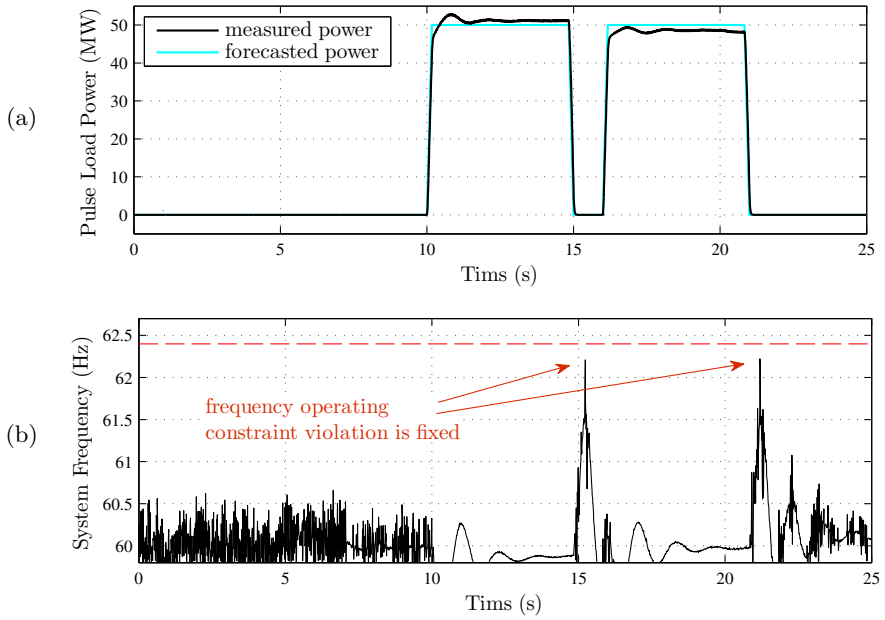

Figure 5.17: Frequency in the system response to the ISCPM set-points (case II). a) pulse load power, and b) system frequency

The adjusted generator and DSTATCOM voltage set-points of the best compromise solution are listed in Table 5.4. In this table, the second row shows MTG1 voltage set-points from the DVC method for any of the five decision intervals, and the third row lists the adjusted ISCPM voltage set-points for MTG1. Similarly, the following rows show the DVC and ISCPM voltage set-points for ATG1, MTG2, ATG2, and DSTATCOM, for the five decision intervals. As an example, DSTATCOM voltage set-points, with and without use of ISCPM method, are also shown in Figure 5.18. In Figure 5.18, DVC and ISCPM voltage

set-points for the DSTATCOM are shown with dashed and solid black lines, respectively. Moreover, DSTATCOM terminal voltage, obtained from the PSCAD simulation, is plotted with the lighter solid line.

Table 5.4: Voltage set-points with and without use of ISCPM method (case II)

interval no, m	$m=1$	$m=2$	$m=3$	$m=4$	$m=5$
$V^*_{MTG1}(m)$	0.9690 pu	0.9690 pu	0.9700 pu	0.9700 pu	0.9700 pu
$\hat{V}_{MTG1}(m)$	0.9720 pu	0.9840 pu	1.0051 pu	0.9796 pu	0.9752 pu
$V^*_{ATG1}(m)$	0.9682 pu	0.9682 pu	0.9692 pu	0.9692 pu	0.9692 pu
$\hat{V}_{ATG1}(m)$	0.9712 pu	0.9832 pu	1.0043 pu	0.9788 pu	0.9744 pu
$V^*_{MTG2}(m)$	0.9690 pu	0.9690 pu	0.9700 pu	0.9700 pu	0.9700 pu
$\hat{V}_{MTG2}(m)$	0.9720 pu	0.9840 pu	1.0051 pu	0.9796 pu	0.9752 pu
$V^*_{ATG2}(m)$	0.9682 pu	0.9682 pu	0.9692 pu	0.9692 pu	0.9692 pu
$\hat{V}_{ATG2}(m)$	0.9712 pu	0.9832 pu	1.0043 pu	0.9788 pu	0.9744 pu
$V^*_{DSAT}(m)$	0.9525 pu	0.9525 pu	0.9535 pu	0.9535 pu	0.9535 pu
$\hat{V}_{DSAT}(m)$	0.9555 pu	0.9672 pu	0.9880 pu	0.9630 pu	0.9586 pu

It was shown in Figure 5.13(c) that when the DGD and DVC set-points were used, propulsion load terminal voltages dropped below 0.95pu in decision intervals 2-4. From Table 5.4 and Figure 5.18(b), it can be observed that the ISCPM method increased voltage set-points, mainly in these decision intervals, in order to alleviate voltage operating constraint violation. In Figure 5.18(b), it can be observed that the DSTATCOM terminal voltage could not track its set-point, in during 10s-15s and 16s-21s, in which the pulses were connected. The DSTATCOM could not track its set-point, since it reactive power output had reached its maximum value, 5MVAr, during the time the pulse was connected, as shown in Figure 5.18(c). Figure 5.18(c) shows DSTATCOM reactive power output, when the adjusted set-points were applied to the system. These ISCPM set-point adjustments alleviated the voltage operating constraint violation. Figure 5.19 shows propulsion and pulse load terminal voltages during the study period, if the adjusted set-points were used. It can be observed that the voltage operating constraint violation was alleviated, since the voltages remained below 0.95pu for less than 2s.

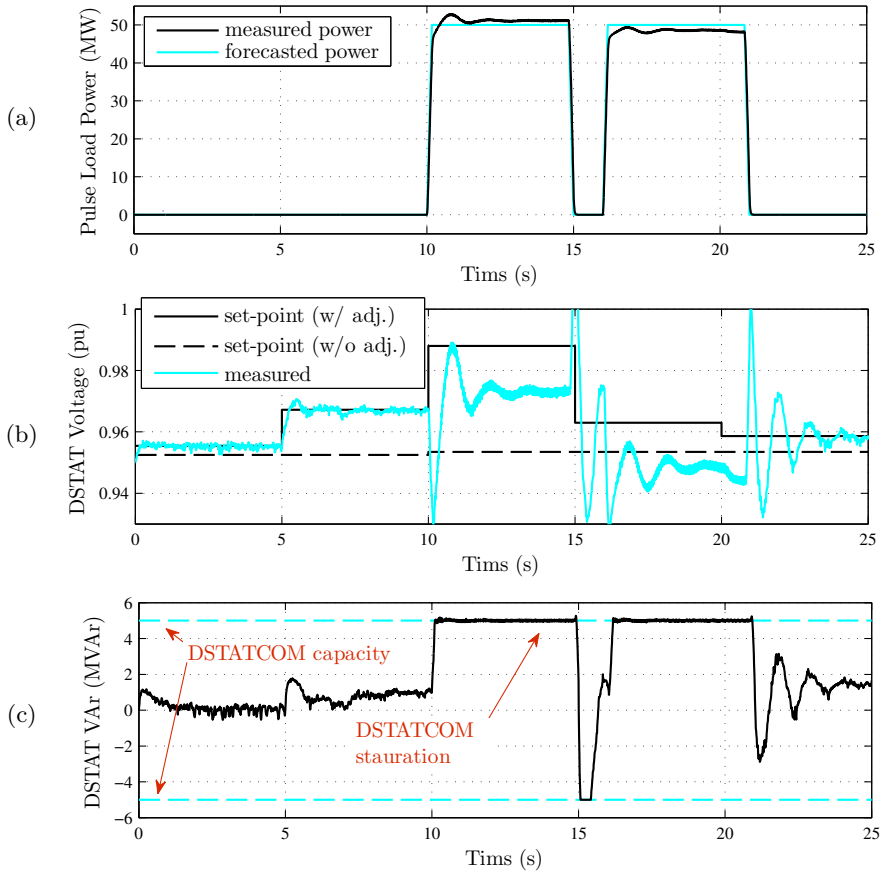

Figure 5.18: DTSTACOM voltage and reactive power in the system response to the ISCPM set-points (case II). a) pulse load power, b) DSTATCOM voltage set-points with and without use of ISCPM method, b) DSTATCOM reactive power

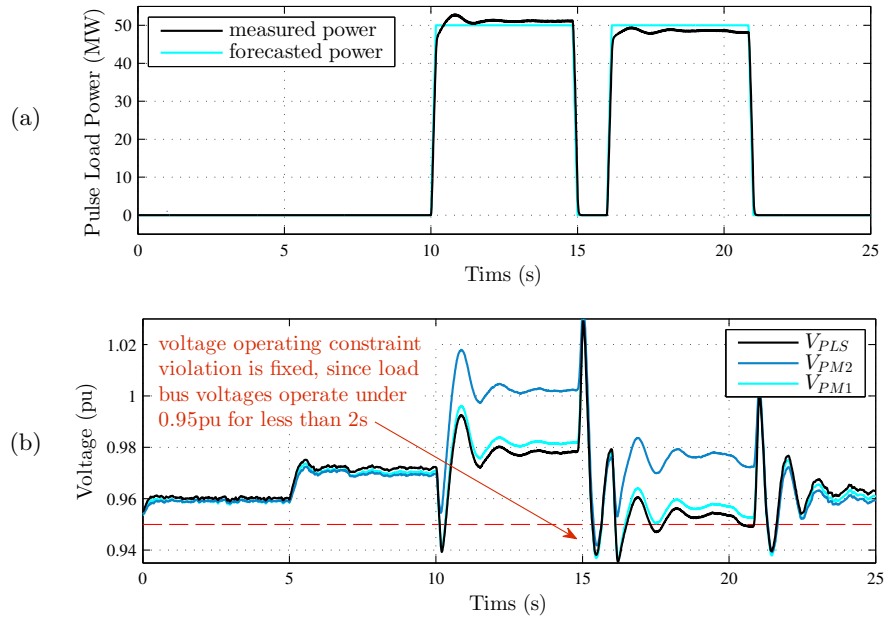

Figure 5.19: Propulsion and pulse load terminal voltages in the system response to the ISCPM set-points (case II). a) pulse load power, and b) propulsion and pulse load terminal voltages

In summary, connection of two 50MW back to back pulses to the system was studied in this case. It was observed that if the set-points provided by the dynamic generation dispatch and dynamic voltage/VAr control methods were used, the system operated outside of the DSR during some periods. Moreover, it was observed that frequency and load bus voltage operating constraints were violated, if the DGD and DVC set-points were used. Next, the ISCPM method was used for the same propulsion and pulse load changes. The PSCAD simulation results, when the adjusted power and voltage set-points were used, showed that both of the constraint violations were alleviated.

5.2.3 Case III: Main Turbine Generator Outage

In case III, performance of the ISCPM method during planned outage of MTG1 is discussed. The main purpose of the study was to illustrate how the ISCPM method could prevent operating constraint violations, when significant generation changes are planned to happen in the system. In this case, the study period was $T = 25$ seconds and the simulation

duration was also 25s. The decision intervals for the Dynamic Generation Dispatch (DGD) and the Dynamic Voltage/VAr Control (DVC) methods were $\tau_g = 5$ and $\tau_q = 5$ seconds, respectively. Therefore, the study period included $n_{\tau_g} = 5$ decision intervals for the DGD method and $n_{\tau_q} = 5$ decision intervals for the DVC method.

The system was initially ($t = 0$s) operating with 38MW load which was composed of 2×15MW propulsion loads and 4×2MW zonal total loads. The set-points provided by the DGD to serve the loads plus losses for MTG1, ATG1, MTG2, and ATG2 were 20.13MW, 1MW, 16MW, and 1MW, respectively. The MTG1 was the system slack generator and its power set-point was fine tuned by its governor to maintain the system frequency. The DVC voltage set-points for the generators were 0.9690pu, 0.9682pu, 0.9690pu, and 0.9682pu, correspondingly. Moreover, the DVC voltage set-point for the DSTATCOM was 0.9525pu. The power of each propulsion motor was forecasted to increase by 2.5MW at 7s. To serve the 5MW increase in total system load at 7s, the dynamic generation dispatch method increased MTG1 power set-point by 5MW in the second decision interval, from $t = 5$s. Also, MTG1 was planned to be disconnected from the system at 10s, and MTG2 power set-point was planned to be increased at 15s, to compensate for MTG1 outage. Therefore, DGD power set-points for the generators were assumed to be $P^*_{G_1}(1) = 20.13$MW, $P^*_{G_1}(2) = 25.14$MW, $P^*_{G_1}(3) = 0$MW, $P^*_{G_1}(4) = 0$MW, $P^*_{G_1}(5) = 0$MW, $P^*_{G_3}(1) = 16$MW, $P^*_{G_3}(2) = 16$MW, $P^*_{G_3}(3) = 16$MW, $P^*_{G_3}(4) = 36$MW, and $P^*_{G_3}(5) = 36$MW. It was also assumed that the dynamic voltage/VAr control method increased all of the voltage set-points by 0.1% starting from the third decision interval at $t = 10$s, in order to compensate for the voltage drop caused by MTG1 outage. As an example, the DVC voltage set-points for the DSTATCOM, the fifth voltage-controlled device in the system, were $V^*_{Q_5}(1) = 0.9525$pu, $V^*_{Q_5}(2) = 0.9525$pu, $V^*_{Q_5}(3) = 0.9535$pu, $V^*_{Q_5}(4) = 0.9535$pu, and $V^*_{Q_5}(5) = 0.9535$pu.

To determine the operating or security constraint violations that may occur, if the DGD and DVC set-points, $P^*_{G_i}(l)$ and $V^*_{Q_j}(m)$, were used, a PSCAD simulation was conducted using these set-points. The system trajectory obtained from this PSCAD simulation is depicted in Figure 5.20. In this figure, x and y axes are two critical parameters and show

the total load in the system and the total power of MTG2 and ATG2. The details for obtaining the risk-based DSR, shown in this figure, was explained in subsection 4.4.4.2. It was explained that the system was secure against unplanned events, if the system trajectory remained on the left hand side of the security border. To obtain the system trajectory shown in this figure, generator and load terminal powers obtained from the PSCAD simulation were used. This figure shows that the system trajectory during [0,25s]. Several points on the trajectory are time stamped. Using this points, it can be seen that the system trajectory was initially inside the secure region. However, it moved outside of the secure region, when the propulsion power increased at $t = 7$s, and was outside of the DSR until $t = 10$s. Therefore, the security constraint against contingencies was violated, if the DGD and DVC set-points were used. Note that after MTG1 outage at 10s, the system DSR was not applicable anymore, since a system component was disconnected. In Figure 5.20, system trajectory before and after MTG1 outage are shown with thick and thin solid lines, respectively.

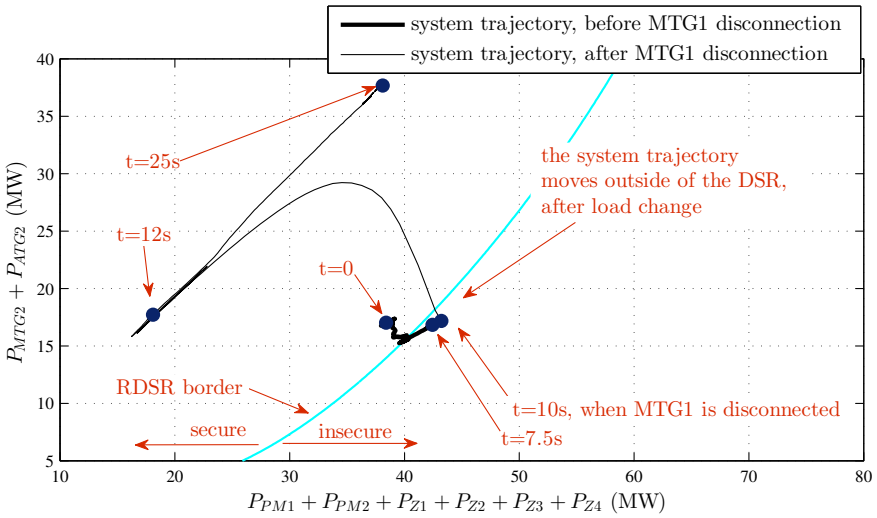

Figure 5.20: System trajectory in the critical parameter space, in the system response to the DGD and DVC set-points (case III)

The set-points provided by DGD and DVC methods also resulted in violation of the operating constraints on propulsion load terminal voltages. Figure 5.21 shows the voltage measured at propulsion and pulse load buses, P_{PM1}, P_{PM2}, and P_{PLS}, when the DGD and DVC set-points were applied to the system. It can be observed that the voltage at propulsion motor buses dropped below 0.95pu after the sharp increase and stayed there for more than 2s. Therefore, the operating constraint on load bus voltages was violated, when the DGD and DVC set-points were applied to the system.

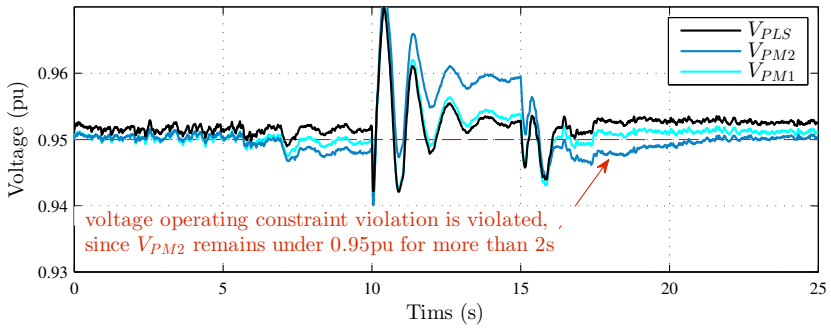

Figure 5.21: Propulsion and pulse load terminal voltages in the system response to the DGD and DVC set-points (case III)

Next, the ISCPM method was applied to the same propulsion load changes. The DGD and DVC set-points for the decision intervals during the [0,25s] study period were the inputs to the ISCPM method. In this study, it was assumed that P_{ATG1} and P_{ATG2} did not participate in power set-point adjustment. The NSGA-II solved the multi-objective optimization problem and obtained a Pareto optimal front. This Pareto front is shown in Figure 5.22. Instead of a 3D plot, the projection of the Pareto optimal front on $f_{o_1} - f_{o_2}$, $f_{o_2} - f_{o_3}$, and $f_{o_3} - f_{o_1}$ planes are depicted in Figure 5.22(a), (b), and (c), respectively. As explained in section 3, f_{o_1}, f_{o_2}, and f_{o_3} are the objectives associated with the generation set-point mismatch, total generation set-point mismatch, and voltage set-point mismatch, correspondingly, and were calculated using (3.10)-(3.12). To obtain the Pareto optimal front shown in this figure, the GA evaluated many solutions during its

generations. The evaluated solutions are also depicted in this figure. As explained earlier, for each of these solutions, a TSAT simulation was conducted to evaluate the operating and security constraints. The Pareto optimal front in this case contained 188 Pareto solutions. From among these solutions, the best compromise solution was picked, using the fuzzy membership method. The objective values for the best compromise solution are also shown in this figure.

To alleviate the security and operating constraint violations, the ISCPM method was used. Figure 5.22 shows the projection of the obtained Pareto optimal front on $f_{o_1} - f_{o_2}$, $f_{o_2} - f_{o_3}$, and $f_{o_3} - f_{o_1}$ planes. Some of the solutions evaluated during the generation of the GA are also shown in this figure. The Pareto optimal front in this case contained 94 Pareto solutions. From among these solutions, the best compromise solution was picked, using the fuzzy membership method. The best compromise solution is also shown in Figure 5.22.

From Figure 5.22, it can be seen that the objective f_{o_1} varied from 6 to 320 MW^2, f_{o_2} from 0.2 321 MW^2, and f_{o_3} from 3E-6 to 0.0551 in the Pareto solutions, respectively. The difference in the order of magnitude of f_{o_1}, f_{o_2}, and f_{o_3} shows the importance of keeping the three objectives separate, as opposed to integrating them together using some weighting factors, which was discussed in section 3. From Figure 5.22, it can also be observed that the three objectives of the best compromise solution were $f_{o_1} = 6.6\text{MW}^2$, $f_{o_2} = 4.3\text{MW}^2$, and $f_{o_3} = 0.0090\text{pu}^2$.

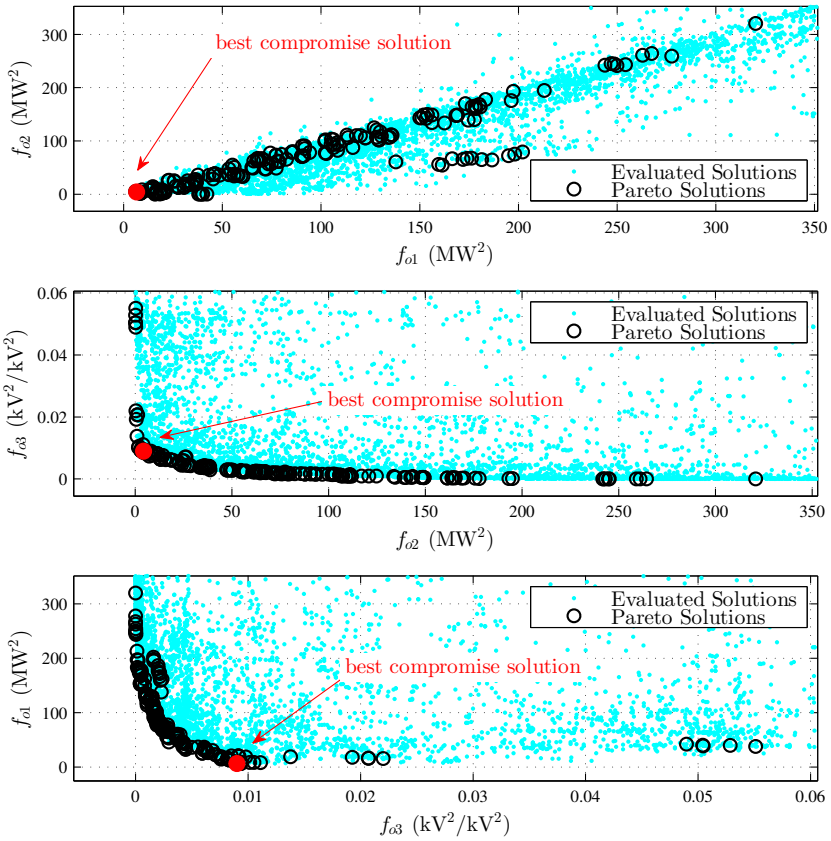

Figure 5.22: Pareto optimal front (case III). a) $f_{o_1} - f_{o_2}$ plane, b) $f_{o_2} - f_{o_3}$ plane, and c) $f_{o_3} - f_{o_1}$ plane

The adjusted P_{MTG1} and P_{MTG2} set-points of the best compromise solution are listed in Table 5.5. In this table, the second row shows the DGD power set-points for MTG1 for the five decision intervals, $l = 1, ..., 5$, and the third row shows the ISCPM adjusted power set-points for MTG1 for the five decision intervals. Similarly, the next two rows show unadjusted and adjusted set-point values for MTG2. As explained earlier, P_{ATG1} and P_{ATG2} did not participate in power set-point adjustment and were constant at 1MW during the study period. In this table, the set-points with and without adjustment are compared, in each of the five decision intervals. MTG power set-points, with and without ISCPM adjustments, are also shown in Figure 5.23. Figures 5.23(a) and (b) show the MTG1 and MTG2 power set-points, respectively, with and without ISCPM adjustments.

Table 5.5: Generator power set-points with and without use of ISCPM method (case III)

interval no, l	$l=1$	$l=2$	$l=3$	$l=4$	$l=5$
$P^{*}_{MTG1}(l)$	20.13 MW	25.14 MW	0.00 MW	0.00 MW	0.00 MW
$\hat{P}_{MTG1}(l)$	19.57 MW	23.08 MW	0.00 MW	0.00 MW	0.00 MW
$P^{*}_{MTG2}(l)$	16.00 MW	16.00 MW	16.00 MW	36.00 MW	36.00 MW
$\hat{P}_{MTG2}(l)$	15.23 MW	16.77 MW	15.74 MW	34.91 MW	35.48 MW

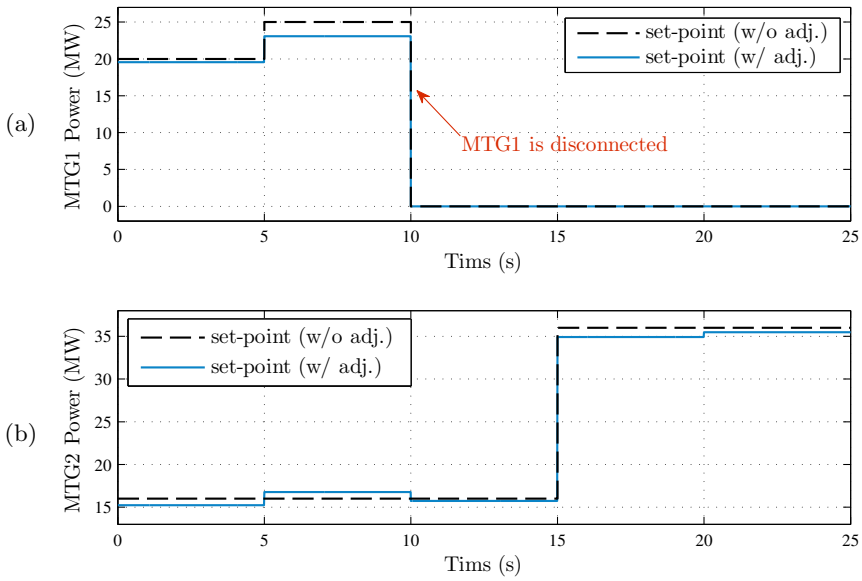

Figure 5.23: Comparison of the generator power set-points with and without use of ISCPM method (case III). a) MTG1 power set-points, and b) MTG2 power set-points

From Table 5.5 and Figure 5.23, it can be observed that the main adjustments to the power set-points happened in the seconds decision interval, in which MTG1 power set-point was decreased and MTG2 power set-point was increased. The shift in generator power set-points made the system secure against unplanned events, since it caused the system trajectory to remain inside the secure region for during the [0,10s] period. Note that the system DSR was not applicable in the [10s,25s] period, since MTG1 was disconnected from the system.

The system trajectory obtained from the PSCAD simulation with the ISCPM set-points is depicted in Figure 5.24. In this figure, x and y axes are two critical parameters and show the total load in the system and the total power of MTG2 and ATG2, respectively. To obtain the system trajectory shown in this figure, generator and load terminal powers obtained from the PSCAD simulation were used. This figure shows that the system trajectory during [0,25s]. Several points on the trajectory are time stamped. It can be observed that the system trajectory remained inside the DSR (left hand side of the border) for the entire study period. Hence, the violation of the dynamic security constraints against contingencies was alleviated, when the ISCPM adjusted set-points were used.

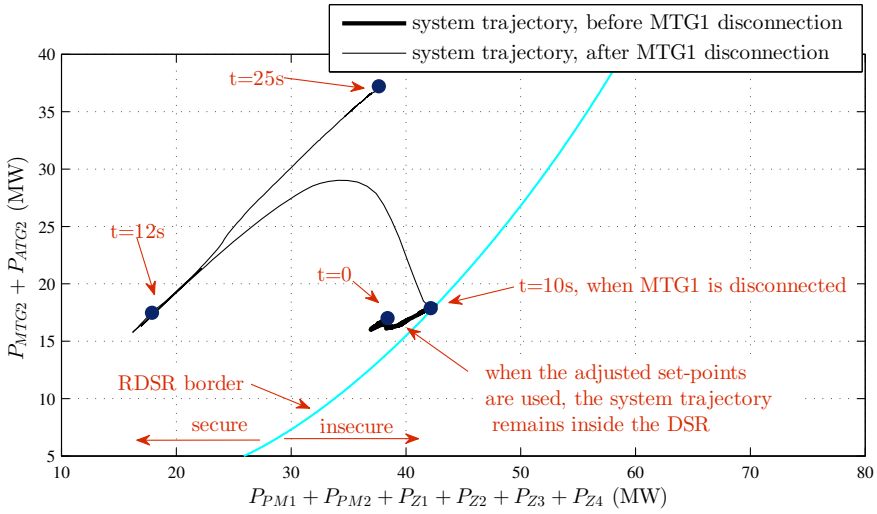

Figure 5.24: System trajectory in the critical parameter space, in the system response to the ISCPM set-points (case III)

Figure 5.25 compares the total planned generator power and the total load plus loss in the system, when the ISCPM adjusted set-points were used. Figure 5.25 shows the total planned generator power (summation of the generator power set-points). This figure also depicts the total load plus loss in the system, obtained from the PSCAD simulation. It can be observed that the total load plus loss was always less than the total planned generation

power, during the [0,25s] study period.

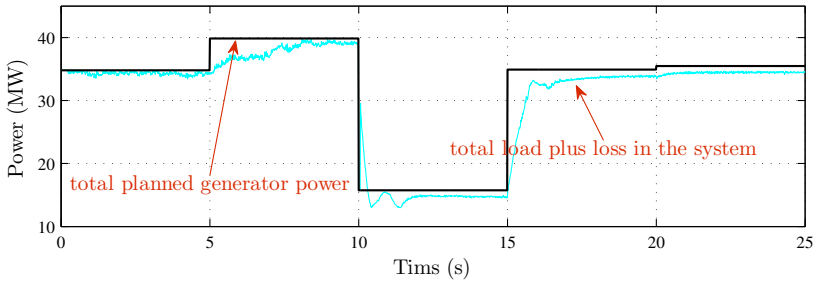

Figure 5.25: Total generator power and total load plus loss in the system response to the ISCPM set-points (case III)

Figure 5.26 shows the power of a propulsion motor in this case. It can be observed that when MTG1 was disconnected at 10s, the real-time load management method reduced propulsion power, to compensate for the generation reduction. When MTG2 power was increased at 15s, the real-time load management method increased the propulsion power. However, since there was not enough generation, propulsion motor powers were smaller than the reference value.

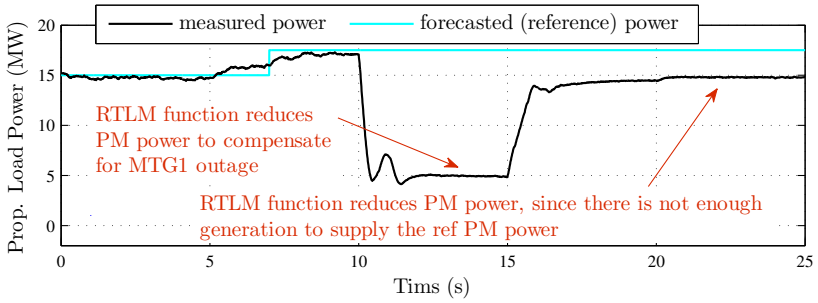

Figure 5.26: Propulsion load power in the system response to the ISCPM set-points (case III)

The adjusted generator and DSTATCOM voltage set-points of the best compromise solution are listed in Table 5.6. In this table, the second row shows MTG1 voltage set-points

from the DVC method for any of the five decision intervals, and the third row lists the adjusted ISCPM voltage set-points for MTG1. Similarly, the following rows show the DVC and ISCPM voltage set-points for ATG1, MTG2, ATG2, and DSTATCOM, for the five decision intervals. As an example, DSTATCOM voltage set-points, with and without use of ISCPM method, are also shown in Figure 5.27. In Figure 5.27, DVC and ISCPM voltage set-points for the DSTATCOM are shown with dashed and solid black lines, respectively. Moreover, DSTATCOM terminal voltage, obtained from the PSCAD simulation, is plotted with the lighter solid line.

Table 5.6: Voltage set-points with and without use of ISCPM method (case III)

interval no, m	$m = 1$	$m = 2$	$m = 3$	$m = 4$	$m = 5$
$V^*_{MTG1}(m)$	0.9690 pu	0.9690 pu	0.9700 pu	0.9700 pu	0.9700 pu
$\hat{V}_{MTG1}(m)$	0.9690 pu	0.9741 pu	0.9704 pu	1.0106 pu	0.9756 pu
$V^*_{ATG1}(m)$	0.9682 pu	0.9682 pu	0.9692 pu	0.9692 pu	0.9692 pu
$\hat{V}_{ATG1}(m)$	0.9682 pu	0.9733 pu	0.9696 pu	1.0097 pu	0.9748 pu
$V^*_{MTG2}(m)$	0.9690 pu	0.9690 pu	0.9700 pu	0.9700 pu	0.9700 pu
$\hat{V}_{MTG2}(m)$	0.9690 pu	0.9741 pu	0.9704 pu	1.0106 pu	0.9756 pu
$V^*_{ATG2}(m)$	0.9682 pu	0.9682 pu	0.9692 pu	0.9692 pu	0.9692 pu
$\hat{V}_{ATG2}(m)$	0.9682 pu	0.9733 pu	0.9696 pu	1.0097 pu	0.9748 pu
$V^*_{DSAT}(m)$	0.9525 pu	0.9525 pu	0.9535 pu	0.9535 pu	0.9535 pu
$\hat{V}_{DSAT}(m)$	0.9525 pu	0.9575 pu	0.9539 pu	0.9933 pu	0.9590 pu

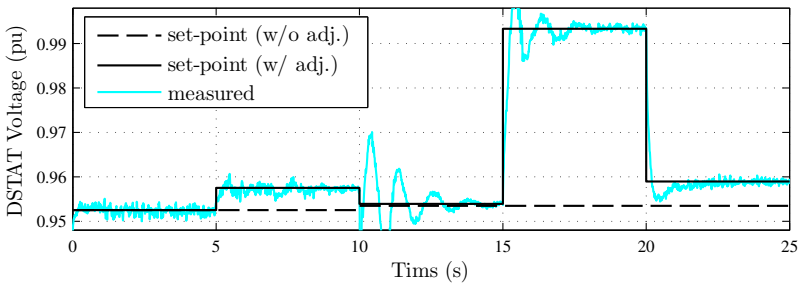

Figure 5.27: Voltage set-points with and without use of ISCPM method (case III)

It was shown in Figure 5.21 that load bus voltages dropped below 0.95pu, if the DGD and DVC set-points were used. The drops happened mainly in decision intervals two and four, where propulsion load was increased and when MTG2 power was increased, respectively. From Table 5.6 and Figure 5.27, it can be observed that the ISCPM method increased voltage set-points in these two decision intervals, in order to alleviate the propulsion load terminal voltage constraint violation. Figure 5.28 shows PM1, PM2, and DSTATCOM (pulse load) terminal voltages obtained from the PSCAD simulation, when the adjusted ISCPM set-points were used. It can be observed that the voltage operating constraint violation was alleviated, since the load bus voltages remained below 0.95pu for less than 2s.

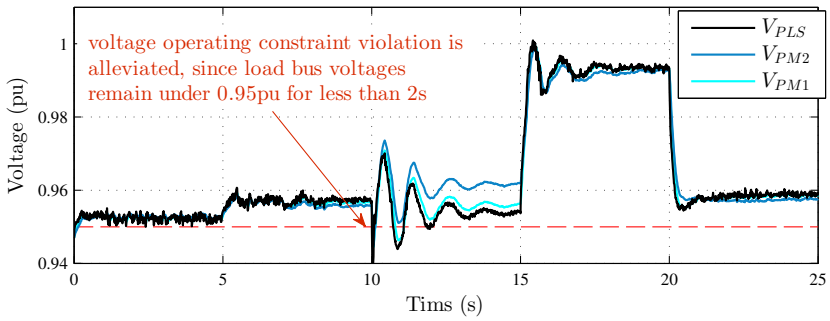

Figure 5.28: Propulsion and pulse load terminal voltages, in the system response to the ISCPM set-points (case III)

In summary, a planned MTG outage was studied in this case. It was observed that if the set-points provided by the dynamic generation dispatch and dynamic voltage/VAr control methods were used, the system operated outside of the system DSR during some periods. Moreover, it was observed that in the system response to these set-points, propulsion load terminal voltage operating constraint was violated. Next, the the ISCPM method was used for the same planned events. The PSCAD simulation results, when the ISCPM power and voltage set-points were used, showed that both of the constraint violations were alleviated.

5.2.4 Case IV: Zonal Load Change and Pulse Load

In case IV, performance of the new ISCPM method during several zonal load changes and pulse load uses in the notional all-electric ship was studied. The main purpose of the study was to illustrate how the ISCPM method works, when the loads inside the DC zones change. Moreover, this study shows how the ISCPM method works for back to back study periods, since in this study the simulation length is longer than the ISCPM study period. In this case, the study period was $T = 15$ seconds and the simulation duration was 30s. As a result, the simulation included two ISCPM study periods. The decision intervals for the Dynamic Generation Dispatch (DGD) and the Dynamic Voltage/VAr Control (DVC) methods were $\tau_g = 5$ and $\tau_q = 5$ seconds, respectively. Therefore, each study period included $n_{\tau_g} = 3$ decision intervals for the DGD method and $n_{\tau_q} = 3$ decision intervals for the DVC method.

In this study, MTG1 and MTG2 were not connected to the system. The system was initially ($t = 0$s) operating with 2MW load which was composed of 4×0.5MW zonal loads. The set-points provided by the DGD to serve the loads plus losses for ATG1 and ATG2 were 1.1MW and 1MW, respectively. The ATG1 was the system slack generator and its power set-point was fine tuned by its governor to maintain the system frequency. The DVC voltage set-points for the generators were 0.955pu and 0.956pu, correspondingly. Moreover, the DVC voltage set-point for the DSTATCOM was 0.951pu.

For the first study period, the load forecast was as follows. The total power of each DC zone was forecasted to increase by 0.5MW at $t = 8$s, by another 0.5MW at $t = 8.5$s, and by another 0.45MW at $t = 9.0$. Hence, the total power of each zone was forecasted to be 0.5MW in $0< t <8$s, 1.0MW in $8\text{s}< t <8.5$s, 1.5MW in $8.5\text{s}< t <9.0$s, and 1.95MW in $9.0\text{s}< t <15$s, and 1.0MW in $23\text{s}< t <30$s. For this period, the DGD and DVC set-points were as follows. It was assumed the DGD method evenly distributed the load changes among the two ATGs, which means that the ATG power set-points were as follows: $P^*_{ATG1}(1) =$ 1.1MW, $P^*_{ATG1}(2) =$ 4.0MW, $P^*_{ATG1}(3) =$ 4.0MW, $P^*_{ATG2}(1) =$ 1.0MW, $P^*_{ATG2}(2) =$ 3.9MW, and $P^*_{ATG2}(3) =$ 3.9MW. Also, it was assumed that the DVC method increased

each of the voltage set-points in decision intervals two and three, by 0.1%, in order to compensate for the voltage drop caused by the load increase. As an example, the DVC voltage set-points for the DSTATCOM were $V^*_{DSTA}(1) = 0.9510$pu, $V^*_{DSTA}(2) = 0.9520$pu, and $V^*_{DSTA}(3) = 0.9520$pu.

To determine the operating constraint violations that may occur, if the DGD and DVC set-points were used, a PSCAD simulation was conducted using these set-points. It was observed that the set-points provided by the DGD and DVC methods resulted in violation of the operating constraints on system frequency and pulse load terminal voltage, as shown in Figure 5.29. Figure 5.29(a) shows the forecasted total power for each zone during the first study period. Figure 5.29(b) shows the system frequency during this study period, obtained from the PSCAD simulation. It can be observed that the frequency increased at 5s and started to decrease at 8s, when the zonal load power increased. This figure shows that the frequency was above 62.4Hz, which is the maximum acceptable frequency, and hence, the frequency constraint was violated. Figure 5.29(c) shows the voltage at the pulse load terminal, obtained from the PSCAD simulation. It can be observed that after the increase in the zonal loads, this voltage stayed below 0.95pu for more than 2s, which was a violation of the voltage operating constraint.

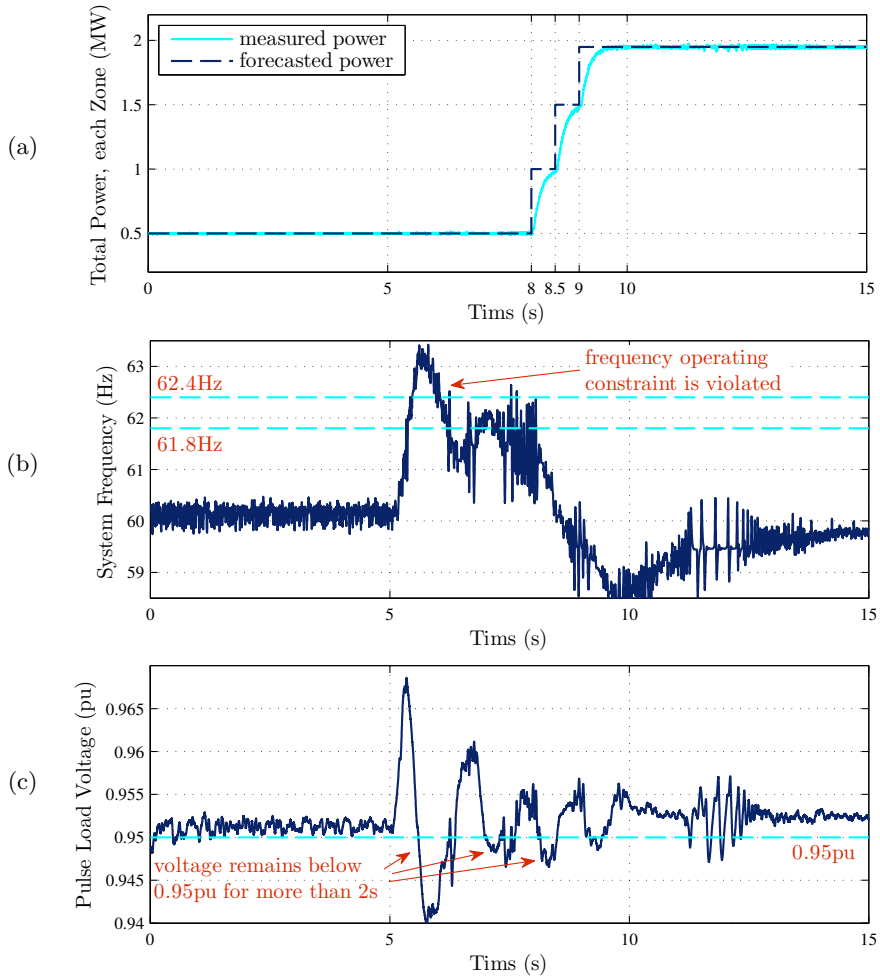

Figure 5.29: Violation of operating constraints in the system response to the DGD and DVC set-points (case IV, first study period). a) forecasted total power for each zone, b) system frequency, and c) pulse load terminal voltage

Next, the ISCPM method was applied to the same zonal load changes in the first study period. The DGD and DVC set-points for the decision intervals during the [0,15s] study period were the inputs to the ISCPM method. The NSGA-II solved the multi-objective optimization problem and obtained a Pareto optimal front. This Pareto front is shown in Figure 5.30. Instead of a 3D plot, the projection of the Pareto optimal front on $f_{o_1} - f_{o_2}$, $f_{o_2} - f_{o_3}$, and $f_{o_3} - f_{o_1}$ planes are depicted in Figure 5.30(a), (b), and (c), respectively. As explained in section 3, f_{o_1}, f_{o_2}, and f_{o_3} are the objectives associated with the generation

set-point mismatch, total generation set-point mismatch, and voltage set-point mismatch, correspondingly, and were calculated using (3.10)-(3.12). To obtain the Pareto optimal front shown in this figure, the GA evaluated many solutions during its generations. The evaluated solutions are also depicted in this figure. As explained earlier, for each of these solutions, a TSAT simulation was conducted to evaluate the operating constraints. From among the Pareto solutions, the best compromise solution was picked, using the fuzzy membership method. The best compromise solution is also shown in this figure. The three objectives of the best compromise solution were $f_{o_1} = 2.26\text{MW}^2$, $f_{o_2} = 4.50\text{MW}^2$, and f_{o_3} =2.4E-5pu^2.

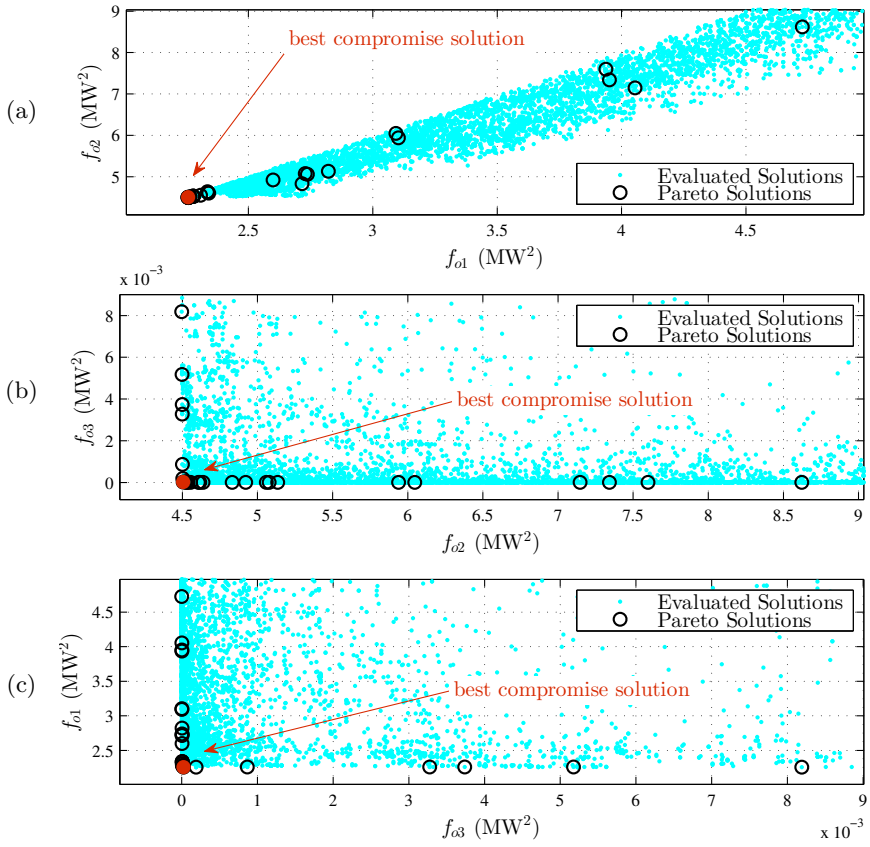

Figure 5.30: Pareto optimal front (case IV, first study period). a) $f_{o_1} - f_{o_2}$ plane, b) $f_{o_2} - f_{o_3}$ plane, and c) $f_{o_3} - f_{o_1}$ plane

The adjusted P_{ATG1} and P_{ATG2} set-points are listed in Table 5.7. In this table, the second row shows the DGD power set-points for ATG1 for the three decision intervals, $l = 1, 2, 3$, and the third row shows the ISCPM adjusted power set-points for ATG1 for these intervals. Similarly, the next two rows show unadjusted and adjusted set-point values for ATG2. ATG power set-points, with and without ISCPM adjustments, are also shown in Figure 5.31. Figure 5.31(a) shows the forecasted power and the measured power from PSCAD simulation for one of the DC zones. Also, Figures 5.31(b) and (c) show the ATG1 and ATG2 power set-points, respectively, with and without use of ISCPM method.

Table 5.7: Generator power set-points with and without use of ISCPM method (case IV, first study period)

interval no, l	$l = 1$	$l = 2$	$l = 3$
$P^*_{ATG1}(l)$	1.10 MW	4.00 MW	4.00 MW
$\hat{P}_{ATG1}(l)$	1.01 MW	2.91 MW	3.96 MW
$P^*_{ATG2}(l)$	3.90 MW	3.90 MW	3.90 MW
$\hat{P}_{ATG2}(l)$	0.98 MW	2.87 MW	3.82 MW

From Table 5.7 and Figure 5.31(b)-(c), it can be observed that the ISCPM method mainly decreased the ATG power set-points in the second decision interval. The reduction in ATG1 and ATG2 power set-points reduced the total power generation in the system, in the second decision interval. As a result, the real-time load management method reduced the total amount of loads connected in each zone. Figure 5.31(a) shows that the total zonal power was less than the forecasted value during 9s-10s. It was shown in Figure 5.29(b) that the frequency rose above 52.4Hz at 5s, when the DGD and DVC set-points were used. The ISCPM reduction alleviated this constraint violation, since the reduction in the total generation power in the second decision interval reduced the frequency overshoot at 5s, as shown in Figure 5.32. This figure shows the system frequency, obtained from PSCAD simulation, if the ISCPM set-points were used. It can be observed that the operating constraint on system frequency was satisfied, since system frequency never exceeded 62.4Hz and operated between 61.8Hz and 62.4Hz for less than 2s.

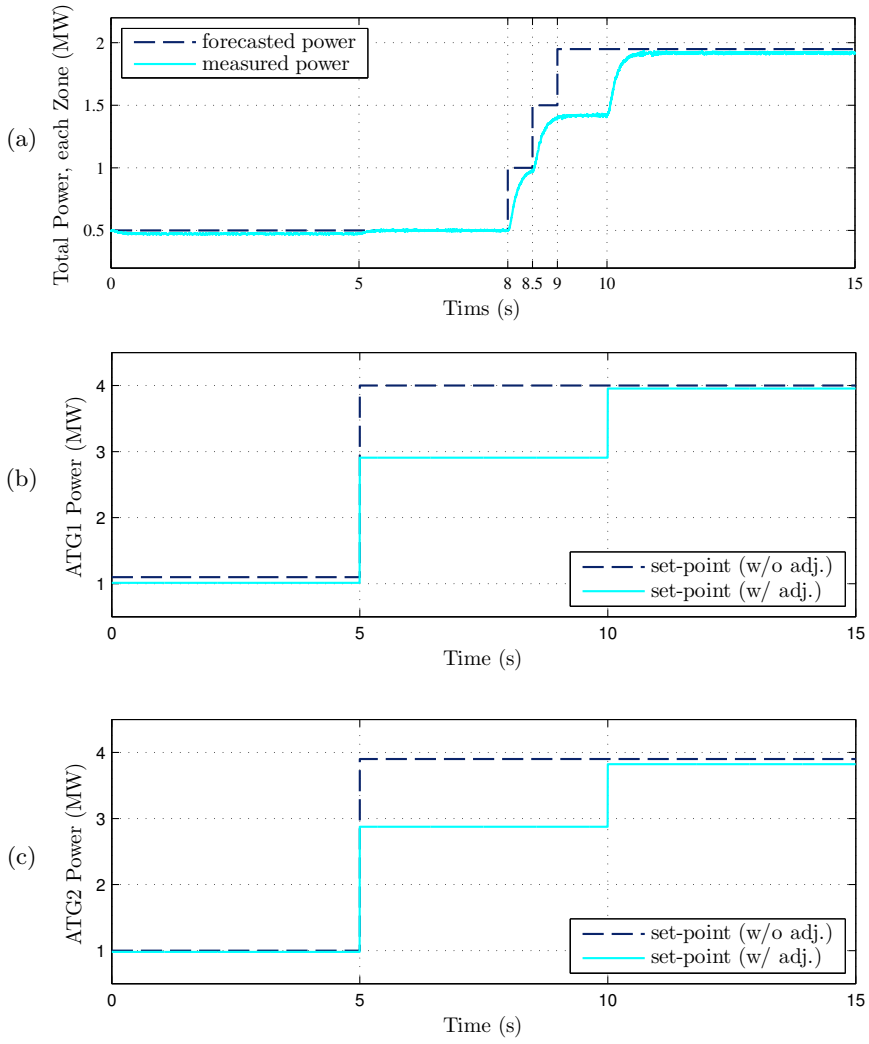

Figure 5.31: Comparison of the generator power set-points with and without use of ISCPM method (case IV, first study period). a) forecasted and measured total power a DC zone, b) ATG1 power set-point, and c) ATG2 power set-point

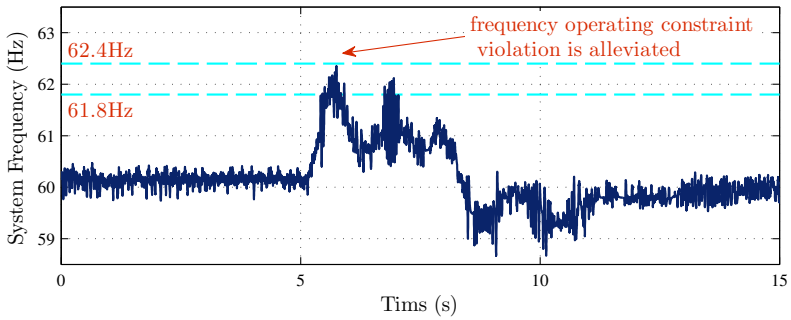

Figure 5.32: Frequency in the system response to the ISCPM set-points (case IV, first study period)

The adjusted generator and DSTATCOM voltage set-points of the best compromise solution are listed in Table 5.8. In this table, the second row shows ATG1 voltage set-points from the DVC method for any of the three decision intervals, and the third row lists the adjusted ISCPM voltage set-points for ATG1. Similarly, the following rows show the DVC and ISCPM voltage set-points for ATG2 and DSTATCOM, for the three decision intervals. As an example, DSTATCOM voltage set-points, with and without use of ISCPM method, are also depicted in Figure 5.33. Figure 5.33(a) shows the forecasted and measured total power for a DC zone. In Figure 5.33(b), DVC and ISCPM voltage set-points for the DSTATCOM are shown with dashed and solid black lines, respectively.

Table 5.8: Voltage set-points with and without use of ISCPM method (case IV, first study period)

interval no, m	$m=1$	$m=2$	$m=3$
$V^*_{ATG1}(m)$	0.9520 pu	0.9530 pu	0.9530 pu
$\hat{V}_{ATG1}(m)$	0.9521 pu	0.9524 pu	0.9548 pu
$V^*_{ATG2}(m)$	0.9530 pu	0.9540 pu	0.9540 pu
$\hat{V}_{ATG2}(m)$	0.9531 pu	0.9534 pu	0.9558 pu
$V^*_{DSTA}(m)$	0.9510 pu	0.9520 pu	0.9520 pu
$\hat{V}_{DSTA}(m)$	0.9511 pu	0.9514 pu	0.9538 pu

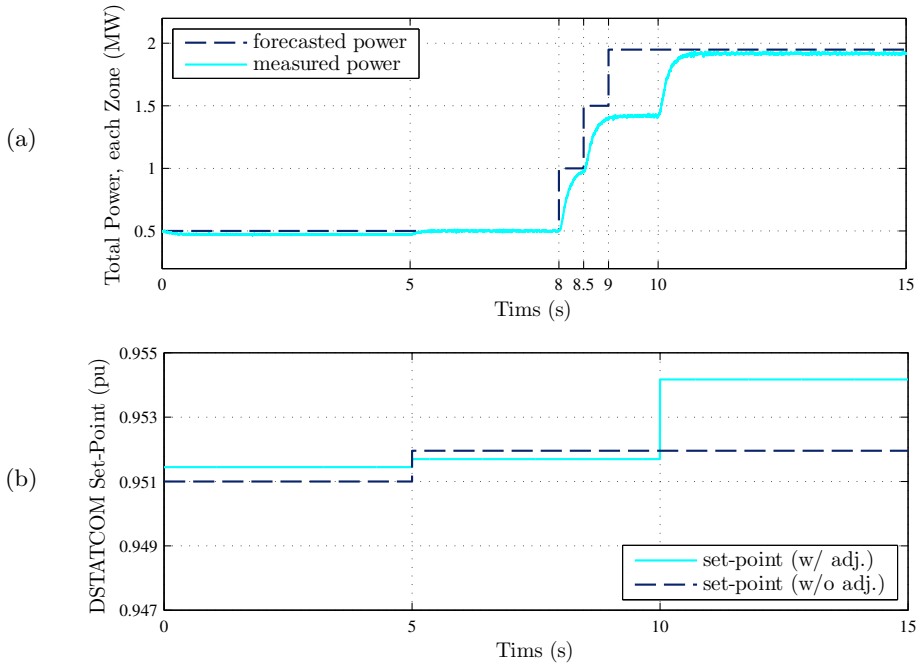

Figure 5.33: Comparison of DSTATCOM voltage set-points with and without use of ISCPM method (case IV, first study period). a) forecasted and measured total power a DC zone, and b) DSTATCOM voltage set-points

From Table 5.8 and Figure 5.33, it can be observed that the ISCPM method mainly increased the voltage set-points in the third decision interval. As shown in Figure 5.33(a), the zonal loads have their highest values during the study period, in this decision interval. The ISCPM adjustments to the DGD and DVC set-points alleviated the load voltage operating constraint violations. Figure 5.34 shows the pulse load terminal voltage, obtained from PSCAD simulation, if the ISCPM set-points were used. The dashed line in this figure shows 0.95pu limit, under which voltage cannot operate for more than 2s. The pulse load operated under 0.95pu voltage for 1.91s, and hence, the voltage operating constraint violation was alleviated.

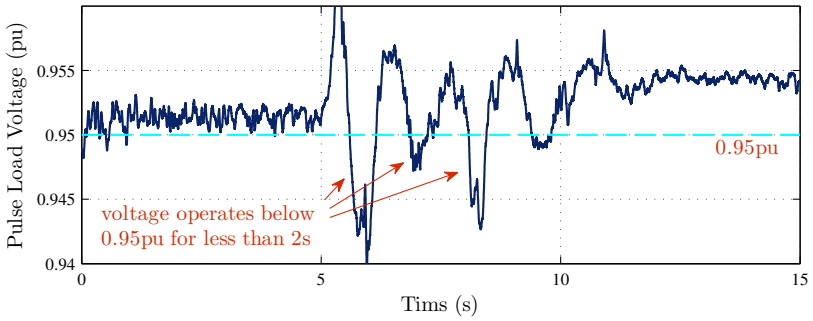

Figure 5.34: Pulse load terminal voltage in the system response to the ISCPM set-points (case IV, first study period)

For the second study period (15s$<t<$30s), a pulse with 4MW height was forecasted to be connected from 16s to 17s and from 18s to 19s. Also, a reduction from 1.95MW to 1.0MW at $t = 23$s was forecasted for the total power of each DC zone. It was assumed that the DGD power set-points for the second study period were as follows: $P^*_{ATG1}(4) = 4.0$MW, $P^*_{ATG1}(5) = 4.0$MW, $P^*_{ATG1}(6) = 2.1$MW, $P^*_{ATG2}(4) = 3.9$MW, $P^*_{ATG2}(5) = 3.9$MW, and $P^*_{ATG2}(6) = 2.0$MW. It was assumed that the DVC method increased the system voltage set-points by 0.15% in the decision interval in which the pulse load was connected. As an example, the DVC voltage set-points for the DSTATCOM in the second study period were $V^*_{DSTA}(4) = 0.9524$pu, $V^*_{DSTA}(5) = 0.9520$pu, and $V^*_{DSTA}(6) = 0.9510$pu.

To determine the operating constraint violations that may occur in the second study period, if the DGD and DVC set-points were used, a PSCAD simulation was conducted using these set-points. It was observed that the set-points provided by the DGD and DVC methods resulted in violation of the operating constraints on system frequency and pulse load terminal voltage, as shown in Figure 5.35. Figure 5.35(a) shows the forecasted and measured power for the pulse load during the second study period. Figure 5.35(b) shows the forecasted and measured total power for each DC zone. Figure 5.35(c) shows the system frequency during this study period, obtained from the PSCAD simulation. It can be observed that the frequency exceeded 62.4Hz after the zonal loads were decreased, and

hence, the frequency constraint was violated. Figure 5.29(d) shows the voltage at the pulse load terminal, obtained from the PSCAD simulation. It can be observed that this voltage operated below 0.95pu for more than 2s, which was a violation of the voltage operating constraint.

Next, the ISCPM method was applied to the same zonal and pulse load changes in the second study period. The NSGA-II solved the multi-objective optimization problem and obtained a Pareto optimal front. This Pareto front is shown in Figure 5.36. In this figure, f_{o_1}, f_{o_2}, and f_{o_3} are the objectives associated with the generation set-point mismatch, total generation set-point mismatch, and voltage set-point mismatch, correspondingly. To obtain the Pareto optimal front shown in this figure, the GA evaluated many solutions during its generations. The evaluated solutions are also depicted in this figure. From among the Pareto solutions, the best compromise solution was picked, using the fuzzy membership method. The best compromise solution is also shown in this figure. The three objectives of the best compromise solution were $f_{o_1} = 0.070\text{MW}^2$, $f_{o_2} = 0.098\text{MW}^2$, and f_{o_3} =2.1E-4pu^2.

The adjusted P_{ATG1} and P_{ATG2} set-points of the best compromise solution, for the second study period, are listed in Table 5.9. In this table, the second row shows the DGD power set-points for ATG1 for the three decision intervals, $l = 1, 2, 3$, and the third row shows the ISCPM adjusted power set-points for ATG1 for the three decision intervals. Similarly, the next two rows show unadjusted and adjusted set-point values for ATG2. ATG power set-points, with and without ISCPM adjustments, are also shown in Figure 5.37. Figure 5.37(a) shows the forecasted power and the measured power from PSCAD simulation for one of the DC zones. Also, Figures 5.37(b) and (c) show the ATG1 and ATG2 power set-points, respectively, with and without use of ISCPM method.

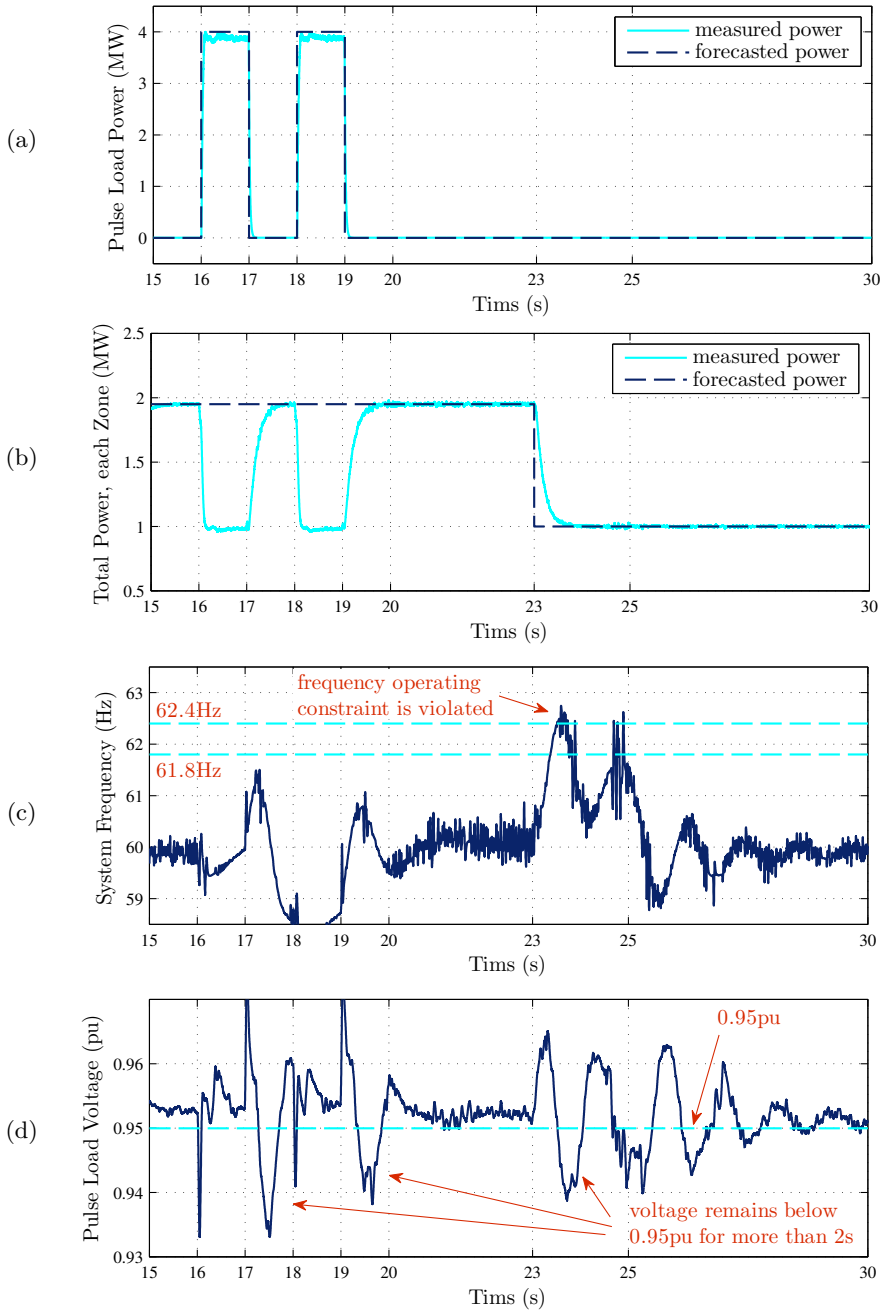

Figure 5.35: Violation of operating constraints in the system response to the DGD and DVC set-points (case IV, second study period). a) forecasted and measured pulse load power, b) forecasted and measured total power for each zone, c) system frequency, and d) pulse load terminal voltage

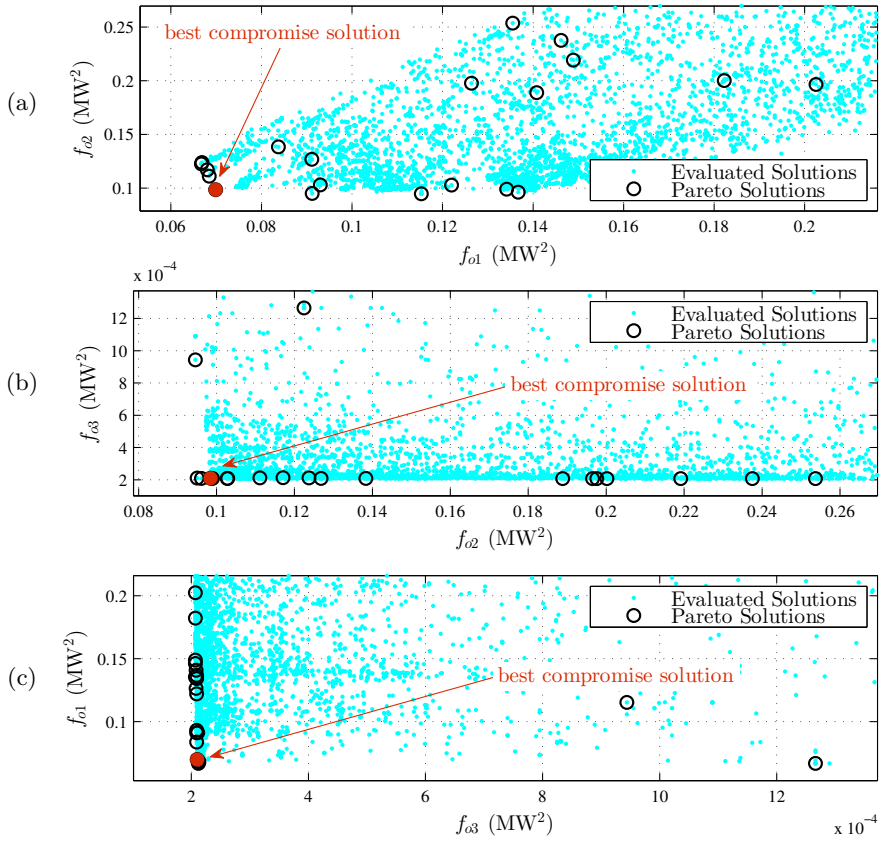

Figure 5.36: Pareto optimal front (case IV, second study period). a) $f_{o_1} - f_{o_2}$ plane, b) $f_{o_2} - f_{o_3}$ plane, and c) $f_{o_3} - f_{o_1}$ plane

Table 5.9: Generator power set-points with and without use of ISCPM method (case IV, second study period)

interval no, l	$l = 4$	$l = 5$	$l = 6$
$P^*_{MTG1}(l)$	4.00 MW	4.00 MW	2.10 MW
$\hat{P}_{MTG1}(l)$	3.79 MW	3.99 MW	2.01 MW
$P^*_{MTG1}(l)$	3.90 MW	3.90 MW	2.00 MW
$\hat{P}_{MTG1}(l)$	3.84 MW	3.78 MW	1.99 MW

Figure 5.37(b) shows that the real-time load management method decreased the total power in each DC zone by about 1MW, when the pulse loads were connected to the system. From Table 5.9 and Figure 5.37(c)-(d), it can be observed that the ISCPM method slightly decreased the ATG power set-points. The reduction in ATG power set-points alleviated the frequency constraint violation, which happened if the DGD and DVC set-points were used, as shown in Figure 5.38. This figure shows the system frequency, obtained from PSCAD simulation, if the ISCPM set-points were used. It can be observed that the operating constraint on system frequency was satisfied, since system frequency never exceeded 62.4Hz and operated between 61.8Hz and 62.4Hz for less than 2s.

The adjusted generator and DSTATCOM voltage set-points of the best compromise solution in the second study period are listed in Table 5.10. In this table, the second row shows ATG1 voltage set-points from the DVC method for any of the three decision intervals, and the third row lists the adjusted ISCPM voltage set-points for ATG1. Similarly, the following rows show the DVC and ISCPM voltage set-points for ATG2 and DSTATCOM, for the three decision intervals. As an example, DSTATCOM voltage set-points, with and without use of ISCPM method, are also depicted in Figure 5.39. Figure 5.39(a) shows the forecasted and measured total power for a DC zone. In Figure 5.39(b), DVC and ISCPM voltage set-points for the DSTATCOM are shown with dashed and solid black lines, respectively.

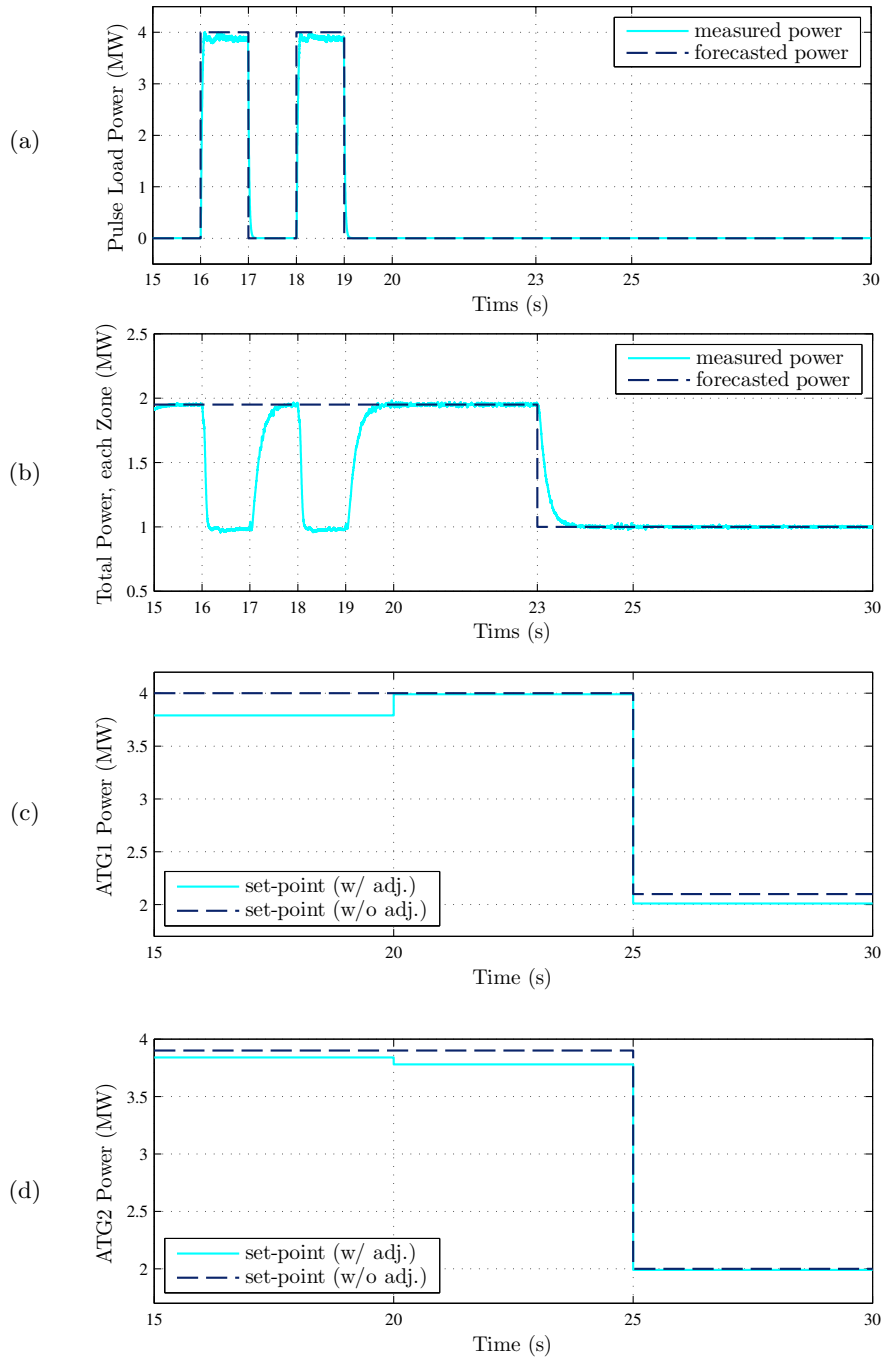

Figure 5.37: Comparison of the generator power set-points with and without use of ISCPM method (case IV, second study period). a) forecasted and measured pulse load power, b) forecasted and measured total power a DC zone, c) ATG1 power set-point, and d) ATG2 power set-point

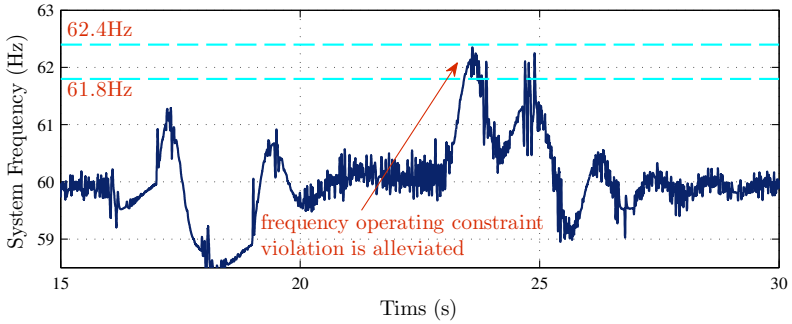

Figure 5.38: Frequency in the system response to the ISCPM set-points (case IV, second study period)

Table 5.10: Voltage set-points with and without use of ISCPM method (case IV, second study period)

interval no, m	$m = 4$	$m = 5$	$m = 6$
$V^*_{ATG1}(m)$	0.9534 pu	0.9530 pu	0.9520 pu
$\hat{V}_{ATG1}(m)$	0.9568 pu	0.9568 pu	0.9568 pu
$V^*_{ATG2}(m)$	0.9544 pu	0.9540 pu	0.9530 pu
$\hat{V}_{ATG2}(m)$	0.9578 pu	0.9578 pu	0.9578 pu
$V^*_{DSTA}(m)$	0.9524 pu	0.9520 pu	0.9510 pu
$\hat{V}_{DSTA}(m)$	0.9558 pu	0.9558 pu	0.9558 pu

From Table 5.10 and Figure 5.39, it can be observed that the ISCPM method increased the voltage set-points in all of the decision intervals. The ISCPM adjustments to the set-points alleviated the load voltage operating constraint violation. Figure 5.40 shows the pulse load terminal voltage, obtained from PSCAD simulation, if the ISCPM set-points were used. The dashed line in this figure shows 0.95pu limit, under which voltage cannot operate for more than 2s. The pulse load operated under 0.95pu voltage for 1.6s, and hence, the voltage operating constraint violation was alleviated.

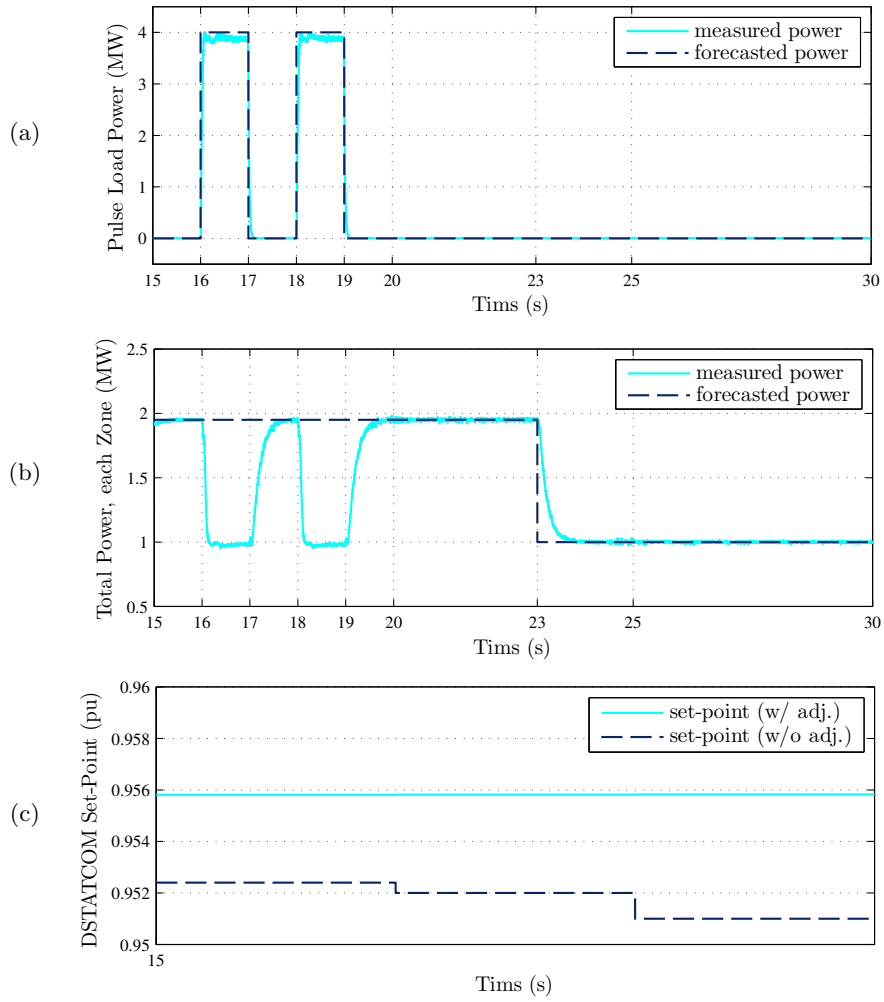

Figure 5.39: Comparison of DSTATCOM voltage set-points with and without use of ISCPM method (case IV, second study period). a) forecasted and measured pulse load power, b) forecasted and measured total power a DC zone, and c) DSTATCOM voltage set-points

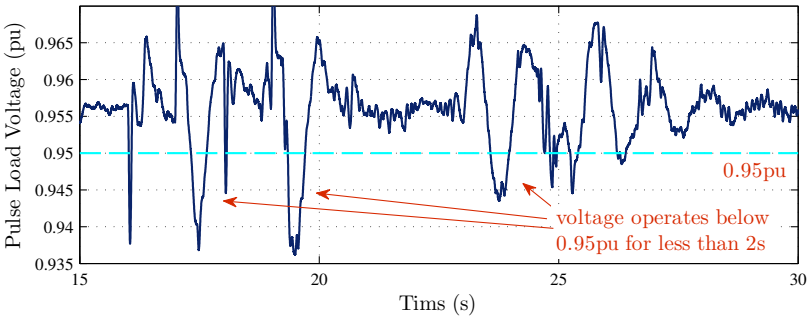

Figure 5.40: Pulse load terminal voltage in the system response to the ISCPM set-points (case IV, second study period)

In summary, several load changes inside DC zones along with pulse load uses were studied in this case. To demonstrate how the ISCPM method is used for back to back study periods, this case was composed of two study periods. It was observed that when the set-points provided by the dynamic generation dispatch and dynamic voltage/VAr control methods were used, the load changes resulted in the violation of load bus voltage operating constraint. Next, the ISCPM method was used for the same load changes. The simulation results, when the adjusted power and voltage set-points were used, showed that all of the constraint violations were alleviated.

5.3 Performance Analysis

The performance of the new ISCPM method was analyzed from two different perspectives: quality of the control solution for power system operation and quality of the Pareto optimal front solution from multi-objective optimization perspective. The performance indices selected for this work, for control systems and Multi-Objective Evolutionary Algorithms (MOEAs) are discussed in subsection 5.3.1. In subsection 5.3.2, the operating points and disturbances used in the performance analysis are introduced. The results of the studies for various disturbance sets are discussed in subsections 5.3.3-5.3.6.

5.3.1 Performance Indices

5.3.1.1 Performance Indices for Control Systems

The shape and the speed of the system quantities, in response to the controller actions, when a disturbance happens, are important in analyzing the performance of a controller [149]. One of the common procedures to analyze a control system performance is to apply a step or an impulse input to the system and determine the output response. The transient response of a control system, to a step change, is commonly characterized by some of the following attributes [150]: 1) delay time, t_d, 2) rise time, t_r, 3) peak time, t_p, 4) maximum overshoot, os, 5) maximum undershoot, us, and 6) settling time, t_s. These attributes are shown in Figure 5.41.

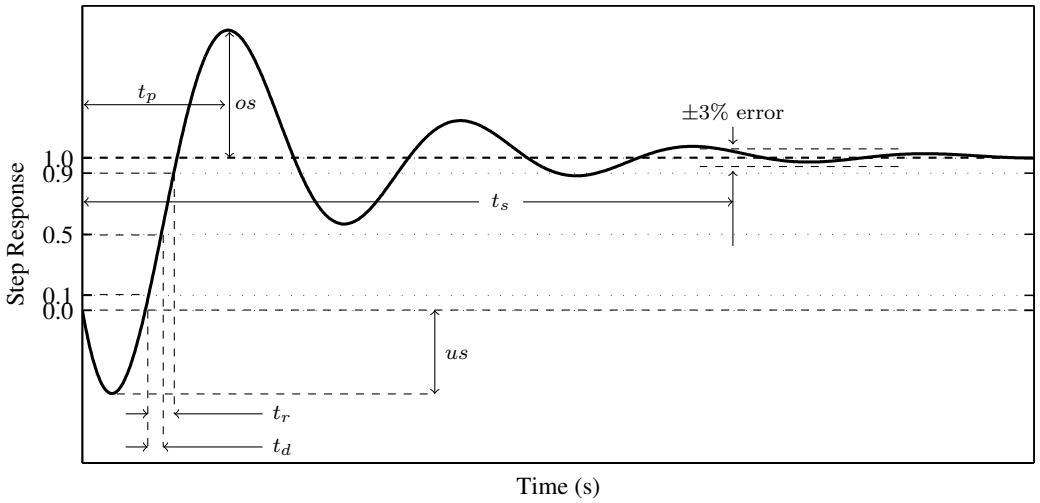

Figure 5.41: Attributes of the transient response of a control system to a step input

Delay time, t_d in Figure 5.41, is the time required for the output to reach 50% of the final value [149, 150]. *Rise time*, t_r in Figure 5.41, is the time required for the output to rise from 10% to 90% of the final value [150, 151]. *Maximum overshoot*, os in Figure 5.41, is the difference between the maximum value of the response and the final value [149–151]. *Maximum undershoot*, us in Figure 5.41, is the maximum negative value of the response

curve [150]. *Peak time*, t_p is the time required for the output to reach the maximum overshoot [150, 151], as shown in Figure 5.41. *Settling time*, t_s in Figure 5.41, is the time required for the system response to reach and stay within a certain percentage of the final value, e.g. 3% or 5% [149–151].

In performance analysis, it is not necessary to use all of the six attributes together, since they are mainly indicators of the response speed and the response shape. To analyze the performance of the new ISCPM method, the maximum overshoot and the settling time indices were chosen [12], since these two indices are commonly used for performance analysis in the control literature, because they can be good indicators of the system response. For each disturbance in each operating point, overshoot and settling time were calculated for the system frequency and load bus voltages. These two quantities were chosen, since the former and the latter are tightly coupled to active and reactive power in the system, respectively, and convey if the system transients are acceptable when disturbances occur.

5.3.1.2 Performance Indices for Multi-Objective Evolutionary Algorithms

In order to analyze the performance of evolutionary multi-objective optimization solving techniques, quantitatively, a variety of performance measures have been developed in the literature. In general, there are three aspects that contribute to the quality of an approximate Pareto set [101, 152–155], which convey how "good" the Pareto front is from various aspects. Firstly, a Pareto set must have enough solutions to be a good representative of the true (theoretical) Pareto front. This aspect of quality is called the "extent" aspect or the "diversity" aspect. Secondly, a Pareto set must be accurate or equivalently, it must be close to the true Pareto set. This aspect of quality is called the "accuracy" aspect or the "closeness" aspect. Thirdly, a Pareto set must have a good distribution, where a good distribution is a distribution close to the uniform distribution. This aspect of quality is called the "distribution" aspect or the "spread" aspect.

Some of the quality indices, widely used in the literature, are error ratio, generational distance, maximum Pareto front error, spacing, maximum spread, overall nondominated

vector generation, and hypervolume. *Error ratio*, I_{ER}, counts the number of solutions in the approximate non-dominated set that are not in the true Pareto set [82, 155]. The true Pareto set is the theoretical Pareto set and the approximate Pareto set is the set of nondominated solutions obtained using a particular solving method. *Generational distance*, I_{GD}, reports the average distance between the approximate Pareto set and the true Pareto set [82, 155]. *Maximum Pareto front error*, I_{MFE}, reports the worst distance among all of the solutions in the approximate Pareto optimal front [82]. *Spacing index*, I_{S}, describes the spread of the solutions in the approximate Pareto set. This metric calculates the relative distance between consecutive solutions in the Pareto set [82, 155]. *Maximum spread*, I_{D}, measures the length of the diagonal of a hyperbox formed by the extreme function values observed in the approximate Pareto optimal set [82, 155]. *Overall nondominated vector generation*, I_{ONVG}, measures the total number of solutions in the approximate Pareto set [155]. *Hypervolume index*, I_{HV}, calculates the volume covered by the solutions in the approximate set [82], for minimization problems.

A summary of the quality indices discussed above for multi-objective evolutionary algorithms is provided in Table 5.11. In this table, $\boldsymbol{\mathcal{P}}$ and $\boldsymbol{\Omega}$ denote the true and the approximate Pareto optimal fronts, respectively. This table describes each index and shows the quality aspect that each index is associated with. It shows that indices 1-3 are associated with accuracy, indices 4-5 with spread, index 6 with extent, and index 7 with accuracy and spread together. This table also indicates whether the true Pareto set, $\boldsymbol{\mathcal{P}}$, is required to compute the index.

Table 5.11: Quality measures for multi-objective evolutionary algorithms

no	index name and notation		index description	quality aspect	$\mathcal{P}$ required?
1	I_{ER}	error ratio	percentage of solutions in $\mathfrak{Q}$ that are not in $\mathcal{P}$	accuracy	yes
2	I_{GD}	generational distance	average distance of the set $\mathfrak{Q}$ to the set $\mathcal{P}$	accuracy	yes
3	I_{MFE}	maximum POF Error	maximum distance among all of the solutions in $\mathfrak{Q}$ with respect to the solutions in $\mathcal{P}$	accuracy	yes
4	I_{S}	spacing	relative distance between consecutive sol's in $\mathfrak{Q}$	spread	no
5	I_{D}	maximum spread	length of the diagonal of a hyperbox formed by the extreme function values in set $\mathfrak{Q}$	spread	no
6	I_{ONVG}	overall nondominated vector generation	number of solutions in set $\mathfrak{Q}$	extent	no
7	I_{HV}	hypervolume	volume covered by the solutions in set $\mathfrak{Q}$	accuracy spread	no

The need for the true Pareto set is an important issue, since the true Pareto set is not known in most of the real-world problems [155]. Hence, for real-world problems, the quality indices that do not require the true Pareto set are used [155]. In the studies performed to evaluate the quality of the Pareto optimal fronts in this dissertation, I_{S} and I_{ONVG} were chosen, since they do not require the true Pareto set. As shown in Table 5.11, indices I_{S} and I_{ONVG} are associated with the spread and the extent aspects of quality, respectively.

The spacing index, I_{S}, is calculated as shown in (5.1) [82, 155]. In (5.1), $\mathfrak{Q}$ is the approximate Pareto set. Also, d_i is the distance of the i-th solution to its closest neighbor in $\mathfrak{Q}$, and $\bar{d}$ is the mean value of the d_i's, which can be calculated by $\bar{d} = \sum_{i=1}^{|\mathfrak{Q}|} d_i/|\mathfrak{Q}|$. Moreover, $|\cdot|$ denotes the number of solutions in a set. The distance d_i in (5.1) is not the Euclidean distance and is calculated by (5.2), in which f_m^i is the value of the m-th objective function for the i-th solution and M is the total number of objectives.

$$I_{\mathrm{S}} = \sqrt{\frac{1}{|\mathfrak{Q}|}\sum_{i=1}^{|\mathfrak{Q}|}\left(d_i - \bar{d}\right)^2} \tag{5.1}$$

$$d_i = \min_{k \in \mathfrak{Q},\, k \neq i} \sum_{m=1}^{M} |f_m^i - f_m^k| \tag{5.2}$$

The overall nondominated vector generation index, I_{ONVG}, is simply calculated as shown in (5.3), in which $|\mathfrak{Q}|$ denotes the number of solutions in the set $\mathfrak{Q}$. Note that

a small I_{ONVG} index means the approximate Pareto set includes only a few solutions which could be a poor representation of the Pareto front.

$$I_{\text{ONVG}} = |\mathbf{\Omega}| \tag{5.3}$$

Multi-objective evolutionary algorithm performance indices, like I_{ONVG} and I_{S}, are usually used to compare the performance of two different solution methods in solving the same problem. In other words, they are usually used in order to observe the trends (improving or degrading), and not to provide an absolute measure of quality [120, 152, 153, 153–156]. As a result, there are no standard values for I_{ONVG} and I_{S} indices in the literature to represent good performance. However, some min/max acceptable values were defined for the performance studies discussed in this dissertation. Regarding I_{ONVG} index, a minimum of 75 solutions was arbitrarily considered to be enough for a good Pareto set in terms of extent. Also, regarding I_{S} index, a maximum of 5% deviation from the average distance between solutions was arbitrarily considered to be a good distribution.

5.3.2 Operating Points and Disturbances

To analyze the performance of the new ISCPM method, several disturbances, divided into four disturbance sets, were defined. These disturbances are defined in Table 5.12. The first set included sharp propulsion disturbances of 20MW and 30MW magnitude increases. The second set included pulse power load disturbances of different magnitudes and durations. For the pulse load, two pulse durations of 1s and 5s, and two pulse power magnitudes of 20MW and 50MW were used. The third set included sequential pulse power loads, which were 1s apart. The same magnitudes and durations were used for the pulses in disturbance sets two and three. The fourth set included outages of the main turbine generators, MTG1 and MTG2.

Table 5.12: Case numbering notation for performance analysis

			Operating Point Number		
Dist. Set	Disturbance Number and Description		OP1	OP2	OP3
Set One	01	sharp propulsion load change: 20MW	101	201	301
	02	sharp propulsion load change: 30MW	102	202	302
Set Two	03	pulse load (single): 20MW height, 1s width	103	203	303
	04	pulse load (single): 50MW height, 1s width	104	204	304
	05	pulse load (single): 20MW height, 5s width	105	205	305
	06	pulse load (single): 50MW height, 5s width	106	206	306
Set Three	07	pulse load (double): 20MW height, 1s width	107	207	307
	08	pulse load (double): 50MW height, 1s width	108	208	308
	09	pulse load (double): 20MW height, 5s width	109	209	309
	10	pulse load (double): 50MW height, 5s width	110	210	310
Set Four	11	generator outage: MTG1	111	211	311
	12	generator outage: MTG2	112	212	312

Since the performance of the ISCPM method also depends on the operating point of the system, three operating points were chosen to represent light loading, medium loading, and heavy loading of the total possible load demand in the notional AES. The three operating points, in the critical parameters space, are depicted in Figure 5.42. In this figure, x and y axes are two critical parameters and show the total power system load demand and the total generation power of MTG2 and ATG2, respectively. The details for obtaining the risk-based DSR, shown in this figure, was explained in subsection 4.4.4.2. It was explained that the system was secure against unplanned events, if the system trajectory remained on the left hand side of the security border.

Figure 5.42 shows that in light loading operating point, OP1, the total system load was 35% of the total generation capacity (80MW) and 48% of the maximum secure loading. The maximum secure loading, considering the security border shown in Figure 5.42, was abut 59MW. As shown in this figure, the maximum secure loading is the maximum system loading which falls inside the secure region. In the medium loading operating point, OP2, the total system load was 48% of the total generation capacity and 66% of the maximum secure loading. In the heavy loading operating point, OP3, the total system load was 60%

of the total generation capacity and 83% of the maximum secure loading. The performance of the new ISCPM method was analyzed at each operating point and for each disturbance, using the aforementioned performance metrics.

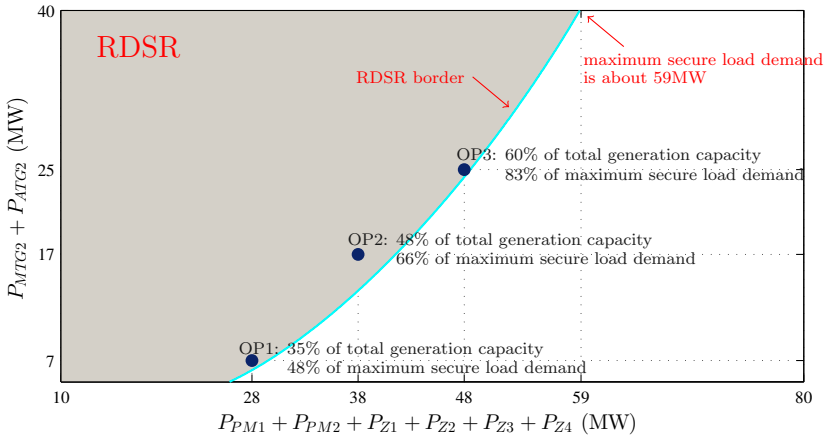

Figure 5.42: Light loading, medium loading, and heavy loading operating points

The naming convention for the 12 disturbances for the various operating points is also shown in Table 5.12. The disturbances in the first operating point, OP1, are denoted with 1XX in which XX is the 2-digit disturbance number. Similarly, the disturbances in OP2 and OP3 are denoted with 2XX and 3XX, respectively. For instance, case 105 denotes the case in which the fifth disturbance is studied, starting from OP1. As another example, case 312 denotes disturbance 12 starting from OP3.

System initial conditions at the three operating points are listed in Tables 5.13-5.15. Table 5.13 shows the real power for propulsion and zonal load demand at each of the three operating points. Table 5.14 shows the generator power set-points, assumed to be provided by the DGD method, at each of the three operating points. Moreover, the generator and DSTATCOM voltage set-points at OP1, OP2, and OP3, assumed to be provided by the DVC method, are listed in Table 5.15.

Table 5.13: Load active power demands at OP1, OP2, and OP3

operating point	P_{PM1}	P_{PM2}	P_{Z1}	P_{Z2}	P_{Z3}	P_{Z4}
OP1	10 MW	10 MW	2 MW	2 MW	2 MW	2 MW
OP2	15 MW	15 MW	2 MW	2 MW	2 MW	2 MW
OP3	20 MW	20 MW	2 MW	2 MW	2 MW	2 MW

Table 5.14: Generator power set-points at OP1, OP2, and OP3

operating point	P_{MTG1}	P_{ATG1}	P_{MTG2}	P_{ATG2}
OP1	20.10 MW	1 MW	6 MW	1 MW
OP2	20.13 MW	1 MW	16 MW	1 MW
OP3	19.22 MW	4 MW	21 MW	1 MW

Table 5.15: Generator and DSTATCOM voltage set-points at OP1, OP2, and OP3

operating point	V_{MTG1}	V_{ATG1}	V_{MTG2}	V_{ATG2}	V_{DSTAT}
OP1	0.9650 pu	0.9646 pu	0.9652 pu	0.9647 pu	0.9515 pu
OP2	0.9690 pu	0.9681 pu	0.9692 pu	0.9682 pu	0.9525 pu
OP3	0.9730 pu	0.9716 pu	0.9733 pu	0.9715 pu	0.9526 pu

5.3.3 Performance Analysis for Disturbance Set One

The first disturbance set included sharp increases in the propulsion load power. The total propulsion load change magnitude was forecasted to be 20MW and 30MW in the first and the second disturbances, respectively. The study period was $T = 25$ seconds. The decision intervals for the dynamic generation dispatch and the dynamic voltage/VAr control methods were assumed to be $\tau_g = 5$ and $\tau_q = 5$ seconds, respectively. Therefore, the study period included $n_{\tau_g} = 5$ decision intervals for the generation dispatch method and $n_{\tau_q} = 5$ decision intervals for the VAr control method.

In each case, the propulsion load was forecasted to increase at $t = 7$s. The total increase in the propulsion power was evenly distributed among the two propulsion motors. Therefore, the power of each propulsion motor was forecasted to increase by 10MW and 15MW, in disturbances 1 and 2, respectively. In each case, two signals were generated to mimic the DGD and DVC output signals in response to the forecasted load, as follows. It

was assumed that the DGD method served the increased system load by evenly distributing the load increase between the two MTGs, starting from the second decision interval at $t = 5$s. It was assumed that the DVC method increased the voltage set-points in the system by 0.3%, starting from the second decision interval at $t = 5$s, to compensate for the voltage drop caused by the load increase.

It was also assumed that the ISCPM method did not adjust ATG power set-points and their power set-points remained constant at their initial values for each operating point during the studies. Therefore in the studies, the ISCPM method could only adjust MTG1 and MTG2 power set-points and generator and DSTATCOM voltage set-points, in each of the five decision intervals.

To illustrate the case setup, consider case 202 as an example. In this case, a 30MW sharp propulsion load increase was studied, at OP2. Figure 5.43 shows the forecasted propulsion load power, and the set-points generated to mimic responses of the DGD and DVC methods, for this case. It can be seen that the forecasted PM power for each PM increased by 15MW at 7s. To serve the increased load, the power set-point for each MTG increased by 15MW, starting from the second decision interval. Also, to compensate for the voltage drop caused by the load increase, generator and DSTATCOM voltage set-points were increased by 0.3%, starting from the second decision interval. Note that in Figure 5.43(c), the scales of the voltage set-points are manipulated, for better readability.

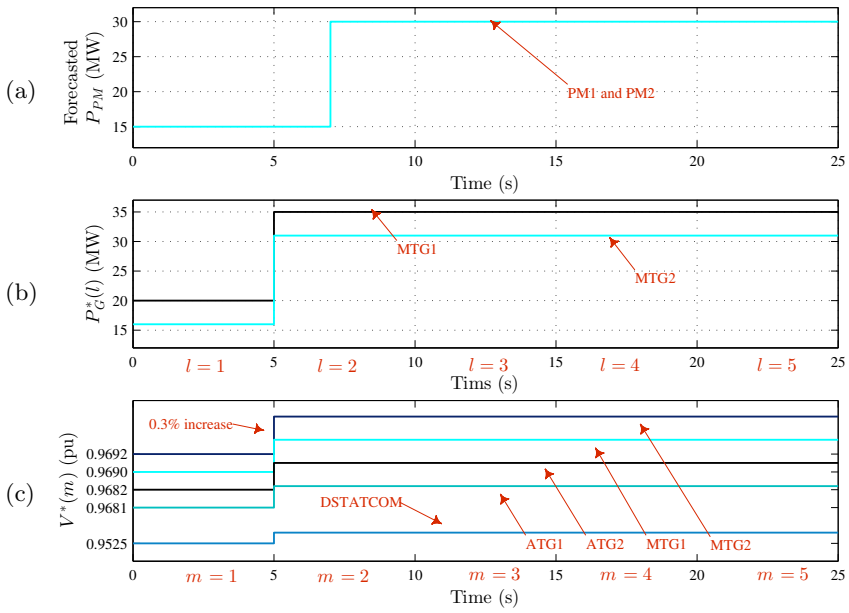

Figure 5.43: Case setup for case 202. a) Forecasted propulsion load power, b) generated power set-points for the DGD method, and c) generated voltage set-points for the DVC method

For each disturbance at each operating point, a PSCAD simulation of the study period was conducted without the ISCPM method, using the generated DGD and DVC set-points. It was observed that the propulsion load increase in each case caused the system trajectory to move outside of the system RDSR. Also, although the voltage set-points were increased, the voltage operating constraint at the PM2 terminal was violated, in each case, since its voltage stayed below 0.95pu for more than 2s. Therefore, the PSCAD simulation results showed that the generated DGD and DVC set-points resulted in security and operating constraint violations, for each case.

Next, the ISCPM method was applied in each case and the adjusted set-points were determined by the ISCPM method. The spacing and overall nondominated vector generation indices were calculated for the Pareto optimal fronts obtained in each case. Then, a PSCAD simulation of the study period was conducted using the adjusted set-points determined by the ISCPM method. Using the simulation results, frequency and voltage maximum overshoot and settling time were calculated, for each case.

The Pareto set quality indices, I_{ONVG} and I_{S}, are listed in Table 5.16, for each case. This table also shows the three objective functions, f_{o_1}, f_{o_2}, and f_{o_3}, for the best compromise solution in each case. The I_{ONVG} index values in this table show that the Pareto sets contained enough Pareto solutions in all cases, except case 302, which is highlighted in this table. In this case, the system was operating at OP3, in which total system load was 48MW, and a 30MW increase in the propulsion power was desired. Since the maximum secure loading is ∼59MW, the feasible space in the optimization problem for this case was very small. Hence, not many Pareto solutions were found in that small feasible space.

The I_{S} index values in Table 5.16 show that the Pareto front in each case had a good distribution, since the spacing index was less than 5% for all of the cases.

Table 5.16: MOEA quality indices for disturbance set one

case no	f_{o_1} (MW^2)	f_{o_2} (MW^2)	f_{o_3} (pu^2)	I_{ONVG}	I_{S} (%)
101	210.77	106.83	2.361E-03	182	3.11
102	769.26	341.32	5.653E-03	204	1.86
201	328.68	218.15	3.919E-03	187	2.59
202	881.47	844.16	5.417E-03	188	1.65
301	613.14	682.11	2.921E-03	143	2.27
302	1379.30	2036.59	3.614E-03	52	4.52

Table 5.16 shows that objective functions at each operating point increased from disturbance 01 to disturbance 02. For instance at OP1, f_{o_1} increased from 210.77 MW^2 to 769.26 MW^2, f_{o_2} increased from 106.83 MW^2 to 341.32 MW^2, and f_{o_3} increased from 2.361E-03 pu^2 to 5.653E-03 pu^2, in disturbance 02 compared to disturbance 01. The increase in the objective values from disturbance 01 to 02 was because the disturbance magnitude increased from 20MW to 30MW. Hence, set-point adjustments required to satisfy security and operating constraints in disturbance 02 were bigger, compared to disturbance 01.

In each case, after determining the best compromise solution (the ISCPM output), the

adjusted set-points were applied to the system model in PSCAD, and frequency and voltage maximum overshoot and settling time were calculated for the system response. Moreover, for comparison purposes, a second PSCAD simulation was conducted using the generated set-points for the DGD and DVC methods, and frequency and voltage maximum overshoot and settling time were calculated. These indices are listed in Table 5.17.

Table 5.17: Power system control quality indices for disturbance set one

	without use of ISCPM method				with use of ISCPM method			
case no	frq os (%)	frq t_s (s)	vlt os (%)	vlt t_s (s)	frq os (%)	frq t_s (s)	vlt os (%)	vlt t_s (s)
101	2.00	0.00	0.71	0.00	1.88	0.00	0.60	0.00
102	2.27	0.00	1.37	0.00	1.99	0.00	0.69	0.00
201	1.97	0.00	0.83	0.00	1.72	0.00	0.53	0.00
202	2.34	0.00	1.42	0.00	1.65	0.00	0.55	0.00
301	1.09	0.00	0.83	0.00	0.98	0.00	0.56	0.00
302	1.48	0.00	1.27	0.00	0.86	0.00	0.56	0.00

To illustrate how the frequency and voltage maximum overshoot and settling time were calculated, Figure 5.44 shows the measured frequency and DSTATCOM voltage in the system response to the ISCPM set-points in case 202. Figure 5.44(a) shows the forecasted and measured powers for a propulsion load. Figure 5.44(b) shows the adjusted MTG power set-points determined by the ISCPM method. Figure 5.44(c) shows the system frequency during the study period. When the MTG power set-points increased at 5s, system frequency deviated by 1.65%, and when the propulsion load increased at 7s, system frequency deviated by 0.38%. Hence, the maximum frequency overshoot in this case was 1.65%. Since the frequency deviation was always less than 3%, the frequency settling time was zero. Figure 5.44(d) shows the voltage at the DSTATCOM terminal. It also shows the adjusted DSTATCOM voltage set-point determined by the ISCPM method. This figure shows that the maximum voltage deviations during intervals 1-5 were 0.37%, 0.55%, 0.30%, 0.17%, and 0.10%, respectively, and hence, the maximum voltage overshoot was 0.55% in this case. Since the voltage deviation from the set-point was always less than 3%, the

voltage settling time was zero.

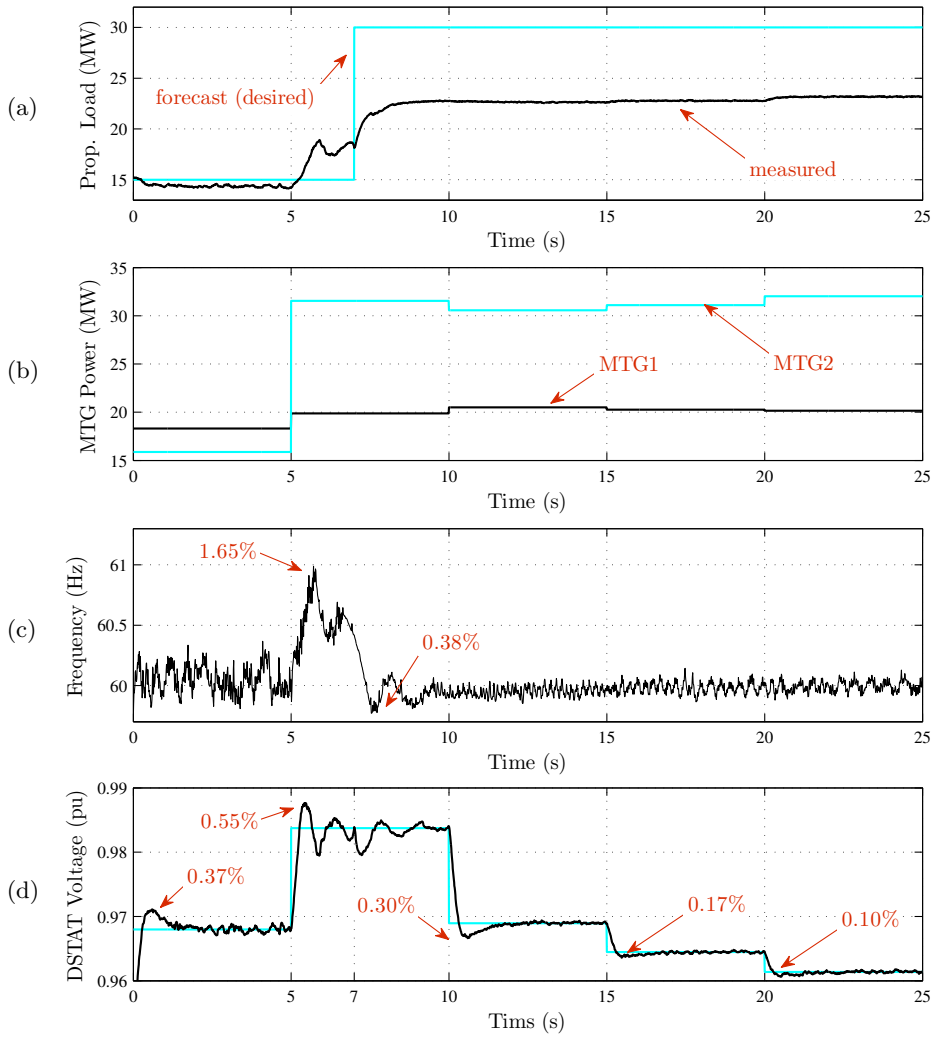

Figure 5.44: Frequency and voltage maximum overshoot and settling time with the ISCPM method in case 202. a) propulsion load forecast and measured power, b) adjusted MTG power set-points, c) measured frequency, and d) DSTATCOM adjusted set-point and measured terminal voltage

Table 5.17 shows that in the system response without the ISCPM method, maximum frequency and voltage overshoot increased from disturbance 01 to 02, at each operating point, since the disturbance magnitude increased from 20MW to 30MW. Since frequency and voltage deviations were small, the settling times for frequency and voltage were zero

in all of the cases.

By comparing the frequency and voltage overshoot with and without the ISCPM method, it can be observed that both of these indices decreased when the ISCPM method was used, for each case. It was because the ISCPM method reduced the total power generation in the system, to satisfy the dynamic security constraints for unplanned events. Consequently, the real-time load management method reduced the propulsion load power in each case, when the adjusted set-points were used. As an example, Figure 5.45 compares the propulsion load power in case 202, with and without use of the ISCPM method. It can be seen that when the adjusted power and voltage set-points were applied to the system, the real-time load management method decreased the propulsion load power from its forecasted (desired) value, since the ISCPM method reduced the total system generation, to satisfy the security constraints.

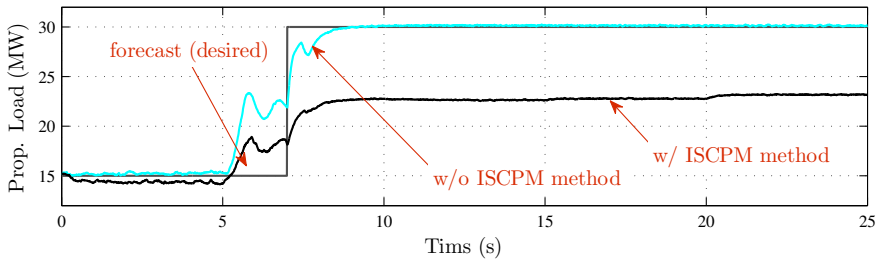

Figure 5.45: Propulsion load power in case 202 with and without use of the ISCPM method

Regarding the acceptability of the system response to the adjusted set-points, Table 5.17 shows that the frequency and voltage maximum overshoots were small and acceptable in all of the six cases in this disturbance set. Moreover, frequency and voltage settling times were zero, due to very small frequency and voltage deviations in all of the cases.

5.3.4 Performance Analysis for Disturbance Set Two

The second disturbance set included pulse load uses. As shown in Table 5.12, for the forecasted pulse loads in this set, two pulse powers of 20MW and 50MW, and two pulse durations of 1s and 5s were used. In each case, the study period was $T = 25$ seconds. The simulation length was also 25s. The decision intervals for the dynamic generation dispatch and the dynamic voltage/VAr control methods were assumed to be $\tau_g = 5$ and $\tau_q = 5$ seconds, respectively. Therefore, the study period included $n_{\tau_g} = 5$ decision intervals for the generation dispatch method and $n_{\tau_q} = 5$ decision intervals for the VAr control method.

In each case, the pulse load was forecasted to connect at 10s, following a 2.5MW increase in each propulsion load's power at 7s. In each case, two signals were generated to mimic the DGD and DVC output signals in response to the forecasted load, as follows. It was assumed that to serve the increase in load demand at 7s, the DGD method increased MTG1 power set-point by 5MW starting from the second decision interval at 5s. Also, if the pulse load power was more than the total system load, the difference was assumed to be evenly distributed among the two MTGs, starting from 10s. It was assumed that the DVC method increased the voltage set-points by 0.1%, in the decision intervals with the pulse load connected.

It was also assume that the ISCPM method did not adjust ATG power set-points and their power set-points remained constant at their initial values for each operating point during the studies. Therefore in the studies, the ISCPM method could only adjust MTG1 and MTG2 power set-points and generator and DSTATCOM voltage set-points, in each of the five decision intervals.

To illustrate the case setup, consider case 104 as an example. In case 104, a pulse with 50MW power and 1s duration was forecasted to be used, starting from OP1. Figure 5.46 shows the forecasted load and and the set-points generated to mimic responses of the DGD and DVC methods, for this case. As shown in this Figure 5.46(a), the power of each PM was forecasted to increase by 2.5MW at 7s. Figure 5.46(b) shows that a 50MW pulse load with 1s duration was forecasted to be connected at 10s. Figure 5.46(c) shows that to

supply the increase in system load at 7s, MTG1 power set-point was increased by 5MW, starting from the second decision interval, $l = 2$. Also, the power set-point of each MTG was increased by 10MW in the third decision interval, since the pulse power was 20MW more than than total system load demand during this interval. Figure 5.46(d) shows that to compensate for the voltage drop caused by the pulse load, the voltage set-points were increased by 0.1% in the third decision interval.

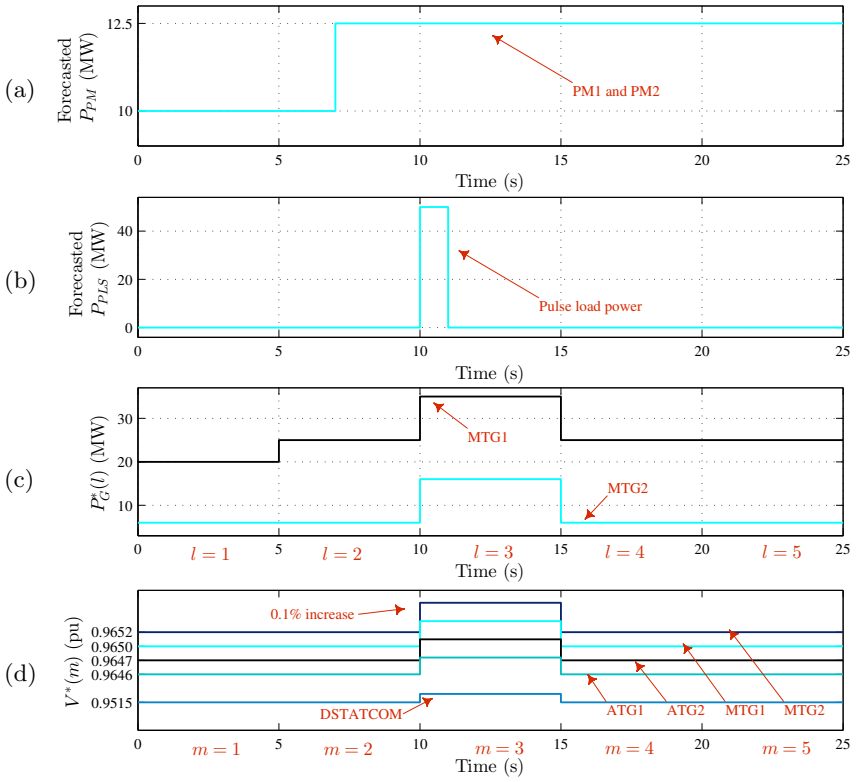

Figure 5.46: Case setup for case 104. a) Forecasted propulsion load power, b) Forecasted pulse load power, c) generated power set-points for the DGD method, and d) generated voltage set-points for the DVC method

In each case, a PSCAD simulation was conducted without the ISCPM method, using the set-points generated for the DGD and DVC methods. It was observed that the propulsion load increase caused the system operating point to move outside of the system RDSR. Also, although the voltage set-points were increased during the time the pulse load was connected,

the voltage at PM2 terminal operated below 0.95pu for more than 2s. Furthermore, the frequency deviation in some cases was more than 2.4Hz, which is the maximum acceptable frequency deviation. Therefore, the PSCAD simulation results showed that the set-points generated for the DGD and DVC methods resulted in security and operating constraint violations, in each case.

Next, the ISCPM method was applied in each case and the adjusted set-points were determined by the ISCPM method. The spacing and overall nondominated vector generation indices were calculated for the Pareto optimal fronts obtained in each case. Then, a PSCAD simulation of the study period was conducted using the adjusted set-points determined by the ISCPM method. Using the simulation results, frequency and voltage maximum overshoot and settling time were calculated, for each case.

The Pareto set quality indices, I_{ONVG} and I_{S}, are listed in Table 5.18, for each case. This table also shows the three objective functions, f_{o1}, f_{o2}, and f_{o3}, for the best compromise solution. The I_{ONVG} index values in this table show that the Pareto sets contained enough (more than 75) Pareto solutions in each case. Therefore, the Pareto sets were acceptable in terms of the extent quality. However, as highlighted in the table, several cases had Pareto fronts with poor distribution, since their spacing index values were bigger than 5%.

Table 5.18 also shows the three objective functions for the best compromise solution in each case. It can be observed that the objective values increased from disturbance 03 to disturbance 04, at each operating point, since the pulse load power increased from 20MW to 50MW and more set-point adjustments were required to satisfy security and operating constraints. Similarly, objective values increased at each operating point from disturbance 05 to disturbance 06, due to the same reason.

Table 5.18: MOEA quality indices for disturbance set two

case no	f_{o_1} (MW^2)	f_{o_2} (MW^2)	f_{o_3} (pu^2)	I_{ONVG}	I_{S} (%)
103	212.25	1.27	3.650E-04	105	5.32
104	528.90	6.15	5.098E-03	130	2.69
105	192.15	2.30	4.120E-04	83	7.80
106	512.61	9.50	1.117E-02	106	4.37
203	122.66	0.59	1.980E-04	150	7.31
204	153.83	6.48	7.320E-04	115	4.31
205	124.77	2.94	4.020E-04	82	7.64
206	181.39	8.35	7.533E-03	174	2.93
303	198.83	13.52	3.880E-04	177	4.62
304	205.12	13.87	3.780E-04	98	4.45
305	175.14	31.98	1.808E-03	129	3.79
306	173.65	35.80	2.106E-03	136	3.06

In each case, after determining the best compromise solution (the ISCPM output), the adjusted set-points were applied to the system model in PSCAD, and frequency and voltage maximum overshoot and settling time were calculated for the system response. Moreover, for comparison purposes, a second PSCAD simulation was conducted using the generated set-points for the DGD and DVC methods, and frequency and voltage maximum overshoot and settling time were calculated. These indices are listed in Table 5.19.

Table 5.19: Power system control quality indices for disturbance set two

	without use of ISCPM method				with use of ISCPM method			
case no	frq os (%)	frq t_s (s)	vlt os (%)	vlt t_s (s)	frq os (%)	frq t_s (s)	vlt os (%)	vlt t_s (s)
103	1.68	0.00	2.67	0.00	1.25	0.00	2.62	0.00
104	4.56	0.45	5.52	0.68	3.81	0.40	5.39	0.55
105	1.58	0.00	3.19	0.09	1.50	0.00	2.43	0.00
106	4.05	0.47	5.52	0.62	4.01	0.47	8.14	0.67
203	1.67	0.00	2.74	0.00	2.09	0.00	2.57	0.00
204	3.88	0.36	4.73	0.56	3.83	0.37	5.13	0.46
205	1.59	0.00	2.99	0.00	1.81	0.00	2.48	0.00
206	4.03	0.43	4.98	0.31	4.01	0.39	6.79	0.60
301	1.35	0.00	2.47	0.00	2.06	0.00	2.39	0.00
302	3.69	0.34	4.03	0.56	3.42	0.35	4.16	0.53
303	1.51	0.00	2.47	0.00	1.64	0.00	2.03	0.00
304	3.65	0.33	5.09	0.24	3.97	0.35	5.42	0.25

To illustrate how the frequency and voltage maximum overshoot and settling time were calculated, Figure 5.47 shows the measured frequency and DSTATCOM voltage in the system response to the ISCPM set-points in case 104. As previously shown in Figure 5.46, a 50MW pulse load with 1s duration was connected to the system at 10s, in this case. Figure 5.47(a) shows forecasted and measured powers for the pulse load. Figure 5.47(b) depicts forecasted and measured powers for the propulsion load and shows that the RLM method decreased the propulsion power when the pulse was connected. Figure 5.47(c) shows the adjusted MTG power set-points determined by the ISCPM method. Figure 5.47(d) shows the system frequency in response to the ISCPM set-points. When the pulse connected, system frequency dropped by 0.77% and when disconnected, system frequency increased by 3.81%. Hence, the maximum frequency overshoot happened after 11s, and it was 3.81%. In Figure 5.47(d), the reference value for the frequency (60Hz) is shown with a solid cyan line. Also, the 3% deviation line is shown with dashed cyan line. It can be observed that when the pulse load disconnected, system frequency was outside of the ±3% range for about 0.40s, after which it remained inside the ±3% range. Therefore, the frequency settling time was 0.40s in this case.

In Figure 5.47(e), the DSTATCOM terminal voltage in case 104 is shown with solid black curve. Also, the DSTATCOM adjusted set-point determined by the ISCPM method is depicted with solid cyan line. Moreover, the ±3% range around the set-point is depicted with dashed cyan line. It can be observed that the maximum voltage deviation happened when the pulse connected at 10s and it was 5.39%. It can also be observed that the DSTATCOM voltage settled inside the ±3% range after 0.55s and hence, the settling time was 0.55s.

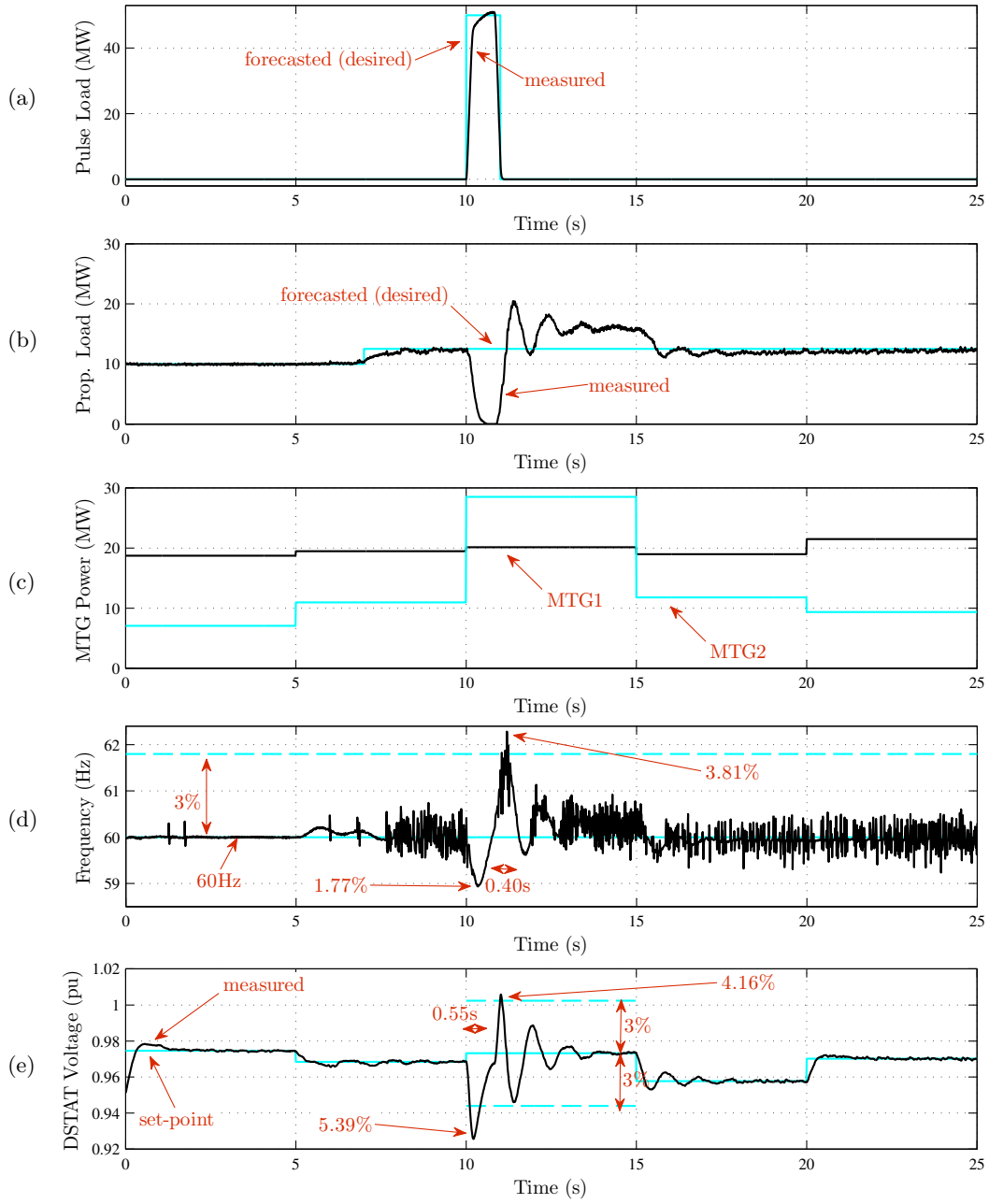

Figure 5.47: Frequency and voltage maximum overshoot and settling time with the ISCPM method in case 104. a) pulse load forecasted and measured power, b) propulsion load forecasted and measured power, c) adjusted MTG power set-points, d) measured frequency, and e) DSTATCOM adjusted set-point and measured terminal voltage

Regarding the trend of change in the control indices, it can be observed in Table 5.19 that maximum overshoot and settling time for frequency and voltage increased from disturbance 03 to disturbance 04, and from disturbance 05 to disturbance 06, at each operating point, due to the increase in pulse power from 20MW to 50MW. Regarding the acceptability of the indices, Table 5.19 shows that without using the ISCPM method, cases 104, 106, and 206 had unacceptable maximum frequency overshoots. These cases correspond to 50MW/1s pulse at OP1, 50MW/5s pulse at OP1, and 50M/5s pulse at OP2, respectively. By comparing the maximum frequency overshoot with and without use of the ISCPM method in these three cases, it can be observed that although the maximum frequency overshoot improved in each of the cases, it was still unacceptable in case 106 and 206. These unacceptable frequency responses happened when the system was operating in light or medium loading (OP1 or OP2), and a pulse with a big magnitude (50MW) was connected to the system.

As an example, Figure 5.48 compares the system frequency response with and without use of ISCPM method in case 104. In this case, a 50MW pulse was connected from 10s to 11s. This figure shows that after the pulse was disconnected at 11s, system frequency had a 4.56% overshoot when the generated set-points for DGD and DVC methods were used. This overshoot was not acceptable. In the system response to the adjusted set-points determined by the ISCPM method, this overshoot was decreased to 3.81%, which was acceptable.

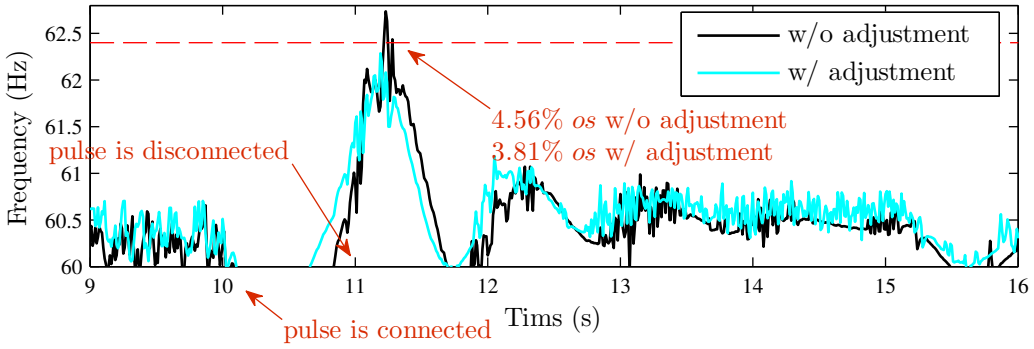

Figure 5.48: Frequency maximum overshoot with and without use of ISCPM method in case 104

As another example, Figure 5.49 compares the system frequency response with and without use of ISCPM method in case 106. In this case, a 50MW pulse was connected from 10s to 15s. This figure shows that in the system response to the set-points generated for the DGD and DVC methods, the frequency had a 4.05% maximum overshoot at 15s, which was not acceptable. In the system response to the ISCPM set-points, this overshoot was improved to 4.01%. However, since it was still above 4%, it was not acceptable.

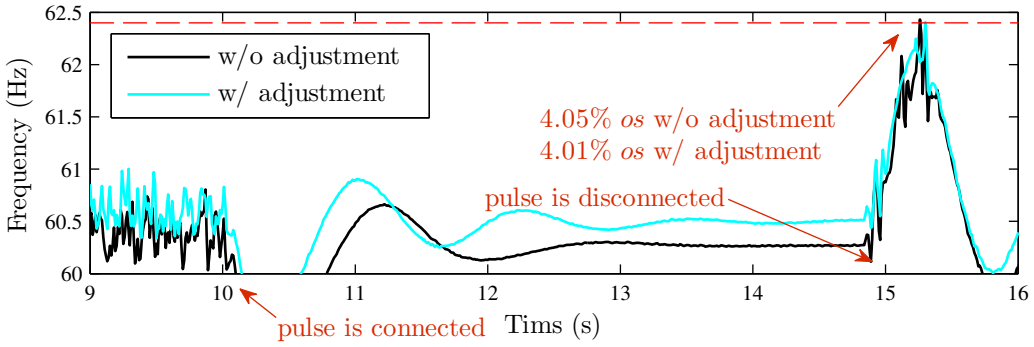

Figure 5.49: Frequency maximum overshoot with and without use of ISCPM method in case 106

By comparing the voltage overshoot with and without use of the ISCPM method in each case in Table 5.19, it can be observed that changes in this index were relatively small. Moreover, the system response in terms of the voltage overshoot was always acceptable.

Also, frequency and voltage settling time were small and acceptable in all of the 12 cases in this disturbance set.

5.3.5 Performance Analysis for Disturbance Set Three

The third disturbance set included two sequential pulse loads, which were 1s apart. As shown in Table 5.12, for the forecasted pulse loads in this set, two pulse powers of 20MW and 50MW, and two pulse durations of 1s and 5s were used. In each case, the study period was $T = 25$ seconds. The simulation length was also 25s. The decision intervals for the dynamic generation dispatch and the dynamic voltage/VAr control methods were assumed to be $\tau_g = 5$ and $\tau_q = 5$ seconds, respectively. Therefore, the study period included $n_{\tau_g} = 5$ decision intervals for the generation dispatch method and $n_{\tau_q} = 5$ decision intervals for the VAr control method.

In each case, the pulse load was forecasted to start at 10s, following a 2.5MW increase in each propulsion load's power at 7s. In each case, two signals were generated to mimic the DGD and DVC output signals in response to the forecasted load, as follows. To serve the load demand increase at 7s, it was assumed that the DGD method increased MTG1 power set-point by 5MW starting from the second decision interval at 5s. Also, if the pulse load power was more than the total system load, the difference was assumed to be evenly distributed among the two MTGs, starting from 10s. It was also assumed that the DVC method increased the voltage set-points by 0.1%, in the decision intervals with the pulse load connected.

It was also assume that the ISCPM method did not adjust ATG power set-points and their power set-points remained constant at their initial values for each operating point during the studies. Therefore in the studies, the ISCPM method could only adjust MTG1 and MTG2 power set-points and generator and DSTATCOM voltage set-points, in each of the five decision intervals.

To illustrate the case setup, consider case 210 as an example. In case 210, two 50MW pulses were forecasted to be connected to the system during 10s-15s and 16s-21s. Figure

5.50 shows the forecasted load and the set-points generated to mimic responses of the DGD and DVC methods, for this case. As shown in this Figure 5.50(a), the power of each PM was forecasted to increase by 2.5MW at 7s. Figure 5.50(b) shows that two 50MW pulse loads with 5s durations were forecasted to be connected at 10s and 15s. Figure 5.50(c) shows that to supply the load demand increase at 7s, MTG1 power set-point was increased by 5MW, starting from the second decision interval, $l = 2$. Also, since the power load power was about 10MW more than the total load demand during intervals 3-5, each MTG power set-point was increased by 5MW at 10s. Figure 5.50(d) shows that to compensate for the voltage drop caused by the pulse load, the generator and DSTATCOM voltage set-points were increased by 0.1% in decision intervals $m = 3$, $m = 4$, and $m = 5$, during which the pulses were connected.

In each case, a PSCAD simulation was conducted without the ISCPM method, using the set-points generated for the DGD and DVC methods. It was observed that the propulsion load increase caused the system operating point to move outside of the system RDSR. Also, although the voltage set-points were increased during the time the pulse load was connected, the voltage at PM2 terminal operated below 0.95pu for more than 2s. Furthermore, the frequency deviation in some cases was more than 2.4Hz, which is the maximum acceptable frequency deviation. Therefore, the PSCAD simulation results showed that the set-points generated for the DGD and DVC methods resulted in security and operating constraint violations, in each case.

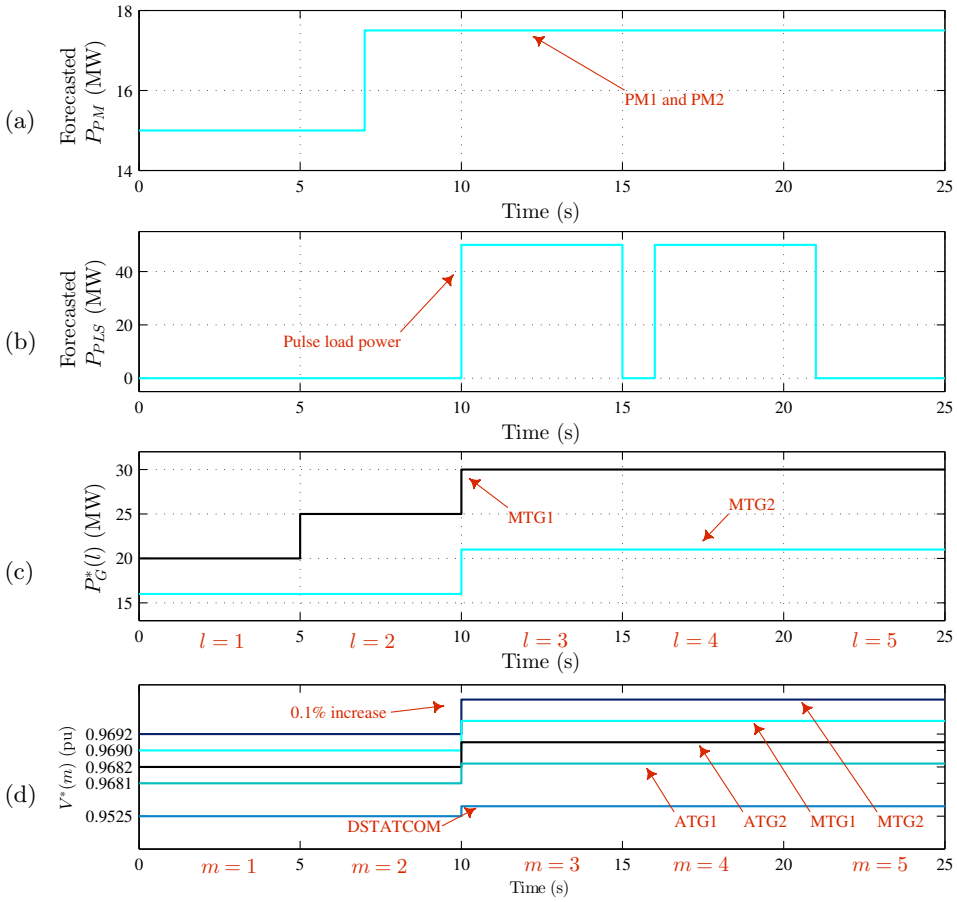

Figure 5.50: Case setup for case 210. a) Forecasted propulsion load, b) Forecasted pulse load, c) generated power set-points for the DGD method, and d) generated voltage set-points for the DVC method

Next, the ISCPM method was applied in each case and the adjusted set-points were determined by the ISCPM method. The spacing and overall nondominated vector generation indices were calculated for the Pareto optimal fronts obtained in each case. Then, a PSCAD simulation of the study period was conducted using the adjusted set-points determined by the ISCPM method. Using the simulation results, frequency and voltage maximum overshoot and settling time were calculated, for each case.

The Pareto set quality indices, I_{ONVG} and I_{S}, are listed in Table 5.20, for each case. This table also shows the three objective functions, f_{o1}, f_{o2}, and f_{o3}, for the best compromise solution in each case. The I_{ONVG} index values in this table show that the Pareto sets

contained enough (more than 75) Pareto solutions in each case. Therefore, the Pareto sets were acceptable in terms of the extent quality. However, as highlighted in this table, cases 208 and 308 had Pareto fronts with poor distribution, since their spacing index was bigger than 5%.

Table 5.20 also shows the objective functions for the best compromise solution in each case. It can be observed that the objective values increased from disturbance 07 to 08, at each operating point, since the pulse power increased from 20MW to 50MW and more set-point adjustments were required to satisfy operating constraints. Similarly, objective values increased at each operating point from disturbance 09 to 10, due to the same reason.

Table 5.20: MOEA quality indices for disturbance set three

case no	f_{o_1} (MW^2)	f_{o_2} (MW^2)	f_{o_3} (pu^2)	I_{ONVG}	I_{S} (%)
107	216.64	0.76	1.200E-05	140	3.55
108	521.22	8.45	2.100E-03	94	4.52
109	342.25	7.28	4.160E-04	154	3.53
110	1229.41	21.55	1.132E-02	125	2.78
207	244.84	2.26	4.860E-04	111	4.32
208	289.07	11.65	2.590E-03	124	6.13
209	390.53	16.16	3.200E-04	158	3.28
210	508.81	15.87	8.444E-03	149	3.53
307	462.67	65.18	1.900E-03	126	3.11
308	421.11	2.96	5.720E-04	118	6.57
309	543.78	211.02	5.500E-04	159	2.61
310	382.18	20.42	2.997E-03	142	4.47

In each case, after determining the best compromise solution (the ISCPM output), the adjusted set-points were applied to the system model in PSCAD, and frequency and voltage maximum overshoot and settling time were calculated for the system response. Moreover, for comparison purposes, a second PSCAD simulation was conducted using the generated set-points for the DGD and DVC methods, and frequency and voltage maximum overshoot and settling time were calculated. These indices are listed in Table 5.21.

Table 5.21: Power system control quality indices for disturbance set three

	without use of ISCPM method				with use of ISCPM method			
case no	frq os (%)	frq t_s (s)	vlt os (%)	vlt t_s (s)	frq os (%)	frq t_s (s)	vlt os (%)	vlt t_s (s)
107	1.68	0.00	2.98	0.00	1.69	0.00	3.11	0.09
108	4.56	0.45	5.52	0.68	4.32	0.48	5.20	0.62
109	2.08	0.00	3.09	0.09	1.55	0.00	3.45	0.10
110	4.16	0.48	5.52	0.62	4.05	0.48	7.72	0.67
207	1.78	0.00	2.74	0.00	1.83	0.00	3.10	0.09
208	4.14	0.39	4.14	0.61	4.05	0.41	5.67	0.60
209	1.66	0.00	2.96	0.00	1.99	0.00	3.11	0.09
210	4.29	0.38	4.92	0.31	3.98	0.46	5.32	0.26
307	1.84	0.00	2.47	0.00	1.65	0.00	2.45	0.00
308	3.54	0.34	4.28	0.57	3.87	0.34	4.21	0.54
309	1.65	0.00	2.47	0.00	1.54	0.00	3.61	0.11
310	3.91	0.42	5.00	0.24	3.99	0.36	5.03	0.24

To illustrate how the frequency and voltage maximum overshoot and settling time were calculated, Figure 5.51 shows the measured frequency and DSTATCOM voltage in the system response to the ISCPM set-points in case 210. As previously shown in Figure 5.50, a 50MW pulse load with 5s duration was connected to the system at 10s, in this case. Figure 5.51(a) shows forecasted and measured powers for the pulse load. Figure 5.51(b) depicts forecasted and measured powers for the propulsion load and shows that the RLM method decreased the propulsion power when the pulse loads were connected. Figure 5.51(c) shows the adjusted MTG power set-points determined by the ISCPM method. Figure 5.51(d) depicts the system frequency in this case and shows that the maximum overshoot happened after the second pulse was disconnected at 21s. The maximum overshoot was 3.98%. In Figure 5.51(d), the reference value for the frequency (60Hz) is shown with solid cyan line. Also, the 3% deviation line is shown with dashed cyan line. It can be observed that when the second pulse load disconnected, the frequency was outside of the ±3% range for about 0.46s, after which it remained inside the ±3% range. Therefore, the frequency settling time was 0.46s in this case.

In Figure 5.51(e), the DSTATCOM terminal voltage in case 210 is shown with solid

black curve. Also, the DSTATCOM adjusted set-point determined by the ISCPM method is depicted with solid cyan line. Moreover, the ±3% range around the set-point is depicted with dashed cyan line. It can be observed that the maximum voltage deviation happened when the first pulse connected at 15s. The maximum overshoot was 5.32%. It can also be observed that after this overshoot, the DSTATCOM voltage settled inside the ±3% range after 0.26s and hence, the settling time was 0.26s.

Regarding the trend of change in the control indices, it can be observed from Table 5.21 that maximum overshoot and settling times for frequency and voltage increased from disturbance 07 to 08, and from 09 to 10, at each operating point, due to the increase in pulse load power from 20MW to 50MW. Regarding the acceptability of the indices, Table 5.21 shows that when set-points generated for the DGD and DVC methods were used, cases 108, 110, 208, and 210 had unacceptable maximum frequency overshoots. These cases correspond to sequential pulse loads of 50MW/1s at OP1, 50MW/5s at OP1, 50MW/1s at OP2, and 50MS/5s at OP2, respectively. By comparing the maximum frequency overshoot with and without use of ISCPM method in these cases, it can be observed that although the maximum frequency overshoot improved in each case, it was still unacceptable in case 108, 110, and 208. These unacceptable frequency responses happened when the system was operating in light or medium loading (OP1 or OP2), and sequential pulses with big powers (50MW) connected to the system.

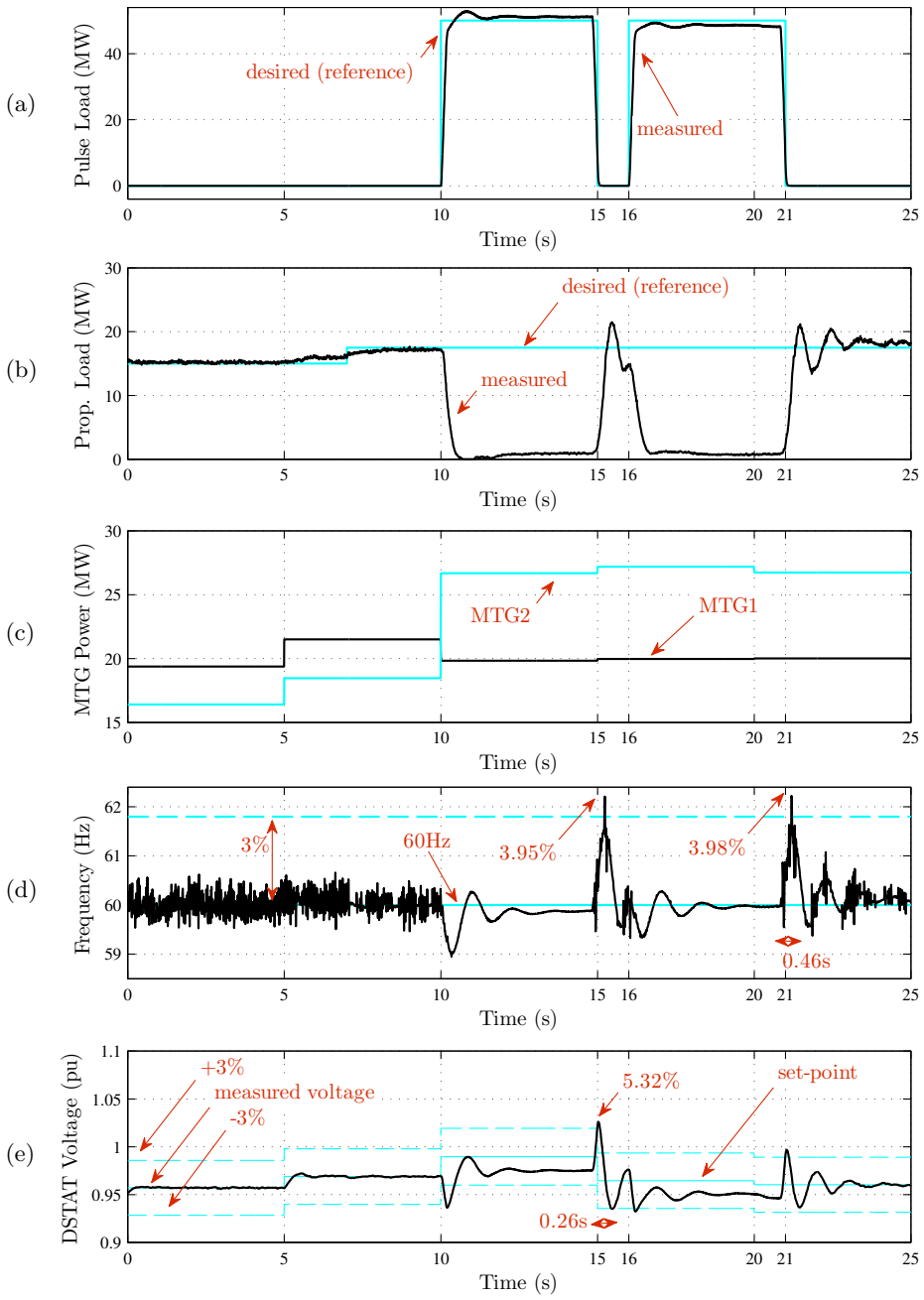

Figure 5.51: Frequency and voltage maximum overshoot and settling time with the ISCPM method in case 210. a) pulse load forecasted and measured power, b) propulsion load forecasted and measured power, c) adjusted MTG power set-points, d) measured frequency, and e) DSTATCOM adjusted set-point and measured terminal voltage

As an example, Figure 5.52 compares the system frequency response with and without use of the ISCPM method in case 210. It can be observed that the system frequency decreased when the pulses connected and increased when the pulses disconnected. In this case, maximum frequency overshoot happened when the second pulse was disconnected at 21s. At this time, system frequency had a 4.29% overshoot, if the set-points generated for the DGD and DVC methods were used. In the system response to the ISCPM set-points, this overshoot was improved to 3.98%, which was acceptable.

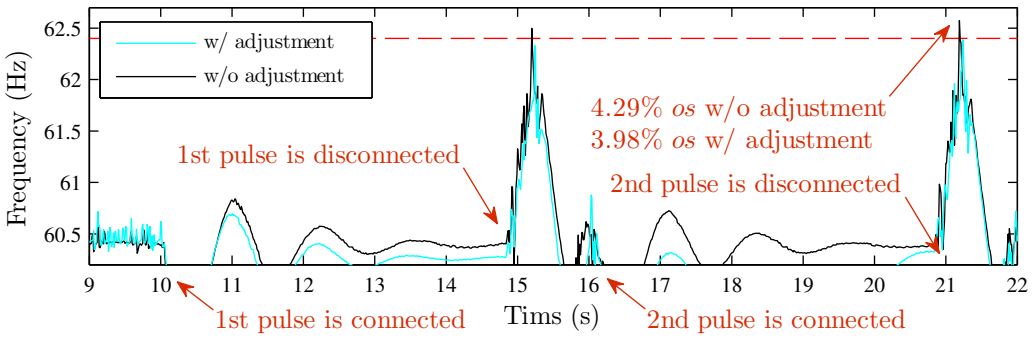

Figure 5.52: Frequency maximum overshoot with and without use of ISCPM method in case 210

In Table 5.21, by comparing the maximum voltage overshoot in the system response with and without use of ISCPM method in each case, it can be observed that the changes in this index were relatively small. Moreover, the system response in terms of the maximum voltage overshoot was always acceptable. Also, frequency and voltage settling times were small and acceptable in all of the 12 cases in this disturbance set.

5.3.6 Performance Analysis for Disturbance Set Four

The fourth disturbance set included planned outage of the main turbine generators, MTG1 and MTG2. For each case in this disturbance set, the study period was $T = 25$ seconds. The simulation length was also 25s. The decision intervals for the dynamic generation dispatch and the dynamic voltage/VAr control methods were assumed to be

$\tau_g = 5$ and $\tau_q = 5$ seconds, respectively. Therefore, the study period included $n_{\tau_g} = 5$ decision intervals for the generation dispatch method and $n_{\tau_q} = 5$ decision intervals for the VAr control method.

In each case, the power of each propulsion motor was forecasted to increase by 2.5MW at 7s. In each case, two signals were generated to mimic the DGD and DVC output signals in response to the forecasted load, as follows. To supply the load demand increase, it was assumed that the DGD method increased MTG1 power set-point by 5MW, starting from the second decision interval at 5s. Also, one of the MTGs was planned to be disconnected at 10s. To compensate for the generation power reduction, it was assumed that the DGD method increased the power of the other MTG with a 5s delay at 15s. Moreover, to compensate for the voltage drop caused by generator outage, it was assumed that the DVC method increased voltage set-points by 0.1%, in decision intervals 3, 4, and 5.

It was also assume that the ISCPM method did not adjust ATG power set-points and their power set-points remained constant at their initial values for each operating point during the studies. Therefore in the studies, the ISCPM method could only adjust MTG1 and MTG2 power set-points and generator and DSTATCOM voltage set-points, in each of the five decision intervals.

To illustrate the case setup, consider case 311 as an example, in which MTG1 outage was studied. Figure 5.53 shows shows the forecasted load and and the set-points generated to mimic responses of the DGD and DVC methods, for this case. As shown in this Figure 5.53(a), the power of each PM was forecasted to increase from 20MW to 22.5MW at 7s. Figure 5.53(b) shows MTG1 power set-point was increased by 5MW at 5s. It also shows that MTG1 power set-point was decreased to zero at 10s, since it was planned to be disconnected at that time. This figure also shows that MTG2 power set-point was increased at 15s, to compensate for MTG1 outage. Figure 5.53(c) shows that the voltage set-points were increased by 0.1% at 10s.

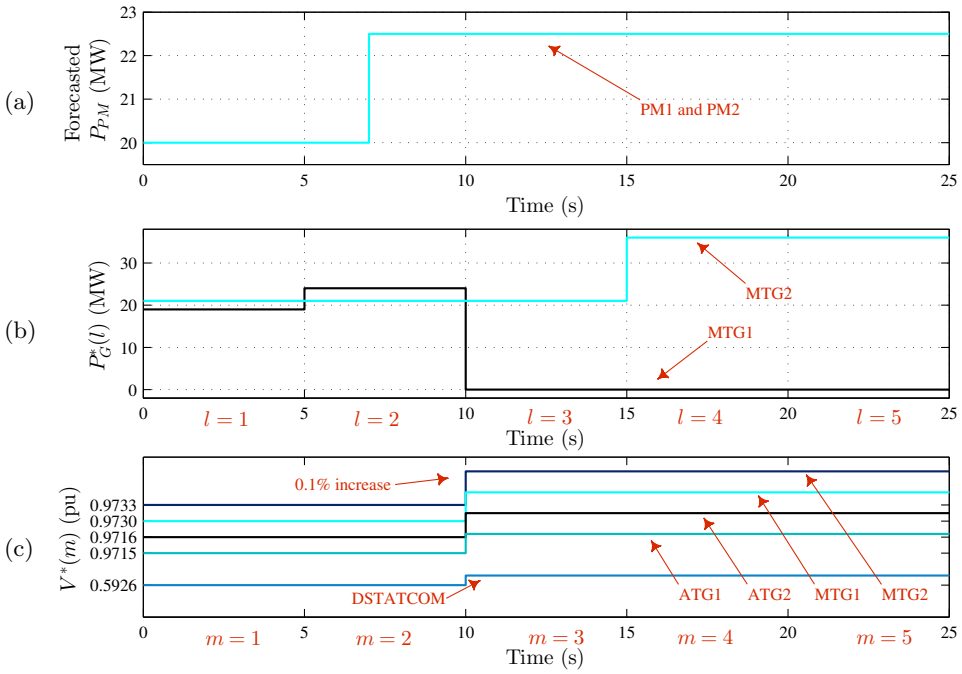

Figure 5.53: Case setup for case 311. a) Forecasted propulsion load, b) generated power set-points for the DGD method, and c) generated voltage set-points for the DVC method

In each case, a PSCAD simulation was conducted without the ISCPM method, using the set-points generated for the DGD and DVC methods. It was observed that the propulsion load increase caused the system operating point to move outside of the system RDSR. Also, although the voltage set-points were increased during decision intervals 3-5, the voltage at PM2 terminal operated below 0.95pu for more than 2s. Therefore, the PSCAD simulation results showed that the set-points generated for the DGD and DVC methods resulted in security and operating constraint violations, in each case.

Next, the ISCPM method was applied in each case and the adjusted set-points were determined by the ISCPM method. The spacing and overall nondominated vector generation indices were calculated for the Pareto optimal fronts obtained in each case. Then, a PSCAD simulation of the study period was conducted using the adjusted set-points determined by the ISCPM method. Using the simulation results, frequency and voltage maximum overshoot and settling time were calculated, for each case.

The Pareto set quality indices, I_{ONVG} and I_{S}, are listed in Table 5.22. This table also shows the three objective functions, f_{o_1}, f_{o_2}, and f_{o_3}, for the best compromise solution in each case. The I_{ONVG} index values in this table show that the Pareto front contained enough Pareto solutions in each case. Also, the I_{S} index values show that the Pareto front in each case had a good disturbance, since the spacing index was less than 5% in all of the cases.

Table 5.22: MOEA quality indices for disturbance set four

case no	f_{o_1} (MW^2)	f_{o_2} (MW^2)	f_{o_3} (pu^2)	I_{ONVG}	I_{S} (%)
111	40.17	10.93	5.617E-03	161	3.02
112	40.75	1.09	2.616E-03	169	2.21
211	6.56	4.28	8.999E-03	185	2.63
212	31.01	28.38	5.311E-03	94	2.51
311	6.74	1.71	3.999E-03	186	2.85
312	51.57	56.27	8.606E-03	77	2.37

In each case, after determining the best compromise solution (the ISCPM output), the adjusted set-points were applied to the system model in PSCAD, and frequency and voltage maximum overshoot and settling time were calculated for the system response. Moreover, for comparison purposes, a second PSCAD simulation was conducted using the generated set-points for the DGD and DVC methods, and frequency and voltage maximum overshoot and settling time were calculated. These indices are listed in Table 5.23.

Table 5.23: Power system control quality indices for disturbance set four

	without use of ISCPM method				with use of ISCPM method			
case no	frq os (%)	frq t_s (s)	vlt os (%)	vlt t_s (s)	frq os (%)	frq t_s (s)	vlt os (%)	vlt t_s (s)
111	2.16	0.00	1.77	0.00	2.07	0.00	3.29	0.00
112	1.40	0.00	2.88	0.00	1.51	0.00	3.10	0.04
211	1.35	0.00	1.97	0.00	1.31	0.00	3.96	0.03
212	1.28	0.00	2.94	0.00	1.41	0.00	3.77	0.06
311	1.43	0.00	1.95	0.00	1.14	0.00	2.29	0.00
312	1.30	0.00	2.21	0.00	0.98	0.00	2.55	0.00

To illustrate how the frequency and voltage maximum overshoot and settling time were calculated, Figure 5.54 shows the measured frequency and DSTATCOM voltage in the system response to the ISCPM set-points in case 311. As previously shown in Figure 5.53, MTG1 was planned to be disconnected at 10s in this case. Figure 5.54(a) depicts forecasted and measured powers for the propulsion load and shows that the RLM method decreased the propulsion power after 10s, due to insufficient generation power. Figure 5.54(b) shows the adjusted MTG power set-points determined by the ISCPM method. Figure 5.54(c) shows the system frequency in response to the ISCPM set-points in this case. It can be observed that the maximum overshoot happened after MTG1 was disconnected at 10s. The maximum overshoot was 1.14%. Since the frequency deviation in this case was always less than 3%, the settling time for frequency was zero.

In Figure 5.54(d), the DSTATCOM terminal voltage in case 311 is shown with solid black curve. Also, the DSTATCOM adjusted set-point determined by the ISCPM method is depicted with solid cyan line. Moreover, the ±3% range around the set-point is depicted with dashed cyan line. It can be observed that the maximum voltage deviation happened when MTG1 was disconnected at 10s. The maximum overshoot was 2.29%. It can also be observed that after this overshoot, the DSTATCOM voltage was always within 3% of its set-point, and hence, the settling time was zero.

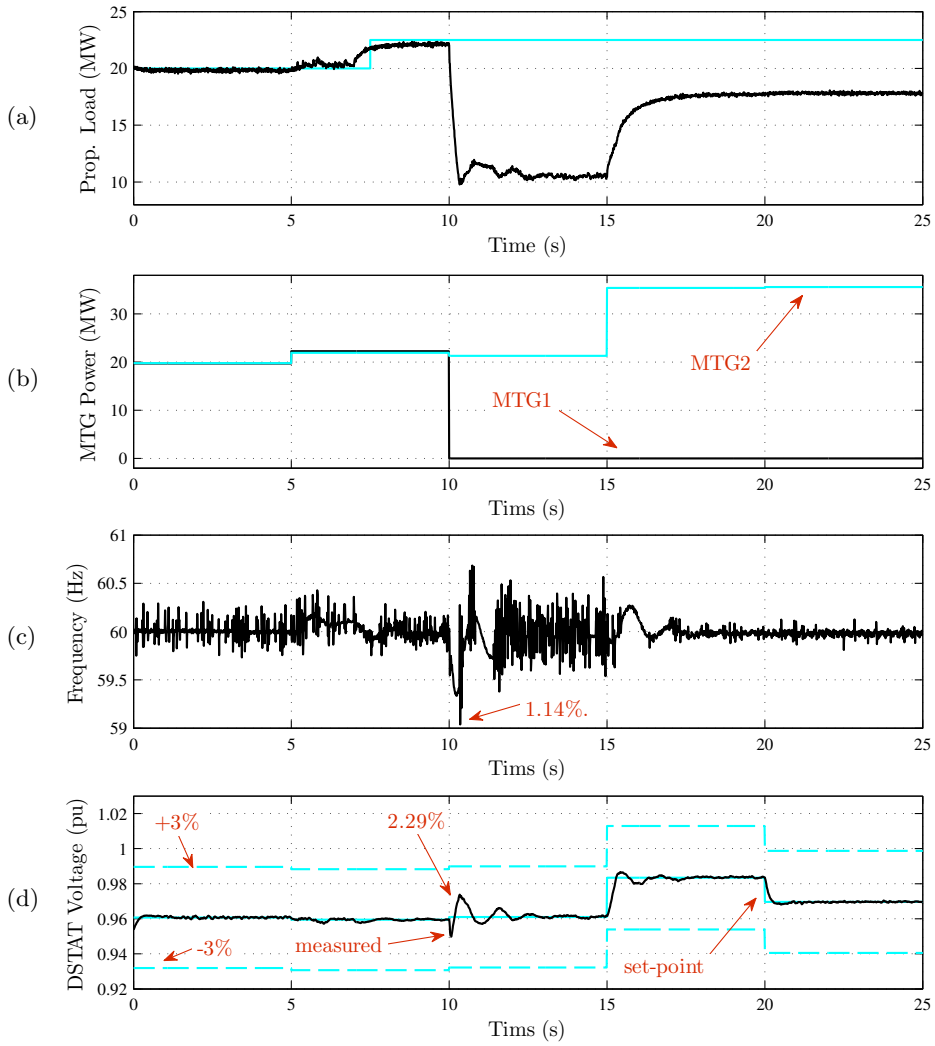

Figure 5.54: Frequency and voltage maximum overshoot and settling time with the ISCPM method in case 311. a) propulsion load forecasted and measured power, b) adjusted MTG power set-points, c) measured frequency, and d) DSTATCOM adjusted set-point and measured terminal voltage

Table 5.23 shows that frequency and voltage maximum overshoot and settling time were relatively small and acceptable, in all of the six cases in this disturbance set, with and without use of ISCPM method. As an example, Figure 5.55 compares the frequency response of the system in case 111, with and without use of ISCPM method. In this case, MTG1 with 25MW power was disconnected at 10s. To compensate for the reduction in system generation, MTG2 power set-point was increased from 6MW to 31MW at 15s.

Figure 5.55 shows that system frequency decreased when MTG1 was disconnected and increased when MTG2 power set-point was increased. In this case, maximum frequency deviation happened after MTG2 power was increased. At this time, the frequency overshoot was 2.16%, if the DGD and DVC set-points were used. The frequency overshoot was 2.07%, if the ISCPM set-points were applied to the system. Both of these values were acceptable for maximum frequency overshoot.

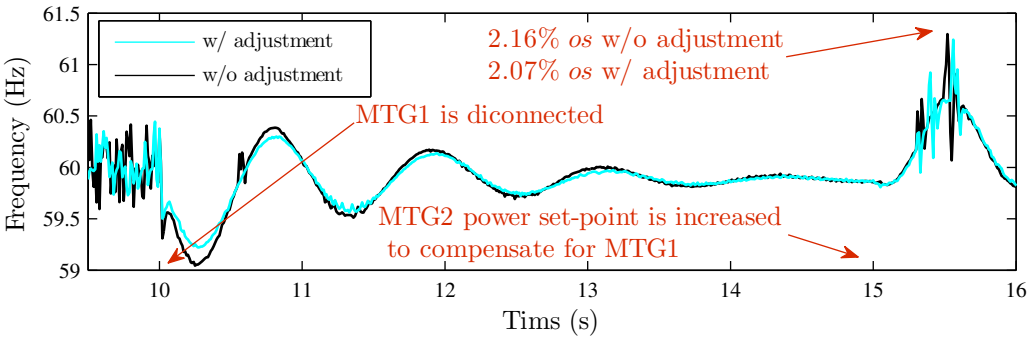

Figure 5.55: Frequency maximum overshoot with and without use of ISCPM method in case 111

5.4 Summary of Findings

In this section, the new ISCPM method was applied to a notional all-electric ship computer model. Four problem-based case studies were presented to illustrate how the new ISCPM power management method works. In case I, a sharp increase in propulsion power was studied. Case II studied connection of sequential pulse loads to the system. In case III, the planned disconnection of an MTG was studied. In Case IV the focus was on DC zones. In this case, several load changes inside the DC zones and connection of a pulse load to the system were studied. In these cases, the system operation with and without use of the ISCPM method were compared. It was observed that if the ISCPM method was not used, the security constraints for planned and unplanned events were violated in several instances. However, if the ISCPM method was used, no security constraint violation was observed. This comparison emphasized on the need to develop an effective

security-constrained power management method for isolated microgrid power systems, like the new ISCPM method.

Next, the results of the extensive studies, conducted to analyze the performance of the new power management method, were presented and discussed. For these studies, several disturbances at various operating points were used. The disturbances included sharp changes in the power of propulsion loads, connection of single and sequential pulse loads to the system, and planned outage of the MTGs. Three operating points were studied, which represented light loading, medium loading, and heavy loading in the notional AES model. At each operating point and for each disturbance, the performance of the new ISCPM method was analyzed from two different perspectives: quality of the Pareto optimal front solution from multi-objective optimization perspective and quality of the control solution from power system operation perspective. For the former, two quality measures were used: I_S and I_{ONVG}. For the latter, four quality measures were used: maximum frequency overshoot, maximum voltage overshoot, frequency settling time, and voltage settling time.

To calculate the multi-objective optimization quality indicies, the ISCPM method was applied to each case and the Pareto optimal front was obtained. Then, I_S and I_{ONVG} indices were calculated for the resulting Pareto optimal front. Next, the ISCPM method determined the best compromise solution. A transient PSCAD simulation was carried out, using the adjusted set-points of the best compromise solution (the output of the ISCPM method). Then, using the PSCAD simulation results, maximum overshoot and settling time for system frequency and load bus voltages were calculated. A summary of the findings, for each index, follows.

The **overall nondominated vector generation index**, I_{ONVG}, reports the number of Pareto solutions in the Pareto optimal front. There is no standard value for I_{ONVG} in the literature to represent good performance. However, an arbitrary limit was used for the performance studies discussed in this dissertation, in which a minimum of 75 solutions was considered to be enough for a good Pareto set in terms of extent. It was observed that the

Pareto front for each case in the four disturbance sets included enough Pareto solutions. The only exception was case 302, in which a total propulsion power increase of 30MW was desirable, while the system was operating in heavy loading (OP3). The poor extent of the Pareto optimal front in this case was because the feasible optimization space was very small, since the system was operating close to its maximum secure loading. Consequently, the NSGA-II method could not generate enough solutions for the Pareto front and hence, the value of the I_{ONVG} index in this case was less than 75.

The **spacing index**, I_{S}, reports the relative distance between the consecutive solutions in the Pareto optimal front. The ideal spread in a Pareto front is the uniform distribution, which has a spacing index of 0%. I_{S} increases as the distribution of solutions deviates from the uniform distribution. Hence, lower values for this index are desired. There is no standard value for I_{S} in the literature to represent good performance. For the performance studies discussed in this dissertation, an arbitrary limit was defined, in which a Pareto front with a maximum of 5% spacing index was considered to be a good Pareto front in terms of spread. The value of the spacing index was acceptable in all of the cases in disturbance set one and four, i.e. sharp propulsion load increase and MTG outage events. However, in several cases in which pulse power loads were used, I_{S} was more than 5%, which indicated a poor spread of solutions in the Pareto front. Not a concrete reason could be found to justify this observation. A possible explanation could be that the spacing index may be poor in extreme disturbances, like the pulse loads studied in this work.

The **maximum frequency overshoot**, reports the maximum deviation from the nominal frequency, and must be less than 4% for shipboard power systems [99]. In general, it was observed that the ISCPM set-point adjustments improved the maximum frequency overshoot. However, in some cases, the frequency overshoot in the system response to the ISCPM set-points was still not acceptable. The cases in which the ISCPM method failed to keep the frequency overshoot below 4% were the following: single 50MW/5s pulse in light loading (case 106), single 50MW/5s pulse in medium loading (case 206), sequential 50MW/1s pulse in light loading (108), sequential 50MW/1s pulse in medium

loading (208), and sequential 50MW/5s pulse in light loading (110). It was concluded that when the system was operating in light or medium loading and a high power pulse load (50MW magnitude) was connected to the system, the ISCPM method could improve the maximum frequency overshoot compared to the case without the ISCPM method, but it was unable to keep the maximum frequency overshoot below 4%.

Two reasons contribute to the unacceptable maximum frequency overshoot in these cases. First, when the system was operating in light or medium loading, a 50MW pulse load was a big disturbance, relative to the system total generation. Hence, this big disturbance caused severe frequency oscillations in the system, which could not be controlled by the actions of the real-time load management method. Second, since the 4% maximum frequency deviation was among the security constraints for planned events included in the ISCPM optimization problem, one could expect that the maximum frequency overshoot in the case studies must also be limited to 4%. This expectation could only be true, if the system model used in the optimization (in TSAT) was the same as the system model used for ISCPM performance studies (in PSCAD). In other words, although the maximum frequency deviation was less than 4% according the TSAT model used in the optimization, it was more than 4% when the simulations were conducted in PSCAD. In simpler words, in the new model-based ISCPM power management method, the difference between the system model used in the optimization and the actual system could cause result in constraint violations.

The **frequency settling time**, reports the time it takes for the frequency to settle within 3% of the nominal value, and must be less than 2s for shipboard power systems [99]. For sharp propulsion load increase events (cases 101, 102, 201, 202, 301, and 302) and MTG outage events (cases 111, 112, 211, 212, 311, and 312), the frequency settling time was zero, since frequency deviation was always less than 3%. Hence, the frequency settling time was acceptable. For cases in which single or sequential pulse loads were used (cases 103-110, 203-210, and 303-310), the frequency settling time was always less than 2s, since the system frequency returned to its 3% range, quickly, in each case. Therefore, the frequency settling

time was acceptable for all of the cases studied in this dissertation, since either the frequency deviation was always less than 3% and hence the frequency settling time was zero, or the frequency deviated more than 3%, but quickly settled inside the ±3% range.

The **maximum voltage overshoot**, reports the maximum voltage deviation from its final value during a disturbance. Since a maximum acceptable value could not be found in the literature, a 10% maximum acceptable voltage overshoot was arbitrarily used in this dissertation. For sharp propulsion load increase events (cases 101, 102, 201, 202, 301, and 302) and MTG outage events (cases 111, 112, 211, 212, 311, and 312), the maximum voltage overshoots were in the range of 0.5%-1%, and 2%-4%, respectively. For cases in which single or sequential pulse loads were used (cases 103-110, 203-210, and 303-310), higher maximum overshoots between 2% and 8% were observed. Hence, the maximum voltage overshoot index was acceptable in each case. The acceptable maximum voltage overshoot for all cases could be because the notional all-electric shipboard power system included a DSTATCOM, which contributed to the good transient voltage behavior in the system.

The **voltage settling time**, reports the time it takes for the voltage to settle within 3% of its final value and must be less than 3s [99]. For sharp propulsion load change events (cases 101, 102, 201, 202, 301, and 302) and MTG outage events (cases 111, 112, 211, 212, 311, and 312), since the voltage deviations were very small, the voltage settling time was almost zero. For cases in which single or sequential pulse loads were used (cases 103-110, 203-210, and 303-310), voltage settling times were between 0s and 0.7s. Therefore, the voltage settling time index was acceptable in all of the cases. The acceptable voltage settling time for all cases could be because the notional all-electric shipboard power system included a DSTATCOM, which contributed to the good transient voltage behavior in the system.

5.5 Section Summary

In this section, several problem-based case studies were presented and discussed. These cases illustrated how the new ISCPM power management approach works. In this work, extensive studies was also carried out to evaluate the performance of the new power management method. The results of the extensive studies were also presented and discussed in this section. In the extensive case studies, the performance of the new power management method at different operating points and for various events (disturbances) was analyzed. Several quality indices were used in the performance analysis, to evaluate the performance of the ISCPM method, quantitatively. The quality indices were used to provide an estimate of the solution quality from power system control and multi-objective optimization perspectives.

6 CONCLUSIONS AND FUTURE WORK

6.1 Summary and Conclusions

This dissertation presented and discussed a new power management method, developed for isolated microgrid power systems during normal/alert states. The new power management method, referred to as the ISCPM method in this dissertation, has several features. First, it manipulates the set-points provided by several control methods operating in normal/alert states in microgrid power systems. Second, it uses a dynamic optimization approach which optimizes the system behavior during a time period in the future. Third, the new power management method not only ensures the system dynamic security for unplanned events, but also ensures that the system operating constraints are not violated during planed events in the study period.

The new power management method was formulated as a Multi-Objective Optimal Control (MOOC) problem [74], in which the set-points provided by various system control methods are minimally adjusted, to satisfy the security constraints for planned and unplanned events. To solve the formulated MOOC problem, an evolutionary multi-objective optimization solver based on the Nondominated Sorting GA II (NSGA-II) [75] was developed, in the new ISCPM method. A model-based approach was developed which links the multi-objective optimization solver to a fast simulation core that conducts transient simulations of the power system model during the GA iterations. The results of the transient simulations are used to evaluate the ISCPM constraints, which include generation-load balance constraints, dynamic security constraints for planned events, and dynamic security constraints for unplanned events.

To evaluate the security constraints for planned events, a point-wise approach adapted from the constraint transcription technique was developed. In this approach, security constraints for planned events were defined on the time that each constrained quantity (such as system frequency or load bus voltages) spends in a constraint band. To evaluate the security constraints for unplanned events, a region-based method was developed. The

Dynamic Secure Region (DSR) assessment method used for conventional large scale power systems was adapted to be applicable for isolated microgrid power systems. In contrast with the approach for conventional power system in which the DSR is obtained around the current operating point, the new approach approximates the dynamic secure region in the entire system operating space.

The performance of the new ISCPM method was studied on a simulated notional isolated microgrid power system computer model for an all-electric ship. To apply the ISCPM method to the notional AES, the multi-objective optimization method was implemented in MATLAB, by adapting the IlliGAL toolbox [145]. The multi-objective optimization solver in MATLAB was linked to the TSAT tool of DSA *Tools*$^{\text{TM}}$ [100], where a transient model of the notional all-electric ship was implemented. The best compromise solution identification was also carried out in MATLAB.

To illustrate how the new ISCPM method works, four problem-based case studies were presented, in which a sharp increase in propulsion load power, connection of sequential pulse power loads to the system, planned outage of a main turbine generator, and several zonal load changes were studied. In these cases, the system operation with and without use of the ISCPM method were compared by conducting two PSCAD simulations. It was observed that if the ISCPM method was not used, the security constraints for planned and unplanned events were violated in several instances. However, if the ISCPM method was used, no security constraint violation was observed. These comparisons emphasized on the need to develop an effective security-constrained power management method for isolated microgrid power systems.

To evaluate the performance of the new ISCPM method on the notional all-electric ship computer model, extensive case studies were conducted at different operating points and during various events. Particularly, three operating points were chosen to represent light loading, medium loading, and heavy loading in the notional all-electric ship model. Moreover, four sets of events were developed which included sharp increases in the propulsion load, serving single pulse power loads, serving sequential pulse loads, and

disconnecting a main turbine generator. At each operating point and for each disturbance, the performance of the new ISCPM method was analyzed from two different perspectives: quality of the Pareto optimal front solution from multi-objective optimization perspective and quality of the control solution for the power system operation perspective. To evaluate the quality of the Pareto optimal front solution from optimization perspective, Overall Nondominated Vector Generation (I_{ONVG}) index and spacing index (I_{S}) [82] were used, which provide an estimate for spread quality and extent quality in a Pareto optimal front, respectively [82]. It was observed that the Pareto front in each case included enough Pareto solutions (there was only one exception) and hence, the I_{ONVG} index was acceptable. The spacing index was acceptable in cases with sharp increases in the propulsion load power and MTG outages. However, in several cases in which pulse loads were used, the spacing index was not acceptable, which indicated a poor spread of solutions in the Pareto optimal front.

To evaluate the quality of the control solution from power system operation perspective, maximum overshoot and settling time [150] for frequency and voltage in the system response to the ISCPM set-points were used. It was observed that the maximum voltage overshoot, frequency settling time, and voltage settling time indices were acceptable in all of the studied cases. However, the maximum frequency overshoot was not acceptable in cases where the system was operating at light or medium loading and a high power power load was used.

Based on the problem-based and extensive case studies, it was concluded that the new ISCPM power management method could effectively operate isolated microgrid power systems in an overall near-optimal state, while satisfying the security constraints for planned and unplanned events. However, since a model-based approach was used for the new ISCPM method, the discrepancy between the system model in the ISCPM method and the actual system could result in constraint violations in some instances.

Regarding the quality of the new ISCPM method from the optimization perspective, the developed NSGA-II approach to solve the ISCPM multi-objective optimal control

problem could generally obtain high quality Pareto optimal fronts, in terms of extent and spread of the solutions. However, in some extreme disturbances, the obtained Pareto optimal fronts were poor in terms of the distribution. From the power system operation perspective, the adjusted power and voltage set-points determined by the ISCPM method generally improved the system response, compared to the case where the ISCPM method was not used. The improvement was more evident for the frequency response of the system. However, although the system frequency response improved when the ISCPM method was used, it was still unacceptable for extreme pulse load disturbances.

6.2 Future Work

In the NSGA-II approach developed for the new ISCPM method in this work, the distribution of the solutions in the obtained Pareto optimal front was poor in some cases. More studies can be conducted to investigate the reasons for the poor distribution of the Pareto front and to determine possible ways of improving the distribution.

In this work, an open-loop model-based approach was used for the new ISCPM power management method. Using a closed loop approach, such as Model Predictive Control (MPC), can be investigated as a possible improvement to the new power management method. A closed loop control may be advantageous, especially for systems with high uncertainties, in which load forecast may be significantly different from the actual load.

In this dissertation, the new power management method was applied to a simulated notional all-electric ship computer model. However, application of the new power management method is not limited to all-electric shipboard power systems. The developed power management approach could also be applied to other types of isolated microgrid power systems, since they share several similarities with all-electric shipboard power systems. In applying the new ISCPM power management method to other types of isolated power systems, new challenges may arise. For example, other microgrid power systems may include energy storage devices. Therefore, effective utilization of these devices must also be addressed by the power management method.

REFERENCES

[1] J. M. Crider and S. D. Sudhoff, "Reducing impact of pulsed power loads on microgrid power systems," *IEEE Trans. Smart Grid*, vol. 1, no. 3, pp. 270–277, 2010.

[2] A. S. Debs, *Modern power systems control and operation.* Boston, MA: Kluwer Academic Publishers, 1987.

[3] T. E. Dy Liacco, S. K. Mitter, R. K. Babickas, and T. J. Kraynak, "Multi-level approach to power system decision problems - the optimizing level," in *Power Industry Computer Applications Conference*, pp. 221–224, 1967.

[4] P. Kundur, N. J. Balu, and M. G. Lauby, *Power system stability and control.* NY: McGraw-Hill, 1994.

[5] Y. Sun, Y. Xinlin, and H. F. Wang, "Approach for optimal power flow with transient stability constraints," *IEE Generation, Transmission and Distribution*, vol. 151, pp. 8–18, 2004.

[6] D. Gan, R. J. Thomas, and R. D. Zimmerman, "Stability-constrained optimal power flow," *IEEE Trans. Power Systems*, vol. 15, no. 2, pp. 535–540, 2000.

[7] H. Beides and G. T. Heydt, "Multi-state power system optimization," in *North American Power Symposium*, pp. 95–104, 1989.

[8] M. La Scala, M. Trovato, and C. Antonelli, "On-line dynamic preventive control: an algorithm for transient security dispatch," *IEEE Trans. Power Systems*, vol. 13, no. 2, pp. 601–610, 1998.

[9] Y. Yuan, J. Kubokawa, and H. Sasaki, "A solution of optimal power flow with multicontingency transient stability constraints," *IEEE Trans. Power Systems*, vol. 18, no. 3, pp. 1094–1102, 2003.

[10] L. Chen, A. Ono, Y. Tada, H. Okamoto, and R. Tanabe, "Optimal operation of power systems constrained by transient stability," *Electrical Engineering in Japan*, vol. 137, no. 1, pp. 17–27, 2001.

[11] X. Fei and J. D. McCalley, "Power system risk assessment and control in a multiobjective framework," *IEEE Trans. Power Systems*, vol. 24, no. 1, pp. 78–85, 2009.

[12] X. Feng, *A bio-inspired multi-agent system framework for real-time load management in all-electric ship power systems*. PhD dissertation, Texas A&M University, 2012.

[13] W. H. Esselman, D. J. Sobajic, and J. Maulbetsch, "Hybrid discrete and continuous control for power systems," *Discrete Event Dynamic Systems*, vol. 9, no. 4, pp. 297–318, 1999.

[14] Q. Shi-Yin and S. Yong-Hua, "The theory of hybrid control systems and its application perspective in electric power systems," in *International Conferences on Info-tech and Info-net*, vol. 4, pp. 85–94, 2001.

[15] T. E. Dy Liacco, *Control of power systems via the multi-level concept*. PhD dissertation, Case Western Reserve University, 1968.

[16] U. G. Knight, *Power systems in emergencies: from contingency planning to crisis management*. NY: John Wiley, 2001.

[17] J. D. McCalley, V. Vittal, and N. Abi-Samra, "An overview of risk based security assessment," in *IEEE Power Engineering Society Summer Meeting*, vol. 1, pp. 173–178, 1999.

[18] L. H. Fink and K. Carlsen, "Operating under stress and strain," *IEEE Spectrum*, vol. 15, no. 3, pp. 48–53, 1978.

[19] A. J. Wood and B. F. Wollenberg, *Power generation, operation and control*. NY: Wiley-Interscience, 2009.

[20] S. C. Savulescu, *Real-Time stability in power systems: techniques for early detection of the risk of blackout.* NY: Springer, 2006.

[21] N. Balu, T. Bertram, A. Bose, V. Brandwajn, G. Cauley, D. Curtice, A. Fouad, L. Fink, M. G. Lauby, B. F. Wollenberg, and J. N. Wrubel, "On-line power system security analysis," *Proceedings of the IEEE*, vol. 80, no. 2, pp. 262–282, 1992.

[22] R. C. Burchett, H. H. Happ, and K. A. Wirgau, "Large scale optimal power flow," *IEEE Trans. Power Apparatus and Systems*, vol. PAS-101, no. 10, pp. 3722–3732, 1982.

[23] C. Jiann-Fuh and C. Shin-Der, "Multiobjective power dispatch with line flow constraints using the fast Newton-Raphson method," *IEEE Trans. Energy Conversion*, vol. 12, no. 1, pp. 86–93, 1997.

[24] F. A. Mohamed and H. N. Koivo, "Microgrid online management and balancing using multiobjective optimization," in *IEEE Lausanne Power Tech*, pp. 639–644, 2007.

[25] B. Zhao, C. X. Guo, and Y. J. Cao, "A multiagent-based particle swarm optimization approach for optimal reactive power dispatch," *IEEE Trans. Power Systems*, vol. 20, no. 2, pp. 1070–1078, 2005.

[26] F. Batrinu, E. Carpaneto, G. Chicco, M. De Donno, R. Napoli, R. Porumb, P. Postolache, and C. Toader, "New nested evolutionary programming approach for voltage control optimization with distributed generation," in *IEEE Mediterranean Electrotechnical Conference*, vol. 3, pp. 1007–1010, 2004.

[27] X. Ding and C. Zhao, "The research of practical method used for dynamic reactive power optimization," in *Electric Utility Deregulation and Restructuring and Power Technologies*, pp. 671–674, 2008.

[28] M. Ettappan and M. Rajaram, "Artificial bee colony algorithm for optimal reactive power dispatch," *International Journal of Applied Engineering Research*, vol. 7, no. 12, pp. 1413–1419, 2012.

[29] P. Mitra and G. K. Venayagamoorthy, "Implementation of an intelligent reconfiguration algorithm for an electric ship's power system," *IEEE Trans. Industry Applications*, vol. 47, no. 5, pp. 2292–2300, 2011.

[30] K. L. Butler-Purry and N. D. R. Sarma, "Self-healing reconfiguration for restoration of naval shipboard power systems," *IEEE Trans. Power Systems*, vol. 19, no. 2, pp. 754–762, 2004.

[31] X. Yan, C. Ka Wing, and L. Mingbo, "Improved BFGS method for optimal power flow calculation with transient stability constraints," in *IEEE Power Engineering Society General Meeting*, vol. 1, pp. 434–439, 2005.

[32] Y. Xia, K. W. Chan, and M. Liu, "Direct nonlinear primal-dual interior-point method for transient stability constrained optimal power flow," *IEEE Generation, Transmission and Distribution*, vol. 152, no. 1, pp. 11–16, 2005.

[33] W. Fu, *Risk assessment and optimization for electric power systems.* PhD dissertation, Iowa State University, 2000.

[34] R. L. LaCarna and J. R. Johnson, "Optimal rescheduling for power system security via pattern recognition and search methods," *IEEE Trans. Systems, Man and Cybernetics*, vol. 9, no. 5, pp. 293–296, 1979.

[35] J. C. Kaltenbach and L. P. Hajdu, "Optimal corrective rescheduling for power system security," *IEEE Trans. Power Apparatus and Systems*, vol. PAS-90, no. 2, pp. 843–851, 1971.

[36] Y. Kato and S. Iwamoto, "Transient stability preventive control for stable operating condition with desired CCT," *IEEE Trans. Power Systems*, vol. 17, no. 4, pp. 1154–1161, 2002.

[37] E. De Tuglie, M. Dicorato, M. La Scala, and P. Scarpellini, "A static optimization approach to assess dynamic available transfer capability," *IEEE Trans. Power Systems*, vol. 15, no. 3, pp. 1069–1076, 2000.

[38] S. M. Chan and F. C. Schweppe, "A generation reallocation and load shedding algorithm," *IEEE Trans. Power Apparatus and Systems*, vol. PAS-98, no. 1, pp. 26–34, 1979.

[39] S. Phichaisawat, Y. H. Song, and G. A. Taylor, "Congestion management considering voltage security constraints," in *International Conference on Power System Technology*, vol. 3, pp. 1819–1823, 2002.

[40] A. C. Chiang, *Elements of dynamic optimization.* NY: McGraw-Hill, 1992.

[41] H. Saadat, *Power system analysis.* NY: McGraw-Hill, 1999.

[42] J. A. Momoh, *Electric power system applications of optimization.* NY: Marcel Dekker, 2001.

[43] S. Agrawal, B. K. Panigrahi, and M. K. Tiwari, "Multiobjective particle swarm algorithm with fuzzy clustering for electrical power dispatch," *IEEE Trans. Evolutionary Computation*, vol. 12, no. 5, pp. 529–541, 2008.

[44] M. A. Abido, "Multiobjective evolutionary algorithms for electric power dispatch problem," *IEEE Trans. Evolutionary Computation*, vol. 10, no. 3, pp. 315–329, 2006.

[45] K. Xie and Y. H. Song, "Dynamic optimal power flow by interior point methods," *IEE Generation, Transmission and Distribution*, vol. 148, no. 1, pp. 76–84, 2001.

[46] W. Wei, W. Daifeng, A. Arapostathis, and K. Davey, "Optimal power generation scheduling of a shipboard power system," in *IEEE Electric Ship Technologies Symposium*, pp. 519–522, 2007.

[47] C. Ting, L. Chen-Ching, and B. M. Howe, "Optimization based load management for the NEPTUNE power system," in *IEEE Power Engineering Society General Meeting*, pp. 1–6, 2007.

[48] X. Feng, K. L. Butler-Purry, and T. Zourntos, "Multi-agent system-based real-time load management for all-electric ship power systems in DC zone level," *IEEE Trans. Power Systems*, vol. 27, no. 4, pp. 1719–1728, 2012.

[49] S. Ashok and R. Banerjee, "An optimization mode for industrial load management," *IEEE Trans. Power Systems*, vol. 16, no. 4, pp. 879–884, 2001.

[50] L. Fang, C. Y. Chung, K. P. Wong, Y. Wei, and X. Guoyu, "Hybrid immune genetic method for dynamic reactive power optimization," in *International Conference on Power System Technology*, pp. 1–6, 2006.

[51] Z. Y. Pan, X. S. Han, and M. Yang, "A practical solution method of dynamic reactive power optimization in AVC," in *International Conference on Sustainable Power Generation and Supply*, pp. 1–5, 2009.

[52] A. Thanikachalam and J. R. Tudor, "Optimal rescheduling of power for system reliability," *IEEE Trans. Power Apparatus and Systems*, vol. PAS-90, no. 5, pp. 2186–2192, 1971.

[53] K. N. Shubhanga and A. M. Kulkarni, "Stability-constrained generation rescheduling using energy margin sensitivities," *IEEE Trans. Power Systems*, vol. 19, no. 3, pp. 1402–1413, 2004.

[54] T. B. Nguyen and M. A. Pai, "Dynamic security-constrained rescheduling of power systems using trajectory sensitivities," *IEEE Trans. Power Systems*, vol. 18, no. 2, pp. 848–854, 2003.

[55] J. Q. Sun, K. W. Chan, and D. Z. Fang, "Optimal generation rescheduling for security operation of power systems using optimal control theory," in *International Conference on Power Electronics and Drive Systems*, pp. 1205–1208, 2007.

[56] A. L. Bettiol, L. Wehenkel, and M. Pavella, "Transient stability-constrained maximum allowable transfer," *IEEE Trans. Power Systems*, vol. 14, no. 2, pp. 654–659, 1999.

[57] C. Roman and W. Rosehart, "Evenly distributed Pareto points in multi-objective optimal power flow," *IEEE Trans. Power Systems*, vol. 21, no. 2, pp. 1011–1012, 2006.

[58] W. D. Rosehart, C. A. Canizares, and V. H. Quintana, "Multiobjective optimal power flows to evaluate voltage security costs in power networks," *IEEE Trans. Power Systems*, vol. 18, no. 2, pp. 578–587, 2003.

[59] R. Yokoyama, S. H. Bae, T. Morita, and H. Sasaki, "Multiobjective optimal generation dispatch based on probability security criteria," *IEEE Trans. Power Systems*, vol. 3, no. 1, pp. 317–324, 1988.

[60] C. S. Chang, K. P. Wong, and B. Fan, "Security-constrained multiobjective generation dispatch using bicriterion global optimisation," *IEEE Generation, Transmission and Distribution*, vol. 142, no. 4, pp. 406–414, 1995.

[61] S. Yongchun, C. Shijie, W. Jinyu, and Z. Yonggao, "Reactive power generation management for the improvement of power system voltage stability margin," in *World Congress on Intelligent Control and Automation*, vol. 2, pp. 7466–7469, 2006.

[62] R. R. Shoults and C. Mo-Shing, "Reactive power control by least squares minimization," *IEEE Trans. Power Apparatus and Systems*, vol. 95, no. 1, pp. 325–334, 1976.

[63] K. R. C. Mamandur, "Emergency adjustments to VAr control variables to alleviate over-voltages, under-voltages, and generator VAr limit violations," *IEEE Trans. Power Apparatus and Systems*, vol. PAS-101, no. 5, pp. 1040–1047, 1982.

[64] G. Opoku and C. M. Ong, "Reactive power control to alleviate bus voltage violations in an AC-DC system," *IEEE Trans. Power Apparatus and Systems*, vol. PAS-104, no. 1, pp. 75–81, 1985.

[65] P. Kundur, J. Paserba, V. Ajjarapu, G. Andersson, A. Bose, C. Canizares, N. Hatziargyriou, D. Hill, A. Stankovic, C. Taylor, T. Van Cutsem, and V. Vittal, "Definition and classification of power system stability," *IEEE Trans. Power Systems*, vol. 19, no. 3, pp. 1387–1401, 2004.

[66] A. Mehrizi-Sani and R. Iravani, "Potential-function based control of a microgrid in islanded and grid-connected modes," *IEEE Trans. Power Systems*, vol. 25, no. 4, pp. 1883–1891, 2010.

[67] J. M. Guerrero, J. C. Vasquez, J. Matas, L. G. de Vicuña, and M. Castilla, "Hierarchical control of droop-controlled AC and DC microgrids – a general approach toward standardization," *IEEE Trans. Industrial Electronics*, vol. 58, no. 1, pp. 158–172, 2011.

[68] D. W. Ross and K. Sungkook, "Dynamic economic dispatch of generation," *IEEE Trans. Power Apparatus and Systems*, vol. PAS-99, no. 6, pp. 2060–2068, 1980.

[69] T. Niknam, R. Azizipanah-Abarghooee, and A. Roosta, "Reserve constrained dynamic economic dispatch: A new fast self-adaptive modified firefly algorithm," *IEEE Systems Journal*, vol. 6, no. 4, pp. 635–646, 2012.

[70] H. Zhong, Q. Xia, Y. Wang, and C. Kang, "Dynamic economic dispatch considering transmission losses using quadratically constrained quadratic program method," *IEEE Trans. Power Systems*, vol. 28, no. 3, pp. 2232–2241, 2013.

[71] M. Falahi, *Dynamic reactive power control of isolated power systems.* PhD dissertation, Texas A&M University, 2012.

[72] F. C. Lu and Y. Y. Hsu, "Reactive power/voltage control in a distribution substation using dynamic programming," *IEE Generation, Transmission and Distribution*, vol. 142, no. 6, pp. 639–645, 1995.

[73] Z. Yi and Z. Anan, "A fast adaptive MOEA and its application to dynamic reactive power optimization," in *International Conference on Computer Engineering and Technology*, vol. 4, pp. 141–143, 2010.

[74] F. Logist, B. Houska, M. Diehl, and J. Van Impe, "Fast Pareto set generation for nonlinear optimal control problems with multiple objectives," *Structural and Multidisciplinary Optimization*, vol. 42, no. 4, pp. 591–603, 2010.

[75] K. Deb, A. Pratap, S. Agarwal, and T. Meyarivan, "A fast and elitist multiobjective genetic algorithm: NSGA-II," *IEEE Trans. Evolutionary Computation*, vol. 6, no. 2, pp. 182–197, 2002.

[76] C. Hung-Ming, F. A. Ituzaro, and K. L. Butler-Purry, "A PC-based test bed for NG IPS ships in PSCAD," in *IEEE Electric Ship Technologies Symposium*, pp. 135–142, 2011.

[77] N. Doerry, "Zonal ship design," *Naval Engineers Journal*, vol. 118, no. 1, pp. 39–53, 2006.

[78] N. Doerry, "Designing electrical power systems for survivability and quality of service," *Naval Engineers Journal*, vol. 119, no. 2, pp. 25–34, 2007.

[79] N. Doerry, "Next generation integrated power system technology development roadmap," Technical Report Ser 05D/349, Naval Sea Systems Command, November 2007.

[80] B. Farhangi and K. L. Butler-Purry, "Transient study of DC zonal electrical distribution system in next generation shipboard integrated power systems using PSCAD," in *North American Power Symposium*, pp. 1–8, 2009.

[81] P. Mitra and G. K. Venayagamoorthy, "An adaptive control strategy for DSTATCOM applications in an electric ship power system," *IEEE Trans. Power Electronics*, vol. 25, no. 1, pp. 95–104, 2010.

[82] K. Deb, *Multi-objective optimization using evolutionary algorithms*. NY: John Wiley & Sons, 2008.

[83] K. Miettinen, *Nonlinear multiobjective optimization*. Boston, MA: Kluwer Academic Publishers, 1999.

[84] C. Hillermeier, *Nonlinear multiobjective optimization: a generalized homotopy approach*. Boston, MA: Birkhauser Verlag, 2001.

[85] Y. Collette and P. Siarry, *Multiobjective optimization: principles and case studeis*. NY: Springer, 2003.

[86] M. Reyes-sierra and C. A. C. Coello, "Multi-objective particle swarm optimizers: a survey of the state-of-the-art," *International Journal of Computaional Intelligence Research*, vol. 2, no. 3, pp. 287–308, 2006.

[87] J. Kennedy and R. C. Eberhart, "Particle swarm optimization," in *IEEE International Conference on Neural Networks*, pp. 1942–1948, 1995.

[88] S. M. Sait and H. Youssef, *Iterative computer algorithms with applications in engineering: solving combinatorial optimization problems*. Los Alamitos, CA: IEEE Computer Society, 1999.

[89] F. Xiao, *Risk based multi-objective security control and congestion management*. PhD dissertation, Iowa State University, 2007.

[90] D. A. V. Veldhuizen and G. B. Lamont, "Multiobjective evolutionary algorithms: analyzing the state-of-the-art," *Evolutionary computation*, vol. 8, no. 2, pp. 125–147, 2000.

[91] A. Konak, D. Coit, and A. Smith, "Multi-objective optimization using genetic algorithms: a tutorial," *Reliability Engineering and System Safety*, vol. 91, no. 9, pp. 992–1007, 2006.

[92] S. Bandaru, R. Tulshyan, and K. Deb, "Modified SBX and adaptive mutation for real world single objective optimization," in *IEEE Congress on Evolutionary Computation*, pp. 1335–1342, 2011.

[93] K. Deb and R. B. Agrawal, "Simulated binary crossover for continuous search space," *Complex Systems*, vol. 9, pp. 1–34, 1994.

[94] T. S. Dillon, "Rescheduling, constrained participation factors and parameter sensitivity in the optimal power flow problem," *IEEE Trans. Power Apparatus and Systems*, vol. PAS-100, no. 5, pp. 2628–2634, 1981.

[95] W. Xiuhua, P. Zailin, L. Yongliang, and L. Haiyan, "Reactive power and voltage control based on improved particle swarm optimization in power system," in *World Congress on Intelligent Control and Automation*, pp. 5291–5295, 2010.

[96] H. Oh, "Optimal planning to include storage devices in power systems," *IEEE Trans. Power Systems*, vol. 26, no. 3, pp. 1118 – 1128, 2010.

[97] C. Gonggui, C. Jinfu, and D. Xianzhong, "Power flow and dynamic optimal power flow including wind farms," in *International Conference on Sustainable Power Generation and Supply*, pp. 1–6, 2009.

[98] C. Haiyan, C. Jinfu, and D. Xianzhong, "Multi-stage dynamic optimal power flow in wind power integrated system," in *IEEE/PES Transmission and Distribution Conference and Exhibition: Asia and Pacific*, pp. 1–5, 2005.

[99] H. R. Stewart, "IEEE recommended practice for electrical installations on shipboard," IEEE Std 45-2002, IEEE, October 2002.

[100] Powertech Labs Inc., *Transient Security Assessment Tool (TSAT) user manual*, April 2011.

[101] A. K. Deb, *Power Line Ampacity System : Theory, Modeling, and Applications*. Boca Raton, FL: CRC Press, 2000.

[102] L. L. Grigsby, *Power system stability and control*. Boca Raton, FL: CRC Press, 2007.

[103] L. Wehenkel, C. Lebrevelec, M. Trotignon, and J. Batut, "Power system security assessment: a position paper," *Electra*, no. 175, pp. 48–78, 1997.

[104] P. Zhang, D. Hu, and L. Min, "Program on technology innovation: probabilistic dynamic security region," EPRI Technical Report 1015335, Electric Power Research Institute (EPRI), July 2007.

[105] J. McCalley and M. Ni, "Decision-making techniques for security constrained power systems," EPRI Technology Review 1001308, Electric Power Research Institute (EPRI), January 2001.

[106] N. Ming, J. D. McCalley, V. Vittal, and T. Tayyib, "Online risk-based security assessment," *IEEE Trans. Power Systems*, vol. 18, no. 1, pp. 258–265, 2003.

[107] D. S. Kirschen, "Power system security," *Power Engineering Journal*, vol. 16, no. 5, pp. 241–248, 2002.

[108] K. Tomsovic, A. Bose, P. Sauer, J. Tong, and A. Sittithumwat, "Integrated security analysis," PSERC Publication 03-06, Power Systems Engineering Research Center (PSERC), May 2004.

[109] V. Vittal, P. Sauer, S. Meliopoulos, and G. K. Stefopoulos, "On-line transient stability assessment scoping study," PSERC Publication 05-04, Power Systems Engineering Research Center (PSERC), February 2005.

[110] J. D. McCalley, S. Wang, Q. L. Zhao, G. Z. Zhou, R. T. Treinen, and A. D. Papalexopoulos, "Security boundary visualization for systems operation," *IEEE Trans. Power Systems*, vol. 12, no. 2, pp. 940–947, 1997.

[111] G. Zhou, *Power system security boundary visualization using intelligent techniques.* PhD dissertation, Iowa State University, 1998.

[112] K. Morison, W. Lei, and P. Kundur, "Power system security assessment," *IEEE Power and Energy Magazine*, vol. 2, no. 5, pp. 30–39, 2004.

[113] Y. Yu, "Direct methods for voltage and transient stability regions," EPRI Technical Update 1010553, Electric Power Research Institute (EPRI), November 2005.

[114] X. Yan, C. Ka Wing, and C. Tak Shing, "A TEF approach for solving transient stability constrained OPF," in *International Conference on Power System Technology*, vol. 2, pp. 1485–1489, 2004.

[115] L. N. Chen, Y. Tada, H. Okamoto, R. Tanabe, and A. Ono, "Optimal operation solutions of power systems with transient stability constraints," *IEEE Trans. Circuits and Systems*, vol. 48, no. 3, pp. 327–339, 2001.

[116] K. L. Teo and K. H. Wong, "Nonlinearly constrained optimal control problems," *Journal of the Australian Mathematical Society, Series B (Applied Mathematics)*, vol. 33, pp. 517–30, 1992.

[117] Y. Yu, "Direct methods for security regions of bulk power system," EPRI Technical Update 1008608, Electric Power Research Institute (EPRI), December 2004.

[118] J. L. C.-H. Awrejcewicz, *Bifurcation and chaos in nonsmooth mechanical systems.* River Edge, NJ: World Scientific, 2003.

[119] A. A. Irizarry-Rivera, *Risk-based operating limits for dynamic security constrained electric power systems.* PhD dissertation, Iowa State University, 1996.

[120] Z. Bo and C. Yi-jia, "Multiple objective particle swarm optimization technique for economic load dispatch," *Journal of Zhejiang University*, vol. 6A, no. 5, pp. 420–427, 2005.

[121] H.-J. Zimmermann, *Fuzzy set theory - and its applications.* London, UK: Kluwer Academic, 1996.

[122] Z. Xia and Z. Jiaqi, "Probabilistic transient stability assessment based on distributed DSA computation tool," in *International Conference on Probabilistic Methods Applied to Power Systems*, pp. 685–690, 2010.

[123] Powertech Labs Inc., *Transient Security Assessment Tool (TSAT) model manual*, April 2011.

[124] Powertech Labs Inc., *User-Defined Model Manual For Transient Security Assessment Tool (TSAT) and Small Signal Analysis Tool (SSAT)*, July 2011.

[125] P. Mitra and G. K. Venayagamoorthy, "Real time implementation of an artificial immune system based controller for a DSTATCOM in an electric ship power system," in *IEEE Industry Applications Society Annual Meeting*, pp. 1–8, 2008.

[126] N. G. Hingorani and L. Gyugyi, *Understanding FACTS: concepts and technology of flexible AC transmission systems.* NY: IEEE Press, 2000.

[127] M. Steurer, M. Andrus, J. Langston, L. Qi, S. Suryanarayanan, S. Woodruff, and P. F. Ribeiro, "Investigating the impact of pulsed power charging demands on shipboard power quality," in *IEEE Electric Ship Technologies Symposium*, pp. 315–321, 2007.

[128] S. L. Woodruff, Q. Li, and M. J. Sloderbeck, "Hardware-in-the-loop experiments on the use of propulsion motors to reduce pulse-load system disturbances," in *IEEE Electric Ship Technologies Symposium*, pp. 1–1, 2007.

[129] I. R. McNab, "Pulsed power for electric guns," *IEEE Trans. Magnetics*, vol. 33, no. 1, pp. 453–460, 1997.

[130] J. J. A. Van der Burgt, P. Van Gelder, and K. van Dijk, "Pulsed power requirements for future naval ships," in *IEEE International Pulsed Power Conference*, vol. 2, pp. 1357–1360, 1999.

[131] V. E. A. Van Acker, *Transient stability assessment and decision-making using risk.* PhD dissertation, Iowa State University, 2000.

[132] B. S. Everitt and G. Dunn, *Applied multivariate data analysis.* Chichester, UK: Wiley, 2010.

[133] D. J. Hand, *Discriminant Analysis, Linear.* Encyclopedia of Biostatistics, NY: John Wiley & Sons, 2005.

[134] Y.-Y. Hsu and C.-L. Chang, "Probabilistic transient stability studies using the conditional probability approach," *IEEE Trans. Power Systems*, vol. 3, no. 4, pp. 1565–1572, 1988.

[135] D. Z. Fang, L. Jing, and T. S. Chung, "Corrected transient energy function-based strategy for stability probability assessment of power systems," *IET Generation, Transmission and Distribution*, vol. 2, no. 3, pp. 424–432, 2008.

[136] E. Chiodo and D. Lauria, "Transient stability evaluation of multimachine power systems: a probabilistic approach based upon the extended equal area criterion," *IEE Generation, Transmission and Distribution*, vol. 141, no. 6, pp. 545–553, 1994.

[137] R. Billinton and P. R. S. Kuruganty, "Probabilistic assessment of transient stability in a practical multimachine system," *IEEE Trans. Power Apparatus and Systems*, vol. PAS-100, no. 7, pp. 3634–3641, 1981.

[138] J. McCalley, V. Vittal, and M. Ni, "On-line risk-based security assessment," EPRI Technology Review 1000411, Electric Power Research Institute (EPRI), November 2000.

[139] B. Cassimere, C. R. Valdez, S. Sudhoff, S. Pekarek, B. Kuhn, D. Delisle, and E. Zivi, "System impact of pulsed power loads on a laboratory scale integrated fight through power (IFTP) system," in *IEEE Electric Ship Technologies Symposium*, pp. 176–183, 2005.

[140] S. Kulkarni and S. Santoso, "Impact of pulse loads on electric ship power system: with and without flywheel energy storage systems," in *IEEE Electric Ship Technologies Symposium*, pp. 568–573, 2009.

[141] P. Mitra and G. K. Venayagamoorthy, "Artificial immune system based DSTATCOM control for an electric ship power system," in *IEEE Power Electronics Specialists Conference*, pp. 718–723, 2008.

[142] V. Salehi, B. Mirafzal, and O. Mohammed, "Pulse-load effects on ship power system stability," in *Annual Conference on IEEE Industrial Electronics Society*, pp. 3353–3358, 2010.

[143] F. Scuiller, "Simulation of an energy storage system to compensate pulsed loads on shipboard electric power system," in *IEEE Electric Ship Technologies Symposium*, pp. 396–401, 2011.

[144] E. Vaahedi, W. Li, T. Chia, and H. Dommel, "Large scale probabilistic transient stability assessment using BC Hydro's on-line tool," *IEEE Trans. Power Systems*, vol. 15, no. 2, pp. 661–667, 2000.

[145] K. Sastry, "Single and multiobjective genetic algorithm toolbox for Matlab in C++," IlliGAL Report No. 2007017, Illinois Genetic Algorithms Laboratory, June 2007.

[146] K. Deb and A. Kumar, "Real-coded genetic algorithms with simulated binary crossover: studies on multimodal and multiobjective problems," *Complex Systems*, vol. 9, no. 6, pp. 431–454, 1995.

[147] K. Deb and D. Deb, "Analyzing mutation schemes for real-parameter genetic algorithms," KanGAL Report 2012016, Kanpur Genetic Algorithms Laboratory, August 2012.

[148] C. Hung-Ming, F. A. Ituzaro, and K. L. Butler-Purry, "A PC-based test bed for NG IPS ships in PSCAD," in *IEEE Electric Ship Technologies Symposium*, pp. 135–142, 2011.

[149] T. E. Fortmann and K. L. Hitz, *An introduction to linear control systems.* NY: Dekker, 1977.

[150] T. T. Tay, I. Mareels, and J. B. Moore, *High performance control.* Boston, MA: Birkhäuser, 1998.

[151] R. C. Dorf and R. H. Bishop, *Modern control systems.* Reading, MA: Addison-Wesley, 1995.

[152] l. Zhang and W. Zeng, "Research on performance measures of multi-objective optimization evolutionary algorithms," in *International Conference on Intelligent System and Knowledge Engineering*, vol. 1, pp. 502–507, 2008.

[153] T. Okabe, Y. Jin, and B. Sendhoff, "A critical survey of performance indices for multi-objective optimization," in *IEEE Congress on Evolutionary Computation*, vol. 2, pp. 878–885, 2003.

[154] J. D. Knowles, L. Thiele, and E. Zitzler, "A tutorial on the performance assessment of stochastic multiobjective optimizers," TIK Report 14, ETH Zurich Computer Engineering and Network Laboratory, 2006.

[155] C. A. Coello Coello, G. B. Lamont, and D. A. Van Veldhuisen, *Evolutionary algorithms for solving multi-objective problems*. NY: Springer, 2007.

[156] E. Zitzler, L. Thiele, M. Laumanns, C. M. Fonseca, and V. G. da Fonseca, "Performance assessment of multiobjective optimizers: an analysis and review," *IEEE Trans. Evolutionary Computation*, vol. 7, no. 2, pp. 117–132, 2003.